

Rowan University

Rowan Digital Works

---

Theses and Dissertations

---

7-2-2016

## A mechanical study of cancer drug-receptor interactions, specifically in G-Quadruplex DNA and Topoisomerase I enzymes

Kelly Ann Mulholland  
*Rowan University*

Follow this and additional works at: <https://rdw.rowan.edu/etd>



Part of the [Bioinformatics Commons](#), and the [Pharmaceutics and Drug Design Commons](#)

---

### Recommended Citation

Mulholland, Kelly Ann, "A mechanical study of cancer drug-receptor interactions, specifically in G-Quadruplex DNA and Topoisomerase I enzymes" (2016). *Theses and Dissertations*. 1733.  
<https://rdw.rowan.edu/etd/1733>

This Thesis is brought to you for free and open access by Rowan Digital Works. It has been accepted for inclusion in Theses and Dissertations by an authorized administrator of Rowan Digital Works. For more information, please contact [graduateresearch@rowan.edu](mailto:graduateresearch@rowan.edu).

**A MECHANICAL STUDY OF CANCER DRUG-RECEPTOR INTERACTIONS,  
SPECIFICALLY IN G-QUADRUPLEX DNA AND TOPOISOMERASE I ENZYMES**

by

Kelly Ann Mulholland

A Thesis

Submitted to the  
Department of Chemistry and Biochemistry  
College of Science and Mathematics  
In partial fulfillment of the requirement  
For the degree of  
Master of Science in Bioinformatics  
at  
Rowan University  
May 6, 2016

Thesis Chair: Chun Wu, Ph.D.

© 2016 Kelly Ann Mulholland

## **Dedication**

I dedicate my thesis work to the late Fredrick Steiner Jr. who always pushed me to be the absolute best version of myself and to strive to accomplish my dreams. His infinite words of wisdom and encouragement will forever ring in my ears.



## **Acknowledgments**

I would like to take a moment to thank my research advisor and mentor Dr. Chun Wu. He has always provided me with endless guidance and encouragement and I am grateful to have had the opportunity to work beside him. His passion and dedication to his work has been absolutely inspiring to me and has been my motivation to continue on my educational journey. I would also like to thank my committee members, Dr. Subash Jonnalagadda and Dr. Mark Hickman, for their insight and support throughout this process. Finally, thank you to the members of Dr. Wu's research group.

This work was supported by Rowan Startup and SEED grant and the National Science Foundation under Grant NSF ACI-1429467 and XSEDE MCB160004.

## Abstract

Kelly Mulholland

A MECHANICAL STUDY OF CANCER DRUG-RECEPTOR INTERACTIONS,  
SPECIFICALLY IN G-QUADRUPLEX DNA AND TOPOISOMERASE I ENZYMES  
2015-2016

Chun Wu, Ph.D

Master of Science in Bioinformatics

Computational methods are becoming essential in drug discovery as they provide information that traditional drug development methods lack. Using these methods we provide information about the binding behavior of small molecules to two specific targets for current cancer therapeutics: G-quadruplex DNA and Topoisomerase I enzyme. The first study focuses on the compound Telomestatin, which induces apoptosis of various cancer cells with a relatively low effect on somatic cells due to its high selectivity toward G-quadruplex over duplex DNA. Three major binding poses were discovered: top end stacking, bottom end stacking and a groove binding. A high resolution structure of this complex does not yet exist, so this is the first time Telomestatin binding modes have been reported. The second study focuses on 8 Camptothecin class Topoisomerase I inhibitors, which have been reported to effectively treat multiple types of cancer, however are limited by their drug resistance. Recent computational studies have indicated that the mutations near the active binding site of the drug can significantly weaken the drug binding and may be a major cause of the drug resistance. Here, a complete study of each Camptothecin analog in each mutated complex in the active binding site is presented. Topotecan and Camptothecin have much smaller binding energy decrease than a set of new Camptothecin derivatives. Lucanthone, a non-Camptothecin, shows comparable results to Topotecan and Camptothecin. In addition, we found a trend between the distance a mutant is to a ligand and the binding energy.

## Table of Contents

Abstract .....	v
List of Figures .....	ix
List of Tables .....	x
Chapter 1: An Introduction to Computational Drug Design.....	1
1.1 Motivations for a Computational Approach .....	1
1.2 Basic Methodologies.....	2
1.2.1 Homology model construction.....	2
1.2.2 Molecular docking .....	3
1.2.3 Molecular dynamics simulations .....	3
1.2.4 MMGBSA binding energy calculations.....	4
1.3 Thesis Outline .....	5
Chapter 2: A Mechanical Study of Anti-Cancer Drug Resistance Caused by 10 Topoisomerase I Mutations, Including 7 Camptothecin Analogs and Lucanthone.....	8
2.1 Introduction.....	8
2.1.1 Topoisomerase I inhibitors .....	8
2.1.2 A history of camptothecin analogs .....	8
2.1.3 Drug resistance in camptothecin analogs.....	9
2.1.4 A computational approach to view drug resistance mechanisms .....	11
2.2 Methods.....	13
2.2.1 Ligand preparation .....	13
2.2.2 Homology model construction.....	13

## Table of Contents (continued)

2.2.3	Glide XP docking.....	14
2.2.4	MMGBSA binding energy calculations.....	15
2.3	Results.....	16
2.3.1	Subtle changes in ligand binding pose were discovered.....	16
2.3.2	Agreement between experimental and predicted results .....	17
2.3.3	Assessment of drug resistance in each ligand.....	20
2.3.4	Assessment of drug resistance in mutant complex .....	22
2.3.5	Analyzing the largest and smallest binding energy changes .....	24
2.4	Discussion .....	28
Chapter 3: A Mechanical Study of Telomestatin Binding to Telomeric G-Quadruplex DNA.....		
32		
3.1	Introduction .....	32
3.1.1	G-Quadruplex DNA as a pharmacological target.....	32
3.1.2	Telomestatin as a G-Quadruplex stabilizer.....	33
3.1.3	Telomestatin analog, L2H.....	34
3.1.4	A computational approach to study telomestatin binding behavior.....	35
3.2	Methods.....	36
3.2.1	Simulation system construction.....	36
3.2.2	Simulation protocols.....	38
3.2.3	Convergence of simulations .....	38
3.2.4	Binding mode identification.....	39
3.2.5	Parameters for characterizing DNA-drug complex.....	39

## Table of Contents (continued)

3.3 Results .....	44
3.1.1 Three drug binding modes were observed in binding simulations.....	44
3.1.2 MMGBSA binding energy data show the bottom binding mode is the most stable mode among the three modes .....	45
3.1.3 Top stacking of telomestatin displayed a similar binding pose to the L2H NMR complex.....	46
3.1.4 Bottom stacking of telomestatin has the greatest percent population and exhibits the strongest binding energy .....	47
3.1.5 Groove binding of telomestatin provides additional support for the selectivity of this ligand to G-quadruplex DNA .....	48
3.4 Discussion .....	49
References.....	53
Appendix A: A Mechanical Study of Anti-Cancer Drug Resistance Caused by 10 Topoisomerase I Mutations, Including 7 Camptothecin Analogs and Lucanthone.....	64
Appendix B: A Mechanical Study of Telomestatin Binding to Telomeric G-Quadruplex DNA.....	164

## List of Figures

Figure	Page
Figure 1. Topoisomerase I Inhibitors.....	9
Figure 2. Schematic Diagram of Mutated Residue Locations .....	10
Figure 3. Crystal Complex of Top 1 with Topotecan.....	11
Figure 4. Clustering of 8 Top 1 Inhibitors to WT and Mutant Complexes .....	14
Figure 5. Correlation Plots.....	18
Figure 6. Mean Change in Binding Energy for Each Top 1 Inhibitor .....	21
Figure 7. Mean Change in Binding Energy for Mutant.....	24
Figure 8. LESN38-D533G Mutated Complex .....	26
Figure 9. Lucanthone-G717V Mutated Complex .....	27
Figure 10. Structures of Telomeric DNA Quadruplex, Telomestatin and L2H.....	33
Figure 11. Comparison of all Telomestatin Binding Modes to L2H .....	37
Figure 12. A Representative Trajectory of Top Stacking Mode.....	41
Figure 13. A Representative Trajectory of Bottom Stacking Mode .....	42
Figure 14. A Representative Trajectory of Groove Binding Mode .....	43
Figure 15. A 3-D Representation of Residues Surrounding Telomestatin and L2H .....	51

## List of Tables

Table	Page
Table 1. Experimental and Predicted Binding Energy of Ligands to WT .....	19
Table 2. Experimental and Predicted Binding Energy Change of Camptothecin.....	19
Table 3. Summary of Using Telomestatin in Treating Various Cancers .....	34
Table 4. Binding Energy of Telomestatin to G-Quadruplex DNA.....	46

## Chapter 1

### An Introduction to Computational Drug Design

#### 1.1 Motivations for a Computational Approach

The traditional drug development process has been effective in designing medications for multiple diseases and illnesses; however it can often be a very costly process. The California Biomedical Research Association released a Drug Development Fact Sheet which discussed the timeline a typical drug follows from start to finish.<sup>[1]</sup> They stated that it takes about 12 years for a drug to travel from the laboratory to the pharmacy. In the drug discovery process, about 5,000-10,000 compounds are created, and of which only about 250 ever move on to pre-clinical studies. Roughly 5 of those 250 compounds are submitted for review by the FDA and only 1 will actually be approved to be placed on the market.<sup>[2]</sup>

The traditional drug discovery process involves exhausting laboratory work to develop a library of compounds that are speculated to work on a specific target. This process, which takes about 3-6 years according to PRMA, is the most costly in terms of both money and time.<sup>[2]</sup> To help solve this issue, computational tools have been developed that predict the binding behavior of a library of compounds to a specific target. Knowing which compounds have the greatest potential before synthesis is essential to quickly developing promising new drug candidates.

A computational approach to designing new drugs begins by studying the pharmacological target. Tools such as Maestro and AMBER are used to display high resolution coordinates in a way that is easy to visualize specific structures.<sup>[3,4]</sup> A library of



compounds can be filtered using high throughput screening (HTS) which screens the compounds based on whether or not they bind to the target in question. The lead compounds that are generated as a result can then be docked to the target and binding energy calculations can help predict which compound have the most favorable binding affinity. These methods, which can take as little as one week, assist traditional drug design in finding a handful of promising compounds to synthesis for further testing.

Utilizing computational methodology to better understand pharmacological mechanisms can provide deeper insights that experimental methods simply cannot. Not only do they aid in deciphering great drug candidates, but they also allow one to visualize the types of interactions that occur. This thesis implicates computational methods in two studies that evaluate both telomestatin to telomeric G-Quadruplex DNA and drug resistance mechanisms in Topoisomerase I inhibitors. The knowledge presented here will facilitate future construction of drugs that target these specific receptors.

## 1.2 Basic Methodologies

**1.2.1 Homology model construction.** Often times a high resolution structure of a receptor is unavailable. When this is the case, a homology model may be created utilizing the structure of a homolog as a template. By altering specific amino acids a desired mutant of the receptor can be achieved. Tools such as the Protein Preparation Wizard in Maestro can then check for inconsistencies in the coordinates, add charges where needed, and optimize the geometry of the complex as a whole.

**1.2.2 Molecular docking.** Determining which compounds bind to a particular target is the first step of filtering through a large library of compounds. Molecular docking software is utilized to accomplish this step. By first obtaining the high resolution coordinates of a receptor in question, the docking software generates a molecular surface for the receptor.<sup>[5, 6]</sup> It then generates the active binding site by filling it with spheres that denote the potential binding locations for atoms on a ligand. The spheres match to the atoms on the ligands to determine the orientations that the ligand may bind. Finally the software will score the best orientation and output a binding pose.

The scoring function will accurately calculate the binding affinity and score the poses of an active site higher than the poses of an inactive site. Finally, the function will score the correct pose of the active site higher than an incorrect pose of the active. The output of the scoring function is a final pose of the molecule in a binding site and a score that represents the strength of the binding which can be related to the binding affinity. The Glide docking program with extra precision (XP) was used in this study to perform a series of hierarchical searches for optimal ligand pose within the binding site of a receptor.

**1.2.3 Molecular dynamics simulations.** The binding interactions that occur within a complex can be understood using computational tools. Understanding these interactions can give insight to the binding behavior of a particular ligand to its target. Molecular dynamics (MD) simulations calculate the motion of atoms in a compound using Newtonian dynamics to determine the force and acceleration of each atom.<sup>[7]</sup> They can probe the structure, dynamics, position, velocity and interaction of a receptor with high spatial and temporal resolution. A MD simulation system utilizes high resolution

coordinates of a particular receptor and a set of parameters to determine its force fields.<sup>[7]</sup> These force fields are set parameters that describe both bonded and non-bonded interactions among atoms. Bonded interactions include a drug-based dihedral angle and unbonded interactions include van der Waals and electrostatic. The system maintains a constant temperature and pressure, and is surrounded by a solvent of water and ions. Implicit and Explicit solvent models can be used to develop a realistic model for interactions between solvent and a molecule.<sup>[8]</sup> The explicit solvent model uses thousands of solvent molecules and is therefore computationally exhausting. For that reason, implicit models are more commonly utilized. The implicit solvent model treats a solvent as a continuous medium using a dielectric constant.<sup>[8]</sup>

After the system is prepared, it is run until it reaches equilibrium. The time progression of the system can be recorded in the form of multiple snapshots, creating what is referred to as a trajectory. These snapshots have their own individual coordinates specific to the position of the atoms in the system. The ligand-receptor complex can be aligned and clustered into unique structural families based on a root mean square deviation (RMSD) of atomic positions to determine the most prevalent binding positions. Further analysis of the binding energy can also provide more details on the complex.

**1.2.4 MMGBSA binding energy calculations.** The binding energy of a ligand to its target receptor can explain a variety of details about the complex as a whole, as well as individual components. MMGBSA, or molecular mechanics generalized Born surface area, was utilized in this study to calculate the binding energy of all complexes.<sup>[9]</sup> This method was used because it allows for energy decomposition into separate components: electrostatic, van der Waals, and surface area. The calculations are performed first on the

receptor alone through minimization, then on the ligand alone.<sup>[9]</sup> Finally, the receptor-ligand complex is calculated and the output contains the contribution of each component on the total binding energy. This value provides a quantitative value in which to find the most favorable bindings. Since solute entropy is not included in our analysis, the binding energies by MMGBSA may over-estimate the true binding free energy (i.e. the binding affinity). However, when the solute conformational entropies in different binding poses are comparable, the relative binding free energy can be estimated from the relative MMGBSA binding energies.<sup>[10]</sup>

### 1.3 Thesis Outline

In Chapter 2, the effect of drug resistance on Topoisomerase I inhibitors is analyzed. Although Camptothecin and its analogs as Topoisomerase I inhibitors can effectively treat cancers, serious drug resistance has been identified for this class of anti-cancer drugs. Recent computational studies have indicated that the mutations near the active binding site of the drug can significantly weaken the drug binding and cause the drug resistance. However, only Topotecan and three mutations have been previously analyzed. Here we present a comprehensive binding study of 10 Topoisomerase 1 mutants (N722S, N722A, D533G, D533N, G503S, G717V, T729A, F361S, G363C, and R364H) and 8 inhibitors including 7 Camptothecin analogs as well as a new generation Topoisomerase I drug, Lucanthone. Utilizing Glide docking followed by MMGBSA calculations, we determined the binding energy for each complex. We examine the relative binding energy changes with reference to the wild type, which are linked to the degree of drug resistance. On this set of mutates, Topotecan and Camptothecin have much smaller binding energy decrease than a set of new Camptothecin derivatives

(Lurtotecan, LESN-38, Gimatécán, Exatécán and Belotécán) currently under clinical trials. Lucanthone shows comparable results to Topotecan and Camptothecin, indicating it may exhibit the least drug resistance and is therefore a promising candidate for future studies as a Topoisomerase I inhibitor. In addition, a trend is observed from our binding energy data that the shorter the distance of a mutant to a ligand, the greater the decrease in binding energy (with one exception). The decomposition of the binding energy together with 2D interaction diagrams of predicted binding poses help decipher the nature of the binding energy decrease. These results may be utilized to further advancement Topoisomerase I inhibitors that are resistant to mutations.

In Chapter 3, the binding complexes of Telomestatin and telomeric G-quadruplex DNA are evaluated. Telomestatin, a natural product isolated from *Streptomyces anulatus*, stabilizes telomeric DNA G-quadruplexes. Treatment with this ligand induces apoptosis of various cancer cells with a relatively low effect on somatic cells due to its high selectivity toward G-quadruplex over duplex DNA. A high resolution structure of a G-quadruplex in complex with telomestatin does not yet exist, and the binding nature of this ligand remains elusive as a result. In this study, we utilized molecular binding simulations and MMGBSA binding energy analysis to decipher the binding nature of Telomestatin to a telomeric G-quadruplex. We identified three major binding poses: bottom stacking, top stacking and a groove binding. The top mode resembles the pose observed in an NMR complex of the same G-quadruplex with telomestatin analog, L2H. The bottom and groove binding poses were not observed in the previous studies of L2H. The bottom stacking mode exhibited the most favorable binding energy among the three modes, while also partially intercalating into the telomeric quadruplex. The dynamic and

energetic properties of these three binding modes are thoroughly examined. “Flip-insertion” and “Slide-insertion” were observed in the bottom intercalation mode. Our finding also provides insight to design more selective DNA quadruplex ligands as anti-cancer agents in the future.

## Chapter 2

### A Mechanical Study of Anti-Cancer Drug Resistance Caused by 10 Topoisomerase I Mutations, Including 7 Camptothecin Analogs and Lucanthone

#### 2.1. Introduction

**2.1.1 Topoisomerase I inhibitors.** Camptothecin (Figure 1A) is a cytotoxic quinolone alkaloid that inhibits DNA enzyme Topoisomerase I (Top1) which is responsible for reducing torsional strain in DNA during replication. The compound, originally isolated in 1966 by Wall and colleagues from the Chinese *Camptothecin acuminata* tree,<sup>[11]</sup> showed remarkable anticancer activity in preliminary clinical trials but also low solubility and severe adverse drug reaction.<sup>[12]</sup> The efforts in creating more soluble Camptothecin analogs lead to two Top1 drugs, Topotecan (Hycamtin) and Irinotecan (Camptostar), which were approved by the FDA in 1996 (Ireontecan is a prodrug that is converted into LESN38 which is the actual Top1 inhibitor).<sup>[13, 14]</sup>

**2.1.2 A history of camptothecin analogs.** Hycamtin and Camptosar are widely used in treating small-cell lung cancer, ovarian cancer, and cervical cancer as second and third-line cancer therapeutics.<sup>[15-17]</sup> In 2014, the Hycamtin oral capsule was developed and approved by FDA. New optimizations are also undergoing to develop more effective anti-cancer drugs with less adverse effects (Figure 1A-C).<sup>[18]</sup> For example, Lurtotecan, which was developed in 1994 by Luzzio et al, exhibited much greater potency than Camptothecin as a Top1 inhibitor in cleavable complex enzyme assays and ex vivo cell cytotoxicity assays.<sup>[19]</sup> Belotecan, a water soluble derivative of Camptothecin, was recently approved for clinical use in South Korea. Gimotecan and Exatecan showed great progress

in solubility and clinical tolerability, making them great candidates as potential oral capsules.<sup>[20]</sup>

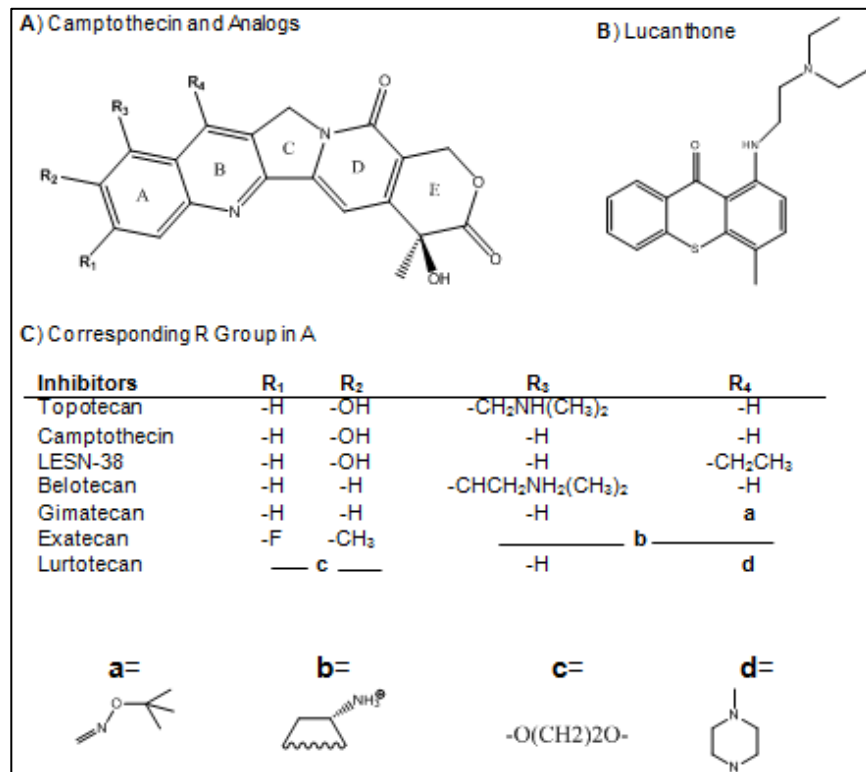


Figure 1. Topoisomerase I inhibitors

**2.1.3 Drug resistance in camptothecin analogs.** Despite these advances, however, drug resistance has been prevalent in Camptothecins.<sup>[21-23]</sup> Point mutations in the Top1-DNA cleavage complex, identified in both mammalian and yeast cell lines, are suggested to play a major role in drug resistance.<sup>[24]</sup> In 1999, Pommier and colleagues suggested eight mutations in the core domain and C-terminal domain (active binding site)



which may lead to Camptothecin resistance (Figure 2).<sup>[25]</sup> Figure 3 provides a visualization of these key residues relative to the Topotecan ligand. In 2004, Chrencik and colleagues provided a structural analysis on Topotecan bound to complexes F361S and N722S which shed even more light on the role of mutations in causing the drug resistance.<sup>[26]</sup> As resistance remains problematic to Camptothecin derivatives, experts are looking for non-Camptothecin drugs with less drug resistance. For example, Lucanthone has been investigated as a promising anti-cancer therapeutic (Figure 1C). Due to its ability to intercalate into Top1 as well as its unique scaffold, Lucanthone may exhibit lower drug resistance than the Camptothecin class.<sup>[27]</sup> Yet, further evidence remains to be reported.

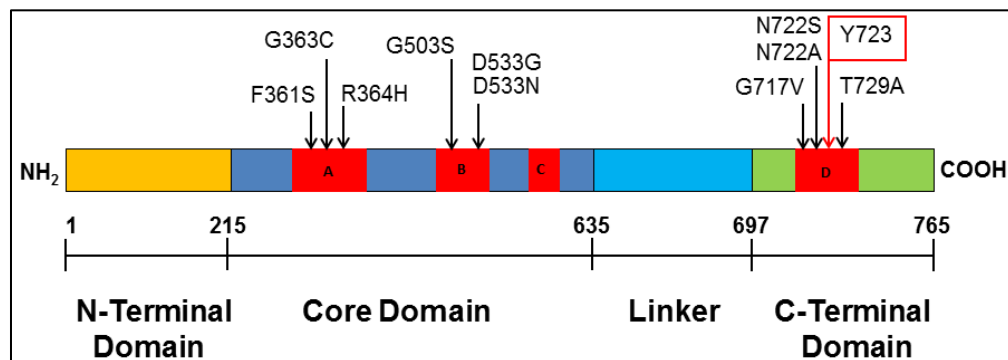
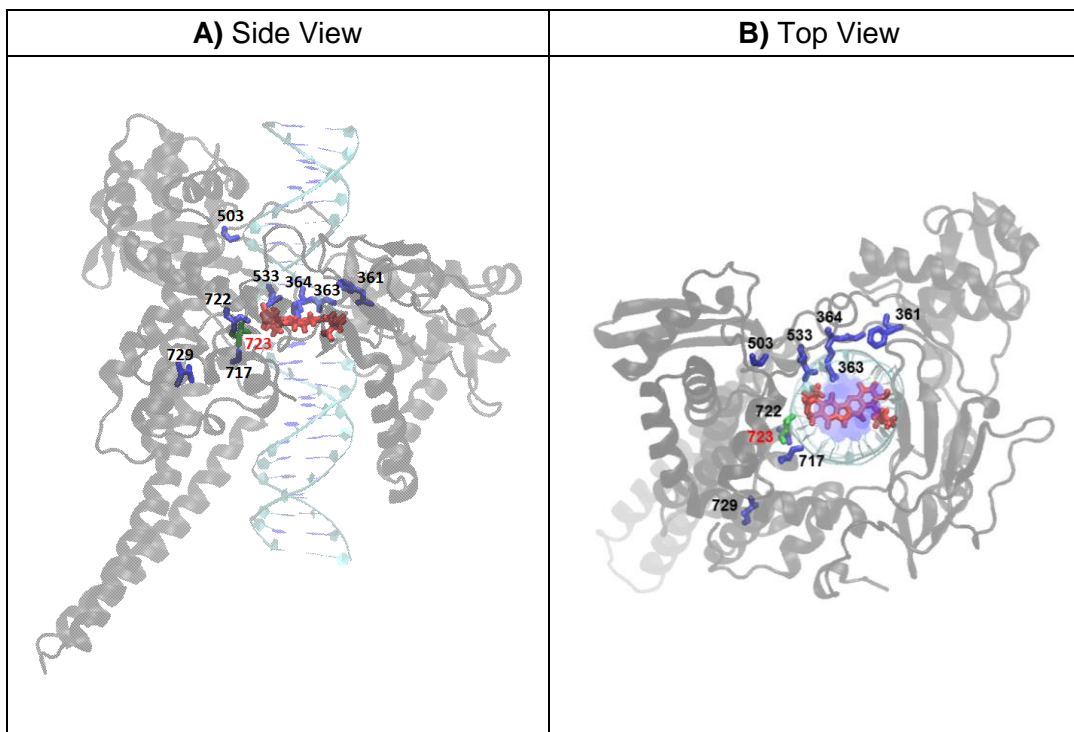


Figure 2. Schematic diagram of mutated residue locations



*Figure 3.* Crystal complex structure of Top 1 with Topotecan in red (PDB ID: 1K4T). The mutating residues are shown in blue, and the key catalytic residue, Y723, is shown in green.

#### 2.1.4 A computational approach to view drug resistance mechanisms.

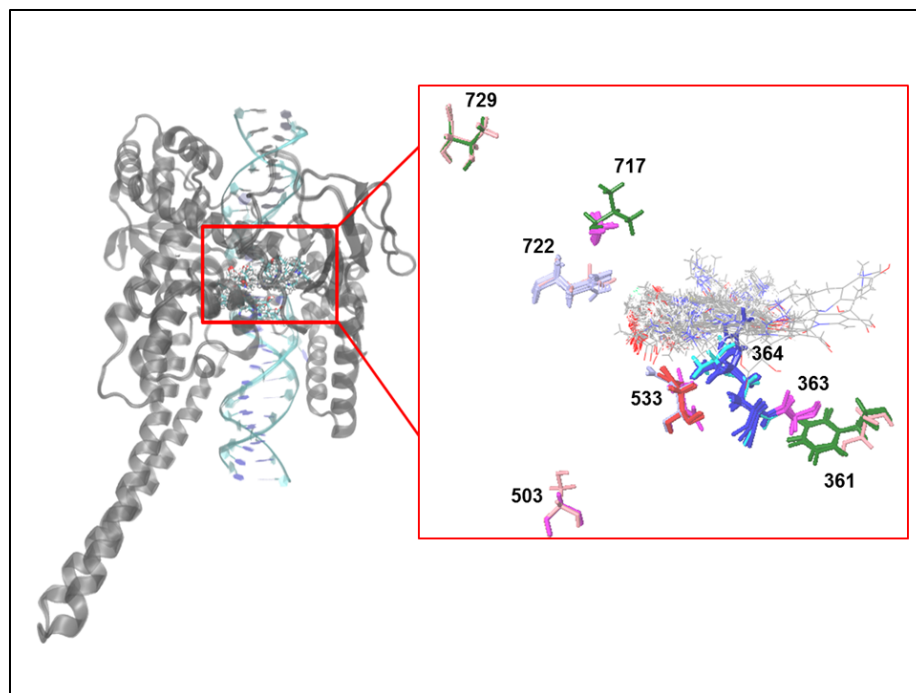
Molecular modeling and simulations have been recently used to decipher the mutation effects on drug binding affinity.<sup>[28, 29]</sup> In 2013, Pan and colleagues utilized molecular modeling to conduct a study on Topotecan resistance by three specific Top1 mutations. They discovered that the mutations E428K, G503S, and D533G also have significant influence on the binding affinities of Topotecan and could indeed be responsible for resistance seen in this drug.<sup>[29]</sup> However, a comprehensive study of major mutations on major Top1 drugs remains to be completed.

In this study, we utilized homology modeling of mutant complexes, Glide extra precision (XP) docking and MMGBSA (molecular mechanics generalized Born with surface area term) calculations to understand the effects of ten key point mutations on binding affinity of eight Top1 inhibitors. We compared these results to the wild type crystal complex, Top1-Topotecan complex (PDB: 1K4T), which provided structural insights on the drug resistance due to the mutations.<sup>[30, 31]</sup> The MMGBSA binding energy change upon a point mutation was calculated for each inhibitor in each mutant complex. A good correlation between our MMGBSA data and the available experimental binding data was obtained. Interestingly, we found that Topotecan and Camptothecin have much smaller binding energy decrease than a set of new Camptothecin derivatives (Lurtotecan, LESN-38, Gimatecan, Exatecan and Belotecan) currently under clinical trials. Lucanthone shows comparable results to Topotecan and Camptothecin, indicating it may exhibit the least drug resistance and is therefore a promising candidate for future studies as a Top1 inhibitor. To decipher the binding nature, we further decomposed the binding free energy to evaluate the contribution of each energetic component.

## 2.2. Methods

**2.2.1 Ligand preparation.** The eight Top1 ligand structures were either obtained from the ZINC database or created using ChemDraw Professional 15.0.<sup>[32]</sup> The ligands were prepared in three steps using Maestro Elements.<sup>[4]</sup> First, hydrogen atoms were added based valence, then Epik (an empirical pka prediction program) was utilized to determine the charge of the molecule at pH 7.<sup>[4]</sup> Finally, the geometry of each ligand was optimized by minimizing the potential energy.

**2.2.2 Homology model construction.** The wild type Top1 crystal structure in complex with topotecan, determined by Stalker et al using X-ray diffraction method, was obtained from the RCSB Protein Data Bank database (PDB id: 1K4T).<sup>[33]</sup> The complex was prepared using the protein preparation wizard of Maestro program in three steps: preprocessing, charge state determination and geometry optimization.<sup>[4]</sup> Using this wild type complex as a template, the ten mutated complexes were generated by altering each of their corresponding amino acids to achieve the point mutation at the desired residue location. These mutant complexes were then prepared using the protein preparation wizard (Figure 4).



*Figure 4.* Clustering of 8 Topoisomerase I inhibitors to WT and 10 Top 1 mutant complexes. For clarity, only WT Top 1 is shown in cartoon. Oxygen atoms are displayed in red, Nitrogen atoms are displayed in blue and Carbon atoms are displayed in yellow.

**2.2.3 Glide XP docking.** The Glide docking program with extra precision (XP) scoring was utilized in our docking study.<sup>[5, 6]</sup> This algorithm performs a series of hierarchical searches for optimal ligand pose within the binding site of a receptor. The first step involved a rough positioning and scoring followed by torsional energy optimization using the new and efficient OPLS3 non-bonded potential energy grid to endure potential poses.<sup>[34]</sup> The pose conformations of the best candidate were refined once again using Monte Carlo sampling. The final docked pose was accomplished and given a docking score, which combines both empirical and force field based terms. After generating a receptor-grid file, each ligand was docked to both the Top1 wild type

structure as well as each of the ten mutated homology models using Glide XP docking. The best ligand pose was output and used in MMGBSA binding energy calculations.

**2.2.4 MMGBSA binding energy calculations.** The MMGBSA binding energy was calculated for the complexes.<sup>[35]</sup> These calculations combine molecular mechanics and the continuum solvent model to calculate binding energy in a way that is less computationally exhaustive. The complexes were each partially minimized by relaxing the ligand and the side chains that were closest to the ligand while all other atoms were fixed. For each ligand, the protein-ligand complex ( $G_{\text{complex}}$ ), the free protein-DNA ( $G_{\text{pro+DNA}}$ ), and the free ligand ( $G_{\text{lig}}$ ) were all subjected to an energy minimization in implicit solvent (Equation 1). This utilizes the molecular mechanics (MM) methods to calculate ligand-receptor interaction energies ( $G_{\text{Conformation}}$ ,  $G_{\text{GBELE}}$ ,  $G_{\text{vdw}}$  and  $G_{\text{lipo}}$ ), with a Gaussian smooth dielectric constant functional method for the electrostatic part of solvation energy (i.e. GB term) and solvent-accessible surface for the non-polar part of solvation energy (Equation 2). Finally, the binding energy change of the mutant complex was calculated by using the wild type complex as the zero energy reference (Equation 3). Analysis of the decomposition of binding free energy values based on electrostatic, van der Waals, hydrophobic, and conformation interactions provides a more detailed understanding of the effect that resistance places on each complex. Two-dimensional diagrams aided in visualizing these decomposition values.

$$\text{Equation 1: } \Delta G = G_{\text{complex}} - G_{\text{pro+DNA}} - G_{\text{lig}}$$

$$\text{Equation 2: } \Delta G = G_{\text{conformation}} + G_{\text{GBELE}} + G_{\text{vdw}} + G_{\text{lipo}}$$

$$\text{Equation 3: } \Delta \Delta G = \Delta G_{\text{Mutant}} - \Delta G_{\text{WT}}$$

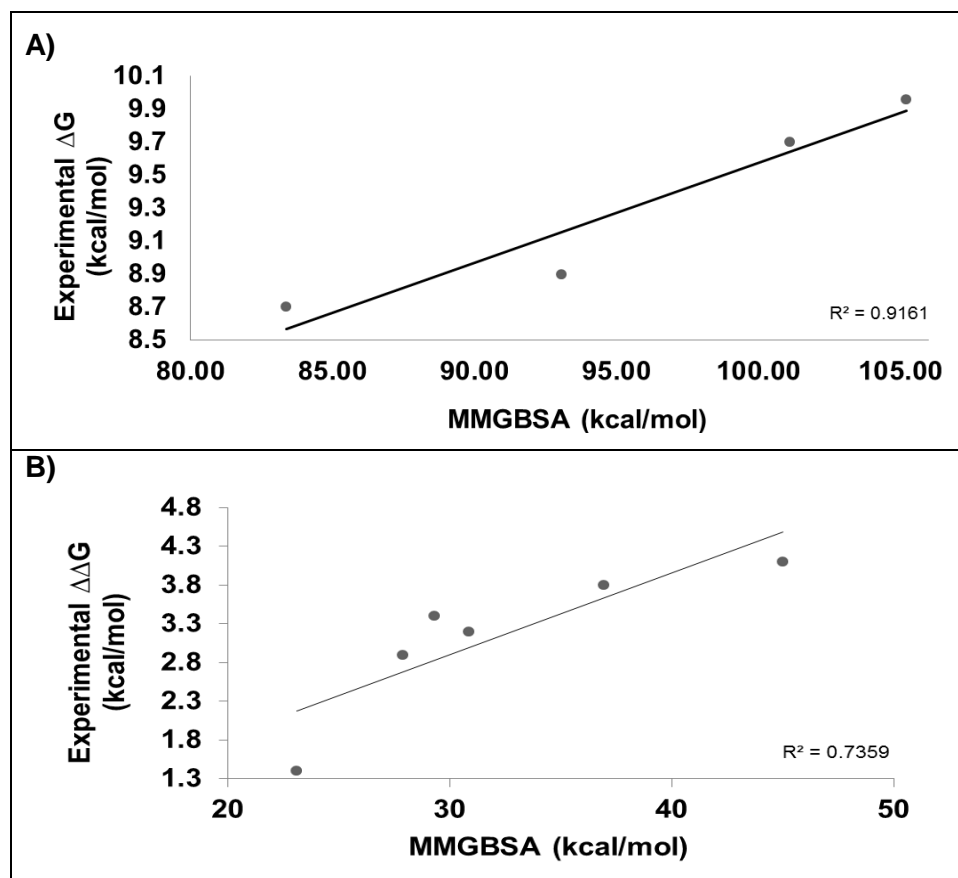
## 2.3 Results

### 2.3.1 Subtle changes in ligand binding pose were discovered. Mutant

homology model and Glide-docking results discovered subtle changes in ligand binding pose as well as side-chain conformation within each complex. We built homology models for 10 mutants based on the wild type crystal structure (Figure 3).<sup>[33]</sup> We then docked each ligand to the homology models and performed MMGBSA calculations in which three geometry optimizations were conducted on a receptor only system, ligand only system and the complex, followed by energy calculation.<sup>[35]</sup> The MMGBSA binding energies and its components are tabulated in the Appendix (Table S1-S8). To visualize the subtle binding pose changes of the ligand within the mutant structure, we superimposed the structure of all complexes based on the sequence alignment. The aligned, 3-Dimensional (3D) representation of each ligand when bound to the complexes can be seen in Figure 4. The binding pose of ligand in each ligand-mutant complex is very similar to the crystal binding pose in Figure 3, in which the lactone ring of ligand binds closely to the active Tyrosine 723 residue. However, we noticed subtle conformation change for both the ligand (Figure 3) and the side chains of the interacting residues with the ligand (data are not shown). The 3D structure of both top view and side view, 2D interaction diagram and of  $\Delta\Delta G$  Decomposition for each complex are included in the Appendix (Figure S4-S83). The interacting residues of each complex (mutant and wild type) with the ligands is also available and provides insight into which residues are present 5Å from the active binding site of each complex (Table S9-19). Again, the subtle differences can be observed for different ligands and different mutants.

**2.3.2 Agreement between experimental and predicted results.** A favorable agreement between experimental binding affinity and calculated binding energy validated the use of computational methods in this study. To validate our computational results, we collected the existing IC<sub>50</sub> values for Camptothecin derivatives on WT Top1 (Table 1). Encouragingly, there is a good agreement between experimental and our predicted values, the correlation coefficient is 0.9161 (Figure 5A). In addition, the IC<sub>50</sub> fold change of Camptothecin in each of these mutated complexes has been also experimentally determined (Table 2).<sup>[25, 36-41]</sup> Our binding free energy data shows the same ranking order in the fold change: N722A > G717V > D533N > G503S > R364H (Figure S1A). The Resistance Correlation Plot (Figure 5B) shows an excellent agreement between the experimental findings and our calculations, giving 0.736 of correlation coefficient. XP docking scores exhibited a lower correlation to the experimental values, so MMGBSA data was used throughout the study.





*Figure 5.* Correlation Plots. **A)** Correlation Between Experimental and Predicted Change in Binding Free Energy of Four Ligands to WT Top 1 (Table 1) **B)** Correlation Between Experimental and Predicted Binding Free Energy Change of Camptothecin to eight Top 1 Mutants (Table 2).

Table 1

*Experimental and predicted binding (free) energy of ligands to wild type Top1.* <sup>16, 18,11, 19</sup>

$$\Delta G_{Binding} = RT \times \ln(IC_{50})$$

Ligand	IC50	Experimental $\Delta G^*$ (kcal/mol)	$\Delta MMGBSA$ (kcal/mol)
Topotecan	50	-10.0	-105.2
LE-SN38	77	-9.7	-101.1
Camptothecin	300	-8.9	-93.1
Lurtotecan	416	-8.7	-83.4

Table 2

*Experimental and predicted binding free energy change of Camptothecin to Top 1 Mutants.* <sup>37,38,25,39,40,41,42</sup>

Mutant	Experimental FC*	Experimental $\Delta\Delta G$ (kcal/mol)	$\Delta\Delta MMGBSA$ (kcal/mol)
T729A	10	1.4	23.1
G503S	134	2.9	27.9
D533N	220	3.2	30.9
D533G	300	3.4	29.3
G717V	600	3.8	36.9
N722S	974	4.1	45.0

\*FC: fold change of dissociation equilibrium constant in comparison to wild type

**2.3.3 Assessment of drug resistance in each ligand.** Among the eight Top1 Inhibitors, Camptothecin, Topotecan and Lucanthone exhibited the lowest mean change in the binding energy to the ten TOP1 mutants. We carried out the MMGBSA binding energy calculations of each docked drug in each complex. The data was organized appropriate to answer two questions: which drug exhibits the lowest resistance to the ten mutants and which mutant complex is responsible for causing the most resistance to these eight drugs. To answer the first question, we group our  $\Delta\Delta G$  data based on the ligand (Figure S1). The mean change in MMGBSA binding energies and standard deviations over the ten mutants were calculated and ordered in Figure 6. In details, the mean change in MMGBSA binding energy in the ten mutated complexes for Camptothecin was 19.2 kcal/mol. This predicted drug resistance was the second lowest following Topotecan. The difference in binding energy between the Camptothecin bound to the wildtype complex and the mutated complexes ranged from 9.1 kcal/mol (R364H) to 38.8 kcal/mol (F361S). Topotecan saw a mean change in binding energy of 18.8 kcal/mol, which was in fact the lowest of all the drugs in this particular study. The predictions ranged from 9.8 kcal/mol (R364H) to 26.8 kcal/mol (D533N). Lucanthone, with the third lowest mean binding energy, had a value of 21.8 kcal/mol. Complex G717V was the lowest of these calculations at 10.3 kcal/mol, while Complex G363C was the highest at 45.8 kcal/mol. The mean binding energy for Lurtotecan was 26.0 kcal/mol. Complex T729A at 12.2 kcal/mol was the lowest, while Complex F361S had the highest at 33.5 kcal/mol. LESN-38 had a mean binding energy of 28.5 kcal/mol. The lowest can be seen in Complex R362H at 15.5 kcal/mol and the highest is Complex D533G at 64.7 kcal/mol. Gimatocan had a mean binding energy of 31.5 kcal/mol. The binding energies for this compound

when bound to mutated complexes ranged from 13.8 kcal/mol (F361S) to 50.4 kcal/mol (D533N). The mean change in binding energy for Exatecan was 32.785 kcal/mol. The predicted range ranged from 10.7 kcal/mol (D533G) to 53.4 kcal/mol (R364H). The largest average change in binding energy between the wildtype and the mutations can be seen when Belotecan is bound to these complexes. The mean predicted binding energy for this compound is 38.9 kcal/mol. The lowest change in binding energy can be seen in R364H at 28.0 kcal/mol, while the highest can be seen in G503S at 49.7 kcal/mol. Clearly, Lucanthone, Lurtotecan, LESN38, Gimatecan, Exatecan and Beotecan have higher mean binding energy change than Topotecan, Camptothecin and Lucantohone, indicating that the former group might have higher drug resistance than the latter group.

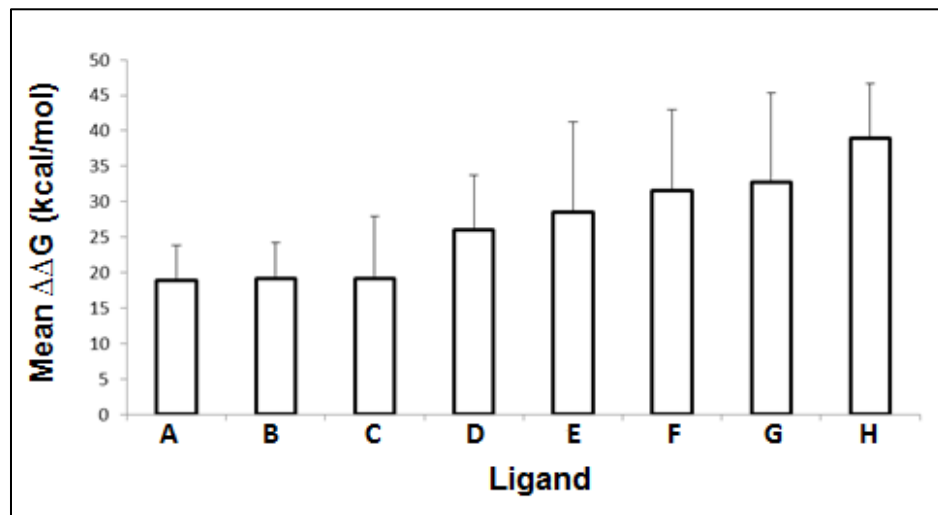


Figure 6. Mean change in binding energy ( $\Delta\Delta G$ ) for each Topoisomerase I inhibitor. A) Topotecan B) Lucanthone C) Camptothecin D) Lurtotecan E) LESN38 F) Gimatecan G) Exatecan H) Belotecan

**2.3.4 Assessment of drug resistance in mutant complex.** Among 10 TOP1 mutants, D533G exhibits the highest mean resistance and T729A the lowest resistance for these 8 drugs. To answer the second question, we cluster our  $\Delta\Delta G$  data based on the mutant (Figure S2). The mean change in MMGBSA binding energy was calculated as well as the standard deviation and the center-to-center distance from the mutant residue to the ligand (Figure 7). The lowest mean change in binding energy can be seen in Complex T729A with at 22.0 kcal/mol. The lowest predicted value for this complex was Camptothecin at 10.7 kcal/mol, and the highest was Belotecan at 44.4 kcal/mol. Complex R364H has a mean change in binding energy of 22.5 kcal/mol. The predicted values range from 9.1 kcal/mol (Camptothecin) to 53.4 kcal/mol (Exatecan). The mean change in binding energy for Complex G717V is 23.4 kcal/mol. The lowest change between wildtype and this particular mutant complex can be seen in Lucanthone (10.3 kcal/mol), while the highest is Exatecan (37.1 kcal/mol). Complex F361S has a mean change in binding energy of 26.0 kcal/mol. The predicted values ranged from 13.8 kcal/mol (Gimatecan) to 38.8 kcal/mol (Camptothecin). Complex G503S has a mean of 26.3 kcal/mol. The lowest change between wildtype and G503S can be seen in Camptothecin (11.1 kcal/mol), while the highest is Belotecan (47.7 kcal/mol). The mean change in binding energy for Complex G363C is 28.9 kcal/mol. The predicted values ranged from 14.6 kcal/mol (Lurtotecan) to 45.8 kcal/mol (Belotecan). Complexes N722S/A have a mean change in binding energy of 29.2 kcal/mol. The lowest change between wildtype and this particular mutated complex can be seen in Camptothecin (21.8 kcal/mol), while the highest is Exatecan (41.0 kcal/mol). Complex D533N has a mean change in binding energy of 32.5 kcal/mol, making it the second largest change in binding energy of all the

mutated complexes. The predicted values range from 16.7 kcal/mol (Camptothecin) to 50.4 kcal/mol (Gimatecan). The highest mean value is seen in Complex D533G with a predicted value of 22.0 kcal/mol. The lowest change between wildtype and this particular mutated complex can be seen in Exatecan (10.7 kcal/mol), while the highest is LESN38 (64.7 kcal/mol).

Our data suggest a negative correlation between the mutation-ligand distance and the binding energy decrease (Figure 7). We observed that the closer the mutated residue is to the active binding site, the higher the decrease in binding free energy for the drug-mutant complex; and vice versa. There was one exception in this pattern, complex R364H, which is about 3 Å from the binding site and showed a lower change in the binding free energy. Interestingly, we discovered through the decomposition of each drug-R364H complex binding energy that electrostatic interaction generally contributed significantly to the stabilization of the histidine in this mutation. Due to its lower polarity when compared to the wild type arginine residue, the histidine forms more hydrogen bonds with the surrounding residues (Figure S3). In contrast, G363C with the similar mutation-ligand distance followed the general trend and did not get the electrostatic stabilization.

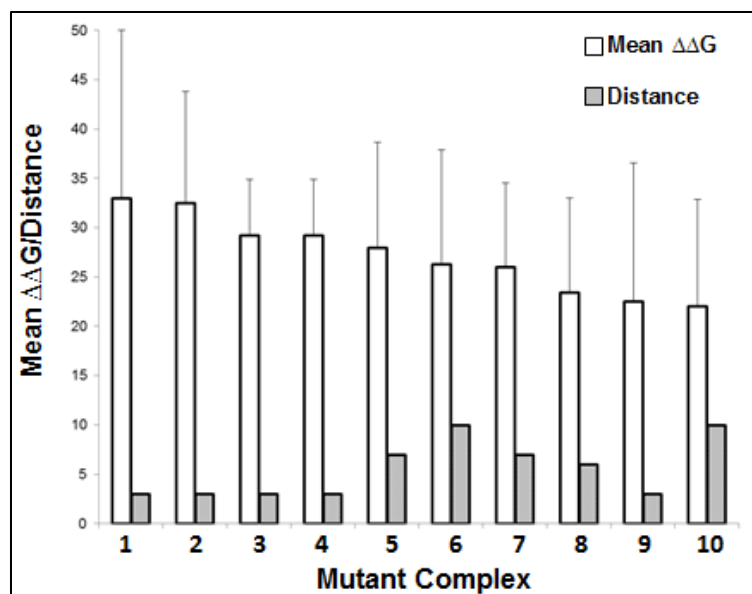
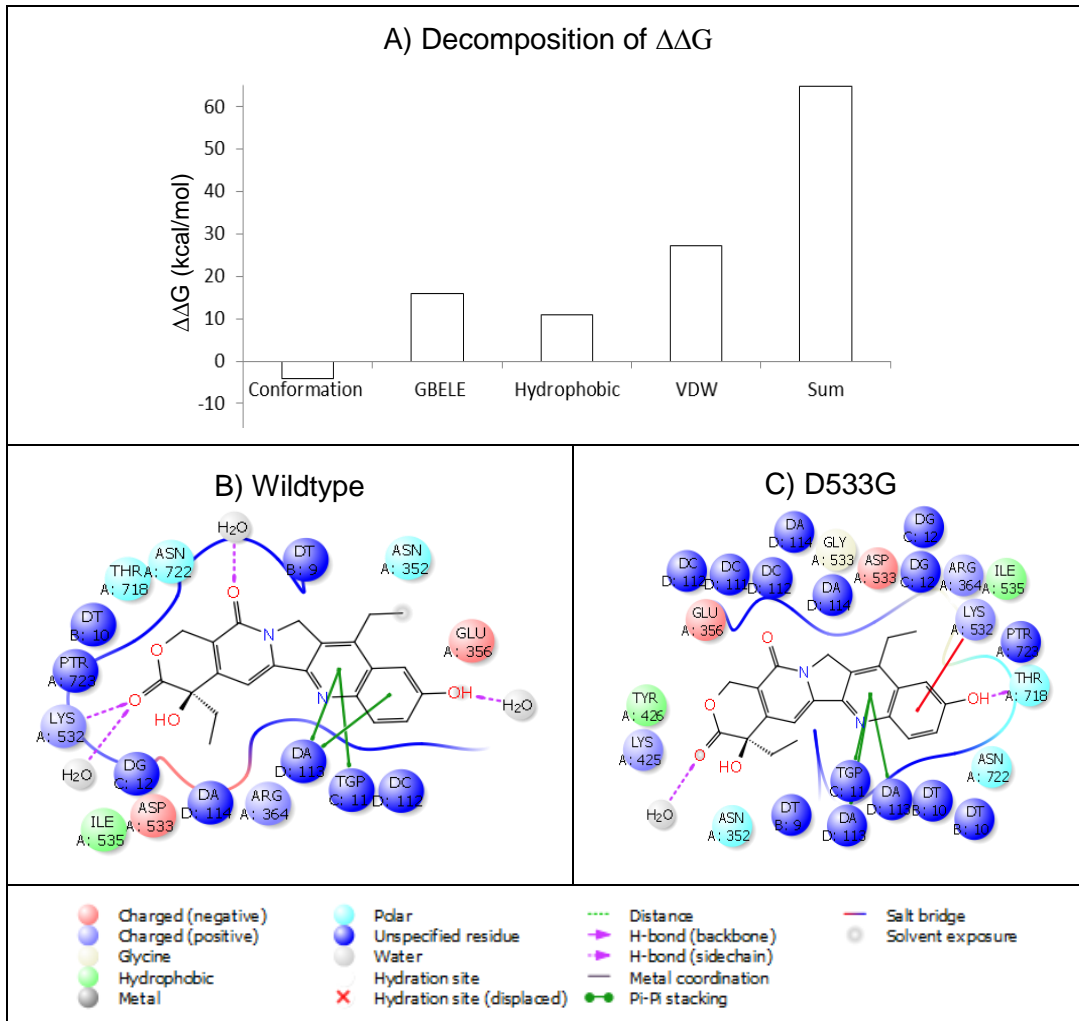


Figure 7. Mean binding energy change ( $\Delta\Delta G$ ) for each mutant and center-to-center distance from mutated residue to ligand. 1) D533G 2) D533N 3) N722A 4) N722S 5) G363C 6) G503S 7) F361S 8) G717V 9) R364H 10) T729A

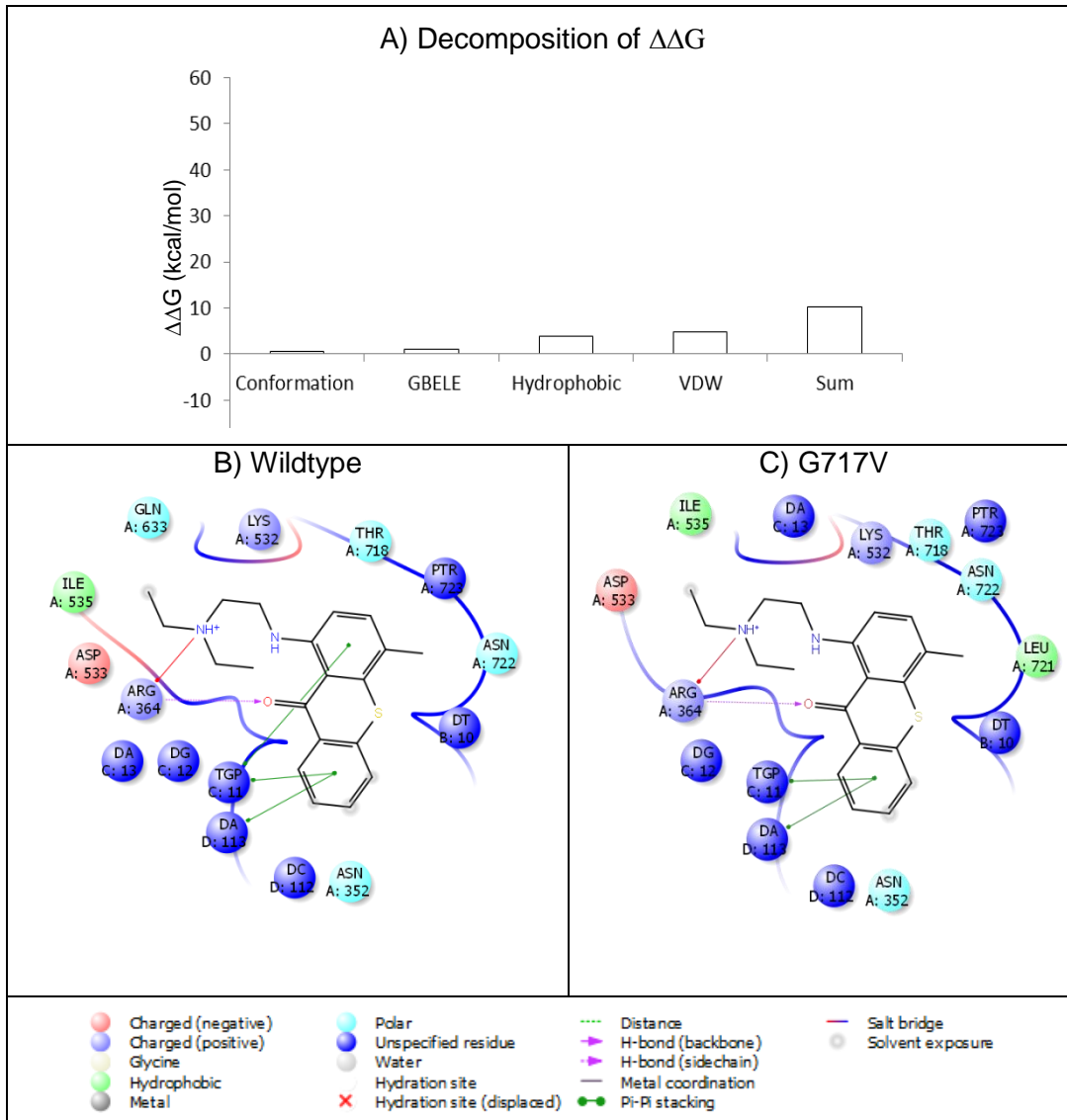
**2.3.5 Analyzing the largest and smallest changes in binding energy.** Whereas complex SN38-D533G show largest decrease of binding energy change, Lucanthone-G717V show least decrease of binding energy change. Complex Resistance was noticed in each complex after a thorough evaluation of both 2D interaction diagrams and MMGBSA binding energy of each mutated complex (see Figures S4-83). Upon further inspection of each mutant-drug complex two complexes were particularly interesting. Complex LESN38-D533G (Figure 8) exhibited the highest resistance with a binding free energy change ( $\Delta\Delta G$ ) of 64.7 kcal/mol. Decomposition indicates a high electrostatic (GBELE) and van der Waal (VDW) contribution (Figure 8A). Significant contribution from van der Waal results in the loss of hydrogen bonding, which can be seen in the loss of hydrogen bonds to both a water molecule and Lys 532 which is not present in the

LESN38-D533G complex (Figure 8B-C). The Lucanthone-G717V Complex exhibits relatively low resistance when compared to the other 79 complexes (Figure 9A). With a binding free energy value of 10.3 kcal/mol, there are both hydrophobic and van der Waals contributions that may be responsible for the loss of  $\pi$ - $\pi$  stacking between TGP11 and Ring A that is seen in the Lucanthone-WT complex, but not the Lucanthone-G717V complex (Figure 9B-C). This finding is especially interesting due to the fact that Lucanthone, a non-Camptothecin Top1 inhibitor, is significantly less resistant to each of the mutated complexes when compared to each Camptothecin analog. Furthermore, SN-38, whose prodrug was approved by the FDA in 1998 for the treatment of cancers in the colon and rectum, exhibits significant resistance to all of the mutated complexes.<sup>[42]</sup> The decomposition of binding free energy along with two-dimensional diagrams obtained through molecular docking provides insight into the resistance mechanisms of each of these complexes (Figures S4-83). Understanding the contributions to resistance for allows for more accurate drug optimization and design





*Figure 8.* LESN38-D533G mutated complex. A) Decomposition of  $\Delta\Delta G$  into conformation, GBELE, hydrophobic and van der Waal components, B) 2D interaction diagram of the LESN38-wildtype complex, C) 2D interaction diagram of the LESN38-D533G complex



*Figure 9.* Lucanthone-G717V mutated complex. A) Decomposition of  $\Delta\Delta G$  into conformation, B) 2D interaction diagram of the Lucanthone-wildtype complex, C) 2D interaction diagram of the Lucanthone-G717V complex

## 2.4 Discussion

Due to the limited rotation in cells, strand separation in DNA by polymerase-helicase complexes can induce supercoiling, creating tension at the replication fork. DNA Top1 prevents the torsional stress of supercoiled DNA by nicking a strand of DNA resulting in a relaxed complex.<sup>[31]</sup> This mechanism of action involves a key residue, Tyrosine 723, which induces nucleophilic attack on a DNA phosphodiester bond through an esterification reaction forming a covalent 3'-phosphotyrosine binary enzyme-DNA complex.<sup>[43]</sup> This new bond is then attacked by the hydroxyl group on the DNA strand and the double-stranded DNA is released. When relegation does not occur, Top1 will remain attached to DNA, blocking the replication fork, and apoptosis will result.<sup>[44]</sup> Camptothecin and its analogs bind to this active site, inhibit the normal function of Top1, and as a result have been extensively studied as cancer therapeutics. To date, there are two Top1 drugs approved by the FDA, and even more undergoing clinic development. These drugs have been widely used in treating small-cell lung cancer, ovarian cancer, and cervical cancer as second and third-line cancer therapeutics.<sup>[15-17]</sup> However, point mutations have been identified as one of the major mechanisms that lead to serious drug resistance.<sup>[22,23]</sup>

Molecular modeling and simulations are powerful tools used to probe the mutation effects on drug resistance. Previous research conducted on the effects of mutations on Camptothecin has provided insight into the experimentally determined cellular resistance exhibited in these complexes.<sup>[24-26,45]</sup> Pan et al. has investigated the Topotecan binding affinity changes due to three point mutations (e.g. E418K, G503S, and D533G) using molecular dynamics simulations followed by MMGBSA binding energy calculations.<sup>[29]</sup>

The binding energy changes from their calculations correlate well with the drug resistance data. Although these studies provide invaluable insights on the Topotecan drug resistance caused by three common point mutations, the effects that all known mutations have on other Top1 drugs remains elusive. In this study, we utilized glide XP docking followed by MMGBSA calculations to analyze the role ten mutations play on the resistance of Top1 to Camptothecin, seven Camptothecin derivatives, and a non-Camptothecin, Lucanthone.

To validate our calculations, we first correlated our predictions against known experimental data. The correlation coefficient between our MMGBSA binding data and the experimental  $IC_{50}$  of four compounds to the wild type Top1 is 0.916. The correlation coefficient between our binding energy changes and the experimental  $IC_{50}$  change due to ten point mutations is 0.736. Following this validation, we extended our analysis to eight drugs and ten mutations. By applying the same calculations to every ligand-mutant complex, we determined that resistance is indeed exhibited throughout. Interestingly, Camptothecin, Lucanthone and Topotecan have the lowest mean resistance to the mutated complexes. The next-generation drug, Lucanthone, is expected to exhibit differences in resistance as it does not share a similar molecular scaffold to the Camptothecin analogs. However, it is surprising that SN-38 (FDA-approved Camptosar) and the other Camptothecin analogs show significantly higher resistance to Camptothecin and Topotecan.

Providing an alternative perspective, the mean change in binding free energy was organized according to mutant complexes to identify the mutation (Figure 7).

Interestingly, we observed that the furthest residue (T729A at  $10+\text{\AA}$  distance) from the

ligand has the least resistance while the residue closest to the ligand (D533G/N at 3Å distance) has the highest resistance overall (Figure 7). This finding confirms that the location of the mutation indeed plays an important role in the functionality of the Top1-drug complex. Complex R364H was the only outlier, and when compared to the closest residue, complex G363C, we discovered that the histidine may be responsible for the lower binding energy because it forms more hydrogen bonds with the surrounding residues due to its low polarity (Figure S3).

Computational methods are becoming more and more important in drug discovery as these methods economically provide detailed structural and energetic information that traditional drug development methods lack. By understanding drug-target interactions in detail, researchers are able to efficiently design promising drug candidates. In our study we utilized Glide XP docking and MMGBSA calculations to analyze resistance mechanisms of ten mutations surrounding the active binding site of Camptothecin, its analogs and a next-generation Top1 inhibitor, Lucanthone. To validate our calculations, we first correlated our predictions against known experimental data. The correlation coefficient between our MMGBSA binding data and the experimental IC<sub>50</sub> of four compounds to the wild type Top1 is 0.916. The correlation coefficient between our binding energy changes and the experimental IC<sub>50</sub> change due to ten point mutations is 0.736. Our data shows that a binding energy change is present in every drug-mutant complex. However, the magnitude of the change depends on the specific mutation and the ligand structure. Among the eight Top1 inhibitors, Camptothecin, Topotecan and Lucanthone exhibit the lowest mean change in the binding energy to the ten Top1 mutants. Among 10 Top1 mutants, D533G exhibits the highest mean resistance and

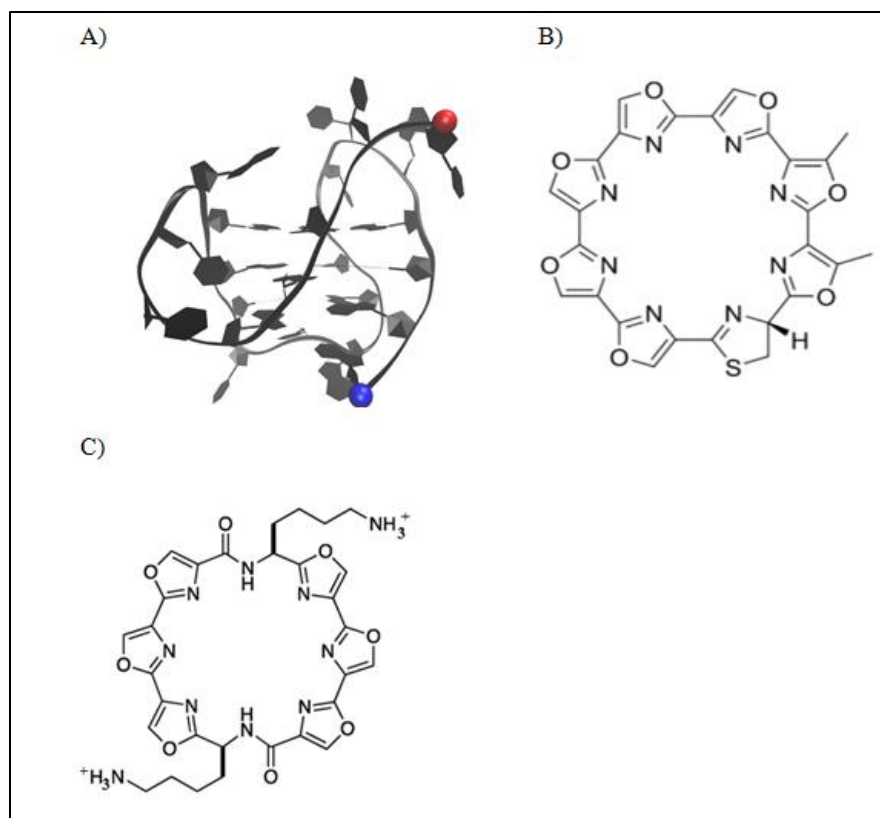
T729A the lowest resistance for these 8 ligands. Interestingly, we observed that the furthest residue (T729A at 10+Å distance) from the ligand has the least resistance while the residue closest to the ligand (D533G/N at 3Å distance) has the highest resistance overall. Our detailed binding information will be valuable for future Top1 inhibitor modifications. Our study on Top1 inhibitors supports the use of computational approaches in assessing mutation effects on drug resistance quickly and with reasonable accuracy for other anti-cancer/anti-virus drugs where point mutations are one of the major sources of drug resistance.

## Chapter 3

### A Mechanical Study of Telomestatin Binding to Telomeric G-Quadruplex DNA

#### 3.1 Introduction

**3.1.1 G-Quadruplex DNA as a pharmacological target.** G-quadruplex DNA consists of multiple stacked guanine-tetrads bound by Hoogsteen base pairing (Figure 10A).<sup>[46, 47]</sup> Computational tools have identified over 350,000 putative G-quadruplex sequences in the human genome, both the promoter regions of genes as well as within telomeres.<sup>[48, 49]</sup> Recent experimental research has confirmed the existence of G-quadruplexes in human cells.<sup>[50-56]</sup> For example, in 2013 Lam and colleagues discovered evidence of G-quadruplexes in sub-telomeres, gene bodies and gene regulatory regions using a quadruplex specific antibody.<sup>[57]</sup> These complexes are over-represented specifically in DNA damage regions and happen to appear more frequently in tumors than in normal tissues.<sup>[58-61]</sup> For that reason, quadruplexes have gained interest as emerging pharmacological targets for developing cancer therapeutics.<sup>[58-62]</sup> The formation of stable G-quadruplexes in the telomere inhibits telomerase by preventing the hybridization of the DNA single strand with the telomerase RNA template. Telomerase elongates the telomere by synthesizing telomeric 'TTAGGG' repeats,<sup>[63, 64]</sup> which is otherwise shortened and eventually leads to apoptosis. Because telomerase is overexpressed in about 85% of cancers,<sup>[65]</sup> inhibiting telomeric G-quadruplexes is a promising anti-cancer strategy.<sup>[66]</sup>



*Figure 10.* Structure of a telomeric DNA quadruplex (A), telomestatin (B), telomestatin analog L2H (C). 5' and 3' of the DNA chain are indicated by a red and blue ball, respectively.

**3.1.2 Telomestatin as a G-Quadruplex stabilizer.** G-quadruplex-specific ligands enhance this mechanism by binding to and stabilizing the telomeric G-quadruplexes.<sup>[67-69]</sup> In addition, G-quadruplex-specific ligands compete with POT1 (protection of telomeres protein 1), which uncaps telomeres, activates a DNA damage response mechanism, and eventually triggers apoptosis of cancer cells.<sup>[70, 71]</sup> Telomestatin, a natural product isolated from *Streptomyces anulatus*, presumably stabilizes telomeric G-quadruplexes (Figure 10B).<sup>[72-74]</sup> Treatment with this ligand



induces apoptosis of various cancer cells with a relatively low effect on somatic cells due to its high selectivity toward G-quadruplex over duplex DNA.<sup>[75]</sup> Recent studies on Telomestatin's potency in multiple cancer cell lines (e.g. leukemic, neuroblastoma, cervical cancer, etc.) suggest the potential of this natural product as a promising cancer therapeutics (Table 3).<sup>[75-78]</sup> For example, in 2012 Miyazaki and colleagues determined that Telomestatin eradicates glioblastoma multiforme (GBM) cells, during both in vitro and in vivo studies, through telomeric g-quadruplex disruption.<sup>[75]</sup>

Table 3

*Summary of using telomestatin in treating various cancers*<sup>75,76,77,78</sup>

Cell Line	Target	Disease
c-Myb	Telomeric G-quadruplex	Glioblastoma multiform
MYCN	Telomeric G-quadruplex	Neuroblastoma
SiHa	Telomeric G-quadruplex	Cervical cancer
HeLa	Telomeric G-quadruplex	Cervical adenocarcinoma
MCF-7	Telomeric G-quadruplex	Breast cancer
K562	Telomeric G-quadruplex	Acute myeloid leukemia

**3.1.3 Telomestatin analog, L2H.** Although Telomestatin has proved to be a model compound for Quadruplex inhibition studies, its low solubility has made it difficult to probe its high-resolution structure in complex with a G- G-quadruplex.<sup>[79]</sup> In

2013, however, Chung et al provided the first NMR structure of a Telomestatin analog, L2H2-6M(2)OTD (L2H), binding to an intramolecular (3+1) human telomeric G-quadruplex (Figure 10C). They determined that the binding occurs through  $\pi$ -stacking and electrostatic interactions.<sup>[79]</sup> Although L2H has provided useful binding information, a detailed binding analysis of the natural product, Telomestatin, will serve as an important tool for more effective analog construction in the future.

### **3.1.4 A computational approach study telomestatin binding behavior.**

Molecular dynamics stability simulations was used probe the structure, dynamics and interaction of G-quadruplexes with high spatial and temporal resolution.<sup>[80]</sup> In this study, we utilized AMBER DNA (parmbsc0) and drug (GAFF) force fields to simulate the binding process between telomestatin and the intramolecular human telomeric G-quadruplex, started from unbound state. We observed top end stacking, bottom end stacking and frontal groove binding modes. The top mode resembles the pose observed in the NMR complex of the same G-quadruplex with L2H. The bottom and groove binding poses were not observed in the previous studies of L2H. The dynamic and energetic properties of these three binding modes are thoroughly examined. Our binding energy analysis on the three binding poses and the NMR pose of L2H deciphers the structure-activity relationship. Its implication on designing better telomestatin analog is discussed.

## 3.2 Methods

**3.2.1 Simulation system construction.** We constructed a DNA-ligand system using the NMR solved human telomeric G-quadruplex structure (Figure S84 left, PDB ID: 2MB3<sup>[79]</sup>) and a telomestatin molecule that was in this study 10 Å away from the DNA (Figure S84 right). This system was solvated in a water box of truncated octahedron with 10 Å water buffer plus K<sup>+</sup> as counter ions to neutralize the system. A refined version of the AMBER ff99 (parmbsc0)<sup>[81]</sup> was applied to represent the DNA fragments, TIP3P model<sup>[82]</sup> was used to represent water, and the recently developed K<sup>+</sup> model by Cheatham group was used for the system.<sup>[83]</sup> The partial charges for a telomestatin molecule were obtained using standard AMBER protocol: the electrostatic potential of the telomestatin molecule was obtained at the HF/6-31G\* level after geometry optimization at the same level; the electrostatic potential using the RESP (Restrained ElectroStatic Potential) method determined the partial charges,<sup>[84]</sup> and other force field parameters were taken from the AMBER GAFF<sup>[85]</sup> force field. The telomestatin force field in Mol2 format can be found in the Appendix (Figure S92). These AMBER force fields are the most common ones used in nucleic acid simulations.<sup>[86-89]</sup> We were able to simulate the binding process of doxorubicin, an anti-cancer drug, to a B-DNA fragment (d(CGATCG)<sub>2</sub>).<sup>[90]</sup> We observed three binding modes including end-stacking, minor groove binding and intercalation mode. Based on the observed binding dynamics in the intercalation mode, we proposed the “Flipping-insertion” mechanism, which is different from the previously assumed “Rise-insertion” mechanism.

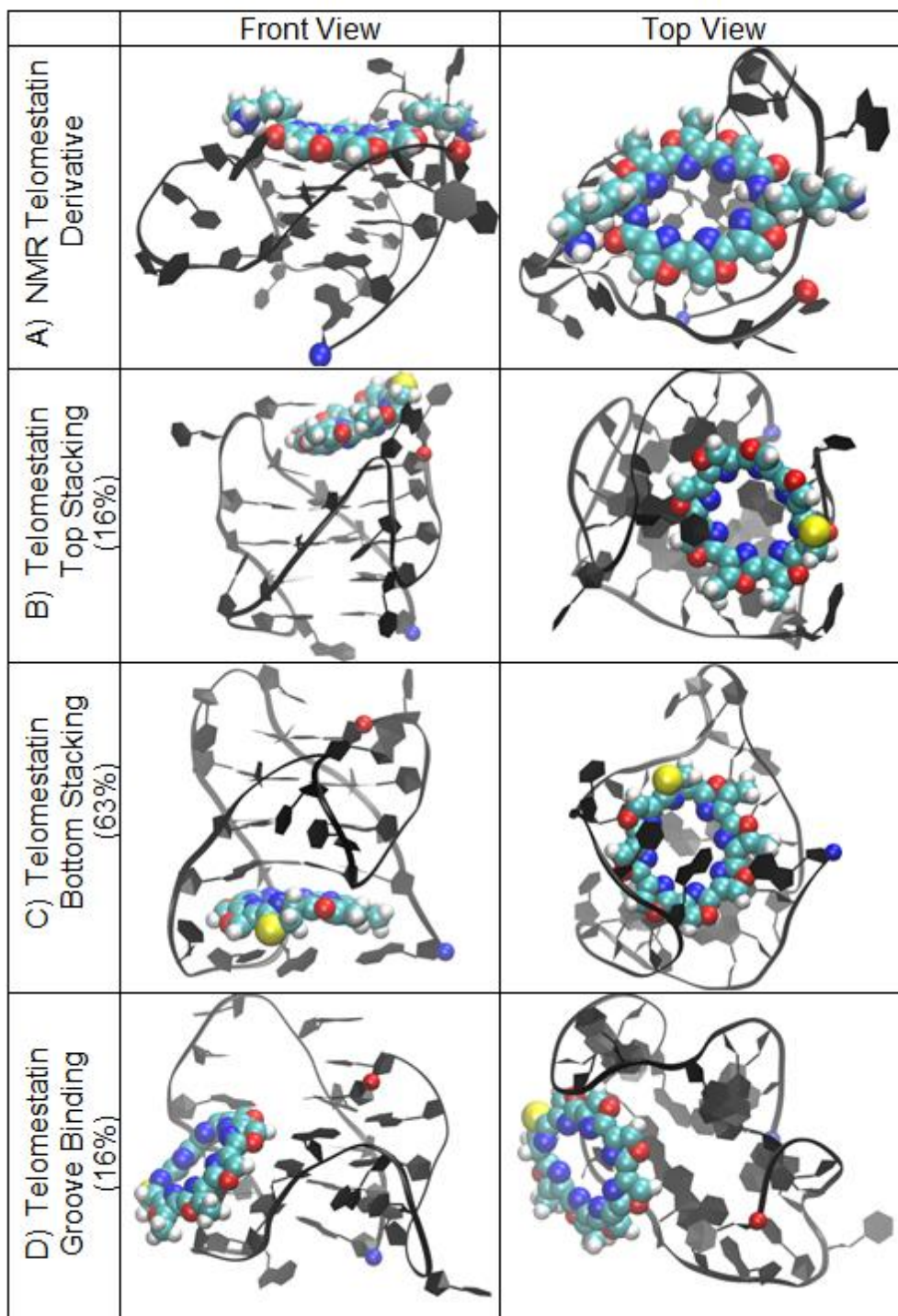


Figure 11. Comparison of the all binding modes between telomestatin and telomestatin derivative (PDB ID: 2MB3) to telomeric G-quadruplex. 5' and 3' of the DNA chain are indicated by a red and blue ball, respectively.

**3.2.2 Simulation protocols.** The ten simulation runs were conducted using the AMBER 14 simulation package<sup>[91]</sup> with refined force fields using Parmbsc1.<sup>[3, 92]</sup> After energy minimization for the initial structure of the system, a total of 10 runs were performed with different initial random velocities. A production run (1000.0 ns) at 300 K, included a short 1.0 ns molecular dynamics in the NPT ensemble mode (constant pressure and temperature) to equilibrate the system density in which the G-quadruplex and ligand were subjected to Cartesian restraints (1.0 kcal/mol/Å) and 999.0 ns dynamics in the equivalent NVT ensemble mode (constant volume and temperature). SHAKE<sup>[93]</sup> was applied to constrain all bonds connecting hydrogen atoms, enabling a 2.0 fs time step in the simulations. The particle-mesh Ewald method<sup>[94]</sup> was used to treat long-range electrostatic interactions under periodic boundary conditions (charge grid spacing of ~1.0 Å, the fourth order of the B-spline charge interpolation; and direct sum tolerance of  $10^{-5}$ ). The cutoff distance for short-range non-bonded interactions was 10 Å, with the long-range van der Waals interactions based on a uniform density approximation. To reduce the computation, non-bonded forces were calculated using a two-stage RESPA approach<sup>[95]</sup> where the short range forces were updated every step and the long range forces were updated every two steps. Temperature was controlled using the Langevin thermostat with a coupling constant of 2.0 ps. The trajectories were saved at 40.0 ps intervals for analysis.

**3.2.3 Convergence of simulations.** The root mean square deviation (RMSD) of DNA backbone heavy was calculated against the starting structure. The flat and small RMSDs (Figure S85) indicate that these systems were stable and the simulations reached a steady state. Atom contacts between the DNA fragment and the drug molecule were

calculated using an atom-to-atom distance cutoff of 3.0 Å. The simulation systems reached a steady state, as indicated by the stable contact number (Figure S86). We defined stable complex as a complex with the number of atom contacts greater than 20. Free drugs bound to different sites as shown in the last snapshots for the ten runs (Figure S87), indicating a good sampling of binding sites.

**3.2.4 Binding mode identification.** Because the DNA backbone was relatively stable in the binding process, we aligned the DNA backbone of the stable complexes from the trajectories by a least square fitting. The aligned complexes were clustered into different structural families based on the 2 Å pair-wise RMSD cutoff of the drug molecule only using Daura algorithm,<sup>[96]</sup> in which the number of neighboring structures was calculated for every structure based on the RMSD cutoff. The structure with the largest number of neighbors together with its neighboring structures were removed to form a structure family and the process continued for the remaining structures until all structures were assigned to a structural family. The centroid structure (i.e. the structure having the largest number of neighbors in the structural family) was used to represent the family. The centroid structures of populated structural families (>1% of total structure population) are shown in Figure S88. Based on visual inspection, the centroid structures were further merged into super-families corresponding to major binding modes (top stacking, bottom stacking and groove binding).

**3.2.5 Parameters for characterizing DNA-drug complex.** We calculated four order parameters to characterize the DNA-drug binding process: the center-to-center distance (D), the drug-base dihedral angle, ligand RMSD and MMGBSA binding energy (G). Distance was defined as the distance from the DNA center to the drug molecule

center. The dihedral angle was defined as the dihedral angle between the plane of the first G-tetrad of the DNA quadruplex and the drug's ring plane. Atom contact number between the DNA quadruplex and the drug molecule was calculated using an atom-to-atom distance cutoff of 3.0 Å. MMGBSA<sup>[97]</sup> (Molecular Mechanics-Generalized Born/Surface Area) module in the AMBER package (GB1 model with mBondi radii set, salt concentration of 0.2 M, and surface tension of 0.0072 kcal/Å<sup>2</sup>) was used to analyze the energetics of the bound complexes to avoid the large energy fluctuation of explicit solvent. A recent study<sup>[10]</sup> shows that GB models make good predictions even for charged molecules when the relative solvation free energy is considered. For our analysis, ions were removed from the systems by assuming that MMGBSA gives a good estimate on the solvation energy of charged DNA systems. This is supported by our previous study, which the binding energy of doxorubicin, an anti-cancer drug, to a B-DNA fragment (d(CGATCG)<sub>2</sub>) was successfully assessed by this MMGBSA protocol.<sup>[90]</sup> Note that since the solute conformational entropy is not included in our analysis, the binding energies by MMGBSA may over-estimate the true binding free energy (i.e. the binding affinity). However, when the solute conformational entropies in different binding poses are comparable, the relative binding free energy can be estimated from the relative MMGBSA binding energies.<sup>[10]</sup>

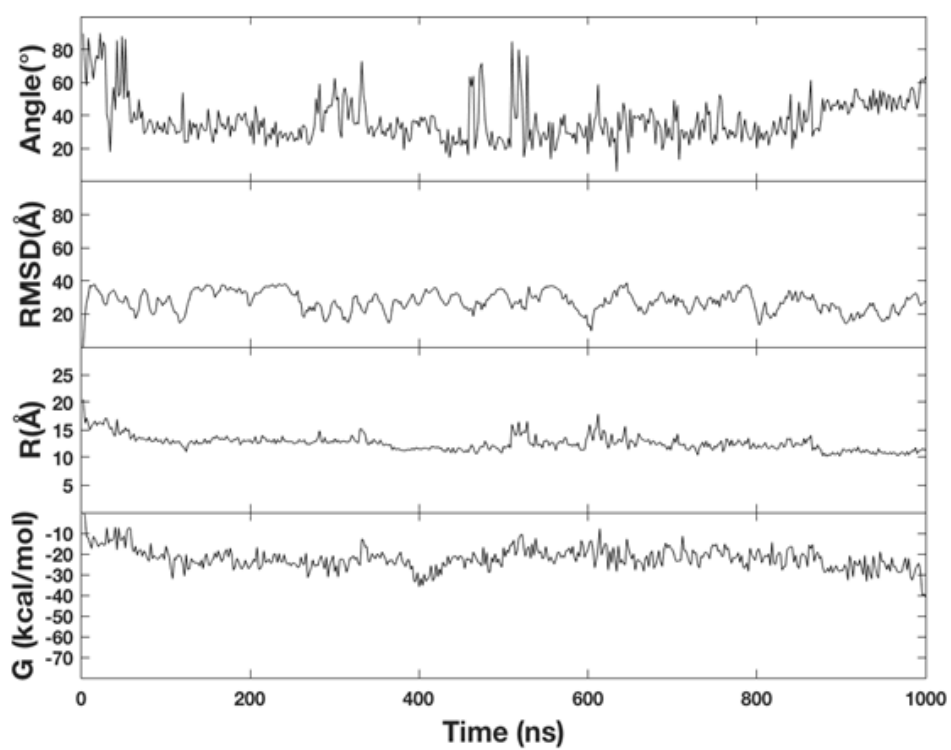
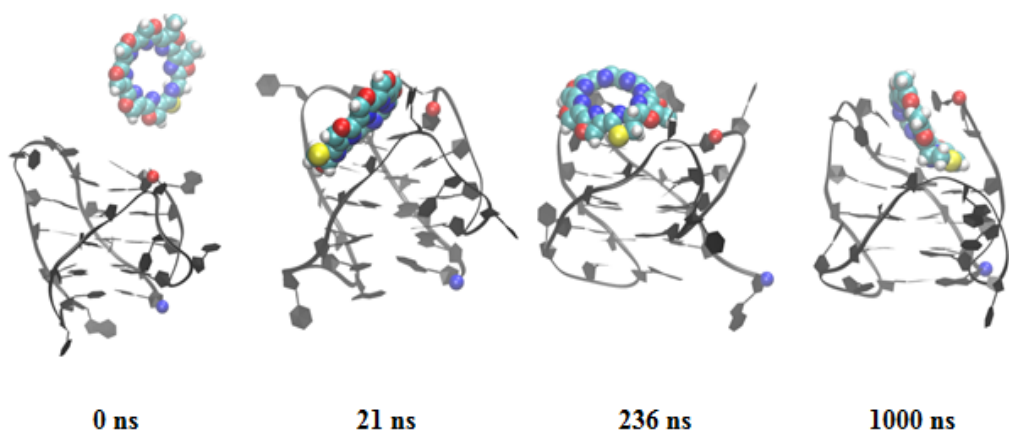
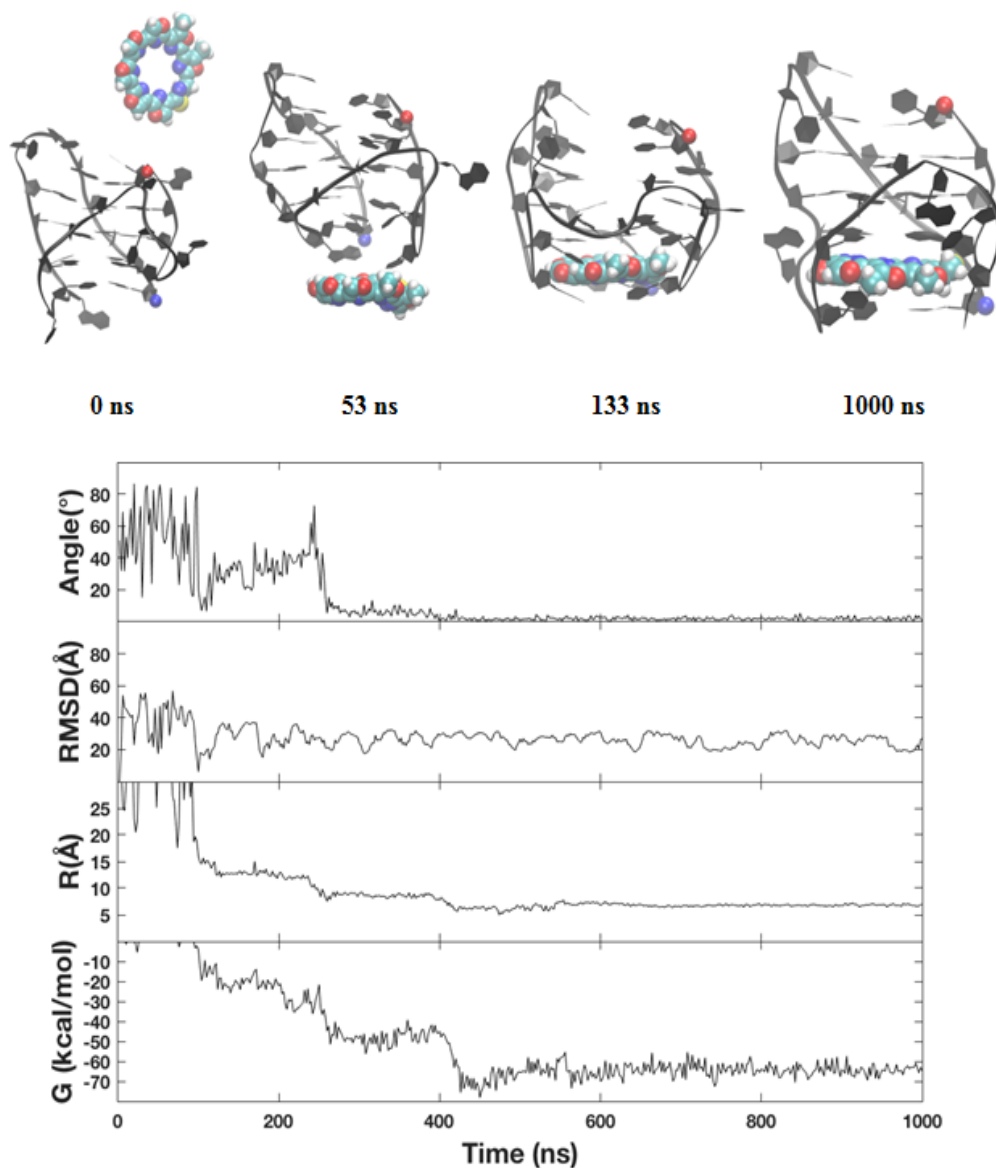
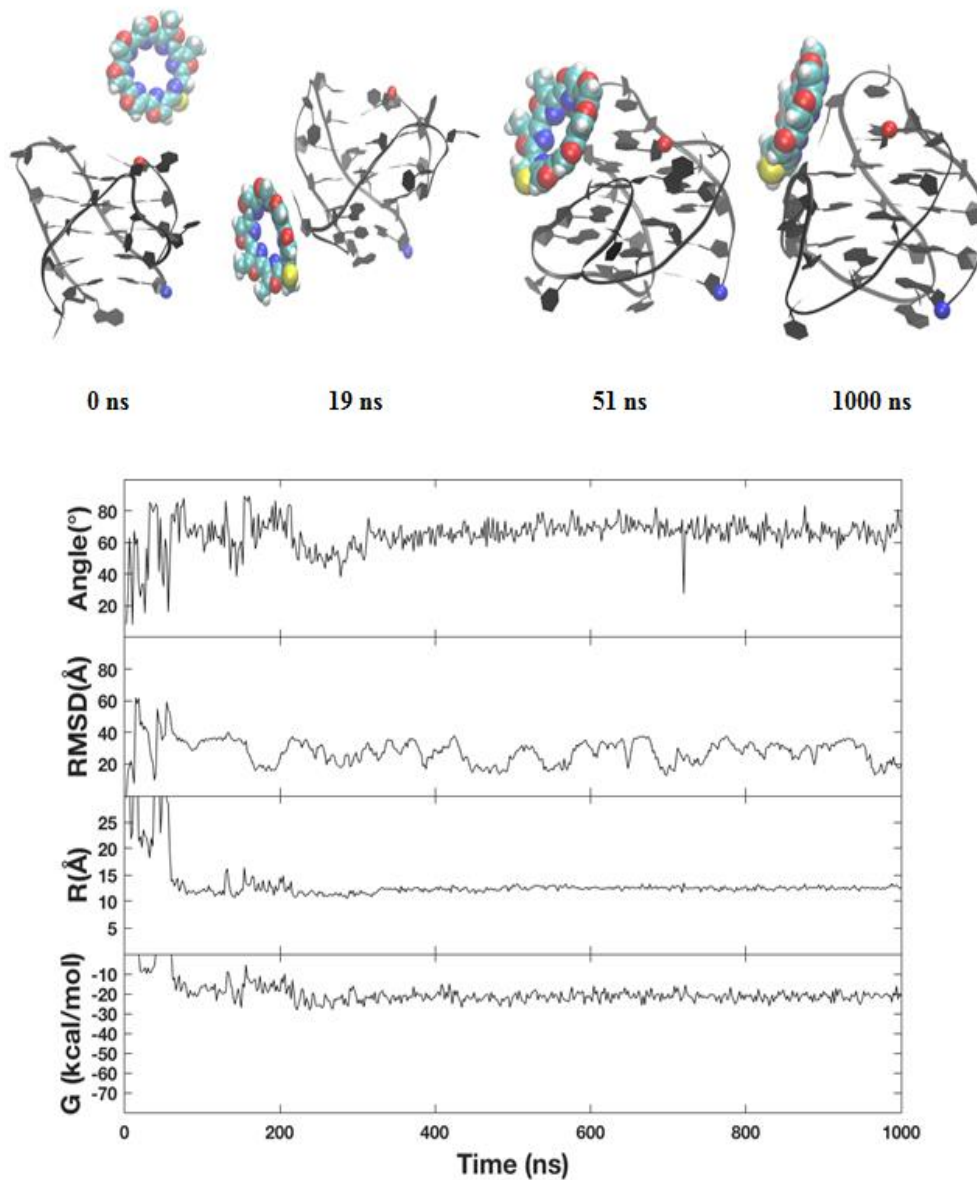


Figure 12. A representative trajectory of the top stacking mode. Center-to-center distance ( $R$ ), the drug-base dihedral angle, ligand RMSD and MM-GBSA binding energy ( $G$ ). 5' and 3' of the DNA chain are indicated by a red and blue ball, respectively.





*Figure 13.* A representative trajectory of the bottom stacking mode. Center-to-center distance ( $R$ ), the drug-base dihedral angle, ligand RMSD and MM-GBSA binding energy ( $G$ ). 5' and 3' of the DNA chain are indicated by a red and blue ball, respectively.



*Figure 14.* A representative trajectory of the groove binding mode. Center-to-center distance ( $R$ ), the drug-base dihedral angle, ligand RMSD and MM-GBSA binding energy ( $G$ ). 5' and 3' of the DNA chain are indicated by a red and blue ball, respectively.

### 3.3 Results

**3.3.1 Three drug binding modes were observed.** Starting from an unbound state (see the method section), ten simulation runs (1000 ns of each) were carried out. The convergence of the binding simulations was confirmed (see the method section). At 1000 ns, the ligand was bound to the G-quadruplex: the ligand binded to the two ends of the quadruplex in seven runs (run 1-7, Figure S87) and binded to the groove/side of the quadruplex in the remaining three runs (run 8-10, Figure S87). The stable complexes, extracted from the ten trajectories (see the method section), were categorized into structural families based on a clustering analysis as described in the method section. By setting a threshold of 1% population, eight structural families of complexes were identified (Figure S88). These eight structural families were further merged into three binding modes: top stacking, bottom stacking and groove binding. End stacking to the top of the quadruplex accounted for 16% of the total population, end binding to the bottom of the quadruplex accounted for 63% and groove binding made up 16% (Figure 11). In the top binding mode, telomestatin stacks on the top of the G-tetrad. This mode is similar to the binding pose of a telomestatin derivative, L2H, to the same telemetric G-quadruplex in the NMR solved complex structure. In the bottom end stacking mode, telomestatin is sandwiched between a G-tetrad and G-triad. In the groove binding mode, telomestatin inserts into the groove. Therefore, it is interesting that the latter two binding modes are the two additional modes for telomestatin, and that L2H is only able to access the first binding mode of telomestatin. The bottom binding mode is particularly interesting, because it is stable (63% of population) and G-quadruplex specific. The partial intercalation between G-tetrad and G-triad, increase its binding affinity to the G-

quadruples. This mode differs from the ligand binding pose observed in existing G-quadruplex-ligand complex structures.<sup>[69, 79, 98-108]</sup>

**3.3.2 Bottom binding mode is the most stable mode of the three modes.** To examine the relative stability for the three binding modes observed, MMGBSA binding energy calculations were conducted on each complex (Table 3). Top stacking, which is the binding pose observed in the L2H NMR complex, displayed the lowest binding energy towards the quadruplex ( $-24.0 \pm 1.3$  kcal/mol). Bottom stacking, on the other hand, displayed the highest total binding energy ( $-53.8 \pm 20.0$  kcal/mol) making this binding pose the most favorable of the three. Telomestatin's ability to intercalate in this bottom stacking pose may explain this (Figure 11C). The groove binding displayed the moderate total binding energy ( $-32.7 \pm 0.2$  kcal/mol). To decipher the binding nature, the binding energy was decomposed into van der Waal (VDW), hydrophobic interaction (SUR), and electrostatic interaction (GBELE). As expected, the bottom stacking pose exhibited the most favorable VDW ( $-77.5 \pm 26.7$  kcal/mol), which is 38 kcal/mol more favorable than that of top stocking pose and 28 kcal/mol more favorable than that of Groove binding pose. Although the bottom binding pose is  $\sim 8-10$  kcal/mol less favorable than those of the other two binding poses, the total binding energy is much stronger than those of the other two binding modes.

To characterize the binding pathway of the three modes, we calculated four order parameters as described in the method section. Here we show the data for a representative trajectory for each mode (Figure 12-14). For the bottom binding mode, the data for another trajectory is included in the Appendix (Figure S89).

**3.3.3 Top stacking of telomestatin displayed a similar binding pose to the L2H NMR complex.** In the representative trajectory of the top stacking mode, telomestatin made initial interaction with the top of the telomeric quadruplex at about 21 ns from the unbound state (Figure 12). From about 21-236 ns of the trajectory, telomestatin flips orientation and the quadruplex exhibits base flipping. The top binding system exhibits large fluctuations in each of the four order studies indicating that telomestatin binding to the top of the quadruplex is not as favorable as the bottom or groove. For example, MMGBSA calculations determined binding energy fluctuating between -10 and -35 kcal/mol (Figure 12). Because the binding pose fails to allow telomestatin to intercalate into the G-Quadruplex the binding affinity less favorable. Additionally, it is unclear where this system reaches a final steady state.

Table 4

*MMGBSA Binding Energy of Telomestatin and L2H2 to G-Quadruplex DNA*<sup>[31-33, 72 109]</sup>

Ligands	Binding Pose	$\Delta_{VDW}$	$\Delta_{SUR}$	$\Delta_{GBELE}$	$\Delta_{TOT}$	$\Delta\Delta G$	TRAP IC <sub>50</sub>	IC <sub>50</sub>
Telomestatin	Top Stacking	-39.4±2.9	-3.1±0.3	18.5±2.0	-24.0±1.3	29.8		
Telomestatin	Bottom Stacking	-77.5±26.7	-4.3±1.3	28.0±1.3	-53.8±20.0	0	5 nM	0.5-4.0 μm
Telomestatin	Groove	-49.2±0.5	-3.7±0.1	20.3±0.5	-32.7±0.2	21.1		
L2H (NMR)	Top Stacking	-	-	-	-	-	20 nM	7.4 μm

$\Delta_{VDW}$  Change of VDW energy in gas phase upon complex formation (Units: kcal/mol)

$\Delta_{SUR}$  Change of energy due to surface area change upon complex formation (Units: kcal/mol)

$\Delta_{GBELE}$  Change of GB reaction field energy + gas phase Elec. energy upon complex formation (Units: kcal/mol)

$\Delta_{TOT} = \Delta_{VDW} + \Delta_{SUR} + \Delta_{GBELE}$  Change of potential energy in water upon complex formation (Units: kcal/mol)

**3.3.4 Bottom stacking of telomestatin has the greatest percent population and strongest binding energy.** Two representative trajectories for the bottom binding were analyzed, the result of one trajectory is shown here and the other trajectory is included in the appendix (Figure S89). In this representative trajectory, telomestatin made the initial interaction with the bottom of the telomeric quadruplex at about 53 ns (Figure 13). Interestingly, a deep intercalation of telomestatin can be seen at 133 ns. How does this intercalation occur? By watching the trajectory, we discovered that the initial contact with the G-quadruplex is concurrent with the flipping out of the bases and welcome telomestatin into the quadruplex. As a result, the ligand is sandwiched between the bottom layers of the quadruplex. We name this interaction mechanism as “flip-intercalation” (Figure S90). We compared this entrance mechanism to an additional bottom stacking trajectory and found that telomestatin intercalates in a different manner (Figure S91). In this system, the ligand enters the quadruplex from the loop closest to the N-terminal where the short loop allows for easy insertion. Clearly, this intercalation is responsible for the high affinity of the bottom stacking mode of the telomestatin-quadruplex complex.

In this trajectory, the intercalation completed within the 450 ns and the ligand stayed there in the remaining time. In the other trajectory (Figure S89), telomestatin completed intercalation within the first 50 ns and stayed there for the remaining 950 ns. Both trajectories support that the bottom stacking mode is indeed the most favorable of the three binding modes seen in the telomestatin-quadruplex systems.

**3.3.5 Groove binding of telomestatin provides additional support for the selectivity of this ligand to G-quadruplex DNA.** In the representative trajectory of the groove binding mode, telomestatin made initial contact with the telomeric quadruplex at 19 ns (Figure 14). After about 51 ns the ligand settles in its final pose. Additionally, this system reaches a steady state after about 200 ns, with minor fluctuations throughout the remainder of the trajectory. The terminal MMGBSA binding energy is ~20 kcal/mol, which is much lower than ~75 kcal/mol of the bottom binding mode.

### 3.4 Discussion

Interest in G-quadruplex DNA as a promising target for future cancer therapeutics has increased after it was recently discovered that quadruplex existence is greater in malignant tumors than in normal tissues.<sup>[110]</sup> Telomestatin is a natural product that has been gaining interest as a potential quadruplex stabilizer (Figure 10B). Its planar shape allows it to create pi-pi stacking with the quadruplex, increasing its affinity towards the target.<sup>79</sup> More importantly, telomestatin's macrocyclic scaffold hinders its ability to bind into a duplex intercalation, and in turn it exhibits low DNA duplex affinity. However, the lack of efficient and systematic synthetic routes along with some of telomestatin molecular limits<sup>[111,112]</sup> (high hydrophobicity and low solubility) has prevented this family of inhibitors from reaching to the market. To address the issues, multiple total syntheses<sup>[111,112]</sup> were developed to obtain telomestatin and its analogues.<sup>[78, 113]</sup> Among these attempts, Rzuczk et al have recently developed a telomestatin derivative L2H containing two alky amine sidechains and six oxazole rings. The solubility of L2H was greatly increased as the two charge sidechains added. Yet, the biological activities of L2H were slightly reduced (Table 4): a) Whereas telomestatin has an IC<sub>50</sub> (Inhibition Concentration at 50% activity) value of 0.5-4.0 μM in various cancer cell lines<sup>[76-78, 114]</sup>, L2H have IC<sub>50</sub> of 7.4 μM.<sup>[109]</sup> b) Whereas telomestatin has TRAP IC<sub>50</sub> of 5 nM<sup>[72]</sup>, L2H has TRAP IC<sub>50</sub>: 20 nM<sup>[109]</sup> (TRAP: The telomere repeat amplification protocol for the human reverse transcriptase, telomerase, that is used for determination of telomerase activity). This reduction is expected, because the side chain charge is supposed to increase the binding affinity of L2H to the DNA G-quadruplex backbone and thus improve the potency of L2H. To understand why, high resolution structures of both



telomestatin and L2H in complex with a telomeric G-quadruplex are a must. Although the NMR structure of L2H in complex with a human telomeric G-quadruplex have been solved by Wan et al in 2013, a high resolution structure of telomestatin with a G-quadruplex is not yet obtained probably due to its low solubility.<sup>[79]</sup> In this study, we utilized molecular dynamics simulations and MMGBSA binding energy calculations to provide a thorough analysis of the binding of telomestatin to a telomeric G-quadruplex DNA. By comparing with the NMR structure, we want to tackle the mentioned question.

In the NMR study<sup>[79]</sup>, only one binding mode was observed, in which L2H binds to the top of the quadruplex in a stacking manor. In contrast, in our simulations we observed that telomestatin binds in three modes to the same telomeric G-quadruplex structure: Top end stacking (13% total population), bottom end stacking (63% total population), and in the front groove (16% total population). The top end stacking mode most closely resembles the L2H binding pose seen in the NMR structure. On one hand, sharing this common binding mode might explain why both L2H and telomestatin can stabilize the telomeric G-quadruplex, inhibit the telomerase, and restrict cancer cell growth. On the other hand, lack of two additional binding modes, in particular the intercalative mode in the bottom of the G-quadruplex, might be the reason L2H is less potent than telomestatin. Therefore, although the addition of two positively charged alkyl amine side chains on two of the six oxazole rings was successful in improving the solubility of the compound, this addition actually prevents the ligand from adopting the intercalation mode, thus reducing the potency of the compound. For example, the NMR structure of L2H shows the compound laying on residues G21, G17, G9 and G3. The residues above the compound, T19 and T2, are unable to close in on L2H. The large

sidechains prevent this from occurring (Figure 15B). In contrast, the planar scaffold of telomestatin allows residues T13, A14 and A24 to close in around and a thus responsible for the partial intercalation (Figure 15A). In fact, our MMGBSA and trajectory analysis show that this intercalation mode is much more stable than the other two modes, thus this mode might contribute most to the higher binding and higher potency of telomestatin over L2H. If this is true, then future development should keep a planar scaffold to favor the intercalation binding mode to the G-quadruplex. The solubility issue should be solved by adding polar/charged functional groups in the plane.

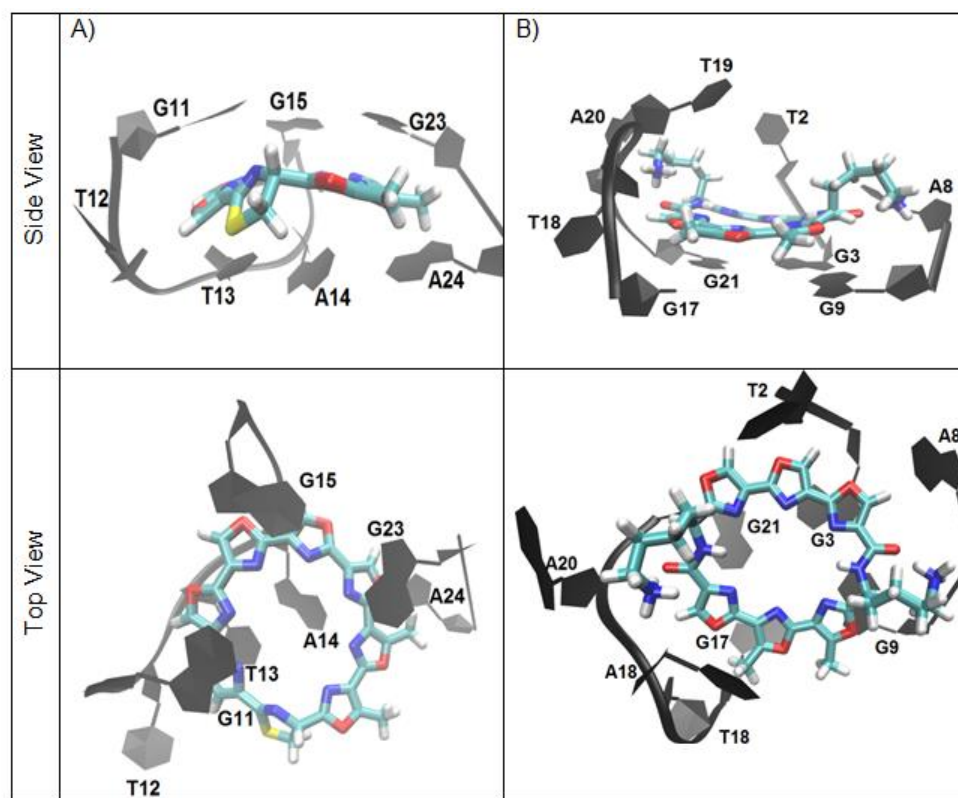


Figure 15. A 3-Dimensional representation of residues surrounding Telomestatin in bottom stacking mode (A) and L2H in top stacking mode (B)

Computational methods have become essential in drug discovery as they provide structural information where experimental results may lack. In this study we utilized molecular dynamics simulations as well as MMGBSA binding energy calculations to evaluate the elusive binding behavior of telomestatin to telomeric G-quadruplex DNA, which has been previously unreported. We have identified three binding modes: top end stacking, bottom end stacking and groove binding. The first mode resembles the pose observed in a NMR structure of the same telomeric G-quadruplex with telomestatin analog, L2H, with a binding energy of  $-24.0 \pm 1.3$  kcal/mol. Groove binding mode was not observed previously to the best of our knowledge, but showed comparable binding energy to the top stacking mode ( $-32.7.7 \pm 0.2$  kcal/mol). Interestingly, the bottom stacking mode showed the best binding energy ( $-53.8 \pm 20.0$  kcal/mol). Telomestatin's planar scaffold allows the compound to bind to three sites on telomeric G-quadruplex with comparable binding affinity to the NMR L2H complex. For this reason, maintaining a planar scaffold is critical in developing quadruplex targeting ligands. Not only does it increase binding selectivity, but it will promote intercalation thus inducing overall binding affinity. These findings may aid future attempts at creating a promising telomeric G-quadruplex stabilizer.

## References

- [1] Association, C. B. R., New Drug Development Process. **2016**
- [2] America, P. R. a. M. o., The Biopharmaceutical Research and Development Process. **2015**.
- [3] Case, D. A.; Cheatham, T. E. I.; Darden, T.; Gohlke, H.; Luo, R.; Merz, K. M.; Onufriev, A.; Simmerling, C.; Wang, B.; Woods, R. J., The Amber biomolecular simulation programs. *Journal of Computational Chemistry* **2005**, 26, 1668-1688.
- [4] Sastry, G. M.; Adzhigirey, M.; Day, T.; Annabhimoju, R.; Sherman, W., Protein and ligand preparation: parameters, protocols, and influence on virtual screening enrichments. *Journal of Computer Aided Molecular Design* **2013**, 27, 221-34.
- [5] Friesner, R.; Murphy, R.; Repasky, M., Extra Precision Glide: Docking and Scoring Incorporating a Model of Hydrophobic Enclosure for Protein-Ligand Complexes. *Journal of Medicinal Chemistry* **2006**, 49, 6177-6196.
- [6] Friesner, R.; Murphy, R.; Repasky, M., Glide: A New Approach for Rapid, Accurate Docking and Scoring. 1. Method and Assessment of Docking Accuracy. *Journal of Medicinal Chemistry* **2004**, 47, 1739-1749.
- [7] Reza Kalani, M.; Tajkhorshid, E., Molecular Dynamics: The Computational Molecular Microscope. *Razavi International Journal of Medicine* **2014**, 2.
- [8] Roux, B.; Simonson, T., Implicit solvent models. *Biophysical Chemistry* **1999**, 78, 1-20.
- [9] Hou, T.; Wang, J.; Li, Y.; Wang, W., Assessing the Performance of the MM/PBSA and MM/GBSA Methods. *Journal of Chemical Information and Modeling* **2011**, 51, 69-82.
- [10] Kongsted, J.; Soderhjelm, P.; Ryde, U., How accurate are continuum solvation models for drug-like molecules? *Journal of Computer-Aided Molecular Design* **2009**, 23, 395-409.
- [11] Bijvoet, J. M.; Peerdeman, A. F.; van Bommel, A. J., The Isolation and Structure of Camptothecin, a Novel Alkaloidal Leukemia and Tumor Inhibitor from *Camptotheca acuminata*. *Nature* **1951**, 169.
- [12] Garcia-Carbonero, R.; Supko, J., Current Perspectives on the Clinical Experience, Pharmacology, and Continued Development of the Camptothecins. *Clinical Cancer Research* **2002**, 8, 641-661.

- [13] Riemsma, R., Jean P Simons, Zahid Bashir, Caroline L Gooch, Jos Kleijnen, Systematic Review of topotecan (Hycamtin) in relapsed small cell lung cancer. *BMC Cancer* **2010**, 10.
- [14] Winokur, S., Network For Oncology Communication & Research. *The Oncologist* **1997**.
- [15] Chen, A. Y.; Chen, P. M. T.; Chen, Y.-J., DNA topoisomerase I drugs and radiotherapy for lung cancer. *Journal of Thoracic Disease* **2012**, 4, 390-397.
- [16] Bruchim, I.; Jarchowsky-Dolberg, O.; Fishman, A., Advanced (>second) line chemotherapy in the treatment of patients with recurrent epithelial ovarian cancer. *European journal of obstetrics, gynecology, and reproductive biology* **2013**, 166, 94-8.
- [17] Dezhenkova, L. G.; Tsvetkov, V. B.; Shtil, A. A., Topoisomerase I and II inhibitors: chemical structure, mechanisms of action and role in cancer chemotherapy. *Russian Chemical Reviews* **2014**, 83, 82-94.
- [18] Sharkey, R.; McBride, W.; Cardillo, T.; Govindan, S.; Wang, Y.; Rossi, E.; Chang, C.-H.; Goldenberg, D., Enhanced Delivery of SN-38 to Human Tumor Xenografts with an Anti-Trop-2-SN-38 Antibody Conjugate (Sacituzumab Govitecan). *Clinical Cancer Research* **2015**, 21, 5131-8.
- [19] Luzzio, M.; Besterman, J.; Emerson, D., Synthesis and Camptothecin Antitumor Activity of Novel Water Soluble Derivatives of as Specific Inhibitors of Topoisomerase I. *Journal of Medicinal Chemistry* **1994**, 38.
- [20] Pommier, Y.; Leo, E.; Zhang, H.; Marchand, C., DNA topoisomerases and their poisoning by anticancer and antibacterial drugs. *Chemistry & biology* **2010**, 17, 421-33.
- [21] Wang, L.-F.; Ting, C.-Y.; Lo, C.-K.; Su, J.-S.; Mickley, L. A.; Fojo, A. T., Identification of Mutations at DNA Topoisomerase I Responsible for Camptothecin Resistance. *Cancer Research* **1997**, 57, 1516-1522.
- [22] Craig, S. B., Stability and compatibility of topotecan hydrochloride for injection with common infusion solutions and containers. *Journal of Pharmaceutical and Biomedical Analysis* **1997**, 16, 199–205.
- [23] Hoki, Y.; Fujimori, A.; Yves, P., Differential cytotoxicity of clinically important camptothecin derivatives in P-glycoprotein-overexpressing cell lines. *Cancer Chemotherapy Pharmacology* **1997**, 40, 433-438.
- [24] Sugimoto, Y.; Tsukahara, S.; Oh-hara, T., Decreased Expression of DNA Topoisomerase I in Camptothecin-resistant Tumor Cell Lines as Determined by a Monoclonal Antibody1. *Cancer Research* **1990**, 50, 6925-6930.

- [25] Pommier, Y., Topoisomerase I inhibitors: selectivity and cellular resistance. *Drug Resistance Updates* **1997**, 2, 307-318.
- [26] Chrencik, J.; Staker, B.; Burgin, A.; Pourquier, P.; Pommier, Y.; Stewart, L.; Redinbo, M., Mechanisms of camptothecin resistance by human topoisomerase I mutations. *Journal of molecular biology* **2004**, 339, 773-84.
- [27] Bases, R.; Mendez, F., Topoisomerase Inhibition by Lucanthone, An Adjuvant In Radiation Therapy. *International Journal of Radiation Oncology Biological Physics* **1997**, 37, 1133-1137.
- [28] Fan, Y., Weinstein, J., Kohn, K., Molecular Modeling Studies of the DNA-Topoisomerase I Ternary Cleavable Complex with Camptothecin. *Journal of Medicinal Chemistry* **1998**, 41, 2216-2226.
- [29] Pan, P.; Li, Y.; Yu, H.; Sun, H.; Hou, T., Molecular Principle of Topotecan Resistance by Topoisomerase I Mutations through Molecular Modeling Approaches. *Journal of Chemical Information and Modeling* **2013**, 53, 997-1006.
- [30] Staker, B. L.; Hjerrild, K.; Feese, M. D.; Behnke, C. A.; Burgin, A. B., Jr.; Stewart, L., The mechanism of topoisomerase I poisoning by a camptothecin analog. *Proceedings of the National Academy of Sciences of the United States of America* **2002**, 99, 15387-92.
- [31] Pommier, Y., Drugging topoisomerases: lessons and challenges. *ACS Chem Biol* **2013**, 8, 82-95.
- [32] Irwin, J., Zinc Database. **2004**.
- [33] Staker, B.; Hjerrild, K.; Feese, M.; Behnke, C.; Burgin, A. B. J.; Stewart, L., Proceedings of the National Academy of Sciences of the United States of America. *Proceedings of the National Academy of Sciences of the United States of America* **2002**, 99, 15387-92.
- [34] Harder, E.; Damm, W.; Maple, J.; Wu, C.; Reboul, M.; Xiang, J. Y.; Wang, L.; Lupyan, D.; Dahlgren, M.; Knight, J.; Kaus, J.; Cerutti, D.; Krilov, G.; Jorgensen, W.; Abel, R.; Friesner, R., OPLS3: A Force Field Providing Broad Coverage of Drug-like Small Molecules and Proteins. *Journal of chemical theory and computation* **2016**, 12, 281-96.
- [35] Li, J.; Abel, R.; Zhu, K.; Cao, Y.; Zhao, S.; Friesner, R., The VSGB 2.0 model: a next generation energy model for high resolution protein structure modeling. *Proteins* **2011**, 79, 2794-812.

- [36] Kubota, N.; Kanzawa, F.; Nishio, K.; Takeda, Y.; Ohmori, T.; Fujiwara, Y.; Terashima, Y.; Saijo, N., Detection of topoisomerase I gene point mutation in CPT-11 resistant lung cancer cell line. *Biochemical and biophysical research communications* **1992**, 188, 571-577.
- [37] Rubin, E.; Pantazis, P.; Toppmeyer, D., Identification of a Mutant Human Topoisomerase I with Intact Catalytic Activity and Resistance to 9-Nitro-camptothecin. *Journal of Biological Chemistry* **1994**, 269, 2433-2439.
- [38] Tanizawa, A.; Pommier, Y., Topoisomerase I Alteration in a Camptothecin-resistant Cell Line Derived from Chinese Hamster DC3F Cells in Culture. *Cancer Research* **1992**, 52, 1848-1854.
- [39] Wang, L.-F.; Ting, C.-Y.; Lo, C.-K.; Su, J.-S.; Mickley, L.; Fojo, A.; Whang-Peng, J.; Hwang, J., Identification of Mutations at DNA Topoisomerase I Responsible for Camptothecin Resistance. *Cancer Research* **1997**, 57, 1516-1522.
- [40] Andoh, T.; Ishii, K.; Suzuki, Y.; Ikegami, Y.; Kusunoki, Y.; Takemoto, Y.; Okada, K., Characterization of a mammalian mutant with a camptothecin-resistant DNA topoisomerase I. *Proceedings of the National Academy of Sciences* **1987**, 84, 5565-5569.
- [41] Fujimori, A.; Harker, W. G.; Kohlhagen, G.; Hoki, Y.; Pommier, Y., Mutation at the catalytic site of topoisomerase I in CEM/C2, a human leukemia cell line resistant to camptothecin. *Cancer Research* **1995**, 55, 1339-1346.
- [42] Winokur, S., Network For Oncology Communication & Research. *The Oncologist* **1997**, 2.
- [43] Eng, W.-k.; Pandit, S.; Sternglanz, R., Mapping of the Active Site Tyrosine of Eukaryotic DNA Topoisomerase I. *The Journal of Biological Chemistry* **1983**, 264, 13373-13376.
- [44] Castelli, S.; Coletta, A.; D'Annessa, I.; Fiorani, P.; Tesauro, C.; Desideri, A., Interaction between natural compounds and human topoisomerase I. *Biological Chemistry* **2012**, 393, 1327-1340.
- [45] Beck, D.; Abdelmalak, M.; Lv, W.; Reddy, P. V. N.; Tender, G.; O'Neill, E.; Agama, K.; Marchand, C.; Pommier, Y.; Cushman, M., Discovery of potent indenoisoquinoline topoisomerase I poisons lacking the 3-nitro toxicophore. *Journal of Medicinal Chemistry* **2015**, 58, 3997-4015.
- [46] Simonsson, T., G-quadruplex DNA structures - Variations on a theme. *Biological Chemistry* **2001**, 382, 621-628.
- [47] Lane, A. N.; Chaires, J. B.; Gray, R. D.; Trent, J. O., Stability and kinetics of G-quadruplex structures. *Nucleic acids research* **2008**, 36, 5482-5515.



- [48] Huppert, J. L.; Balasubramanian, S., Prevalence of quadruplexes in the human genome. *Nucleic acids research* **2005**, 33, 2908-16.
- [49] Huppert, J. L.; Balasubramanian, S., G-quadruplexes in promoters throughout the human genome. *Nucleic acids research* **2007**, 35, 406-413.
- [50] Murat, P.; Balasubramanian, S., Existence and consequences of G-quadruplex structures in DNA. *Current Opinion in Genetics and Development* **2014**, 25, 22-29.
- [51] Biffi, G.; Tannahill, D.; McCafferty, J.; Balasubramanian, S., Quantitative visualization of DNA G-quadruplex structures in human cells. *Nature chemistry* **2013**, 5, 182-6.
- [52] Granotier, C.; Pennarun, G.; Riou, L.; Hoffschir, F.; Gauthier, L. R.; De Cian, A.; Gomez, D.; Mandine, E.; Riou, J. F.; Mergny, J. L.; Mailliet, P.; Dutrillaux, B.; Boussin, F. D., Preferential binding of a G-quadruplex ligand to human chromosome ends. *Nucleic acids research* **2005**, 33, 4182-4190.
- [53] Di Antonio, M.; Rodriguez, R.; Balasubramanian, S., Experimental approaches to identify cellular G-quadruplex structures and functions. *Methods* **2012**, 57, 84-92.
- [54] Hansel, R.; Foldynova-Trantirkova, S.; Lohr, F.; Buck, J.; Bongartz, E.; Bamberg, E.; Schwalbe, H.; Dotsch, V.; Trantirek, L., Evaluation of Parameters Critical for Observing Nucleic Acids Inside Living *Xenopus laevis* Oocytes by In-Cell NMR Spectroscopy. *Journal of the American Chemical Society* **2009**, 131, 15761-15768.
- [55] Hansel, R.; Lohr, F.; Foldynova-Trantirkova, S.; Bamberg, E.; Trantirek, L.; Dotsch, V., The parallel G-quadruplex structure of vertebrate telomeric repeat sequences is not the preferred folding topology under physiological conditions. *Nucleic acids research* **2011**, 39, 5768-5775.
- [56] Hansel, R.; Lohr, F.; Trantirek, L.; Dotsch, V., High-Resolution Insight into G-Overhang Architecture. *Journal of the American Chemical Society* **2013**, 135, 2816-2824.
- [57] Lam, E. Y. N.; Beraldi, D.; Tannahill, D.; Balasubramanian, S., G-quadruplex structures are stable and detectable in human genomic DNA. *Nature Communications* **2013**, 4.
- [58] Duchler, M., G-quadruplexes: targets and tools in anticancer drug design. *Journal of drug targeting* **2012**, 20, 389-400.
- [59] Shalaby, T.; Fiaschetti, G.; Nagasawa, K.; Shin-ya, K.; Baumgartner, M.; Grotzer, M., G-quadruplexes as potential therapeutic targets for embryonal tumors. *Molecules* **2013**, 18, 12500-37.



- [60] Cree, S. L.; Kennedy, M. A., Relevance of G-quadruplex structures to pharmacogenetics. *Frontiers in Pharmacology* **2014**, *5*.
- [61] Onel, B.; Lin, C.; Yang, D., DNA G-quadruplex and its potential as anticancer drug target. *Science China-Chemistry* **2014**, *57*, 1605-1614.
- [62] Balasubramanian, S.; Hurley, L. H.; Neidle, S., Targeting G-quadruplexes in gene promoters: a novel anticancer strategy? *Nature reviews. Drug discovery* **2011**, *10*, 261-75.
- [63] Gray, R. D.; Trent, J. O.; Chaires, J. B., Folding and unfolding pathways of the human telomeric G-quadruplex. *Journal of Molecular Biology* **2014**, *426*, 1629-50.
- [64] Stewart, S. A.; Weinberg, R. A. Telomeres: Cancer to human aging. In *Annual Review of Cell and Developmental Biology*; 2006; Vol. 22, pp 531-557.
- [65] Kim, N. W.; Piatyszek, M. A.; Prowse, K. R.; Harley, C. B.; West, M. D.; Ho, P. L. C.; Coviello, G. M.; Wright, W. E.; Weinrich, S. L.; Shay, J. W., Specific Association Of Human Telomerase Activity With Immortal Cells AND Cancer. *Science* **1994**, *266*, 2011-2015.
- [66] Shay, J. W.; Wright, W. E., Telomerase therapeutics for cancer: challenges and new directions. *Nature reviews. Drug discovery* **2006**, *5*, 577-584.
- [67] Gowan, S. M.; Heald, R.; Stevens, M. F. G.; Kelland, L. R., Potent inhibition of telomerase by small-molecule pentacyclic acridines capable of interacting with G-quadruplexes. *Molecular Pharmacology* **2001**, *60*, 981-988.
- [68] Gunaratnam, M.; Greciano, O.; Martins, C.; Reszka, A. P.; Schultes, C. M.; Morjani, H.; Riou, J. F.; Neidle, S., Mechanism of acridine-based telomerase inhibition and telomere shortening. *Biochemical Pharmacology* **2007**, *74*, 679-689.
- [69] Neidle, S., Quadruplex Nucleic Acids as Novel Therapeutic Targets. *Journal of Medicinal Chemistry* **2016**.
- [70] Temime-Smaali, N.; Guittat, L.; Sidibe, A.; Shin-ya, K.; Trentesaux, C.; Riou, J.-F., The G-Quadruplex Ligand Telomestatin Impairs Binding of Topoisomerase III alpha to G-Quadruplex-Forming Oligonucleotides and Uncaps Telomeres in ALT Cells. *PloS one* **2009**, *4*.
- [71] Gomez, D.; O'Donohue, M.-F.; Wenner, T.; Douarre, C.; Macadre, J.; Koebel, P.; Giraud-Panis, M.-J.; Kaplan, H.; Kolkes, A.; Shin-ya, K.; Riou, J.-F., The G-quadruplex ligand telomestatin inhibits POT1 binding to Telomeric sequences in vitro and induces GFP-POT1 dissociation from telomeres in human cells. *Cancer Research* **2006**, *66*, 6908-6912.

[72] Shin-ya, K.; Wierzba, K.; Matsuo, K.-i., Telomestatin, a Novel Telomerase Inhibitor from *Streptomyces anulatus* *Journal of American Chemical Society* **2001**, 123, 1262-1263.

[73] Gomez, D.; Paterski, R.; Lemarteleur, T.; Shin-ya, K.; Mergny, J. L.; Riou, J. F., Interaction of telomestatin with the telomeric single-strand overhang. *Journal of Biological Chemistry* **2004**, 279, 41487-41494.

[74] Kim, M. Y.; Vankayalapati, H.; Kazuo, S.; Wierzba, K.; Hurley, L. H., Telomestatin, a potent telomerase inhibitor that interacts quite specifically with the human telomeric intramolecular G-quadruplex. *Journal of the American Chemical Society* **2002**, 124, 2098-2099.

[75] Miyazaki, T.; Pan, Y.; Joshi, K.; Purohit, D.; Hu, B.; Demir, H.; Mazumder, S.; Okabe, S.; Yamori, T.; Viapiano, M.; Shin-ya, K.; Seimiya, H.; Nakano, I., Telomestatin Impairs Glioma Stem Cell Survival and Growth through the Disruption of Telomeric G-Quadruplex and Inhibition of the Proto-oncogene, c-Myb. *Clinical Cancer Research* **2012**, 18, 1268-1280.

[76] Binz, N.; Shalaby, T.; Rivera, P.; Shin-Ya, K.; Grotzer, M. A., Telomerase inhibition, telomere shortening, cell growth suppression and induction of apoptosis by telomestatin in childhood neuroblastoma cells. *European journal of cancer* **2005**, 41, 2873-2881.

[77] Tahara, H.; Shin-ya, K.; Seimiya, H.; Yamada, H.; Tsuruo, T.; Ide, T., G-quadruplex stabilization by telomestatin induces TRF2 protein dissociation from telomeres and anaphase bridge formation accompanied by loss of the 3' telomeric overhang in cancer cells. *Oncogene* **2006**, 25, 1955-1966.

[78] Tauchi, T.; Shin-ya, K.; Sashida, G.; Sumi, M.; Nakajima, A.; Shimamoto, T.; Ohyashiki, J. H.; Ohyashiki, K., Activity of a novel G-quadruplex-interactive telomerase inhibitor, telomestatin (SOT-095), against human leukemia cells: involvement of ATM-dependent DNA damage response pathways. *Oncogene* **2003**, 22, 5338-5347.

[79] Chung, W. J.; Heddi, B.; Tera, M.; Iida, K.; Nagasawa, K.; Anh Tuan, P., Solution Structure of an Intramolecular (3+1) Human Telomeric G-Quadruplex Bound to a Telomestatin Derivative. *Journal of the American Chemical Society* **2013**, 135, 13495-13501.

[80] Spomer, J.; Cang, X.; Cheatham, T. E., 3rd, Molecular dynamics simulations of G-DNA and perspectives on the simulation of nucleic acid structures. *Methods* **2012**, 57, 25-39.

[81] Pérez, A.; Marchán, I.; Svozil, D.; Spomer, J.; Cheatham, T. E. r.; Laughton, C. A.; Orozco, M., Refinement of the AMBER Force Field for Nucleic Acids: Improving the Description of  $\alpha/\gamma$  Conformers. *Biophysical Journal* **2007**, 92, 3817-3829.

- [82] Jorgensen, W. L.; Chandrasekhar, J.; Madura, J. D.; Impey, R. W.; Klein, M. L., Comparisons of simple potential functions for simulating liquid water. *Journal of Physical Chemistry* **1983**, 79, 926-935.
- [83] Joung, I. S.; Cheatham, T. E., Determination of alkali and halide monovalent ion parameters for use in explicitly solvated biomolecular simulations. *Journal of Physical Chemistry B* **2008**, 112, 9020-9041.
- [84] Bayly, C. I.; Cieplak, P.; Cornell, W. D.; Kollman, P. A., A Well-Behaved Electrostatic Potential Based Method Using Charge Restraints for Deriving Atomic Charges - the Resp Model. *Journal of Physical Chemistry* **1993**, 97, 10269-10280.
- [85] Wang, J. M.; Wolf, R. M.; Caldwell, J. W.; Kollman, P. A.; Case, D. A., Development and testing of a general amber force field. *Journal of Computational Chemistry* **2004**, 25, 1157-1174.
- [86] Lavery, R.; Zakrzewska, K.; Beveridge, D.; Bishop, T. C.; Case, D. A.; Cheatham, T. E. I.; Dixit, S.; Jayaram, B.; Lankas, F.; Laughton, C.; Maddocks, J. H.; Michon, A.; Osman, R.; Orozco, M.; Perez, A.; Singh, T.; Spackova, N.; Sponer, J., A systematic molecular dynamics study of nearest-neighbor effects on base pair and base pair step conformations and fluctuations in B-DNA *Nucleic acids research* **2010**, 38, 299-313.
- [87] Cosconati, S.; Marinelli, L.; Trotta, R.; Virno, A.; De Tito, S.; Romagnoli, R.; Pagano, B.; Limongelli, V.; Giancola, C.; Baraldi, P. G.; Mayol, L.; Novellino, E.; Randazzo, A., Structural and Conformational Requisites in DNA Quadruplex Groove Binding: Another Piece to the Puzzle. *Journal of the American Chemistry Society* **2010**, 132, 6425-6433.
- [88] Fadna, E.; Spackova, N. a.; Sarzynska, J.; Koca, J.; Orozco, M.; Cheatham, T. E., III.; Kulinski, T.; Sponer, J., Single Stranded Loops of Quadruplex DNA As Key Benchmark for Testing Nucleic Acids Force Fields. *Journal of Chemical Theory and Computation* **2009**, 5, 2514-2530
- [89] Mukherjee, A.; Lavery, R.; Bagchi, B.; Hynes, J. T., On the Molecular Mechanism of Drug Intercalation into DNA: A Simulation Study of the Intercalation Pathway, Free Energy, and DNA Structural Changes. *Journal of the American Chemical Society* **2008**, 130, 9747-9755.
- [90] Lei, H.; Wang, X.; Wu, C., Early stage intercalation of doxorubicin to DNA fragments observed in molecular dynamics binding simulations. *Journal of Molecular Graphics & Modelling* **2012**, 38, 279-89.

- [91] D.A. Case; V. Babin; J.T. Berryman; R.M. Betz; Q. Cai, D. S.; Cerutti; T.E. Cheatham, I.; T.A. Darden; R.E. Duke; H. Gohlke; A.W. Goetz; S. Gusarov; N. Homeyer; P. Janowski; J. Kaus; I. Kolossváry; A. Kovalenko; T.S. Lee; S. LeGrand; T. Luchko; R. Luo; B. Madej; K.M. Merz; F. Paesani; D.R. Roe; A. Roitberg; C. Sagui; R. Salomon-Ferrer; G. Seabra; C.L. Simmerling; W. Smith; J. Swails; R.C. Walker; J. Wang; R.M. Wolf; and, X. W.; Kollman, P. A., *AMBER 14*. **2014**.
- [92] Ivani, I.; Dans, P. D.; Noy, A.; Perez, A.; Faustino, I.; Hospital, A.; Walther, J.; Andrio, P.; Goni, R.; Balaceanu, A.; Portella, G.; Battistini, F.; Gelpi, J. L.; Gonzalez, C.; Vendruscolo, M.; Laughton, C. A.; Harris, S. A.; Case, D. A.; Orozco, M., Parmbsc1: a refined force field for DNA simulations. *Nature methods* **2016**, 13, 55-8.
- [93] Ryckaert, J.; Ciccotti, G.; Berendsen, H. J. C., Numerical Integration of the Cartesian Equations of Motion of a System with Constraints: Molecular Dynamics of n-Alkanes. *Journal of Chemical Physics* **1977**, 23, 327-341.
- [94] Essmann, U.; Perera, L.; Berkowitz, M. L.; Darden, T. A.; Lee, H.; Pedersen, L. G., A smooth particle mesh Ewald method. *Journal of Chemical Physics* **1995**, 103, 8577-8593.
- [95] Procacci, P.; Berne, B. J., Multiple Time-Scale Methods For Constant-Pressure Molecular-Dynamics Simulations Of Molecular-Systems. *Molec. Phys.* **1994**, 83, 255-272.
- [96] Daura, X.; Gademann, K.; Jaun, B.; Seebach, D.; van Gunsteren, W. F.; Mark, A. E., Peptide folding: When simulation meets experiment. *Angewandte Chemie-International Edition* **1999**, 38, 236-240.
- [97] Kollman, P. A.; Massova, I.; Reyes, C.; Kuhn, B.; Huo, S.; Chong, L.; Lee, M.; Lee, T.; Duan, Y.; Wang, W.; Donini, O.; Cieplak, P.; Srinivasan, J.; Case, D. A.; Cheatham, T. E. I., Calculating Structures and Free Energies of Complex Molecules: Combining Molecular Mechanics and Continuum Model. *Accounts of Chemical Research* **2000**, 33, 889-897.
- [98] Ohnmacht, S. A.; Neidle, S., Small-molecule quadruplex-targeted drug discovery. *Bioorganic & medicinal chemistry letters* **2014**, 24, 2602-12.
- [99] Nicoludis, J. M.; Miller, S. T.; Jeffrey, P. D.; Barrett, S. P.; Rablen, P. R.; Lawton, T. J.; Yatsunyk, L. A., Optimized end-stacking provides specificity of N-methyl mesoporphyrin IX for human telomeric G-quadruplex DNA. *Journal of the American Chemical Society* **2012**, 134, 20446-56.
- [100] Phan, A. T.; Kuryavyi, V.; Gaw, H. Y.; Patel, D. J., Small-molecule interaction with a five-guanine-tract G-quadruplex structure from the human MYC promoter. *Nature Chemical Biology* **2005**, 1, 167-173.

- [101] Clark, G. R.; Pytel, P. D.; Squire, C. J., The high-resolution crystal structure of a parallel intermolecular DNA G-4 quadruplex/drug complex employing syn glycosyl linkages. *Nucleic acids research* **2012**, 40, 5731-8.
- [102] Campbell, N. H.; Parkinson, G. N.; Reszka, A. P.; Neidle, S., Structural basis of DNA quadruplex recognition by an acridine drug. *Journal of the American Chemical Society* **2008**, 130, 6722-+.
- [103] Campbell, N. H.; Karim, N. H.; Parkinson, G. N.; Gunaratnam, M.; Petrucci, V.; Todd, A. K.; Vilar, R.; Neidle, S., Molecular basis of structure-activity relationships between salphen metal complexes and human telomeric DNA quadruplexes. *Journal of Medicinal Chemistry* **2012**, 55, 209-22.
- [104] Collie, G. W.; Promontorio, R.; Hampel, S. M.; Micco, M.; Neidle, S.; Parkinson, G. N., Structural basis for telomeric G-quadruplex targeting by naphthalene diimide ligands. *Journal of the American Chemical Society* **2012**, 134, 2723-31.
- [105] Dai, J.; Carver, M.; Hurley, L. H.; Yang, D., Solution structure of a 2:1 quindoline-c-MYC G-quadruplex: insights into G-quadruplex-interactive small molecule drug design. *Journal of the American Chemical Society* **2011**, 133, 17673-80.
- [106] Gavathiotis, E.; Heald, R. A.; Stevens, M. F. G.; Searle, M. S., Drug Recognition and Stabilisation of the Parallel-stranded DNA Quadruplex d(TTAGGGT)<sub>4</sub> Containing the Human Telomeric Repeat. *Journal of Molecular Biology* **2003**, 334, 25-36.
- [107] Hounsou, C.; Guittat, L.; Monchaud, D.; Jourdan, M.; Saettel, N.; Mergny, J. L.; Teulade-Fichou, M. P., G-quadruplex recognition by quinacridines: a SAR, NMR, and biological study. *ChemMedChem* **2007**, 2, 655-66.
- [108] Bazzicalupi, C.; Ferraroni, M.; Bilia, A. R.; Scheggi, F.; Gratteri, P., The crystal structure of human telomeric DNA complexed with berberine: an interesting case of stacked ligand to G-tetrad ratio higher than 1:1. *Nucleic acids research* **2013**, 41, 632-8.
- [109] Tera, M.; Ishizuka, H.; Takagi, M.; Suganuma, M.; Shin-ya, K.; Nagasawa, K., Macrocyclic hexaoxazoles as sequence- and mode-selective G-quadruplex binders. *Angewandte Chemie* **2008**, 47, 5557-60.
- [110] Biffi, G.; Tannahill, D.; Miller, J.; Howat, W. J.; Balasubramanian, S., Elevated Levels of G-Quadruplex Formation in Human Stomach and Liver Cancer Tissues. *PLoS one* **2014**, 9.
- [111] Doi, T.; Shibata, K.; Yoshida, M.; Takagi, M.; Tera, M.; Nagasawa, K.; Shin-ya, K.; Takahashi, T., (S)-Stereoisomer of telomestatin as a potent G-quadruplex binder and telomerase inhibitor. *Organic & biomolecular chemistry* **2011**, 9, 387-393.

[112] Doi, T.; Yoshida, M.; Shin-ya, K.; Takahashi, T., Total synthesis of (R)-telomestatin. *Organic Letters* **2006**, 8, 4165-4167.

[113] Shalaby, T.; von Bueren, A. O.; Huerlimann, M.-L.; Fiaschetti, G.; Castelletti, D.; Masayuki, T.; Nagasawa, K.; Arcaro, A.; Jelesarov, I.; Shin-ya, K.; Grotzer, M., Disabling c-Myc in Childhood Medulloblastoma and Atypical Teratoid/Rhabdoid Tumor Cells by the Potent G-Quadruplex Interactive Agent S2T1-6OTD. *Molecular cancer therapeutics* **2010**, 9, 167-179.

[114] Shamma, M. A.; Reis, R. J. S.; Li, C.; Koley, H.; Hurley, L. H.; Anderson, K. C.; Munshi, N. C., Telomerase inhibition and cell growth arrest after telomestatin treatment in multiple myeloma. *Clinical Cancer Research* **2004**, 10, 770-776.

## Appendix A

### A Mechanical Study of Anti-Cancer Drug Resistance Caused by 10 Topoisomerase I Mutations, Including 7 Camptothecin Analogs and Lucanthone

Table S1. Decomposition of MM-GBSA binding energies (kcal/mol) for SN-38.

Target	$\Delta$ Conformation	$\Delta$ GBELE	$\Delta$ Hydrophobic	$\Delta$ VDW	$\Delta$ Sum	$\Delta\Delta$ Conformation	$\Delta\Delta$ GBELE	$\Delta\Delta$ Hydrophobic	$\Delta\Delta$ VDW	$\Delta\Delta$ Sum
1K4T	4.0	8.4	-24.4	-89.2	-101.1	-	-	-	-	-
G363C	2.2	8.6	-15.9	-75.5	-80.5	-1.9	0.2	8.5	13.7	20.5
G717V	2.5	13.4	-16.3	-76.8	-77.3	-1.5	4.9	8.1	12.4	23.8
N722A	2.9	14.4	-15.9	-74.6	-73.2	-1.1	6.0	8.5	14.6	27.9
N722S	2.9	14.4	-15.9	-74.6	-73.2	-1.1	6.0	8.5	14.6	27.9
R364H	3.0	3.1	-16.7	-75.0	-85.6	-1.0	-5.3	7.7	14.2	15.5
G503S	2.4	16.5	-15.5	-80.4	-77.0	-1.6	8.1	8.8	8.8	24.1
D533N	2.9	14.9	-15.3	-77.7	-75.3	-1.2	6.5	9.1	11.4	25.8
F361S	2.3	5.7	-23.0	-55.2	-70.3	3.8	-2.8	1.4	34.0	30.8
T729A	6.9	6.8	-15.6	-75.4	-77.3	2.6	-1.7	8.8	13.8	23.7
D533G	14.7	24.3	-13.5	-61.9	-36.4	-4.0	15.8	10.9	27.3	64.7

$\Delta\Delta G = \Delta\Delta G_{\text{Mutant}} - \Delta\Delta G_{\text{Wildtype}}$   
 $= \Delta\text{Conformation} + \Delta\text{GBELE} + \Delta\text{Hydrophobic} + \Delta\text{VDW}$ , GBELE=  
 GB+Coulom+Hbond, Hydrophobic=LIPO, VDW= VDW+Pi stacking +self-contact  
 correction.  $\Delta\Delta G = \Delta G_{\text{Mutant}} - \Delta G_{\text{Wildtype}}$

Table S2. Decomposition of MM-GBSA binding energies (kcal/mol) for Topotecan.

Target	$\Delta$ Conformation	$\Delta$ GBELE	$\Delta$ Hydrophobic	$\Delta$ VDW	$\Delta$ Sum	$\Delta\Delta$ Conformation	$\Delta\Delta$ GBELE	$\Delta\Delta$ Hydrophobic	$\Delta\Delta$ VDW	$\Delta\Delta$ Sum
1K4T	4.0	0.4	-25.8	-83.8	-105.2	-	-	-	-	-
G363C	3.6	3.7	-16.2	-81.0	-89.8	-0.4	3.3	9.6	2.8	15.4
G717V	3.8	4.1	-16.0	-83.2	-91.3	-0.3	3.7	9.8	0.6	13.9
N722A	4.2	10.6	-16.7	-78.9	-80.9	0.2	10.2	9.1	4.9	24.3
N722S	4.2	10.6	-16.7	-78.9	-80.9	0.2	10.2	9.1	4.9	24.3
R364H	4.3	-1.8	-17.0	-80.9	-95.4	0.3	-2.2	8.8	2.9	9.8
G503S	5.7	-1.5	-12.7	-76.9	-85.5	1.6	-1.9	13.1	6.9	19.7
D533N	3.1	18.8	-16.7	-83.6	-78.5	-1.0	18.4	9.1	0.2	26.7
F361S	5.0	-2.8	-12.8	-79.4	-89.9	0.9	-3.2	13.1	4.4	15.3
T729A	5.5	-0.7	-12.6	-78.5	-86.3	1.4	-1.1	13.2	5.3	18.9
D533G	4.7	1.0	-13.6	-77.1	-85.1	0.6	0.6	12.2	6.7	20.1

$\Delta\Delta G = \Delta\Delta G_{\text{Mutant}} - \Delta\Delta G_{\text{Wildtype}}$   
 $= \Delta\text{Conformation} + \Delta\text{GBELE} + \Delta\text{Hydrophobic} + \Delta\text{VDW}$ , GBELE=  
 GB+Coulom+Hbond, Hydrophobic=LIPO, VDW= VDW+Pi stacking +self-contact  
 correction.  $\Delta\Delta G = \Delta G_{\text{Mutant}} - \Delta G_{\text{Wildtype}}$



Table S3. Decomposition of MM-GBSA binding energies (kcal/mol) for Camptothecin.

Target	$\Delta$ Conformation	$\Delta$ GBELE	$\Delta$ Hydrophobic	$\Delta$ VDW	$\Delta$ Sum	$\Delta\Delta$ Conformation	$\Delta\Delta$ GBELE	$\Delta\Delta$ Hydrophobic	$\Delta\Delta$ VDW	$\Delta\Delta$ Sum
1K4T	3.3	12.6	-22.8	-86.1	-93.1	-	-	-	-	-
G363C	1.3	13.6	-15.7	-76.7	-77.5	-2.0	1.0	7.1	9.4	15.5
G717V	1.0	16.6	-16.0	-77.7	-76.1	-2.3	4.0	6.8	8.4	17.0
N722A	2.0	18.7	-15.9	-76.0	-71.2	-1.3	6.1	7.0	10.1	21.8
N722S	2.0	18.7	-15.9	-76.0	-71.2	-1.3	6.1	7.0	10.1	21.8
R364H	1.9	6.2	-16.5	-75.6	-83.9	-1.4	-6.4	6.4	10.5	9.1
G503S	0.8	11.7	-15.2	-79.2	-81.9	-2.5	-0.9	7.6	6.9	11.1
D533N	1.3	14.5	-15.2	-77.0	-76.3	-2.0	1.9	7.7	9.2	16.7
F361S	6.8	15.8	-11.4	-65.3	-54.2	3.5	3.2	11.4	20.8	38.8
T729A	0.1	11.1	-15.3	-78.2	-82.3	-3.2	-1.5	7.5	7.9	10.7
D533G	6.9	10.7	-11.5	-69.9	-63.7	3.6	-1.9	11.4	16.2	29.3

$\Delta G = \Delta\text{Conformation} + \Delta\text{GBELE} + \Delta\text{Hydrophobic} + \Delta\text{VDW}$ , GBELE= GB+Coulom+Hbond, Hydrophobic=LIPO, VDW= VDW+Pi stacking +self-contact correction.  $\Delta\Delta G = \Delta G_{\text{Mutant}} - \Delta G_{\text{Wildtype}}$

Table S4. Decomposition of MM-GBSA binding energies (kcal/mol) for Exatecan.

Target	$\Delta$ Conformation	$\Delta$ GBELE	$\Delta$ Hydrophobic	$\Delta$ VDW	$\Delta$ Sum	$\Delta\Delta$ Conformation	$\Delta\Delta$ GBELE	$\Delta\Delta$ Hydrophobic	$\Delta\Delta$ VDW	$\Delta\Delta$ Sum
1K4T	3.2	23.8	-33.0	-66.9	-72.9	-	-	-	-	-
G363C	6.0	38.9	-19.1	-65.1	-39.3	2.8	15.1	13.9	1.9	33.6
G717V	4.9	40.8	-19.4	-62.1	-35.8	1.7	17.0	13.6	4.9	37.1
N722A	7.3	44.6	-19.6	-64.2	-31.9	4.1	20.8	13.4	2.7	41.0
N722S	7.3	44.6	-19.6	-64.2	-31.9	4.1	20.8	13.4	2.7	41.0
R364H	10.6	42.0	-19.6	-52.6	-19.6	7.4	18.2	13.4	14.3	53.4
G503S	7.8	32.9	-18.7	-59.9	-38.0	4.6	9.1	15.7	7.0	35.0
D533N	3.0	39.7	-13.4	-62.2	-33.0	-0.2	15.9	21.1	4.7	40.0
F361S	5.7	15.9	-30.2	-45.5	-54.2	2.6	-7.9	12.1	21.4	18.8
T729A	4.2	35.9	-24.3	-71.7	-55.8	1.0	12.2	-1.7	-4.8	17.1
D533G	0.5	33.2	-22.2	-73.7	-62.2	-2.7	9.4	-1.8	-6.8	10.7

$\Delta G = \Delta\text{Conformation} + \Delta\text{GBELE} + \Delta\text{Hydrophobic} + \Delta\text{VDW}$ , GBELE= GB+Coulom+Hbond, Hydrophobic=LIPO, VDW= VDW+Pi stacking +self-contact correction.  $\Delta\Delta G = \Delta G_{\text{Mutant}} - \Delta G_{\text{Wildtype}}$

Table S5. Decomposition of MM-GBSA binding energies (kcal/mol) for Gimatcan.

Target	$\Delta$ Conformation	$\Delta$ GBELE	$\Delta$ Hydrophobic	$\Delta$ VDW	$\Delta$ Sum	$\Delta\Delta$ Conformation	$\Delta\Delta$ GBELE	$\Delta\Delta$ Hydrophobic	$\Delta\Delta$ VDW	$\Delta\Delta$ Sum
1K4T	6.0	22.6	-34.3	-84.2	-89.8	-	-	-	-	-
G363C	6.9	36.1	-24.6	-75.8	-57.5	0.8	13.4	9.7	8.3	32.3
G717V	7.5	35.8	-25.0	-77.0	-58.7	1.4	13.2	9.3	7.2	31.1
N722A	6.0	36.4	-25.6	-74.6	-57.7	0.0	13.8	8.6	9.6	32.0
N722S	6.0	36.4	-25.6	-74.6	-57.7	0.0	13.8	8.6	9.6	32.0
R364H	5.8	24.4	-26.1	-75.7	-71.7	-0.3	1.7	8.2	8.5	18.1
G503S	2.3	34.2	-24.7	-79.8	-68.0	-3.7	11.6	9.6	4.4	21.8
D533N	6.0	40.6	-14.4	-71.6	-39.4	0.0	18.0	19.9	12.6	50.4
F361S	3.6	14.2	-33.0	-60.9	-76.0	-2.4	-8.4	1.3	23.3	13.8
T729A	7.5	36.7	-25.6	-74.8	-56.1	1.5	14.1	8.7	9.4	33.7
D533G	6.5	39.9	-14.9	-71.2	-39.7	0.4	17.2	19.4	13.0	50.1

$\Delta G = \Delta\text{Conformation} + \Delta\text{GBELE} + \Delta\text{Hydrophobic} + \Delta\text{VDW}$ , GBELE= GB+Coulom+Hbond, Hydrophobic=LIPO, VDW= VDW+Pi stacking +self-contact correction.  $\Delta\Delta G = \Delta G_{\text{Mutant}} - \Delta G_{\text{Wildtype}}$



Table S6. Decomposition of MM-GBSA binding energies (kcal/mol) for Belotecan.

Target	$\Delta$ Conformation	$\Delta$ GBELE	$\Delta$ Hydrophobic	$\Delta$ VDW	$\Delta$ Sum	$\Delta\Delta$ Conformation	$\Delta\Delta$ GBELE	$\Delta\Delta$ Hydrophobic	$\Delta\Delta$ VDW	$\Delta\Delta$ Sum
1K4T	3.6	13.7	-32.6	-84.7	-100.0	-	-	-	-	-
G363C	12.7	25.1	-21.6	-70.4	-54.2	9.2	11.4	11.0	14.2	45.8
G717V	3.9	28.9	-23.6	-73.2	-64.0	0.3	15.2	9.0	11.5	36.0
N722A	-4.6	28.1	-21.5	-71.0	-69.0	-8.2	14.4	11.1	13.7	31.0
N722S	-4.6	28.1	-21.5	-71.0	-69.0	-8.2	14.4	11.1	13.7	31.0
R364H	4.8	13.0	-23.2	-66.6	-72.0	1.2	-0.7	9.4	18.1	28.0
G503S	9.3	22.4	-13.5	-68.5	-50.3	5.7	8.7	19.1	16.2	49.7
D533N	3.4	38.1	-23.6	-70.2	-52.2	-0.2	24.4	9.0	14.5	47.8
F361S	5.8	13.6	-30.3	-57.9	-68.7	2.2	0.0	2.3	26.8	31.3
T729A	8.9	26.0	-23.8	-66.7	-55.6	5.3	12.3	8.8	18.0	44.4
D533G	2.5	30.5	-21.7	-67.5	-56.2	-1.0	16.8	10.9	17.1	43.8

$\Delta\Delta G = \Delta\Delta G_{Mutant} - \Delta\Delta G_{Wildtype}$   
 $= \Delta\Delta\text{Conformation} + \Delta\Delta\text{GBELE} + \Delta\Delta\text{Hydrophobic} + \Delta\Delta\text{VDW}$ , GBELE= GB+Coulom+Hbond, Hydrophobic=LIPO, VDW= VDW+Pi stacking +self-contact correction.

Table S7. Decomposition of MM-GBSA binding energies (kcal/mol) for Lucanthone.

Target	$\Delta$ Conformation	$\Delta$ GBELE	$\Delta$ Hydrophobic	$\Delta$ VDW	$\Delta$ Sum	$\Delta\Delta$ Conformation	$\Delta\Delta$ GBELE	$\Delta\Delta$ Hydrophobic	$\Delta\Delta$ VDW	$\Delta\Delta$ Sum
1K4T	2.7	14.8	-24.3	-64.9	-71.7	-	-	-	-	-
G363C	9.1	20.1	-25.1	-56.9	-52.8	6.4	5.4	-0.8	8.0	18.9
G717V	3.3	15.9	-20.6	-60.0	-61.4	0.6	1.1	3.8	4.9	10.3
N722A	4.5	27.2	-15.5	-63.5	-47.3	1.7	12.4	8.8	1.4	24.4
N722S	4.5	27.2	-15.5	-63.5	-47.3	1.7	12.4	8.8	1.4	24.4
R364H	6.2	5.2	-18.9	-51.0	-58.5	3.4	-9.6	5.5	13.9	13.2
G503S	0.4	22.5	-17.4	-61.3	-55.9	-2.4	7.7	7.0	3.6	15.9
D533N	-0.3	25.8	-11.9	-61.5	-47.8	-3.0	11.1	12.5	3.4	24.0
F361	2.7	25.9	-13.2	-61.7	-46.3	0.0	11.1	11.2	3.2	25.5
T729A	2.2	19.2	-12.9	-65.0	-55.5	-0.5	4.4	11.4	-0.1	15.2
D533G	2.4	24.2	-14.7	-63.8	-51.9	-0.4	9.4	9.6	1.1	19.8

$\Delta\Delta G = \Delta\Delta G_{Mutant} - \Delta\Delta G_{Wildtype}$   
 $= \Delta\Delta\text{Conformation} + \Delta\Delta\text{GBELE} + \Delta\Delta\text{Hydrophobic} + \Delta\Delta\text{VDW}$ , GBELE= GB+Coulom+Hbond, Hydrophobic=LIPO, VDW= VDW+Pi stacking +self-contact correction.

Table S8. Decomposition of MM-GBSA binding energies (kcal/mol) for Lurtotecan.

Target	$\Delta$ Conformation	$\Delta$ GBELE	$\Delta$ Hydrophobic	$\Delta$ VDW	$\Delta$ Sum	$\Delta\Delta$ Conformation	$\Delta\Delta$ GBELE	$\Delta\Delta$ Hydrophobic	$\Delta\Delta$ VDW	$\Delta\Delta$ Sum
1K4T	13.0	-25.3	-21.1	-49.9	-83.4	-	-	-	-	-
G363C	16.0	-17.5	-21.0	-46.2	-68.8	3.0	7.8	0.1	3.7	14.6
G717V	23.8	-17.2	-21.5	-50.2	-65.1	10.9	8.1	-0.3	-0.3	18.3
N722A	26.4	-12.1	-20.5	-46.1	-52.3	13.4	13.2	0.6	3.9	31.1
N722S	26.4	-12.1	-20.5	-46.1	-52.3	13.4	13.2	0.6	3.9	31.1
R364H	39.4	-4.2	-22.5	-63.1	-50.4	26.4	21.0	-1.4	-13.1	32.9
G503S	26.0	-19.7	-21.5	-35.7	-50.8	13.1	5.6	-0.3	14.2	32.5
D533N	21.6	-17.3	-21.8	-37.5	-55.1	8.7	7.9	-0.7	12.4	28.3
F361S	26.5	-19.5	-21.5	-35.3	-49.8	13.6	5.7	-0.4	14.6	33.5
T729A	14.5	-13.1	-21.2	-51.4	-71.2	1.5	12.2	0.0	-1.4	12.2
D533G	20.6	-16.6	-22.3	-40.0	-58.3	7.6	8.7	-1.1	9.9	25.1

$\Delta\Delta G = \Delta\Delta\text{Conformation} + \Delta\Delta\text{GBELE} + \Delta\Delta\text{Hydrophobic} + \Delta\Delta\text{VDW}$ , GBELE= GB+Coulom+Hbond, Hydrophobic=LIPO, VDW= VDW+Pi stacking +self-contact correction.

Table S9. Interacting residues on WT with ligands

Camptothecin	Topotecan	LE-SN38	Lurotecán	Exatecan	Irinotecan	Belotecan	Luanthone	Gimatecan	%
H20	H20	H20	H20	H20		H20		H20	77.8
		DT9				DT9		DT9	33.3
DT10	DT10	DT10	DT10	DT10	DT10	DT10	DT10	DT10	100.0
DG12	DG12	DG12	DG12	DG12	DG12	DG12	DG12	DG12	100.0
		DC111	DC111	DC111					33.3
DC112	DC112	DC112	DC112	DC112	DC112	DC112	DC112	DC112	100.0
DA113	DA113	DA113	DA113	DA113	DA113	DA113	DA113	DA113	100.0
DA114		DA114	DA114	DA114	DA114	DA114	DA114	DA114	88.9
TGP11	TGP11	TGP11	TGP11	TGP11	TGP11	TGP11	TGP11	TGP11	100.0
		ALA351	ALA351		ALA351	ALA351		ALA351	44.4
ASN352	ASN352	ASN352	ASN352	ASN352	ASN352	ASN352	ASN352	ASN352	100.0
	LYS354				LYS354				22.2
					ILE355				11.1
GLU356	GLU356	GLU356	GLU356	GLU356	GLU356	GLU356	GLU356	GLU356	100.0
ARG364	ARG364	ARG364	ARG364	ARG364	ARG364	ARG364	ARG364	ARG364	100.0
			LYS374		LYS374				22.2
					ILE377				11.1
			TRP416						11.1
			LYS425	LYS425	LYS425				33.3
			TYR426			TYR426		TYR426	33.3
			ILE427		ILE427	ILE427		ILE427	44.4
			MET428		MET428	MET428		MET428	44.4
			LEU429						11.1
			ASN430						11.1
			PRO431						11.1
			LYS436						11.1
	ARG488				ARG488			ARG488	33.3
LYS532	LYS532	LYS532	LYS532	LYS532	LYS532	LYS532	LYS532	LYS532	100.0
ASP533	ASP533	ASP533	ASP533	ASP533	ASP533	ASP533	ASP533	ASP533	100.0
ILE535	ILE535	ILE535	ILE535		ILE535	ILE535	ILE535	ILE535	88.9
					ASN631				11.1
					HID632			HID632	33.3
					GLN633				11.1
					ALA715				11.1
THR718	THR718	THR718	THR718	THR718	THR718	THR718	THR718	THR718	100.0
ASN722	ASN722	ASN722	ASN722	ASN722	ASN722	ASN722	ASN722	ASN722	100.0
PTR723	PTR723	PTR723	PTR723	PTR723	PTR723	PTR723	PTR723	PTR723	100.0

\*The distance cutoff between a ligand and contacting residues/water molecules is 5Å.

Table S10. Interacting residues on D533G with ligands. The highlighted row indicates the mutated residue is present within 5Å of the ligand.

Camptothecin	Topotecan	LE-SN38	Lurotecian	Exatecan	Irinotecan	Belotecan	Luanthone	Gimatecan	%
H20	H20	H20	H20		H20	H20		H20	77.8
		DT9	DT9		DT9			DT9	44.4
DT10	DT10	DT10	DT10	DT10	DT10	DT10	DT10	DT10	100.0
DG12	DG12	DG12	DG12	DG12	DG12	DG12	DG12	DG12	100.0
							DA13		11.1
DC112	DC112	DC112	DC112	DC112	DC112	DC112	DC112	DC112	100.0
DA113	DA113	DA113	DA113	DA113	DA113	DA113	DA113	DA113	100.0
DA114	DA114	DA114	DA114	DA114	DA114		DA114	DA114	88.9
TGP11	TGP11	TGP11	TGP11	TGP11	TGP11	TGP11	TGP11	TGP11	100.0
					ILE350				11.1
			ALA351		ALA351			ALA351	33.3
ASN352	ASN352	ASN352	ASN352	ASN352	ASN352	ASN352	ASN352	ASN352	100.0
					ILE355				11.1
GLU356	GLU356	GLU356	GLU356	GLU356	GLU356	GLU356		GLU356	88.9
ARG364	ARG364	ARG364	ARG364	ARG364	ARG364	ARG364	ARG364	ARG364	100.0
			LYS374		LYS374				22.2
	TRP416		TRP416		TRP416			TRP416	44.4
	LYS425		LYS425		LYS425	LYS425		LYS425	55.6
	TYR426		TYR426		TYR426	TYR426		TYR426	55.6
			ILE427		ILE427			ILE427	33.3
			MET428		MET428			MET428	33.3
			LEU429		LEU429				22.2
			ASN430						11.1
			PRO431						11.1
			LYS436		LYS436				22.2
ARG488	ARG488	ARG488	ARG488	ARG488	ARG488	ARG488		ARG488	88.9
LYS532	LYS532	LYS532	LYS532	LYS532	LYS532	LYS532	LYS532	LYS532	100.0
GLY533	GLY533	GLY533	GLY533	GLY533	GLY533	GLY533	GLY533	GLY533	100.0
ILE535	ILE535	ILE535	ILE535		ILE535	ILE535	ILE535	ILE535	100.0
	HIS632								11.1
THR718	THR718	THR718		THR718	THR718	THR718	THR718	THR718	88.9
ASN722	ASN722	ASN722	ASN722	ASN722	ASN722	ASN722	ASN722	ASN722	100.0
PTR723	PTR723	PTR723	PTR723	PTR723	PTR723	PTR723	PTR723	PTR723	100.0

\*The distance cutoff between a ligand and contacting residues/water molecules is 5Å.

Table S11. Interacting residues on D533N with ligands. The highlighted row indicates the mutated residue is present within 5Å of the ligand.

Camptothecin	Topotecan	LE-SN38	Lurotecan	Exatecan	Irinotecan	Belotecan	Luanthone	Gimatecan	%
H20	H20	H20	H20		H20	H20		H20	77.8
		DT9	DT9		DT9			DT9	44.4
DT10	DT10	DT10	DT10	DT10	DT10	DT10	DT10	DT10	100.0
DG12	DG12	DG12	DG12	DG12	DG12	DG12	DG12	DG12	100.0
							DA13		11.1
DC112	DC112	DC112	DC112	DC112	DC112	DC112	DC112	DC112	100.0
DA113	DA113	DA113	DA113	DA113	DA113	DA113	DA113	DA113	100.0
DA114			DA114	DA114	DA114		DA114	DA114	66.7
TGP11	TGP11	TGP11	TGP11	TGP11	TGP11	TGP11	TGP11	TGP11	100.0
					ILE350				11.1
			ALA351		ALA351			ALA351	33.3
ASN352	ASN352	ASN352	ASN352	ASN352	ASN352	ASN352	ASN352	ASN352	100.0
			LYS354						11.1
					ILE355				11.1
GLU356	GLU356	GLU356	GLU356	GLU356	GLU356	GLU356		GLU356	88.9
ARG364	ARG364	ARG364	ARG364	ARG364	ARG364	ARG364	ARG364	ARG364	100.0
			LYS374						11.1
			TRP416		TRP416			TRP416	44.4
			LYS425	LYS425	LYS425	LYS425		LYS425	66.7
			TYR426	TYR426	TYR426	TYR426		TYR426	66.7
					ILE427			ILE427	22.2
			MET428		MET428			MET428	33.3
			LEU429		LEU429				22.2
			ASN430						11.1
			PRO431						11.1
			LYS436		LYS436				22.2
ARG488	ARG488	ARG488				ARG488		ARG488	55.6
LYS532	LYS532	LYS532	LYS532	LYS532	LYS532	LYS532	LYS532	LYS532	100.0
ASN533	ASN533	ASN533	ASN533	ASN533	ASN533	ASN533	ASN533	ASN533	100.0
ILE535	ILE535	ILE535	ILE535		ILE535	ILE535	ILE535	ILE535	88.9
						HIS632			11.1
THR718	THR718	THR718	THR718	THR718	THR718	THR718	THR718	THR718	100.0
					LEU721		LEU721		22.2
ASN722	ASN722	ASN722	ASN722	ASN722	ASN722	ASN722	ASN722	ASN722	100.0
PTR723	PTR723	PTR723	PTR723	PTR723	PTR723	PTR723	PTR723	PTR723	100.0

\*The distance cutoff between a ligand and contacting residues/water molecules is 5Å.

Table S12. Interacting residues on F361S with ligands

Camptothecin	Topotecan	LE-SN38	Lurotecán	Exatecan	Irinotecan	Belotecan	Luanthone	Gimatecan	%
H20	H20	H20	H20			H20		H20	66.7
								DT9	44.4
DT10	DT10	DT10	DT10	DT10	DT10	DT10	DT10	DT10	100.0
DG12	DG12	DG12	DG12	DG12	DG12	DG12	DG12	DG12	100.0
								DA13	11.1
								DA14	11.1
								DA15	11.1
								DT110	11.1
DC112	DC112	DC112	DC112	DC112	DC112	DC112	DC112	DC112	100.0
DA113	DA113	DA113	DA113	DA113	DA113	DA113	DA113	DA113	100.0
DA114		DA114	DA114	DA114	DA114			DA114	77.8
TGP11	TGP11	TGP11	TGP11	TGP11	TGP11	TGP11	TGP11	TGP11	100.0
								MET263	11.1
								HIS266	11.1
								TYR268	11.1
			ALA351					ALA351	22.2
ASN352	ASN352	ASN352	ASN352	ASN352		ASN352	ASN352	ASN352	88.9
				LYS354					11.1
GLU356	GLU356	GLU356	GLU356	GLU356	GLU356	GLU356		GLU356	88.9
					GLY363				11.1
ARG364	ARG364	ARG364	ARG364	ARG364	ARG364	ARG364	ARG364	ARG364	100.0
								LYS374	11.1
								TRP416	22.2
								LYS425	55.6
	LYS425		LYS425	LYS425		LYS425		LYS425	44.4
	TYR426			TYR426		TYR426		TYR426	44.4
								ILE427	11.1
								MET428	22.2
								LEU429	11.1
								ASN430	11.1
								PRO431	11.1
								LYS436	11.1
ARG488	ARG488	ARG488			ARG488	ARG488	ARG488	ARG488	88.9
LYS532	LYS532	LYS532	LYS532	LYS532	LYS532	LYS532	LYS532	LYS532	100.0
ASP533	ASP533	ASP533	ASP533	ASP533	ASP533	ASP533	ASP533	ASP533	100.0
ILE535	ILE535	ILE535	ILE535	ILE535	ILE535	ILE535	ILE535	ILE535	100.0
								HIS632	22.2
								GLN633	22.2
								ARG634	11.1
								ALA635	11.1
							ALA715		11.1
THR718	THR718	THR718	THR718	THR718	THR718	THR718	THR718	THR718	100.0
ASN722	ASN722	ASN722	ASN722	ASN722	ASN722	ASN722	ASN722	ASN722	100.0
PTR723	PTR723	PTR723	PTR723	PTR723	PTR723	PTR723	PTR723	PTR723	100.0

\*The distance cutoff between a ligand and contacting residues/water molecules is 5Å.

Table S13. Interacting residues on G363C with ligands

Camptothecin	Topotecan	LE-SN38	Lurotecian	Exatecan	Irinotecan	Belotecan	Luanthone	Gimatecan	%
H20	H20	H20	H20		H20	H20		H20	77.8
		DT9			DT9				22.2
DT10	DT10	DT10	DT10	DT10	DT10	DT10	DT10	DT10	100.0
DG12	DG12	DG12	DG12	DG12	DG12	DG12	DG12	DG12	100.0
			DC111						11.1
DC112	DC112	DC112	DC112	DC112	DC112	DC112	DC112	DC112	100.0
DA113	DA113	DA113	DA113	DA113	DA113	DA113	DA113	DA113	100.0
DA114	DA114	DA114	DA114	DA114	DA114				66.7
TGP11	TGP11	TGP11	TGP11	TGP11	TGP11	TGP11	TGP11	TGP11	100.0
			ALA351					ALA351	22.2
ASN352	ASN352	ASN352	ASN352	ASN352	ASN352	ASN352	ASN352	ASN352	100.0
				LYS354					11.1
					ILE355				11.1
GLU356	GLU356	GLU356	GLU356	GLU356	GLU356	GLU356		GLU356	88.9
					PHE361				11.1
ARG364	ARG364	ARG364	ARG364	ARG364	ARG364	ARG364	ARG364	ARG364	100.0
					LYS374				11.1
					ARG375				11.1
					ILE377				11.1
	TRP416		TRP416		TRP416				33.3
					THR417				11.1
					GLU418				11.1
					ILE420				11.1
	LYS425		LYS425	LYS425	LYS425	LYS425		LYS425	66.7
	TYR426		TYR426	TYR426	TYR426			TYR426	55.6
								ILE427	22.2
								MET428	22.2
								LEU429	11.1
								ASN430	11.1
								PRO431	11.1
								LYS436	11.1
ARG488	ARG488	ARG488			ARG488	ARG488	ARG488	ARG488	77.8
LYS532	LYS532	LYS532	LYS532	LYS532	LYS532	LYS532	LYS532	LYS532	100.0
ASP533	ASP533	ASP533	ASP533	ASP533	ASP533	ASP533	ASP533	ASP533	100.0
ILE535	ILE535	ILE535	ILE535		ILE535	ILE535	ILE535	ILE535	88.9
							ASN631		11.1
	HIS632						HIS632	HIS632	33.3
							GLN633		11.1
							ARG634		11.1
THR718	THR718	THR718	THR718	THR718	THR718	THR718	THR718	THR718	100.0
ASN722	ASN722	ASN722	ASN722	ASN722	ASN722	ASN722	ASN722	ASN722	100.0
PTR723	PTR723	PTR723	PTR723	PTR723	PTR723	PTR723	PTR723	PTR723	100.0

\*The distance cutoff between a ligand and contacting residues/water molecules is 5Å.

Table S14. Interacting residues on G503S with ligands

Camptothecin	Topotecan	LE-SN38	Lurotecán	Exatecan	Irinotecan	Belotecan	Luanthone	Gimatecan	%
H20	H20	H20	H20			H20		H20	66.7
			DT9					DT9	22.2
DT10	DT10	DT10	DT10	DT10	DT10	DT10	DT10	DT10	100.0
DG12	DG12	DG12	DG12	DG12	DG12	DG12	DG12	DG12	100.0
					DA13				11.1
					DA14				11.1
					DA15				11.1
	DC111								11.1
DC112	DC112	DC112	DC112	DC112	DC112	DC112	DC112	DC112	100.0
DA113	DA113	DA113	DA113	DA113	DA113	DA113	DA113	DA113	100.0
DA114		DA114	DA114	DA114	DA114			DA114	66.7
TGP11	TGP11	TGP11	TGP11	TGP11	TGP11	TGP11	TGP11	TGP11	100.0
					TYR268				11.1
					HIS266				11.1
			ALA351					ALA351	22.2
ASN352	ASN352	ASN352	ASN352	ASN352		ASN352	ASN352	ASN352	88.9
	LYS354			LYS354					22.2
GLU356	GLU356	GLU356	GLU356	GLU356		GLU356		GLU356	77.8
					ARG362				11.1
ARG364	ARG364	ARG364	ARG364	ARG364	ARG364	ARG364	ARG364	ARG364	100.0
			LYS374						11.1
								TRP416	11.1
	LYS425		LYS425	LYS425		LYS425		LYS425	55.6
				TYR426		TYR426		TYR426	33.3
								ILE427	11.1
			MET428					MET428	22.2
			LEU429						11.1
			ASN430						11.1
			PRO431						11.1
			LYS436						11.1
ARG488	ARG488	ARG488			ARG488	ARG488	ARG488	ARG488	88.9
LYS532	LYS532	LYS532	LYS532	LYS532	LYS532	LYS532	LYS532	LYS532	100.0
ASP533	ASP533	ASP533	ASP533	ASP533	ASP533	ASP533	ASP533	ASP533	100.0
ILE535	ILE535	ILE535	ILE535		ILE535	ILE535	ILE535	ILE535	100.0
					HIS632		HIS632		22.2
					GLN633		GLN633		22.2
THR718	THR718	THR718	THR718	THR718	THR718	THR718	THR718	THR718	100.0
				LEU721					11.1
ASN722	ASN722	ASN722	ASN722	ASN722	ASN722	ASN722	ASN722	ASN722	100.0
PTR723	PTR723	PTR723	PTR723	PTR723	PTR723	PTR723	PTR723	PTR723	100.0

\*The distance cutoff between a ligand and contacting residues/water molecules is 5Å.

Table S15. Interacting residues on G717V with ligands

Camptothecin	Topotecan	LE-SN38	Lurotecian	Exatecan	Irinotecan	Belotecan	Luanthone	Gimatecan	%
H20	H20	H20	H20		H20	H20		H20	77.8
		DT9	DT9		DT9			DT9	44.4
DT10	DT10	DT10	DT10	DT10	DT10	DT10	DT10	DT10	100.0
DG12	DG12	DG12	DG12	DG12	DG12	DG12	DG12	DG12	100.0
			DC111	DC111					22.2
DC112	DC112	DC112	DC112	DC112	DC112	DC112	DC112	DC112	100.0
DA113	DA113	DA113	DA113	DA113	DA113	DA113	DA113	DA113	100.0
DA114	DA114	DA114	DA114	DA114	DA114			DA114	77.8
TGP11	TGP11	TGP11	TGP11	TGP11	TGP11	TGP11	TGP11	TGP11	100.0
			ALA351					ALA351	22.2
ASN352	ASN352	ASN352	ASN352	ASN352	ASN352	ASN352	ASN352	ASN352	100.0
					LYS354				11.1
					ILE355				11.1
GLU356	GLU356	GLU356	GLU356	GLU356	GLU356	GLU356		GLU356	88.9
					PRO357				11.1
					PRO358				11.1
ARG364	ARG364	ARG364	ARG364	ARG364	ARG364	ARG364	ARG364	ARG364	100.0
					GLY369				11.1
			LYS374		LYS374				22.2
					ARG375				11.1
	TRP416		TRP416		TRP416				33.3
					GLU418				11.1
					ASN419				11.1
					ILE420				11.1
	LYS425		LYS425	LYS425	LYS425	LYS425		LYS425	66.7
	THR426		TYR426	TYR426	TYR426		TYR426	TYR426	66.7
			ILE427					ILE427	22.2
			MET428					MET428	22.2
			LEU429						11.1
			ASN430						11.1
			PRO431						11.1
ARG488	ARG488	ARG488			ARG488	ARG488		ARG488	66.7
LYS532	LYS532	LYS532	LYS532	LYS532	LYS532	LYS532	LYS532	LYS532	100.0
ASP533	ASP533	ASP533	ASP533	ASP533	ASP533	ASP533	ASP533	ASP533	100.0
ILE535	ILE535	ILE535	ILE535	ILE535	ILE535	ILE535	ILE535	ILE535	88.9
THR718	THR718	THR718	THR718	THR718	THR718	THR718	THR718	THR718	100.0
							LEU721		11.1
ASN722	ASN722	ASN722	ASN722	ASN722	ASN722	ASN722	ASN722	ASN722	100.0
PTR723	PTR723	PTR723	PTR723	PTR723	PTR723	PTR723	PTR723	PTR723	100.0

\*The distance cutoff between a ligand and contacting residues/water molecules is 5Å.



Table S16. Interacting residues on N722A with ligands. The highlighted row indicates the mutated residue is present within 5Å of the ligand.

Camptothecin	Topotecan	LE-SN38	Lurotecian	Exatecan	Irinotecan	Belotecan	Luanthone	Gimatecan	%
H20	H20	H20	H20		H20	H20		H20	77.8
		DT9	DT9		DT9			DT9	44.4
DT10	DT10	DT10	DT10	DT10	DT10	DT10	DT10	DT10	100.0
DG12	DG12	DG12	DG12	DG12	DG12	DG12		DG12	88.9
	DC111	0	DC111						22.2
DC112	DC112	DC112	DC112	DC112	DC112	DC112	DC112	DC112	100.0
DA113	DA113	DA113	DA113	DA113	DA113	DA113	DA113	DA113	100.0
DA114	DA114	DA114	DA114	DA114	DA114	DA114		DA114	66.7
TGP11	TGP11	TGP11	TGP11	TGP11	TGP11	TGP11	TGP11	TGP11	100.0
			ALA351					ALA351	22.2
ASN352	ASN352	ASN352	ASN352	ASN352	ASN352	ASN352	ASN352	ASN352	100.0
	LYS354	0	LYS354				PHE353		11.1
							LYS354		33.3
							ILE3355		11.1
GLU356	GLU356	GLU356	GLU356	GLU356	GLU356	GLU356	GLU356	GLU356	100.0
					PRO357				11.1
					PRO358				11.1
ARG364	ARG364	ARG364	ARG364	ARG364	ARG364	ARG364	ARG364	ARG364	100.0
			LYS374		LYS374				22.2
					ARG375				11.1
					ILE377				11.1
			TRP416		TRP416		TRP416		33.3
					THR417				11.1
					GLU418				11.1
					ASN419				11.1
					ILE420				11.1
	LYS425		LYS425	LYS425	LYS425	LYS425		LYS425	66.7
			TYR426	TYR426	TYR426	TYR426	TYR426	TYR426	66.7
			ILE427				ILE427		33.3
			MET428					MET428	22.2
			LEU429						11.1
			ASN430						11.1
			PRO431						11.1
			LYS436						11.1
ARG488	ARG488	ARG488			ARG488	ARG488		ARG488	66.7
LYS532	LYS532	LYS532	LYS532	LYS532	LYS532	LYS532		LYS532	88.9
ASP533	ASP533	ASP533	ASP533	ASP533	ASP533	ASP533		ASP533	88.9
ILE535	ILE535	ILE535	ILE535		ILE535	ILE535		ILE535	77.8
								HIS632	11.1
THR718	THR718	THR718	THR718	THR718	THR718	THR718		THR718	88.9
								LEU721	11.1
ALA722	ALA722	ALA722	ALA722	ALA722	ALA722	ALA722	ALA722	ALA722	100.0
PTR723	PTR723	PTR723	PTR723	PTR723	PTR723	PTR723		PTR723	88.9

\*The distance cutoff between a ligand and contacting residues/water molecules is 5Å.

Table S17. Interacting residues on N722S with ligands. The highlighted row indicates the mutated residue is present within 5Å of the ligand.

Camptothecin	Topotecan	LE-SN38	Lurotecancan	Exatecan	Irinotecan	Belotecan	Luanthone	Gimatecan	%
H20	H20	H20	H20		H20	H20		H20	77.8
		DT9	DT9		DT9			DT9	44.4
DT10	DT10	DT10	DT10	DT10	DT10	DT10	DT10	DT10	100.0
DG12	DG12	DG12	DG12	DG12	DG12	DG12		DG12	88.9
	DC111		DC111						22.2
DC112	DC112	DC112	DC112	DC112	DC112	DC112	DC112	DC112	100.0
DA113	DA113	DA113	DA113	DA113	DA113	DA113	DA113	DA113	100.0
DA114		DA114	DA114	DA114	DA114			DA114	66.7
TGP11	TGP11	TGP11	TGP11	TGP11	TGP11	TGP11	TGP11	TGP11	100.0
			ALA351					ALA351	22.2
ASN352	ASN352	ASN352	ASN352	ASN352	ASN352	ASN352	ASN352	ASN352	100.0
							PHE353		11.1
				LYS354			LYS354		33.3
							ILE3355		11.1
GLU356	GLU356	GLU356	GLU356	GLU356	GLU356	GLU356	GLU356	GLU356	100.0
					PRO357				11.1
					PRO358				11.1
ARG364	ARG364	ARG364	ARG364	ARG364	ARG364	ARG364	ARG364	ARG364	100.0
			LYS374		LYS374				22.2
					ARG375				11.1
					ILE377				11.1
			TRP416		TRP416		TRP416		33.3
					THR417				11.1
					GLU418				11.1
					ASN419				11.1
					ILE420				11.1
	LYS425		LYS425	LYS425	LYS425	LYS425		LYS425	66.7
			TYR426	TYR426	TYR426	TYR426	TYR426	TYR426	66.7
			ILE427				ILE427	ILE427	33.3
			MET428					MET428	22.2
			LEU429						11.1
			ASN430						11.1
			PRO431						11.1
			LYS436						11.1
ARG488	ARG488	ARG488			ARG488	ARG488		ARG488	66.7
LYS532	LYS532	LYS532	LYS532	LYS532	LYS532	LYS532		LYS532	88.9
ASP533	ASP533	ASP533	ASP533	ASP533	ASP533	ASP533		ASP533	88.9
ILE535	ILE535	ILE535	ILE535		ILE535	ILE535		ILE535	77.8
								HIS632	11.1
THR718	THR718	THR718	THR718	THR718	THR718	THR718		THR718	88.9
				LEU721					11.1
SER722	SER722	SER722	SER722	SER722	SER722	SER722	SER722	SER722	100.0
PTR723	PTR723	PTR723	PTR723	PTR723	PTR723	PTR723		PTR723	88.9

\*The distance cutoff between a ligand and contacting residues/water molecules is 5Å.

Table S18. Interacting residues on R364H with ligands. The highlighted row indicates the mutated residue is present within 5Å of the ligand.

Camptothecin	Topotecan	LE-SN38	Lurotecian	Exatecan	Irinotecan	Belotecan	Luanthone	Gimatecan	%
H20	H20	H20	H20		H20	H20		H20	77.8
		DT9	DT9		DT9			DT9	44.4
DT10	DT10	DT10	DT10	DT10	DT10	DT10	DT10	DT10	100.0
DG12	DG12	DG12	DG12	DG12	DG12	DG12	DG12	DG12	100.0
		DC111		DC111	DC111				33.3
DC112	DC112	DC112	DC112	DC112	DC112	DC112	DC112	DC112	100.0
DA113	DA113	DA113	DA113	DA113	DA113	DA113	DA113	DA113	100.0
		DA114						DA114	22.2
TGP11	TGP11	TGP11	TGP11	TGP11	TGP11	TGP11	TGP11	TGP11	100.0
			ALA351		ALA351			ALA351	33.3
ASN352	ASN352	ASN352	ASN352	ASN352	ASN352	ASN352	ASN352	ASN352	100.0
	LYS354				LYS354				22.2
	ILE355				ILE355				22.2
GLU356	GLU356	GLU356	GLU356	GLU356	GLU356	GLU356		GLU356	88.9
HIS364	HIS364	HIS364	HIS364	HIS364	HIS364	HIS364	HIS364	HIS364	100.0
			LYS374						11.1
LYS532	LYS532	LYS532	LYS532	LYS532	LYS532	LYS532	LYS532	LYS532	100.0
ASP533	ASP533	ASP533	ASP533	ASP533	ASP533	ASP533	ASP533	ASP533	100.0
ILE535	ILE535	ILE535	ILE535		ILE535	ILE535	ILE535	ILE535	88.9
					TRP416				11.1
	LYS425		LYS425	LYS425		LYS425		LYS425	55.6
				TYR426	TYR426	TYR426		TYR426	44.4
					ILE427			ILE427	22.2
			MET428		MET428			MET428	33.3
			LEU429		LEU429				22.2
			ASN430						11.1
			PRO431						11.1
			LYS436		LYS436				22.2
ARG488	ARG488	ARG488	ARG488		ARG488	ARG488	ARG488	ARG488	88.9
							ASN631		11.1
						HIS632	HIS632	HIS632	33.3
							GLN633		11.1
							ALA715		11.1
THR718	THR718	THR718	THR718	THR718	THR718	THR718	THR718	THR718	100.0
				LEU721			LEU721		22.2
ASN722	ASN722	ASN722	ASN722	ASN722	ASN722	ASN722	ASN722	ASN722	100.0
PTR723	PTR723	PTR723	PTR723	PTR723	PTR723	PTR723	PTR723	PTR723	100.0

\*The distance cutoff between a ligand and contacting residues/water molecules is 5Å.

Table S19. Interacting residues on T729A with ligands

Camptothecin	Topotecan	LE-SN38	Lurotecanc	Exatecan	Irinotecan	Belotecan	Luanthone	Gimatecan	%
H20	H20	H20	H20	H20	H20	H20		H20	88.9
DG12	DG112		DG12	DG12	DG12	DG12	DG12	DG12	88.9
DA114		DA114	DA114	DA114	DA114				55.6
DT10	DT10	DT10	DT10	DT10	DT10	DT10	DT10	DT10	100.0
DA113	DA113	DA113	DA113	DA113	DA113	DA113	DA113	DA113	100.0
DC112	DA112	DC112	DC112	DC112	DC112	DC112	DC112	DC112	100.0
			DT9		DT9			DT9	33.3
							DA13		11.1
					DC8				11.1
TGP11	TGP11	TGP11	TGP11	TGP11	TGP11	TGP11	TGP11	TGP11	100.0
	ALA351		ALA351		ALA351	ALA351		ALA351	55.6
ASN352	ASN352	ASN352	ASN352	ASN352	ASN352	ASN352	ASN352	ASN352	100.0
					ILE355				11.1
GLU356	GLU356	GLU356	GLU356	GLU356	GLU356	GLU356		GLU356	88.9
ARG364	ARG364	ARG364	ARG364	ARG364	ARG364	ARG364	ARG364	ARG364	100.0
			LYS374						11.1
			TRP416		TRP416				22.2
	LYS425		LYS425	LYS425	LYS425			LYS425	55.6
	TYR426		TYR426	TYR426	TYR426	TYR426		TYR426	66.7
	ILE427		ILE427		ILE427	ILE427		ILE427	55.6
			MET428		MET428	MET428		MET428	44.4
			LEU429		LEU429				22.2
			ASN430		ASN430				22.2
			PRO431						11.1
			LYS436		LYS436				22.2
ARG488	ARG488	ARG488	ARG488	ARG488	ARG488	ARG488		ARG488	88.9
LYS532	LYS532	LYS532	LYS532	LYS532	LYS532	LYS532	LYS532	LYS532	100.0
ASP533	ASP533	ASP533	ASP533	ASP533	ASP533	ASP533	ASP533	ASP533	100.0
ILE535	ILE535	ILE535	ILE535		ILE535	ILE535	ILE535	ILE535	88.9
							GLN633		11.1
THR718	THR718	THR718	THR718	THR718	THR718	THR718	THR718	THR718	100.0
ASN722	ASN722	ASN722	ASN722	ASN722	ASN722	ASN722	ASN722	ASN722	100.0
PTR723	PTR723	PTR723	PTR723	PTR723	PTR723	PTR723	PTR723	PTR723	100.0

\*The distance cutoff between a ligand and contacting residues/water molecules is 5Å.

Figure S1. Change in binding energy ( $\Delta\Delta G$ ) of Top I inhibitors to mutants

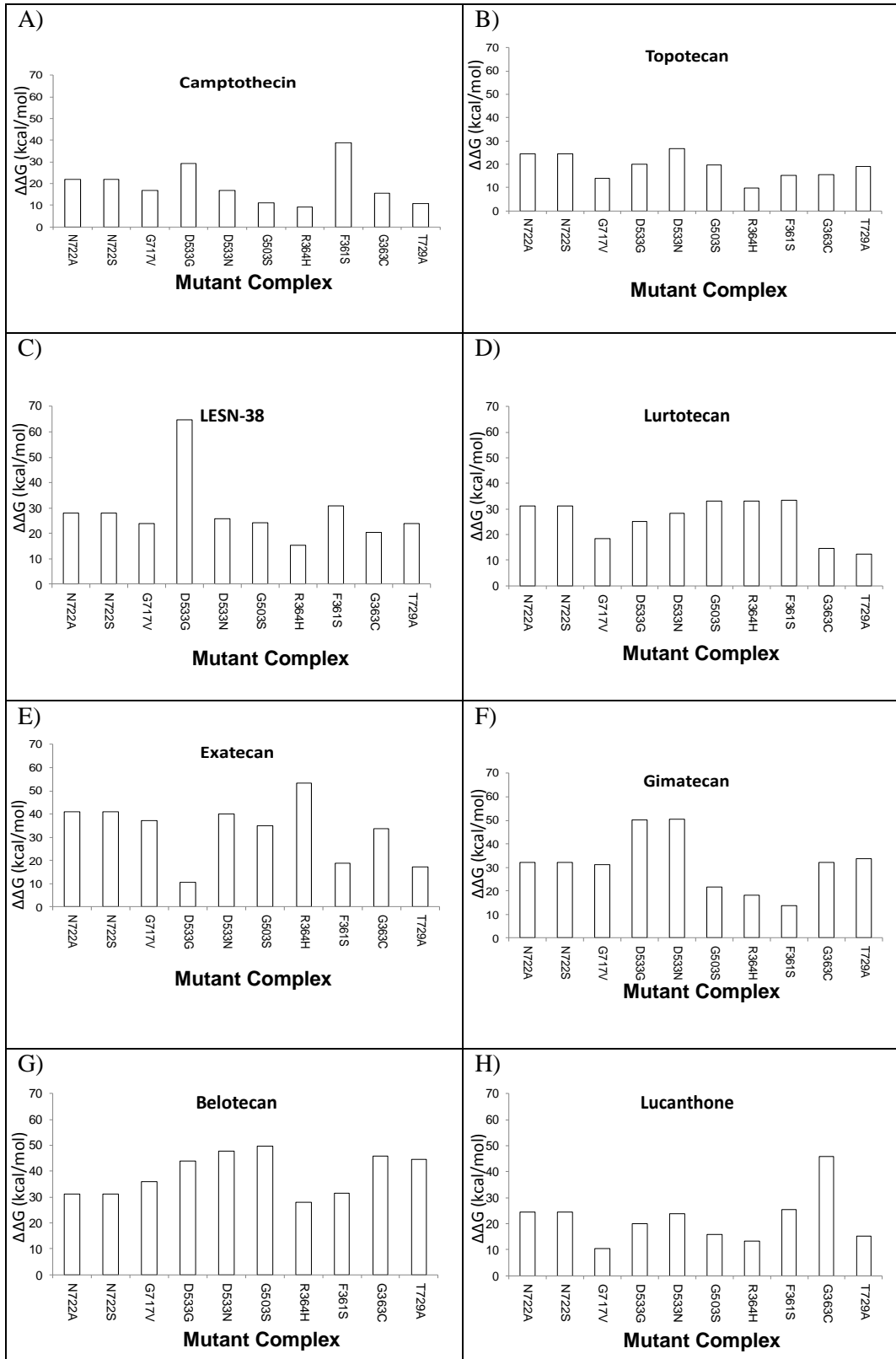


Figure S2. Change in binding energy ( $\Delta\Delta G$ ) of Top I inhibitors A-H bound to mutated complexes. **A)** Camptothecin **B)** Topotecan **C)** SN-38 **D)** Lurtotecan **E)** Exatecan **F)** Gimimatecan **G)** Belotecan **H)** Lucanthone

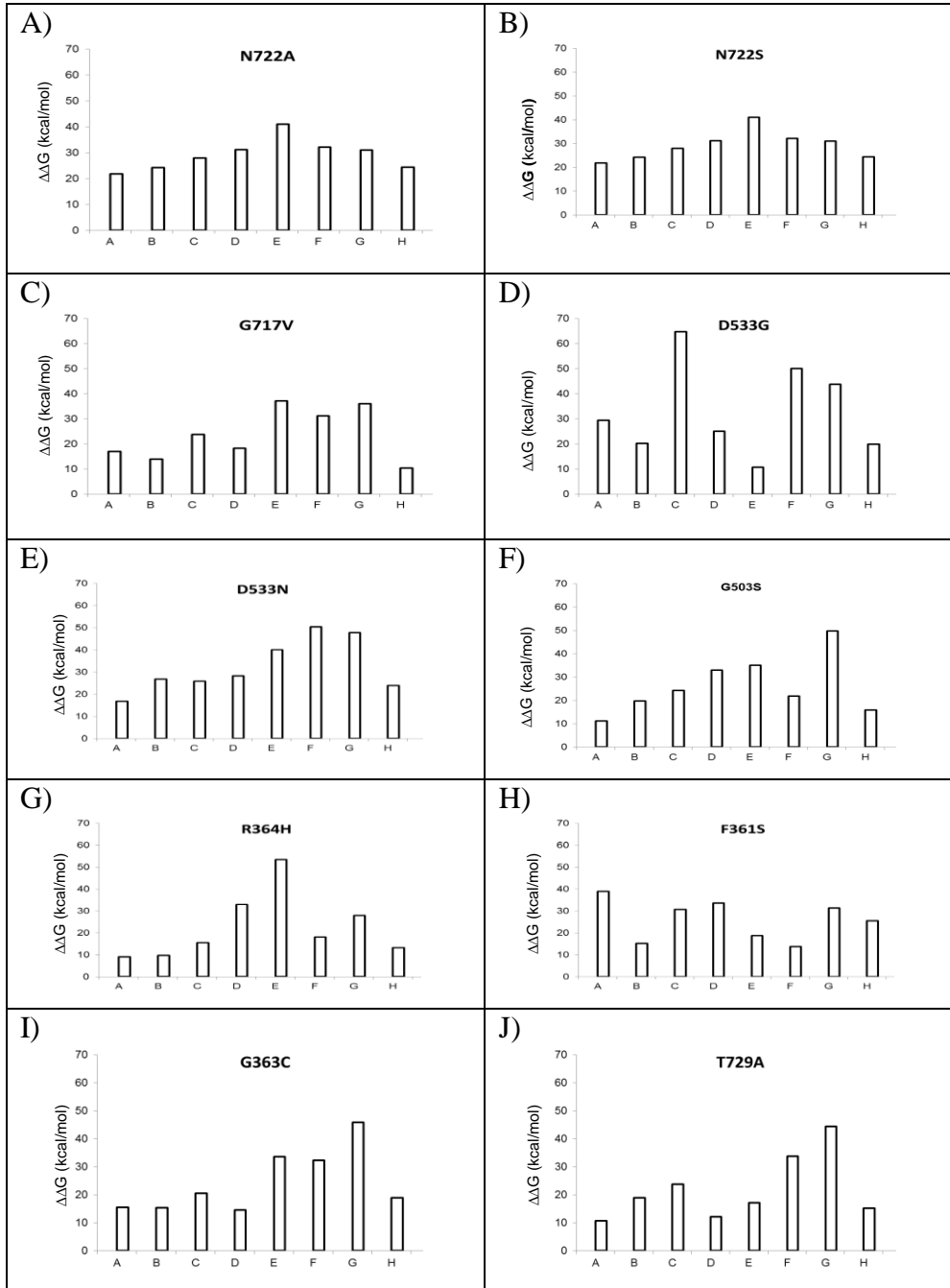
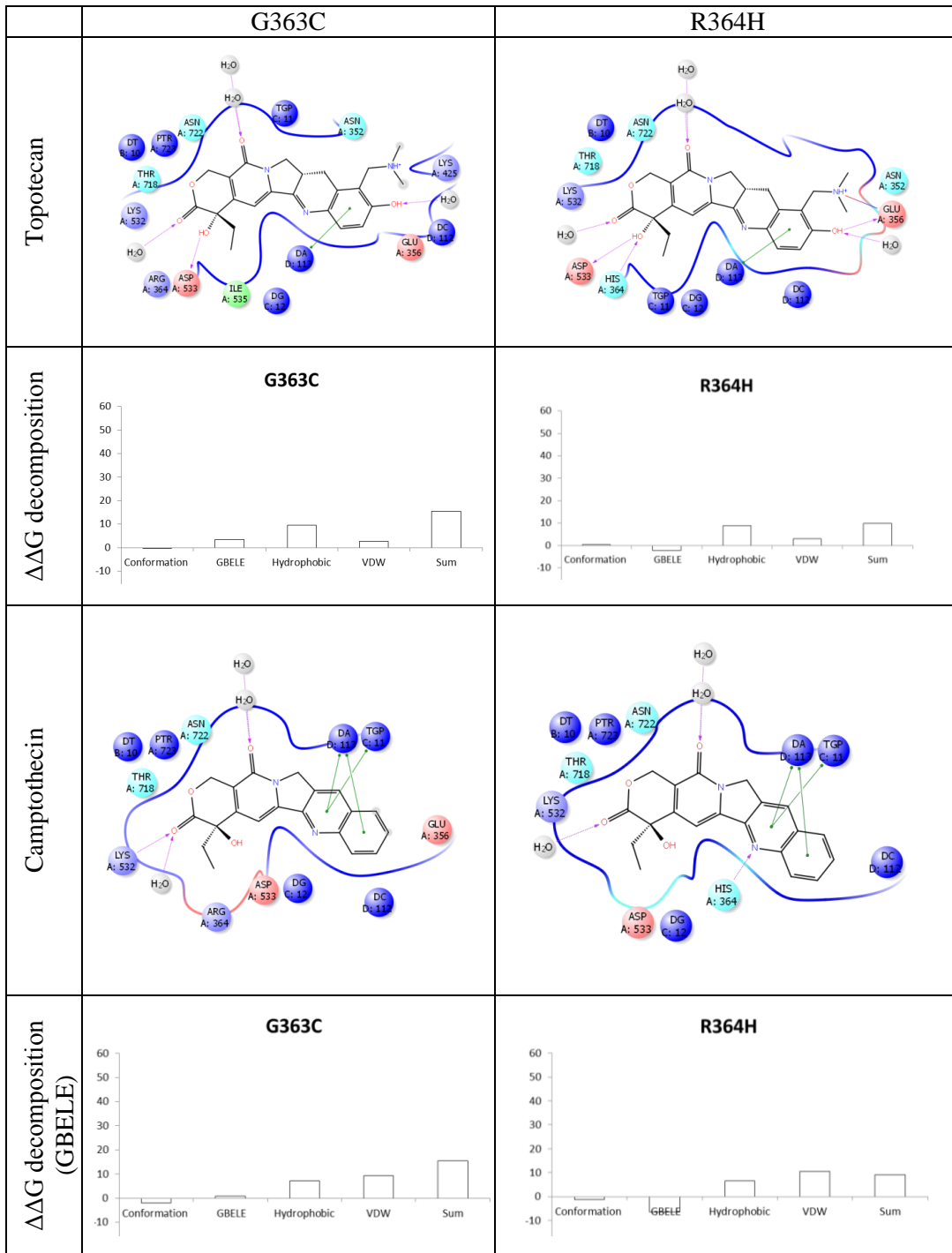


Figure S3. Comparison of mutated complexes G363C and R364H



SN38		
$\Delta\Delta G$ decomposition (GBELE)	<p style="text-align: center;"><b>G363C</b></p>	<p style="text-align: center;"><b>R364H</b></p>
Lurtotecan		
$\Delta\Delta G$ decomposition	<p style="text-align: center;"><b>G363C</b></p>	<p style="text-align: center;"><b>R364H</b></p>



Exatecan																										
ΔΔG decomposition	<p><b>G363C</b></p> <table border="1"> <thead> <tr> <th>Category</th> <th>ΔΔG</th> </tr> </thead> <tbody> <tr> <td>Conformation</td> <td>~5</td> </tr> <tr> <td>GBELE</td> <td>~15</td> </tr> <tr> <td>Hydrophobic</td> <td>~15</td> </tr> <tr> <td>VDW</td> <td>~5</td> </tr> <tr> <td>Sum</td> <td>~35</td> </tr> </tbody> </table>	Category	ΔΔG	Conformation	~5	GBELE	~15	Hydrophobic	~15	VDW	~5	Sum	~35	<p><b>R364H</b></p> <table border="1"> <thead> <tr> <th>Category</th> <th>ΔΔG</th> </tr> </thead> <tbody> <tr> <td>Conformation</td> <td>~5</td> </tr> <tr> <td>GBELE</td> <td>~18</td> </tr> <tr> <td>Hydrophobic</td> <td>~12</td> </tr> <tr> <td>VDW</td> <td>~12</td> </tr> <tr> <td>Sum</td> <td>~55</td> </tr> </tbody> </table>	Category	ΔΔG	Conformation	~5	GBELE	~18	Hydrophobic	~12	VDW	~12	Sum	~55
Category	ΔΔG																									
Conformation	~5																									
GBELE	~15																									
Hydrophobic	~15																									
VDW	~5																									
Sum	~35																									
Category	ΔΔG																									
Conformation	~5																									
GBELE	~18																									
Hydrophobic	~12																									
VDW	~12																									
Sum	~55																									
Belotecan																										
ΔΔG decomposition	<p><b>G363C</b></p> <table border="1"> <thead> <tr> <th>Category</th> <th>ΔΔG</th> </tr> </thead> <tbody> <tr> <td>Conformation</td> <td>~10</td> </tr> <tr> <td>GBELE</td> <td>~12</td> </tr> <tr> <td>Hydrophobic</td> <td>~12</td> </tr> <tr> <td>VDW</td> <td>~15</td> </tr> <tr> <td>Sum</td> <td>~45</td> </tr> </tbody> </table>	Category	ΔΔG	Conformation	~10	GBELE	~12	Hydrophobic	~12	VDW	~15	Sum	~45	<p><b>R364H</b></p> <table border="1"> <thead> <tr> <th>Category</th> <th>ΔΔG</th> </tr> </thead> <tbody> <tr> <td>Conformation</td> <td>~2</td> </tr> <tr> <td>GBELE</td> <td>~2</td> </tr> <tr> <td>Hydrophobic</td> <td>~10</td> </tr> <tr> <td>VDW</td> <td>~18</td> </tr> <tr> <td>Sum</td> <td>~28</td> </tr> </tbody> </table>	Category	ΔΔG	Conformation	~2	GBELE	~2	Hydrophobic	~10	VDW	~18	Sum	~28
Category	ΔΔG																									
Conformation	~10																									
GBELE	~12																									
Hydrophobic	~12																									
VDW	~15																									
Sum	~45																									
Category	ΔΔG																									
Conformation	~2																									
GBELE	~2																									
Hydrophobic	~10																									
VDW	~18																									
Sum	~28																									
Gimatecan																										

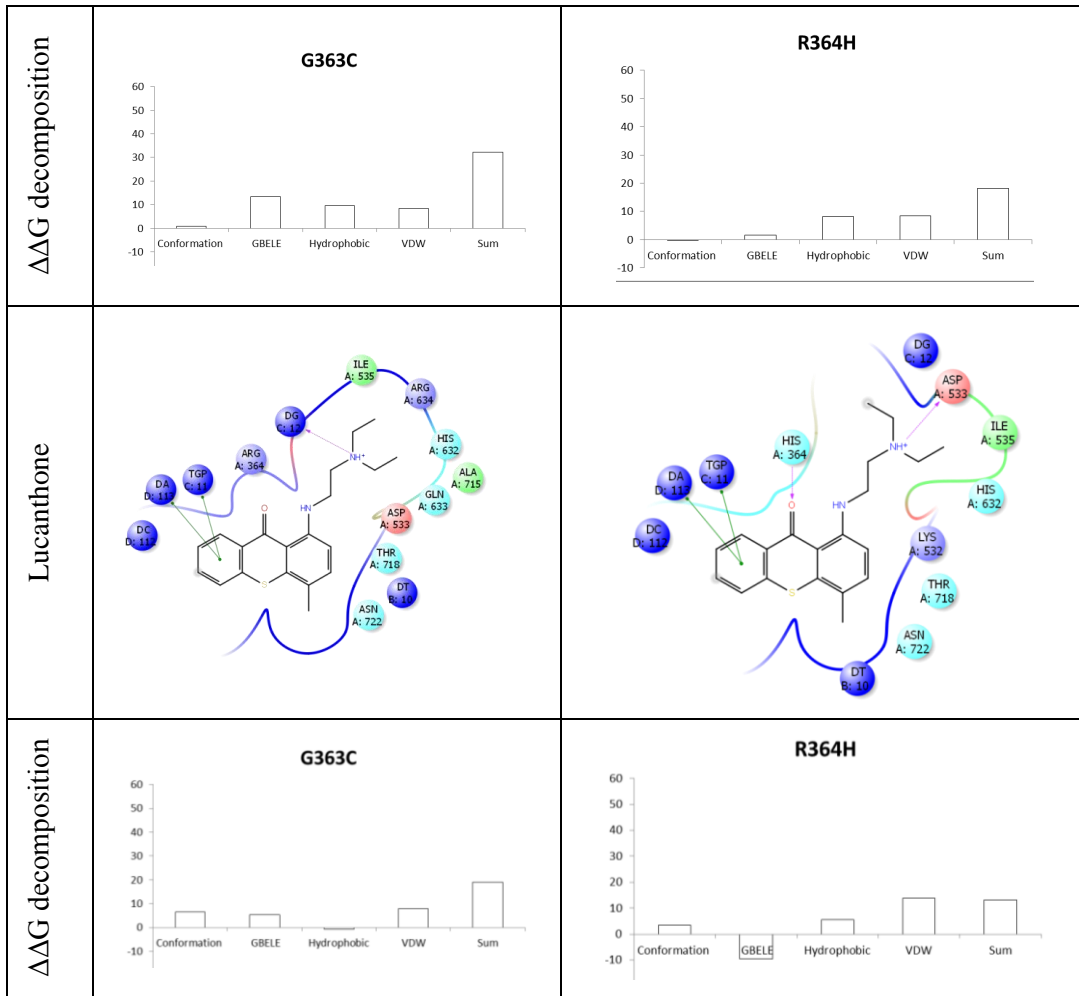


Figure S4. Camptothecin Bound to Complex N722A. **A)** 3D top view of complex **B)** 3D side view of complex **C)** Decomposition of  $\Delta\Delta G$  **D)** 2D Representation of the binding within the complex

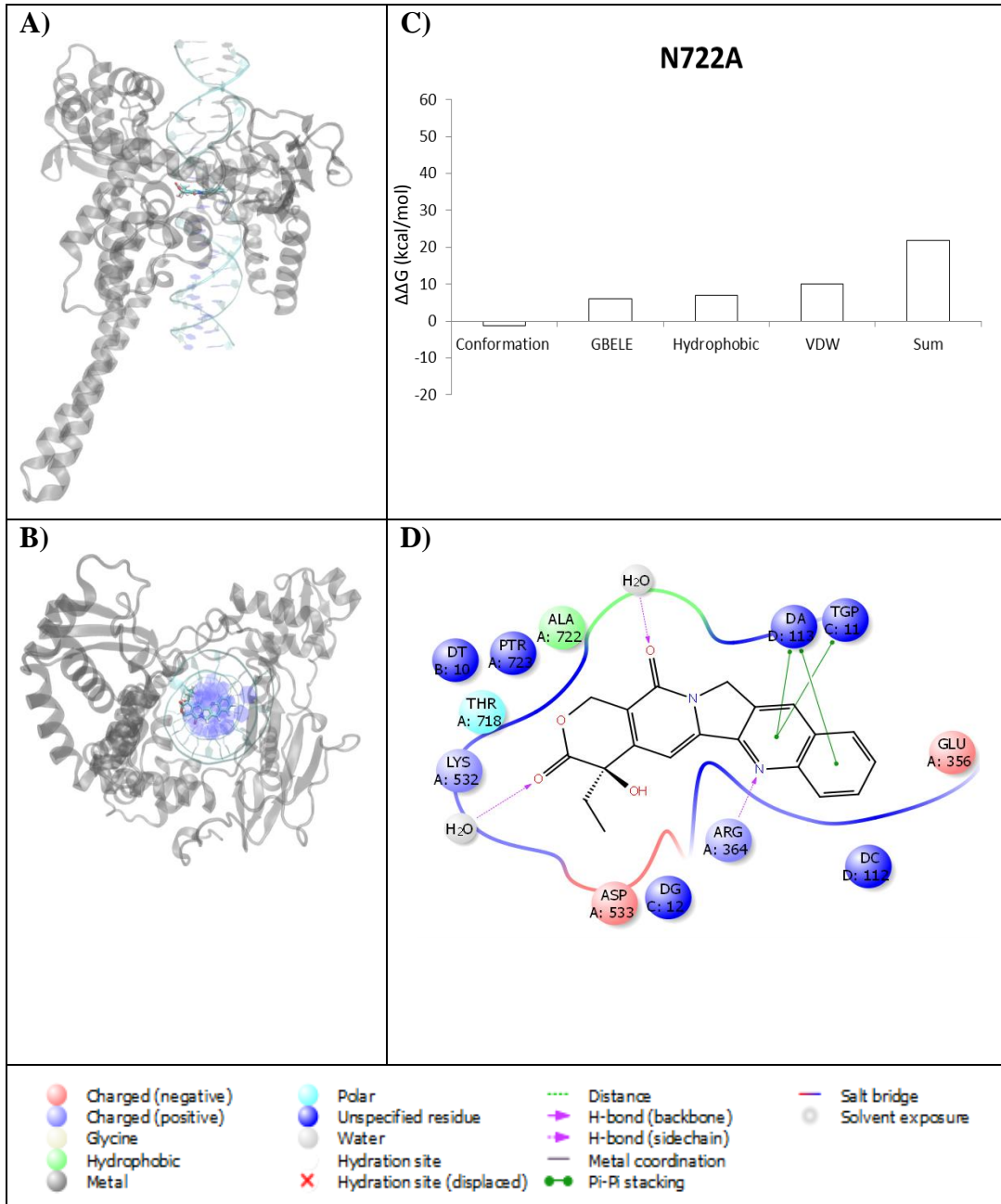


Figure S5. Camptothecin Bound to Complex N722S. **A)** 3D top view of complex **B)** 3D side view of complex **C)** Decomposition of  $\Delta\Delta G$  **D)** 2D Representation of the binding within the complex

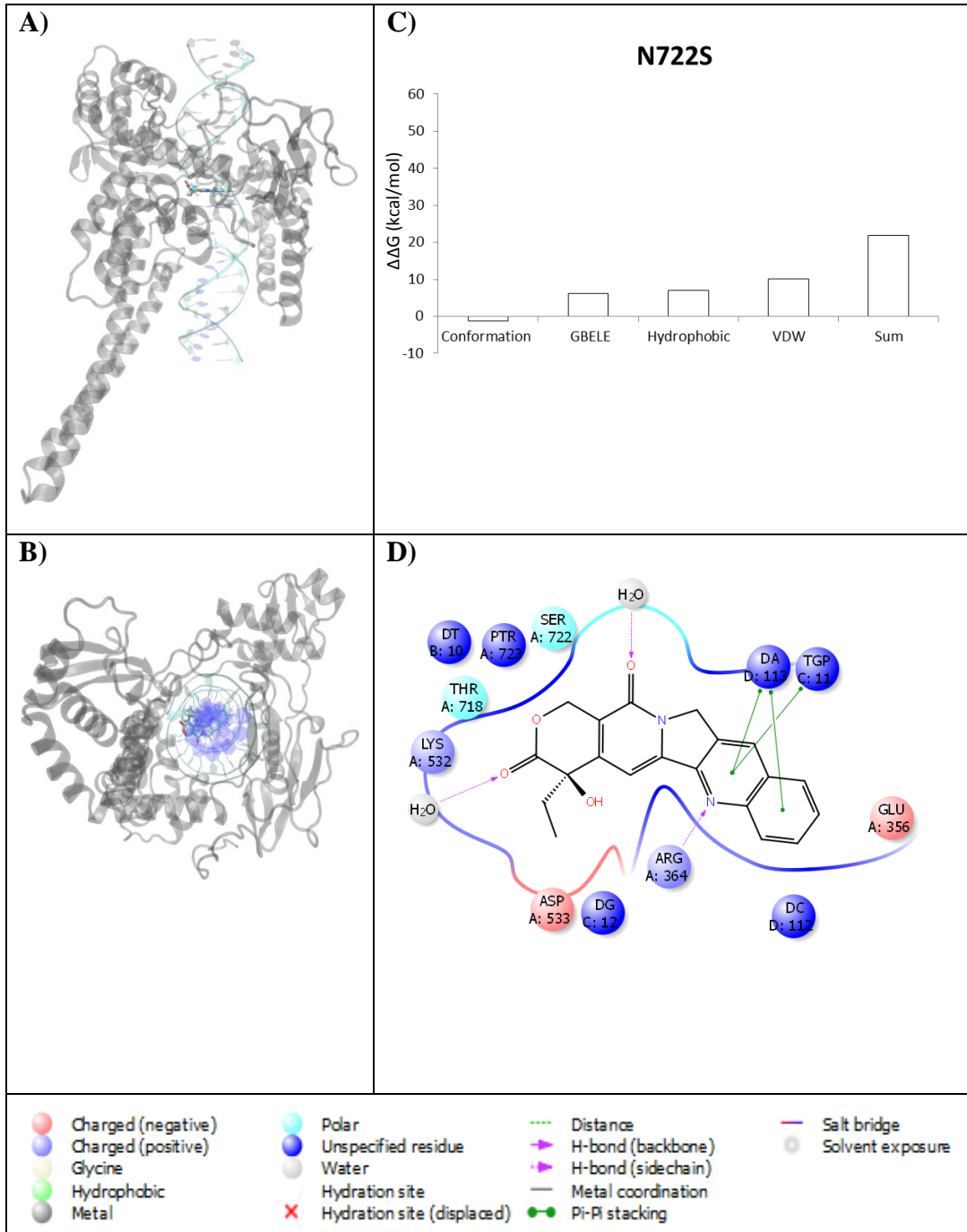


Figure S6. Camptothecin Bound to Complex G717V. **A)** 3D top view of complex **B)** 3D side view of complex **C)** Decomposition of  $\Delta\Delta G$  **D)** 2D Representation of the binding within the complex

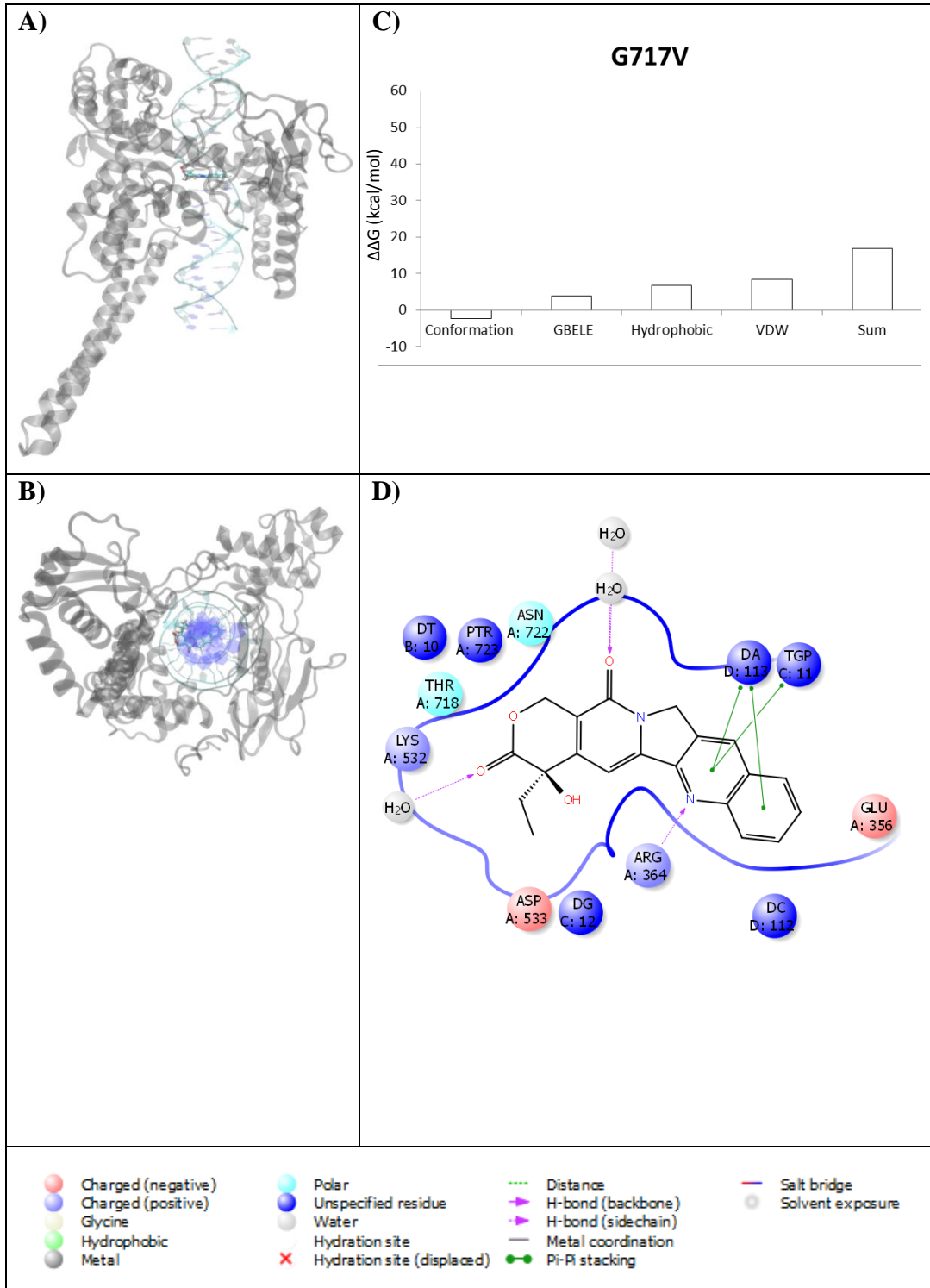


Figure S7. Camptothecin Bound to Complex D533G. **A)** 3D top view of complex **B)** 3D side view of complex **C)** Decomposition of  $\Delta\Delta G$  **D)** 2D Representation of the binding within the complex

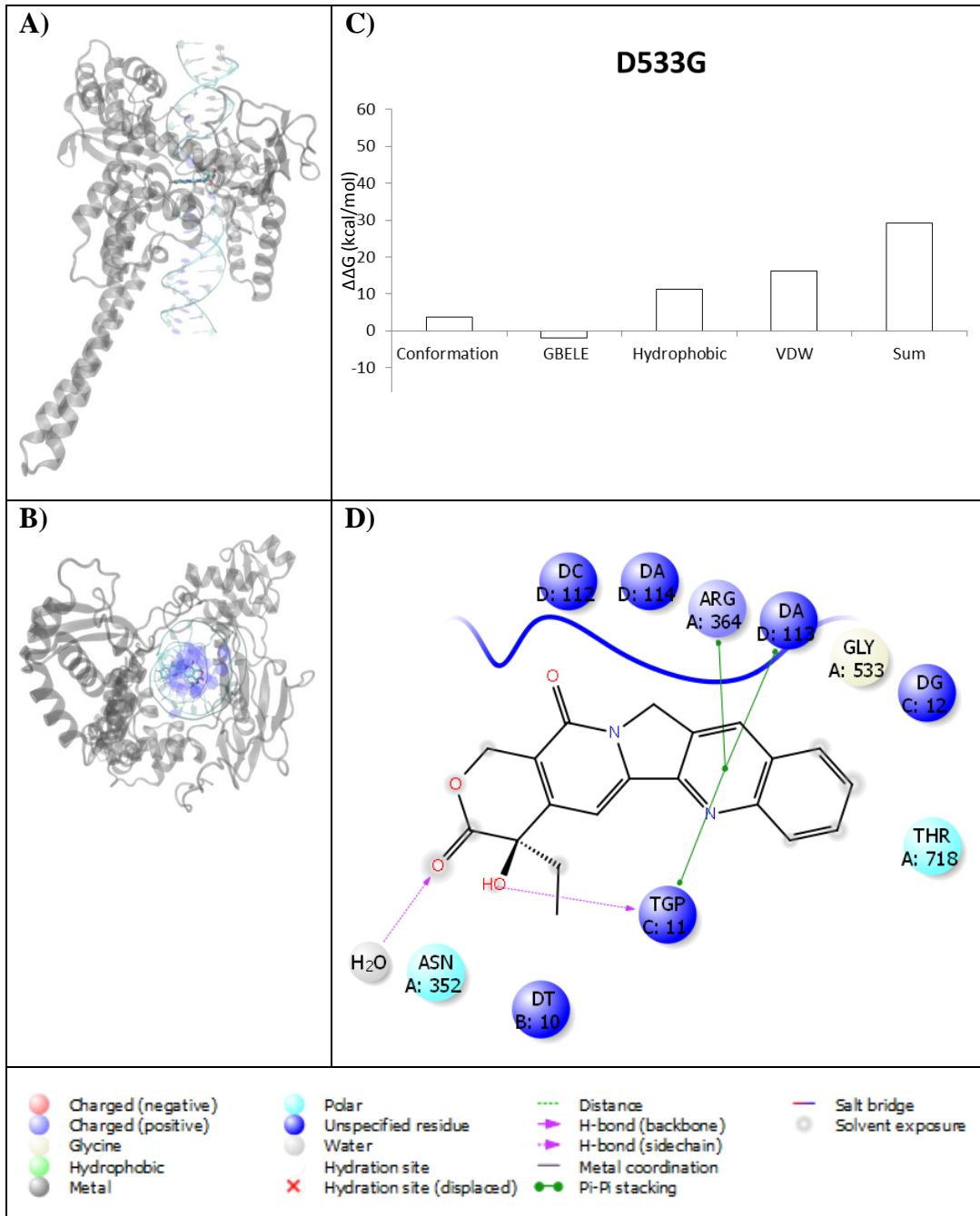


Figure S8. Camptothecin Bound to Complex D533N. **A)** 3D top view of complex **B)** 3D side view of complex **C)** Decomposition of  $\Delta\Delta G$  **D)** 2D Representation of the binding within the complex

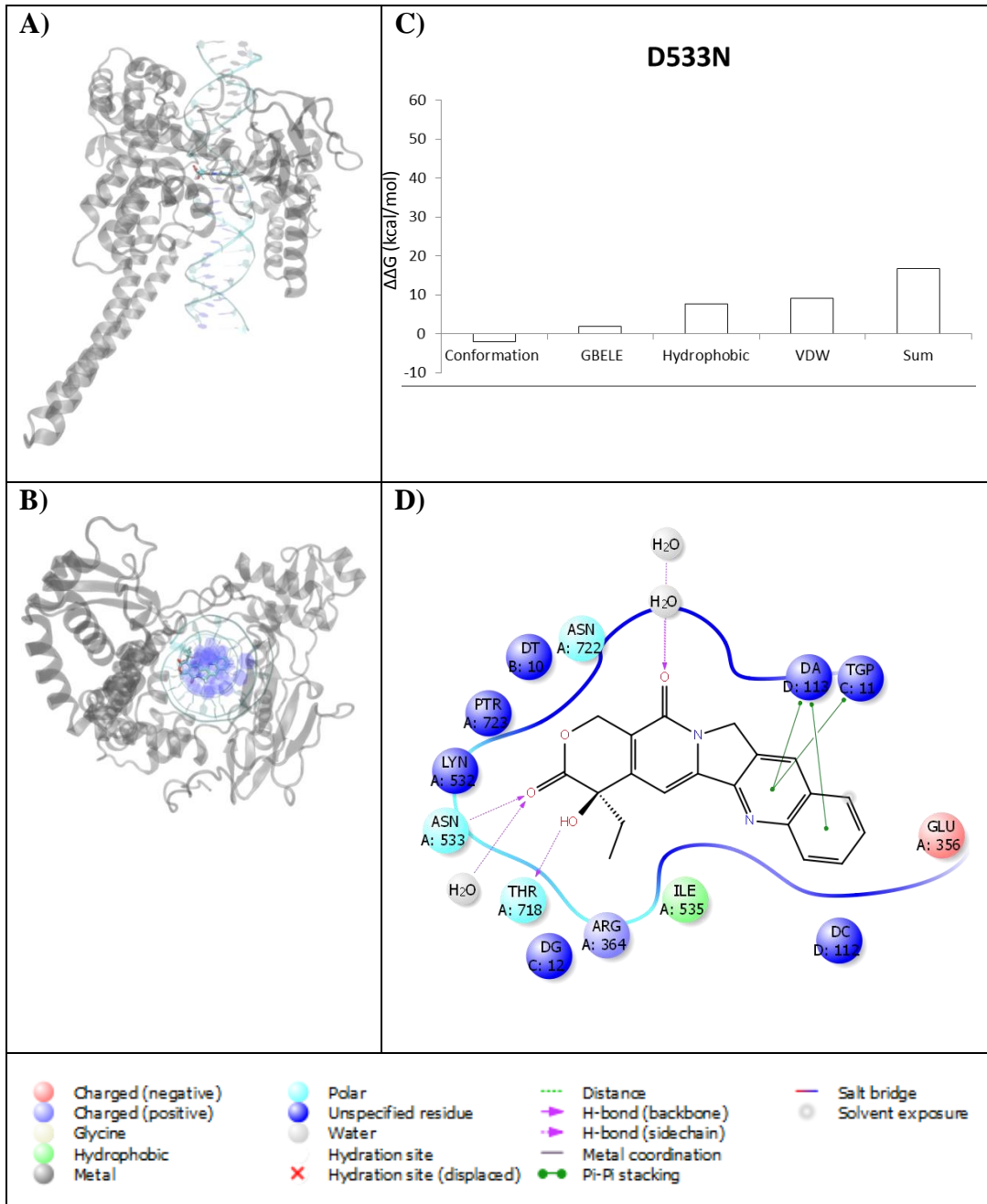


Figure S9. Camptothecin Bound to Complex G503S. **A)** 3D top view of complex **B)** 3D side view of complex **C)** Decomposition of  $\Delta\Delta G$  **D)** 2D Representation of the binding within the complex

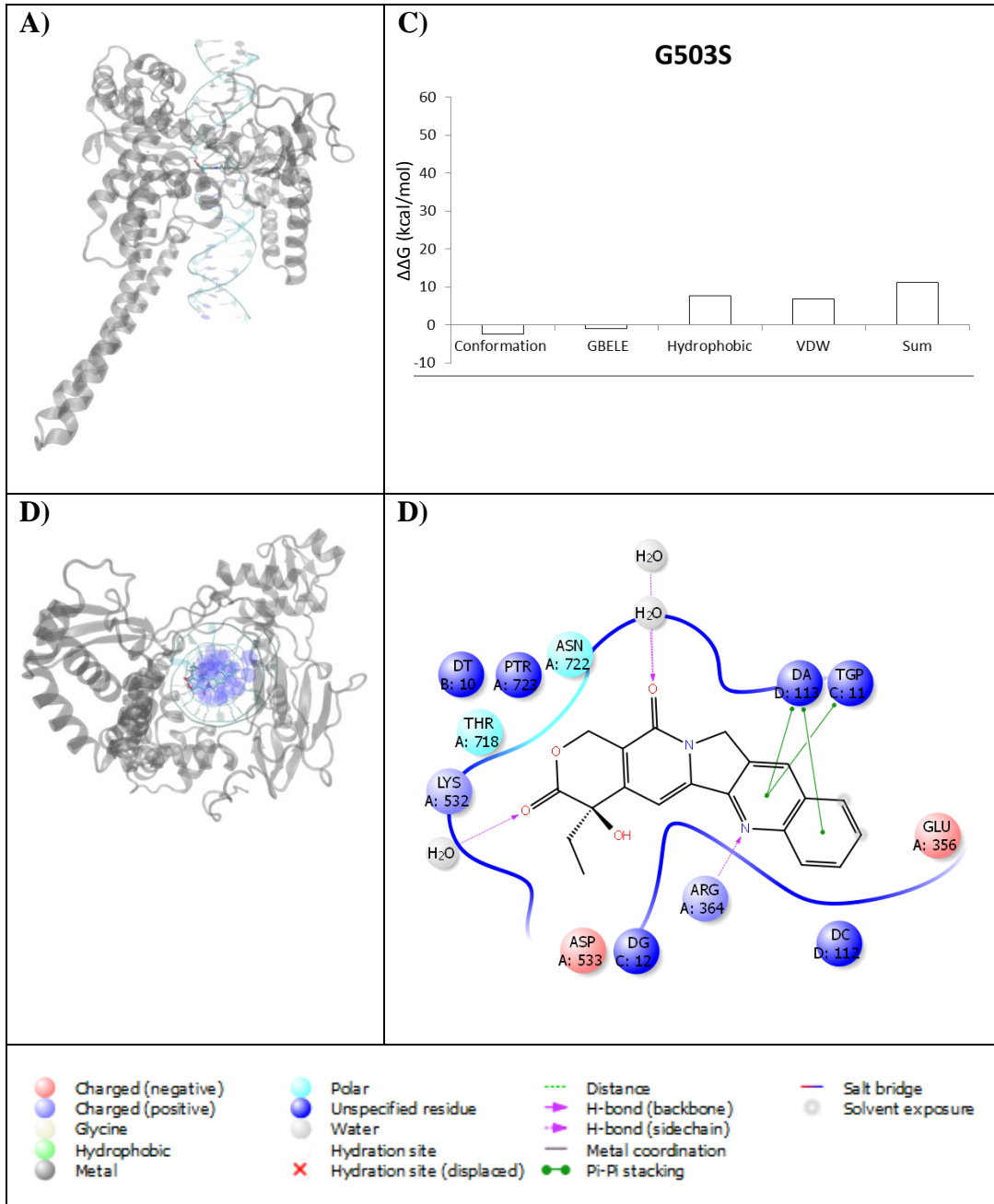




Figure S10. Camptothecin Bound to Complex R364H. **A)** 3D top view of complex **B)** 3D side view of complex **C)** Decomposition of  $\Delta\Delta G$  **D)** 2D Representation of the binding within the complex

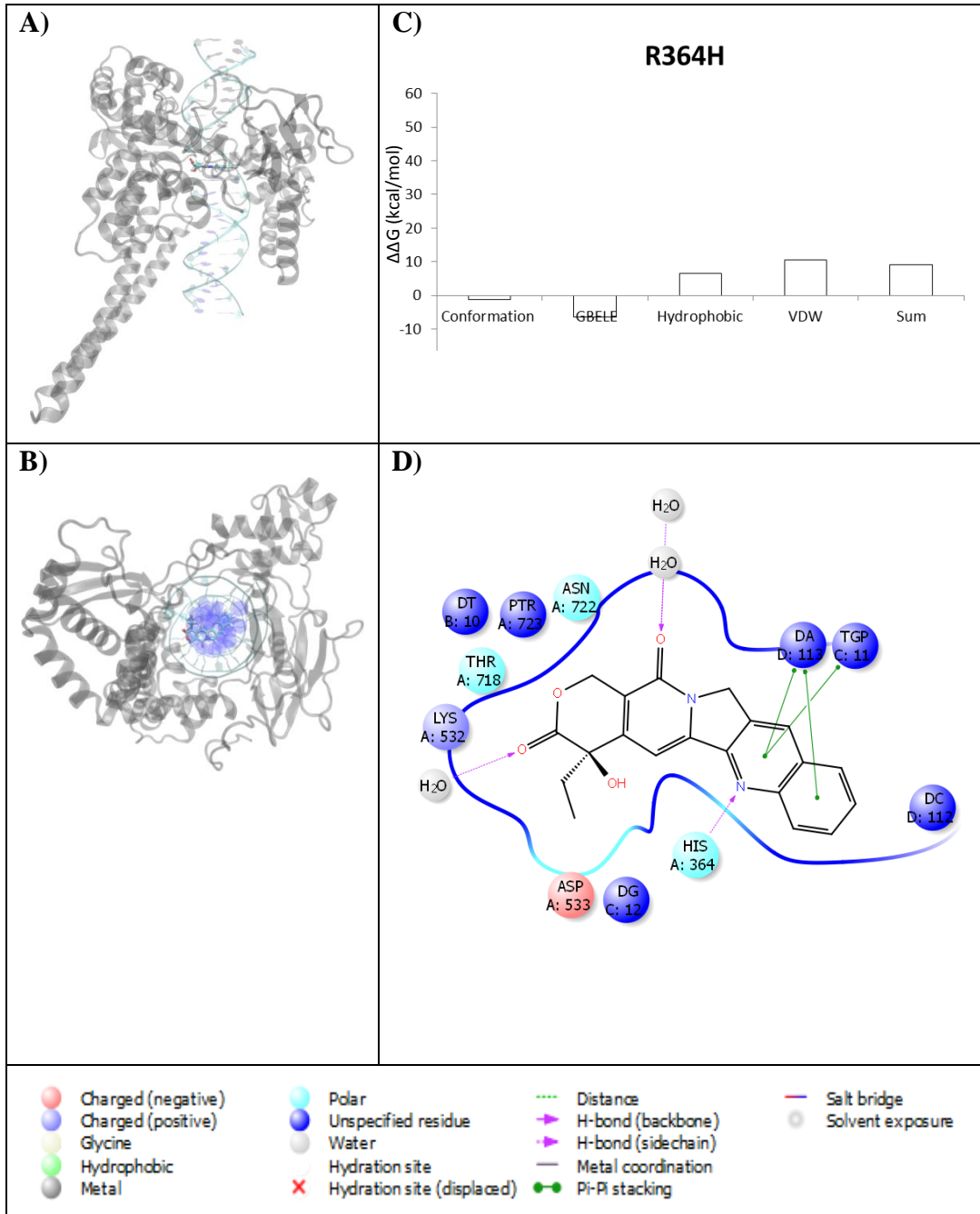


Figure S11. Camptothecin Bound to Complex F361S. **A)** 3D top view of complex **B)** 3D side view of complex **C)** Decomposition of  $\Delta\Delta G$  **D)** 2D Representation of the binding within the complex

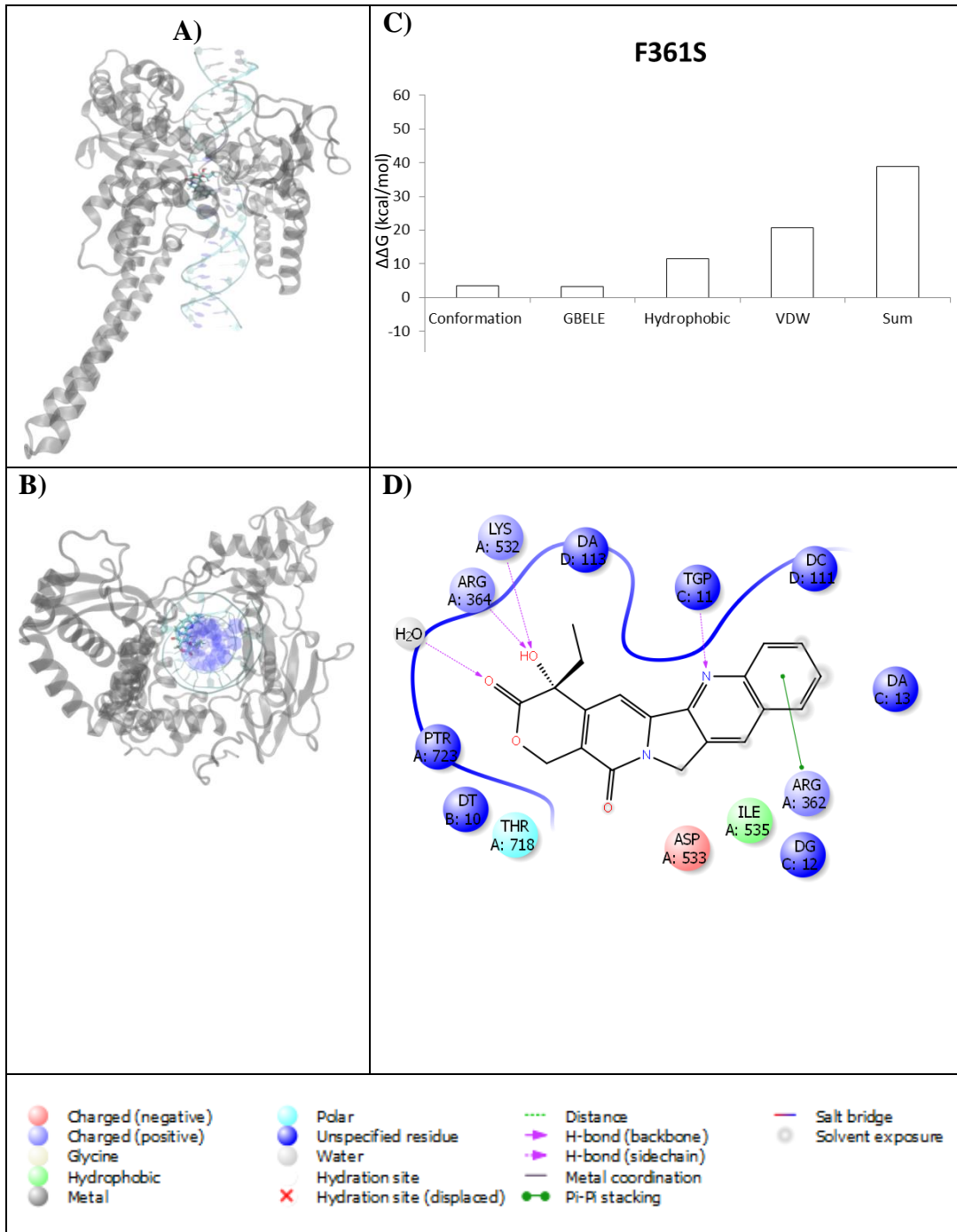


Figure S12. Camptothecin Bound to Complex G363C. **A)** 3D top view of complex **B)** 3D side view of complex **C)** Decomposition of  $\Delta\Delta G$  **D)** 2D Representation of the binding within the complex

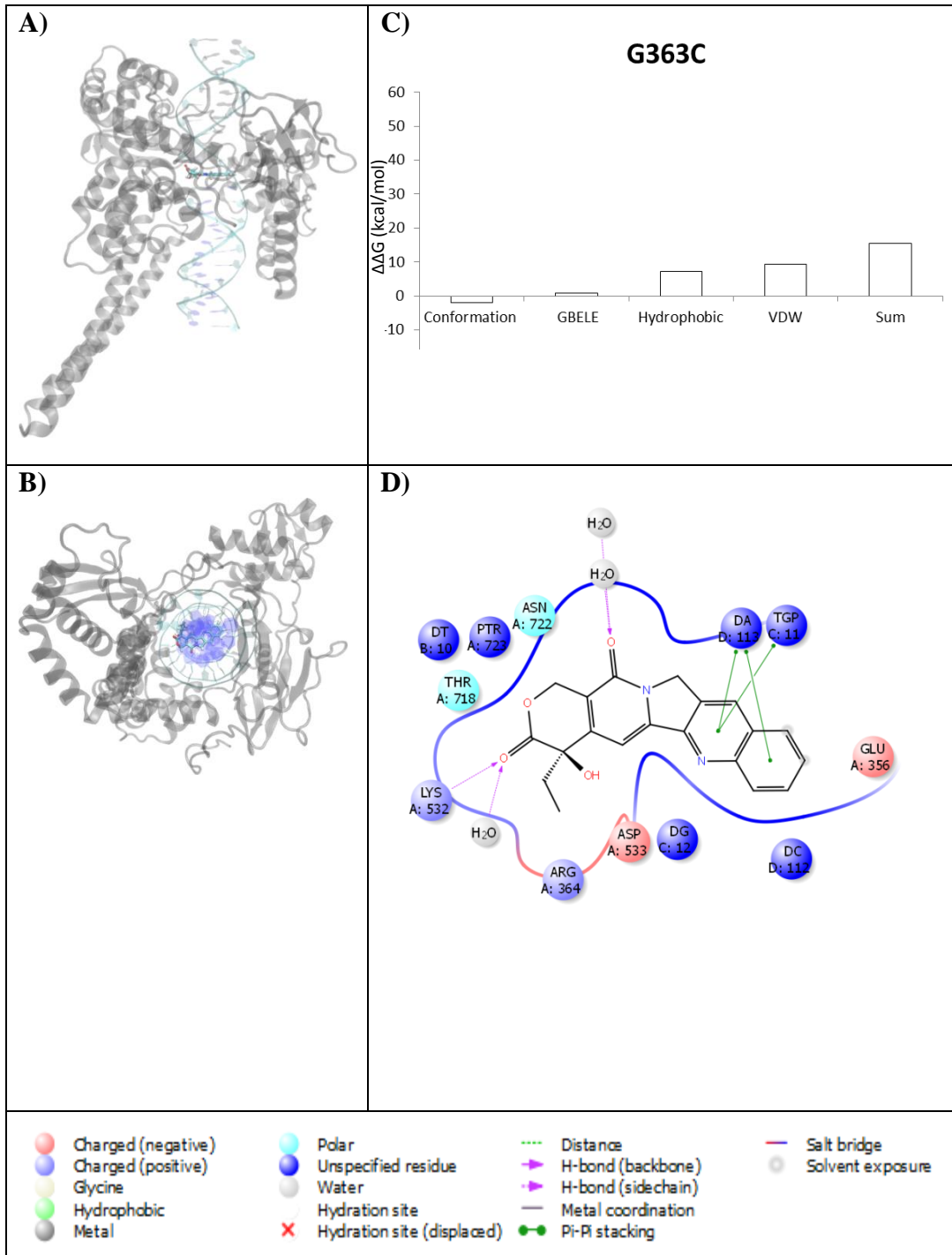


Figure S13. Camptothecin Bound to Complex T729A. **A)** 3D top view of complex **B)** 3D side view of complex **C)** Decomposition of  $\Delta\Delta G$  **D)** 2D Representation of the binding within the complex

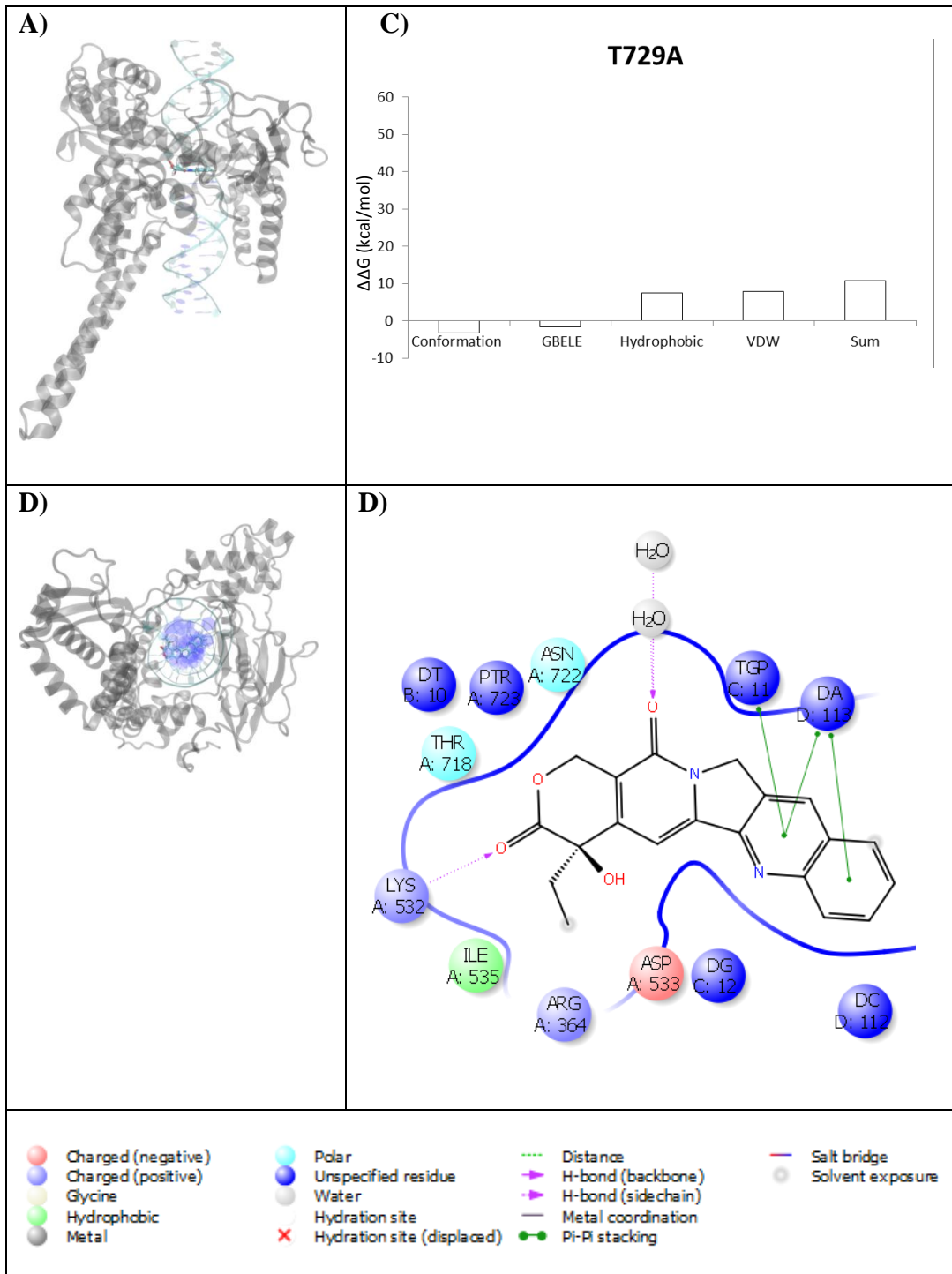


Figure S14. Topotecan Bound to Complex N722A. **A)** 3D top view of complex **B)** 3D side view of complex **C)** Decomposition of  $\Delta\Delta G$  **D)** 2D Representation of the binding within the complex

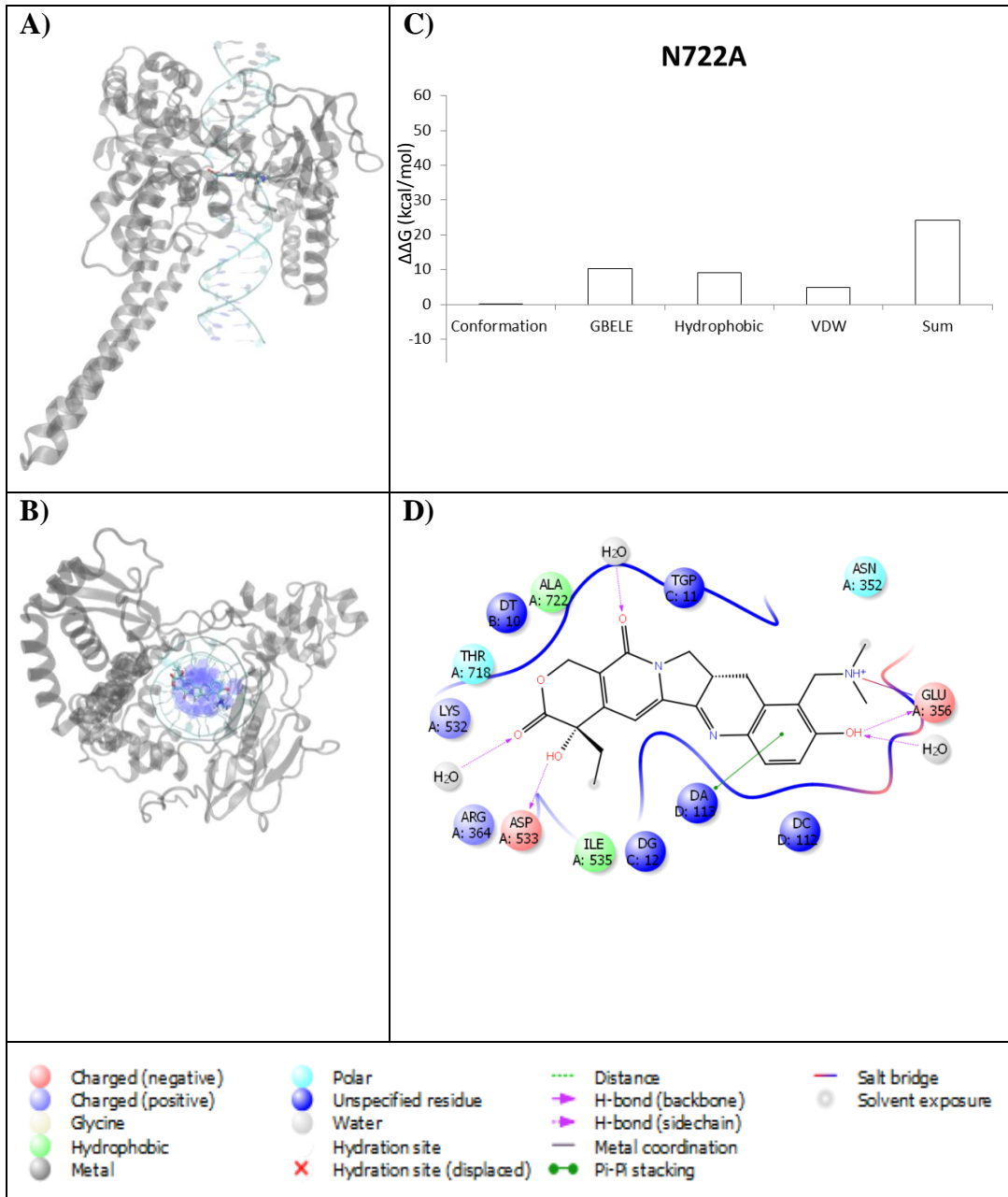


Figure S15. Topotecan Bound to Complex N722S. **A)** 3D top view of complex **B)** 3D side view of complex **C)** Decomposition of  $\Delta\Delta G$  **D)** 2D Representation of the binding within the complex

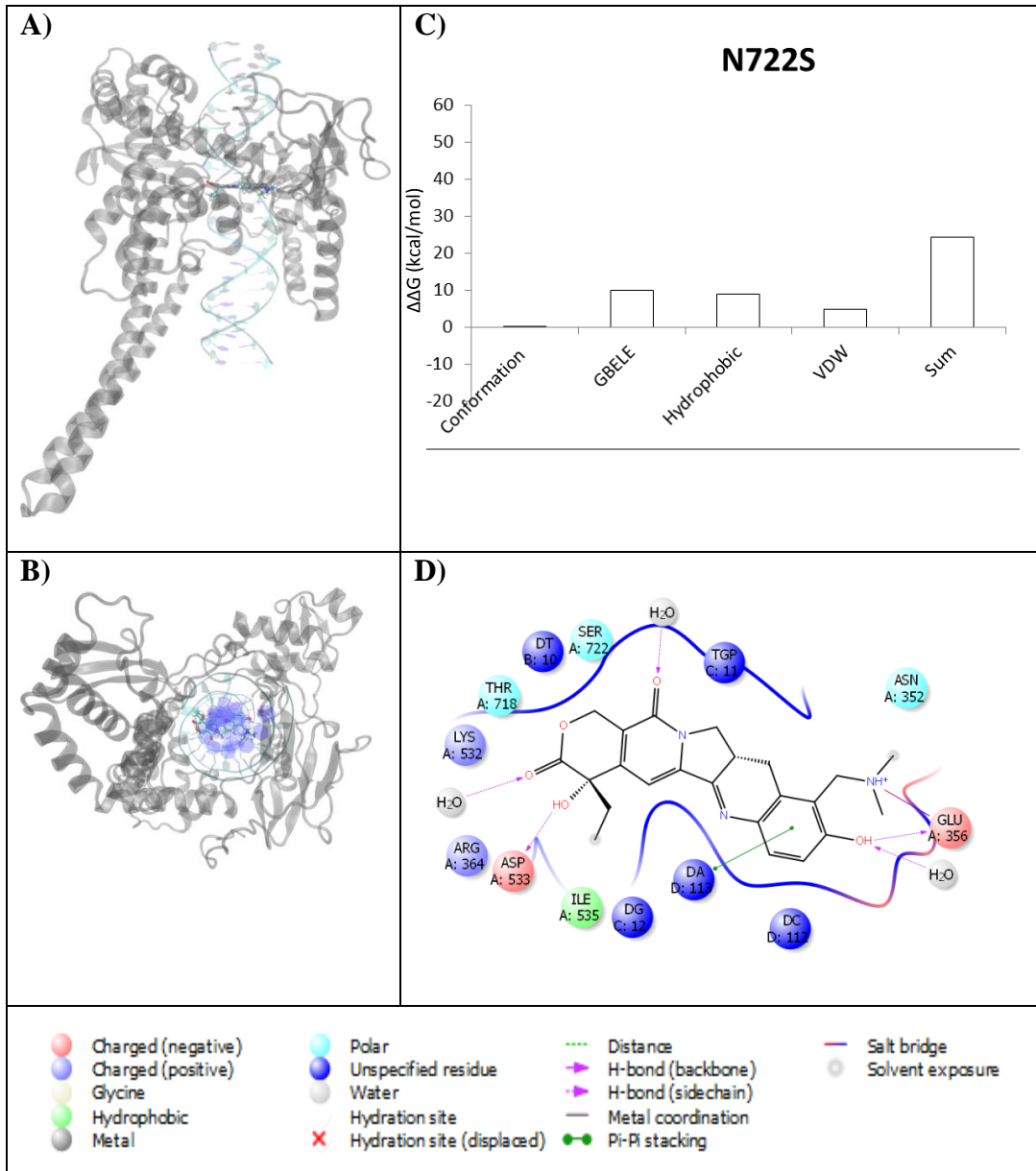


Figure S16. Topotecan Bound to Complex G717V. **A)** 3D top view of complex **B)** 3D side view of complex **C)** Decomposition of  $\Delta\Delta G$  **D)** 2D Representation of the binding within the complex

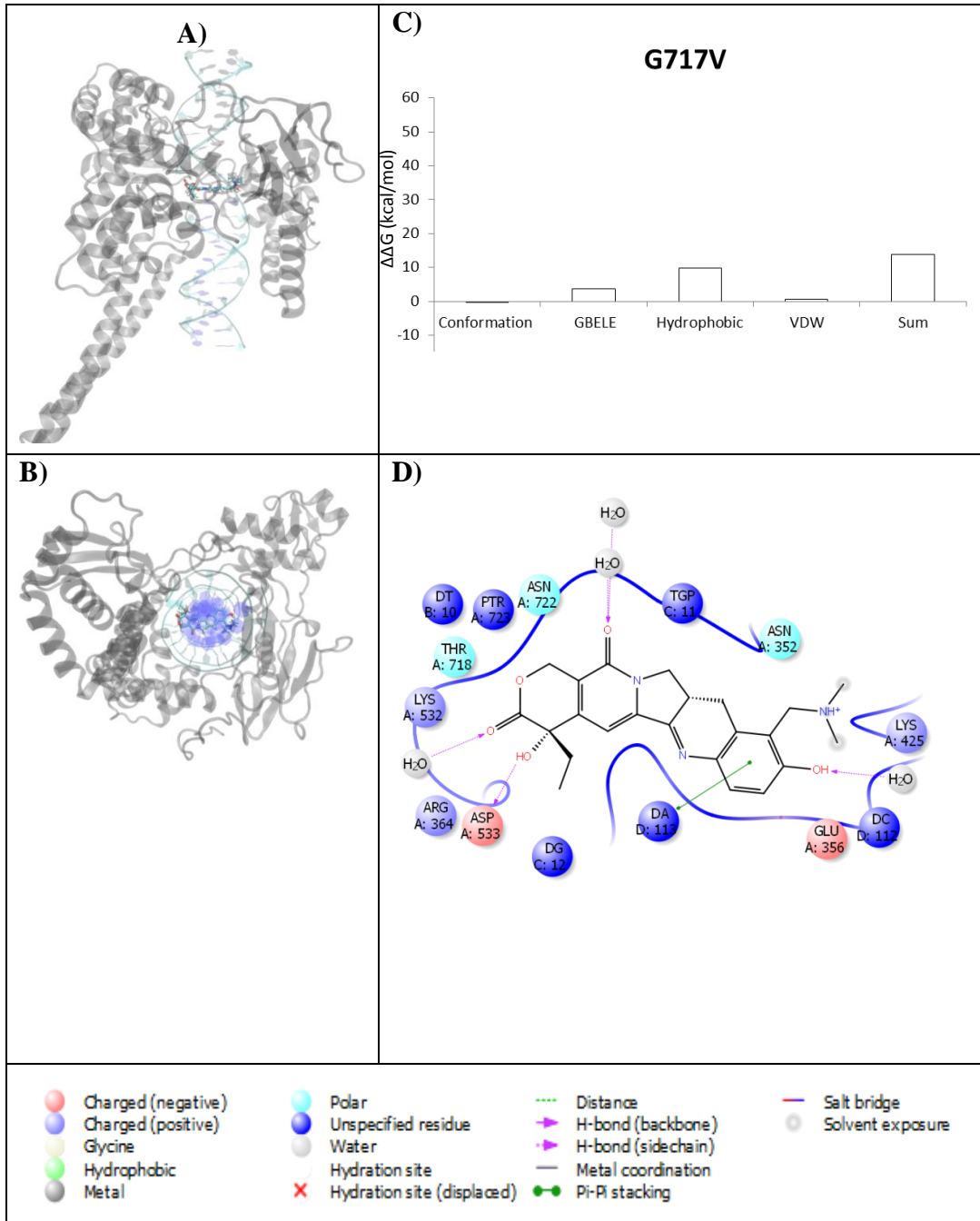




Figure S17. Topotecan Bound to Complex D533G. **A)** 3D top view of complex **B)** 3D side view of complex **C)** Decomposition of  $\Delta\Delta G$  **D)** 2D Representation of the binding within the complex

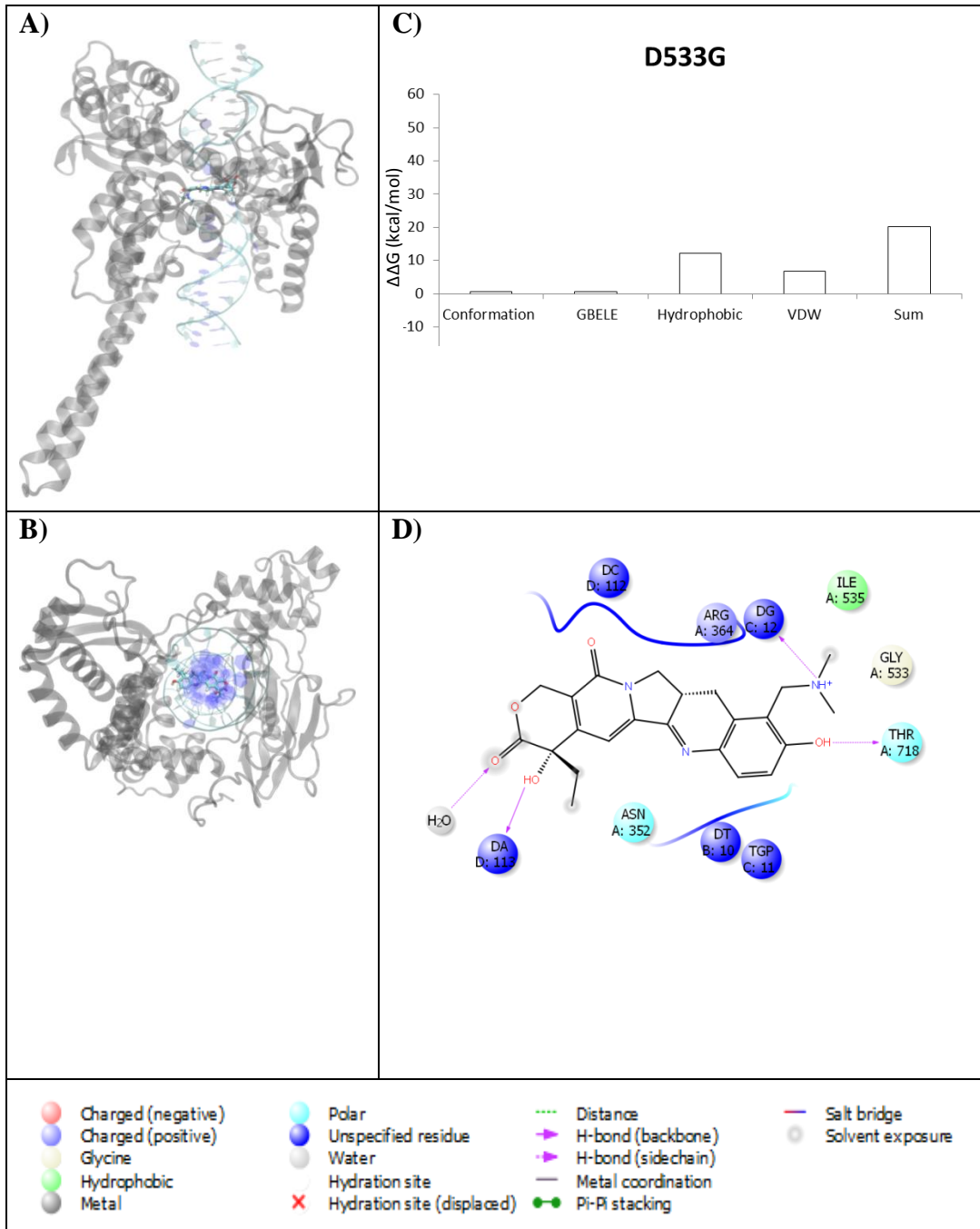




Figure S18. Topotecan Bound to Complex D533N. **A)** 3D top view of complex **B)** 3D side view of complex **C)** Decomposition of  $\Delta\Delta G$  **D)** 2D Representation of the binding within the complex

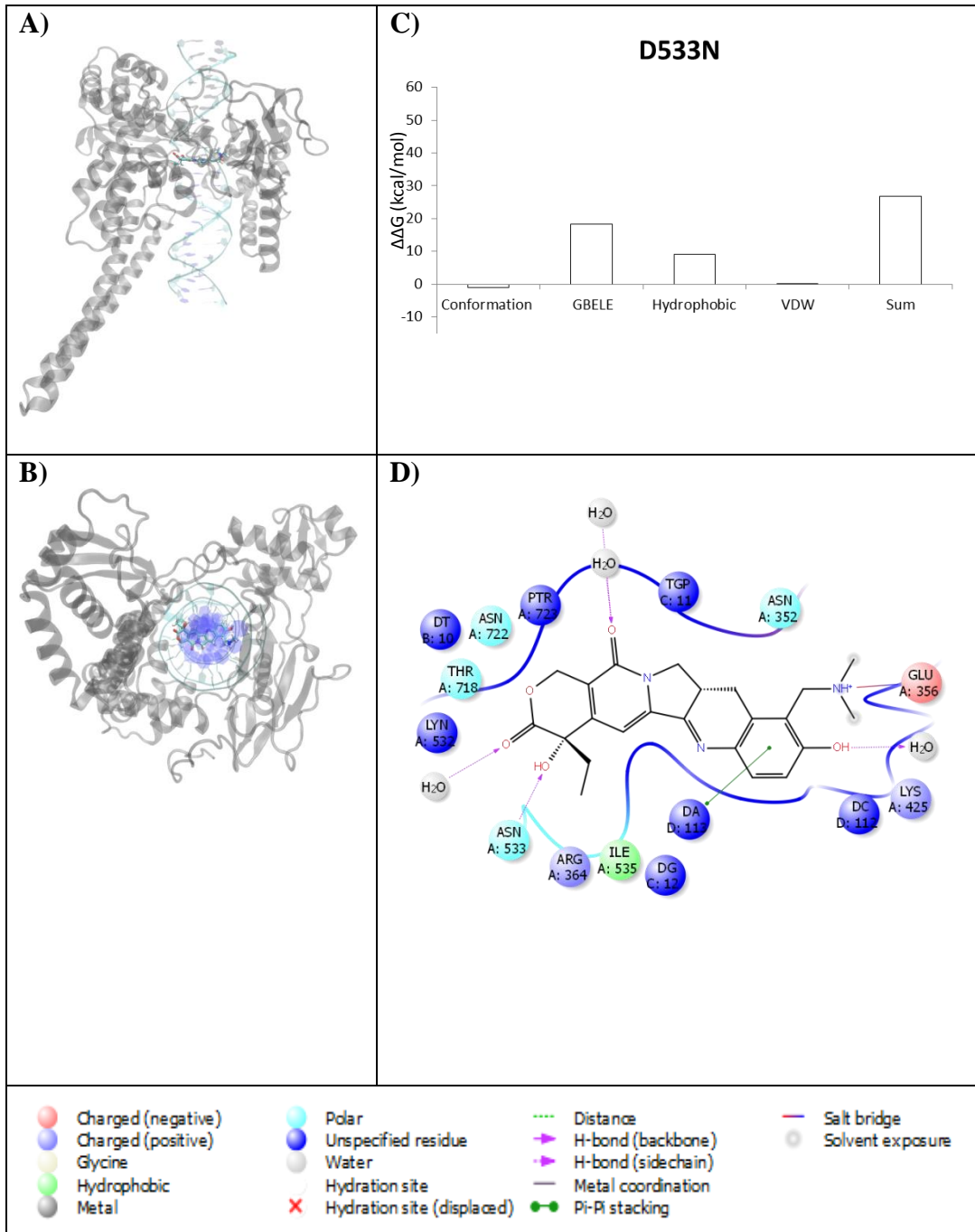


Figure S19. Topotecan Bound to Complex G503S. **A)** 3D top view of complex **B)** 3D side view of complex **C)** Decomposition of  $\Delta\Delta G$  **D)** 2D Representation of the binding within the complex

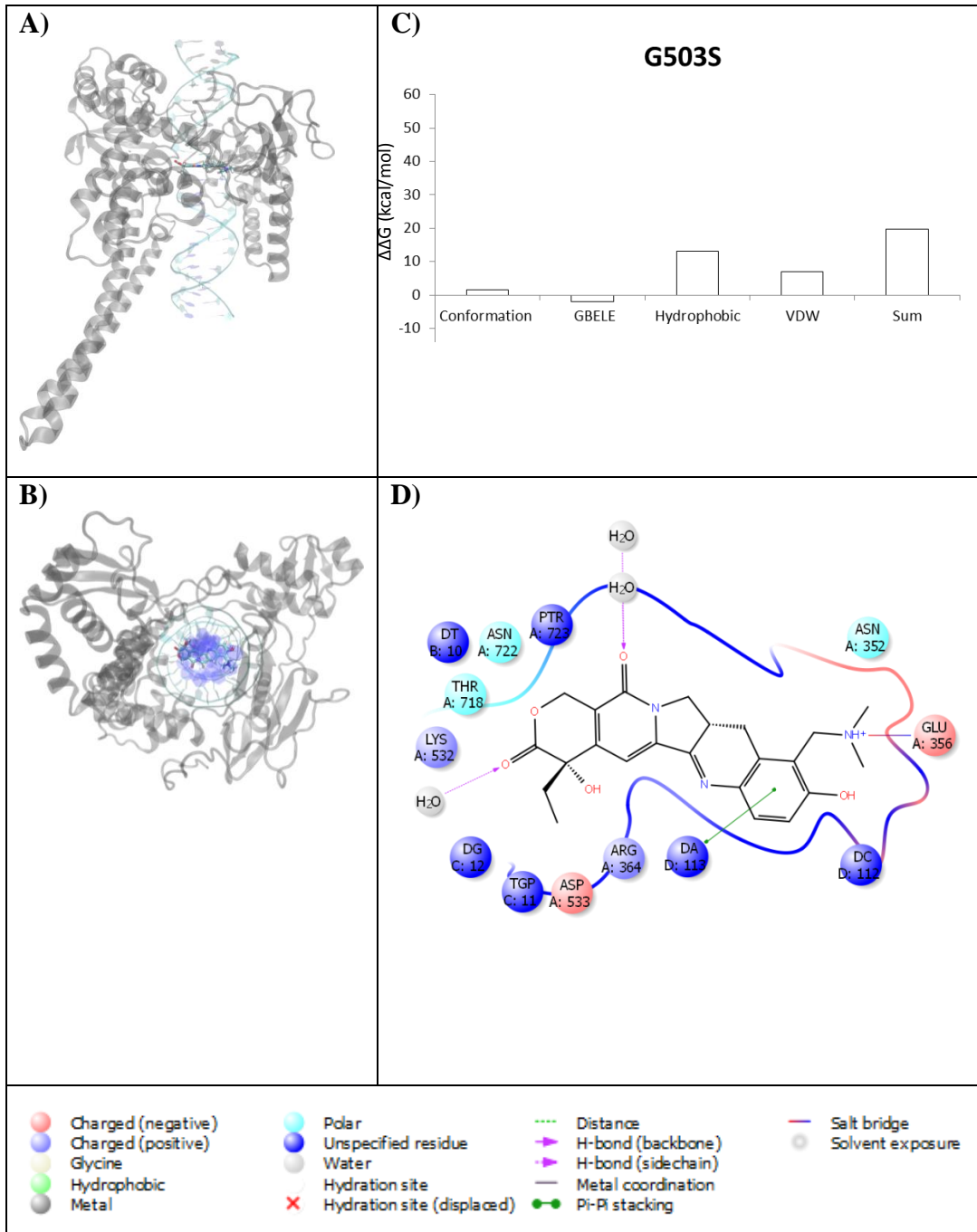


Figure S20. Topotecan Bound to Complex R364H. **A)** 3D top view of complex **B)** 3D side view of complex **C)** Decomposition of  $\Delta\Delta G$  **D)** 2D Representation of the binding within the complex

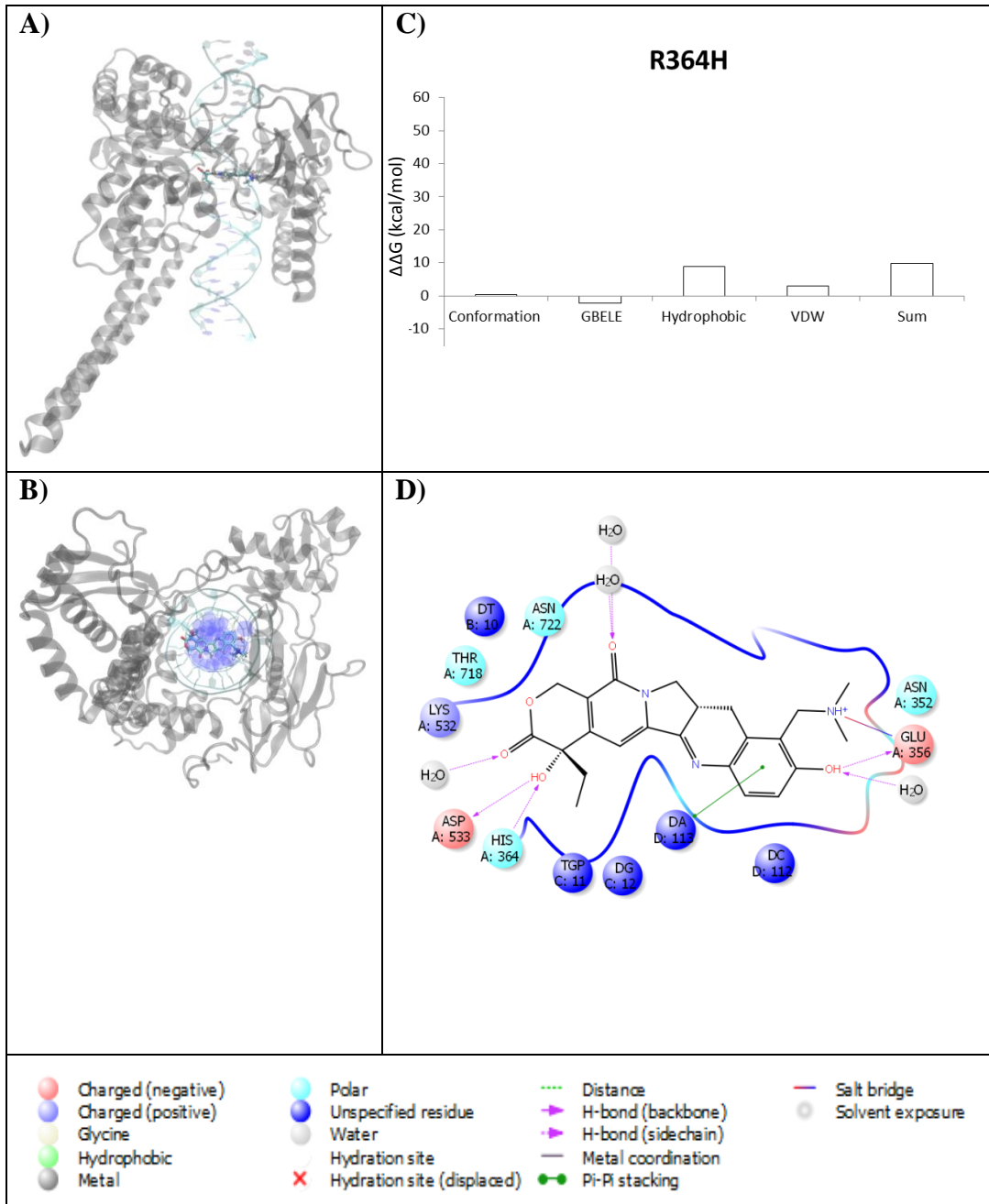


Figure S21. Topotecan Bound to Complex F361S. **A)** 3D top view of complex **B)** 3D side view of complex **C)** Decomposition of  $\Delta\Delta G$  **D)** 2D Representation of the binding within the complex

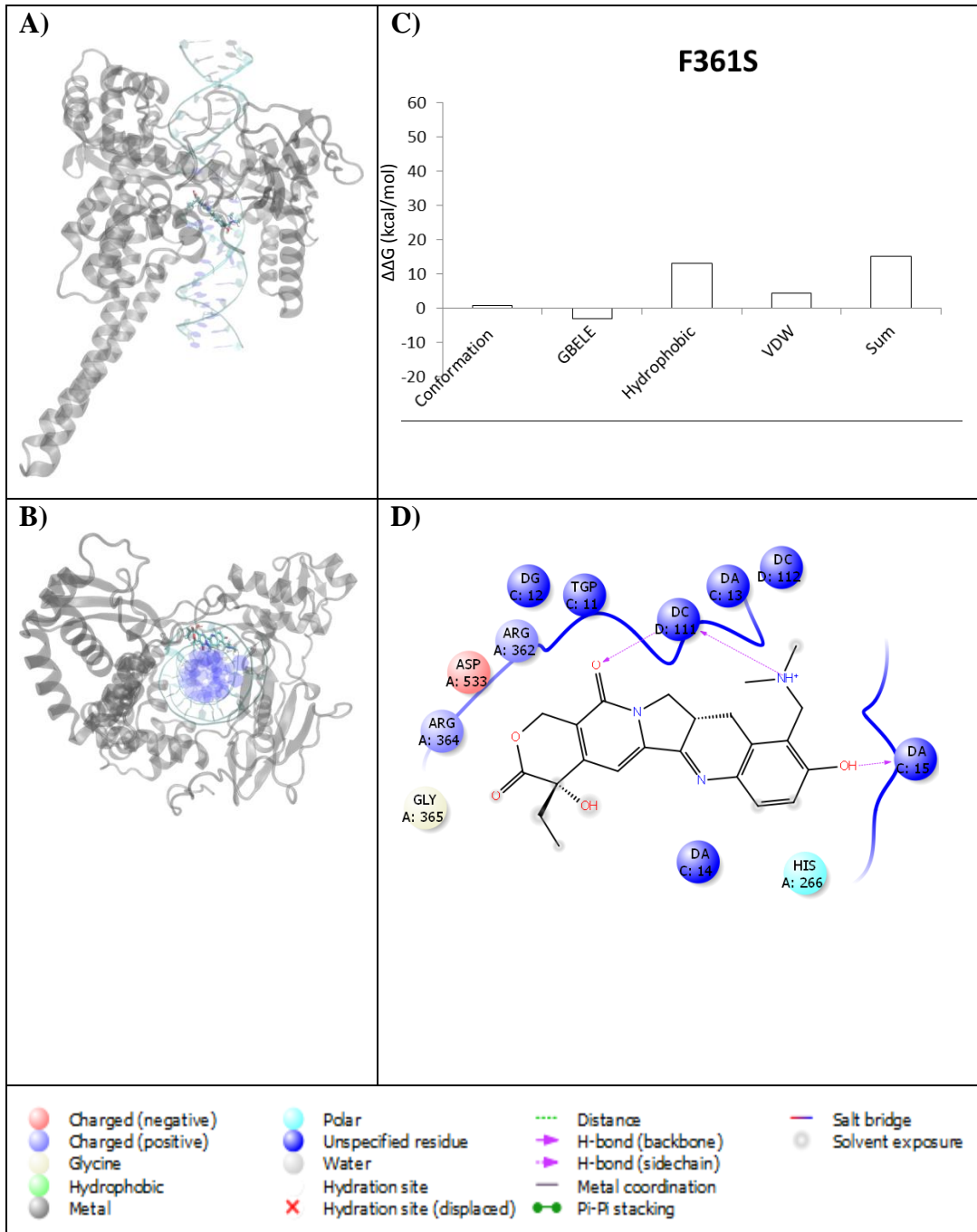


Figure S22. Topotecan Bound to Complex G363C. **A)** 3D top view of complex **B)** 3D side view of complex **C)** Decomposition of  $\Delta\Delta G$  **D)** 2D Representation of the binding within the complex

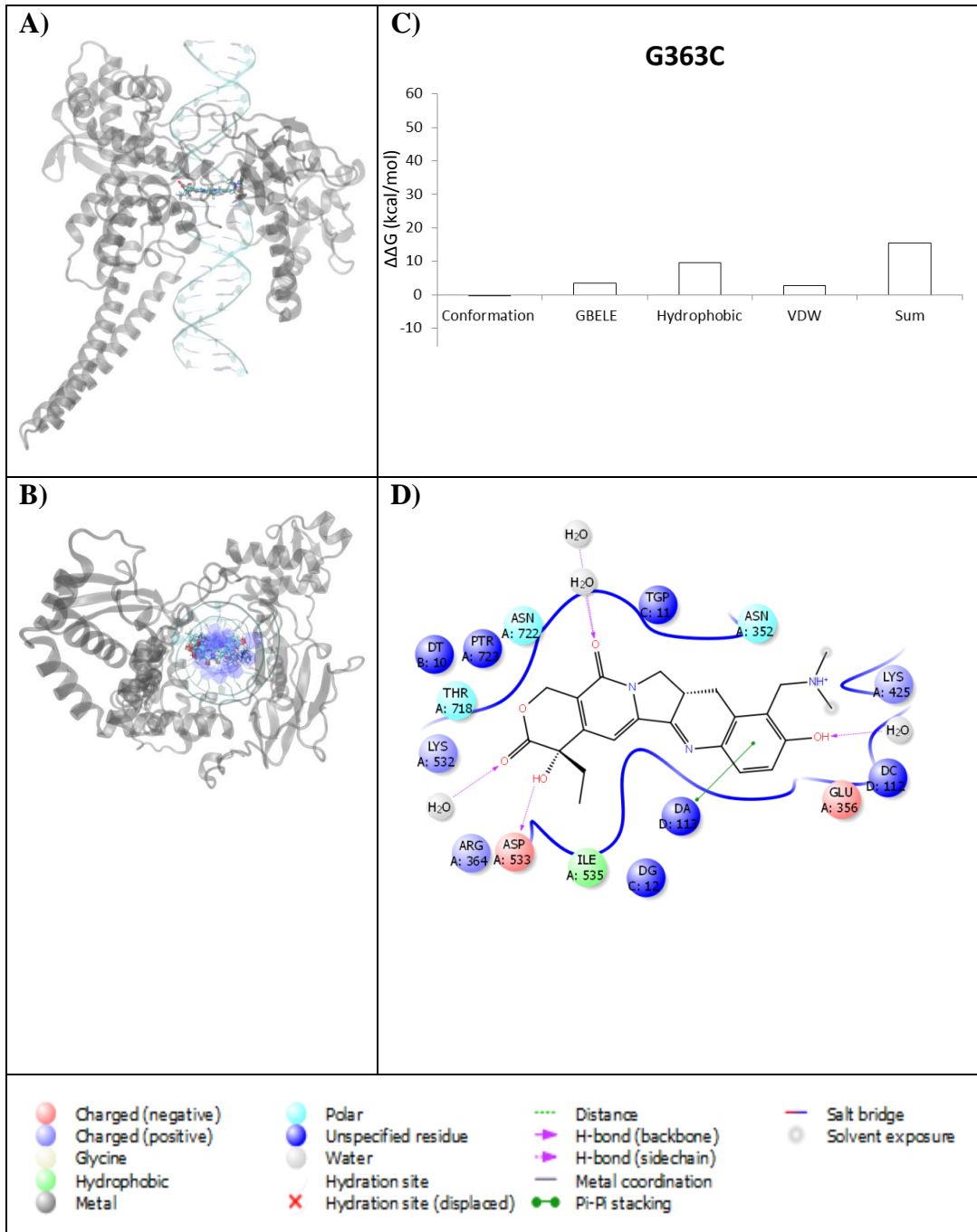


Figure S23. Topotecan Bound to Complex T729A. **A)** 3D top view of complex **B)** 3D side view of complex **C)** Decomposition of  $\Delta\Delta G$  **D)** 2D Representation of the binding within the complex

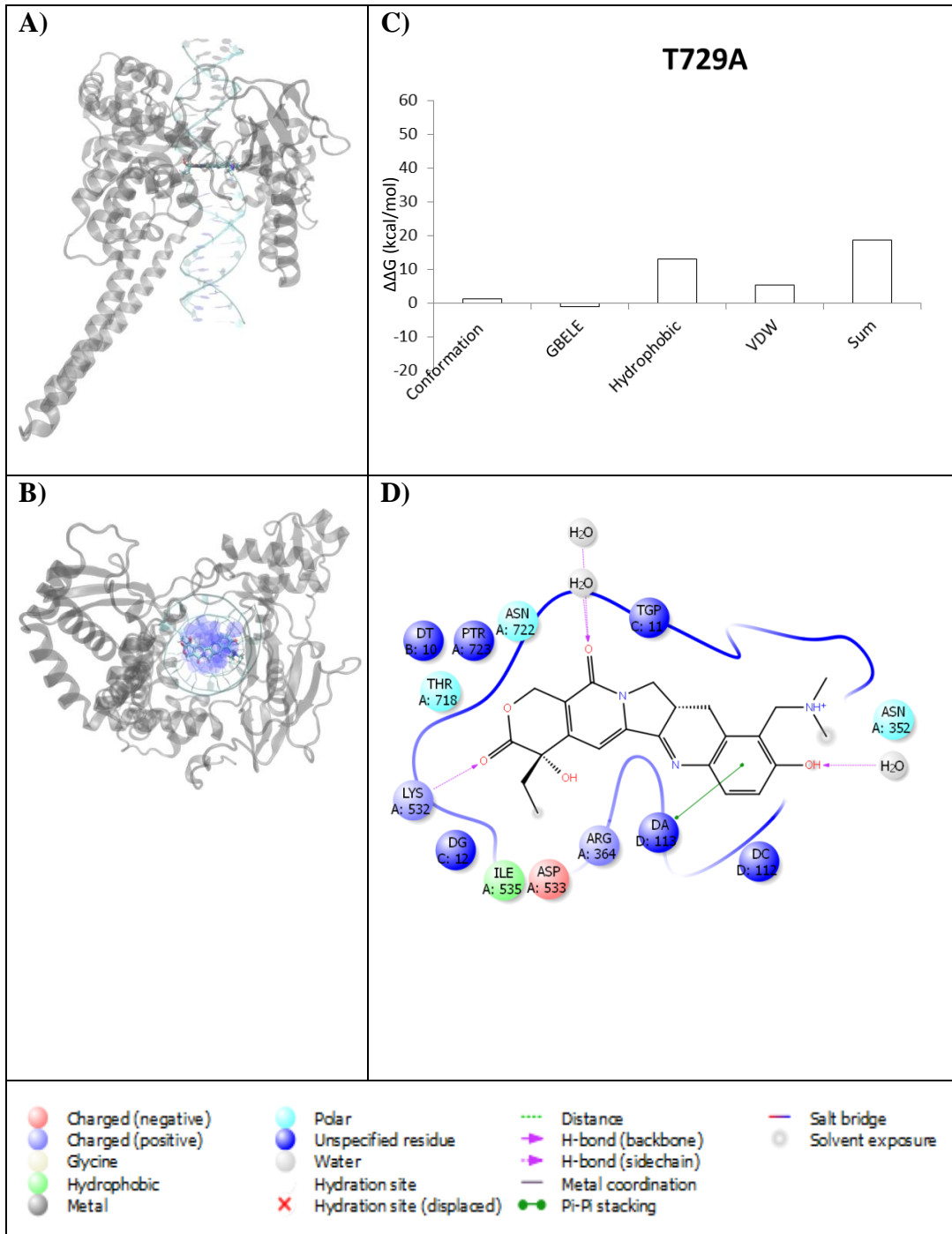


Figure S24. SN38 Bound to Complex N722A. **A)** 3D top view of complex **B)** 3D side view of complex **C)** Decomposition of  $\Delta\Delta G$  **D)** 2D Representation of the binding within the complex

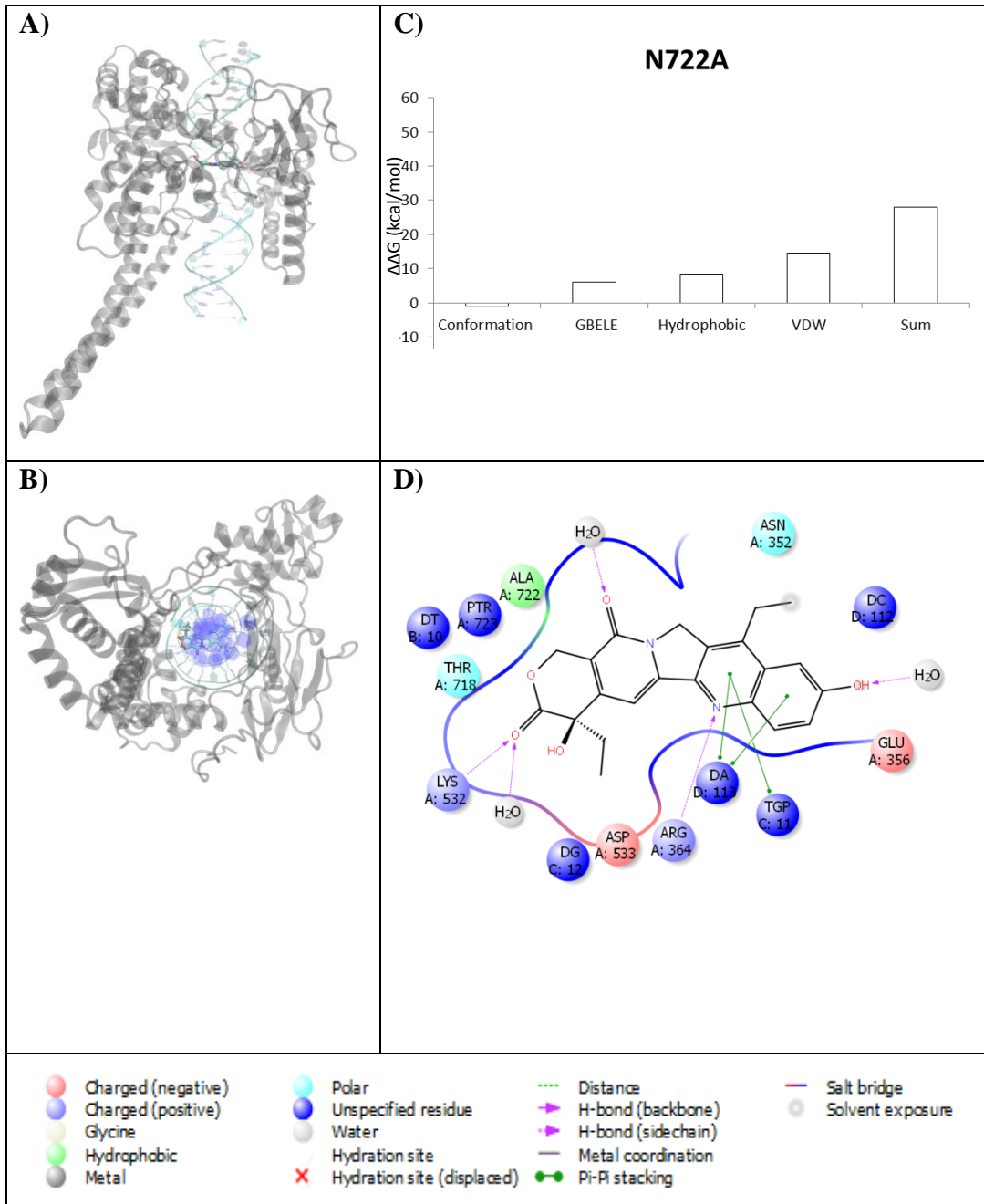




Figure S25. SN38 Bound to Complex N722S. **A)** 3D top view of complex **B)** 3D side view of complex **C)** Decomposition of  $\Delta\Delta G$  **D)** 2D Representation of the binding within the complex

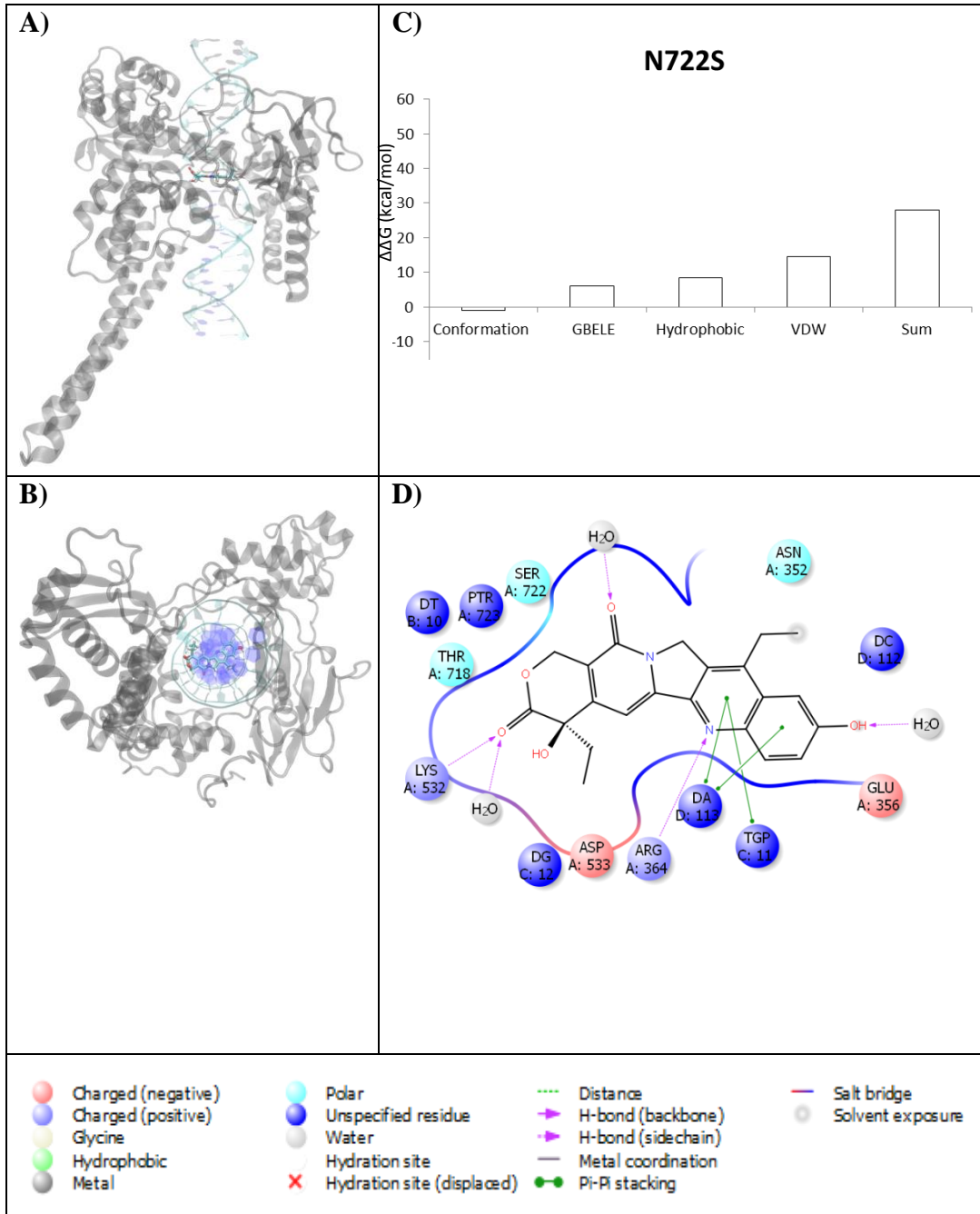




Figure S26. SN38 Bound to Complex G717V. **A)** 3D top view of complex **B)** 3D side view of complex **C)** Decomposition of  $\Delta\Delta G$  **D)** 2D Representation of the binding within the complex

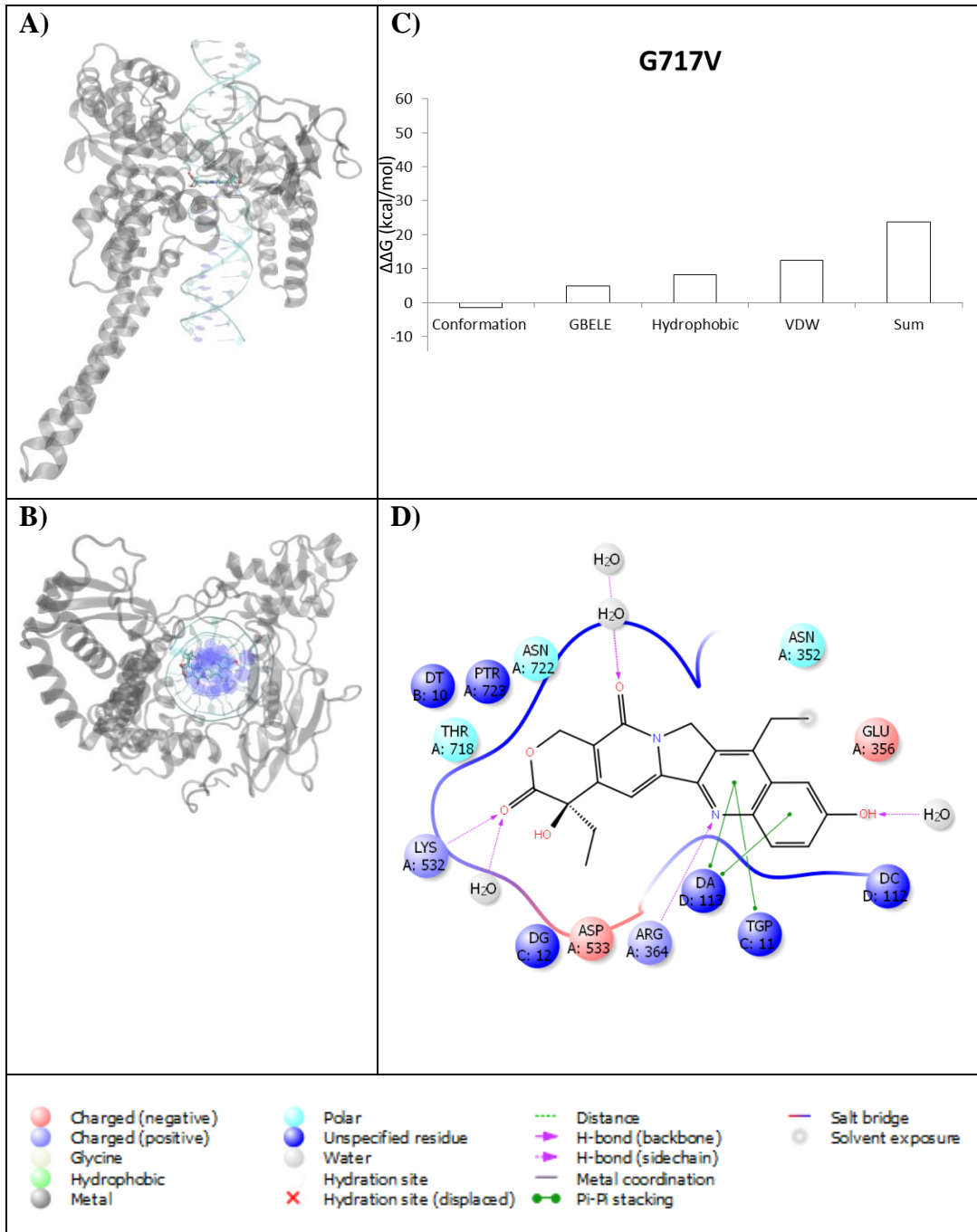


Figure S27. SN38 Bound to Complex D533G. **A)** 3D top view of complex **B)** 3D side view of complex **C)** Decomposition of  $\Delta\Delta G$  **D)** 2D Representation of the binding within the complex

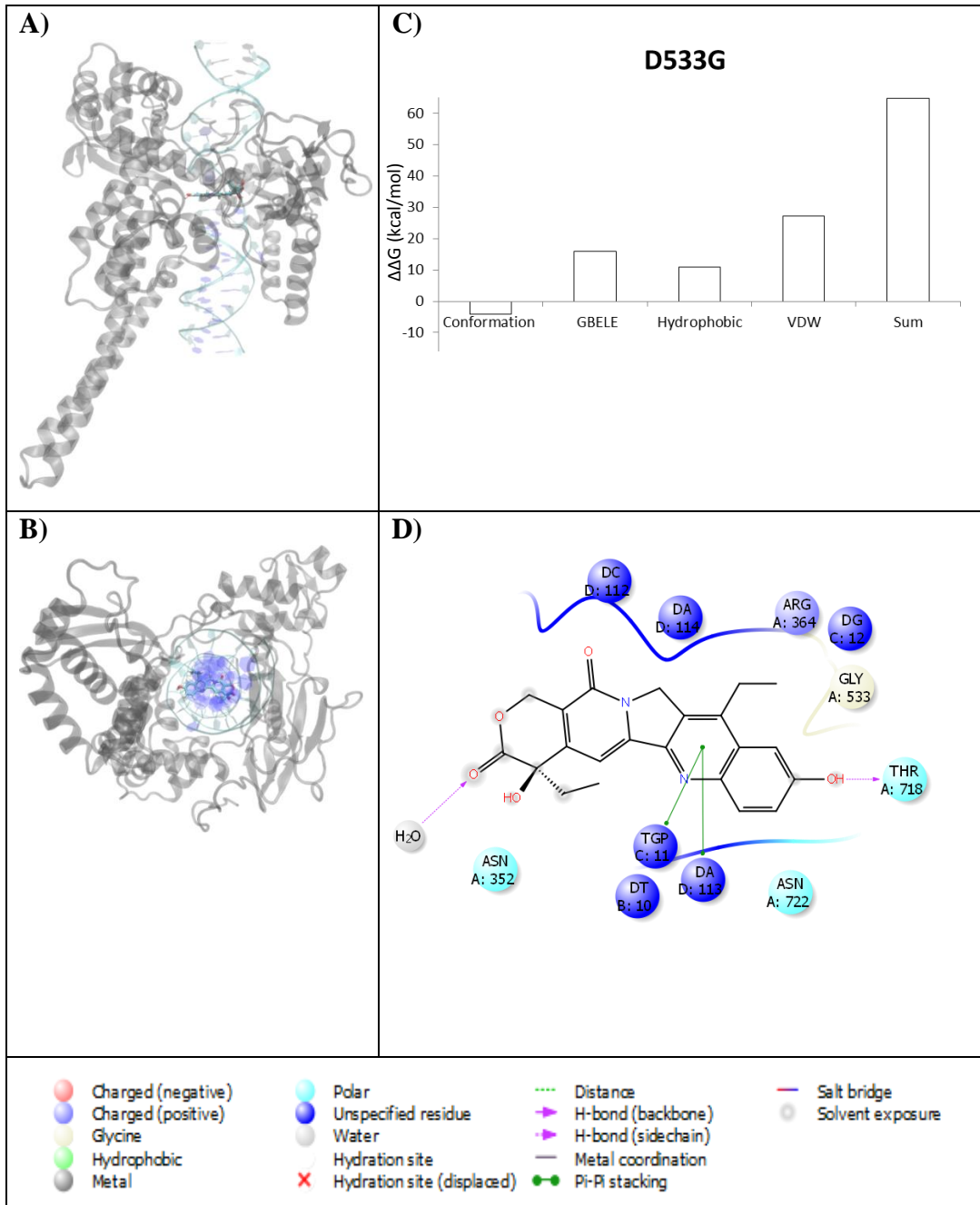


Figure S28. SN38 Bound to Complex D533N. **A)** 3D top view of complex **B)** 3D side view of complex **C)** Decomposition of  $\Delta\Delta G$  **D)** 2D Representation of the binding within the complex

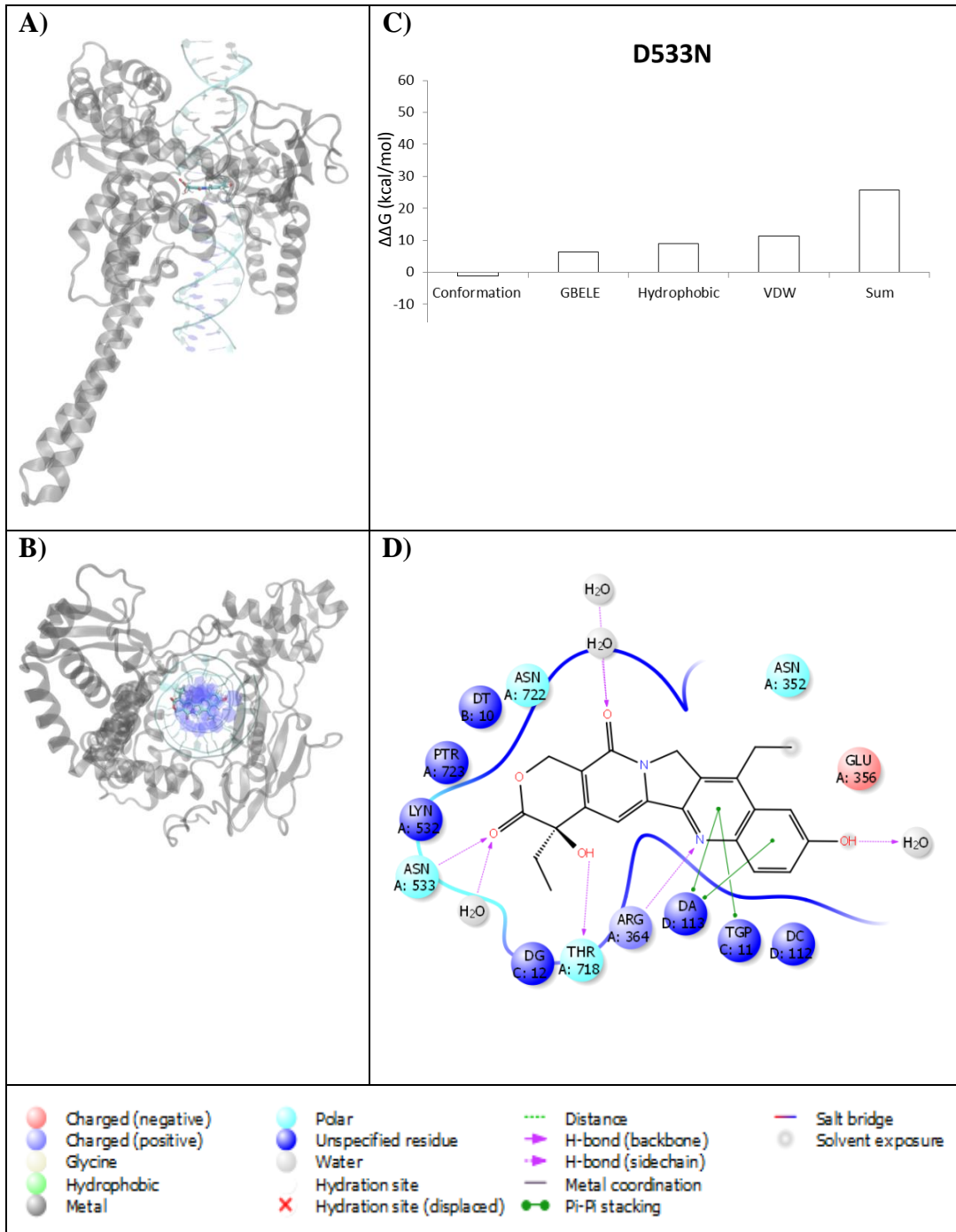


Figure S29. SN38 Bound to Complex G503S. **A)** 3D top view of complex **B)** 3D side view of complex **C)** Decomposition of  $\Delta\Delta G$  **D)** 2D Representation of the binding within the complex

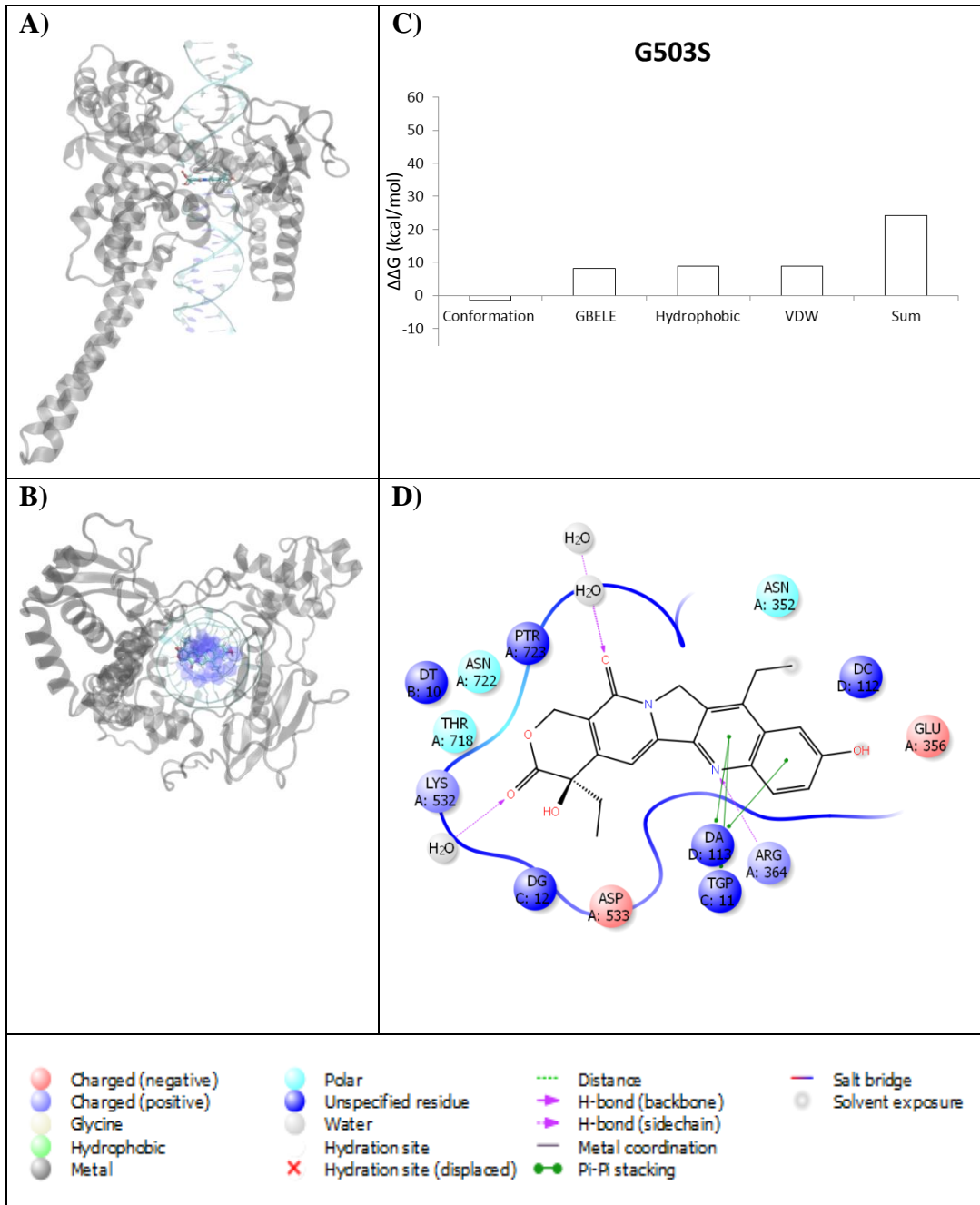


Figure S30. SN38 Bound to Complex R364H. **A)** 3D top view of complex **B)** 3D side view of complex **C)** Decomposition of  $\Delta\Delta G$  **D)** 2D Representation of the binding within the complex

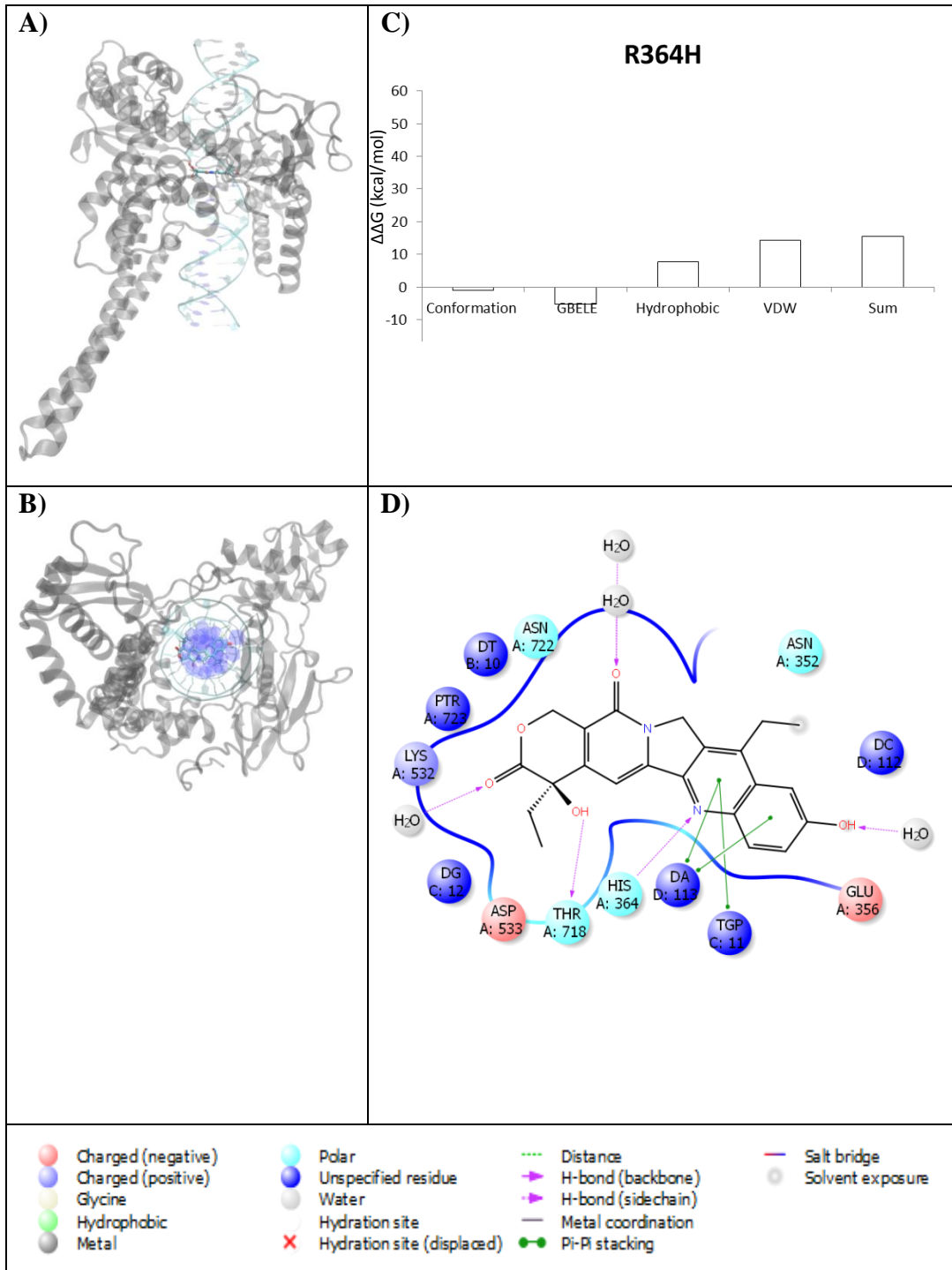


Figure S31. SN38 Bound to Complex F361S. **A)** 3D top view of complex **B)** 3D side view of complex **C)** Decomposition of  $\Delta\Delta G$  **D)** 2D Representation of the binding within the complex

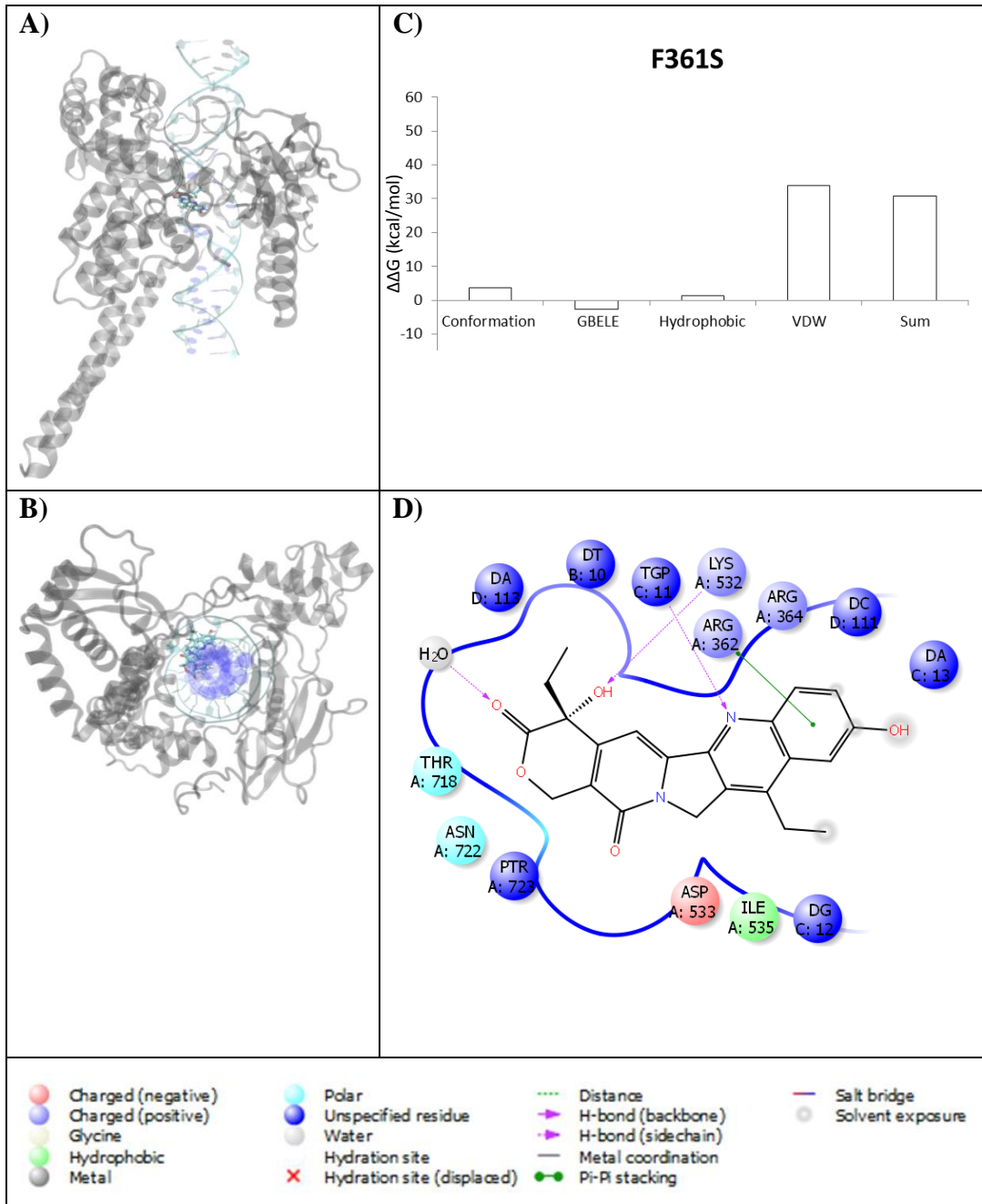


Figure S32. SN38 Bound to Complex G363C. **A)** 3D top view of complex **B)** 3D side view of complex **C)** Decomposition of  $\Delta\Delta G$  **D)** 2D Representation of the binding within the complex

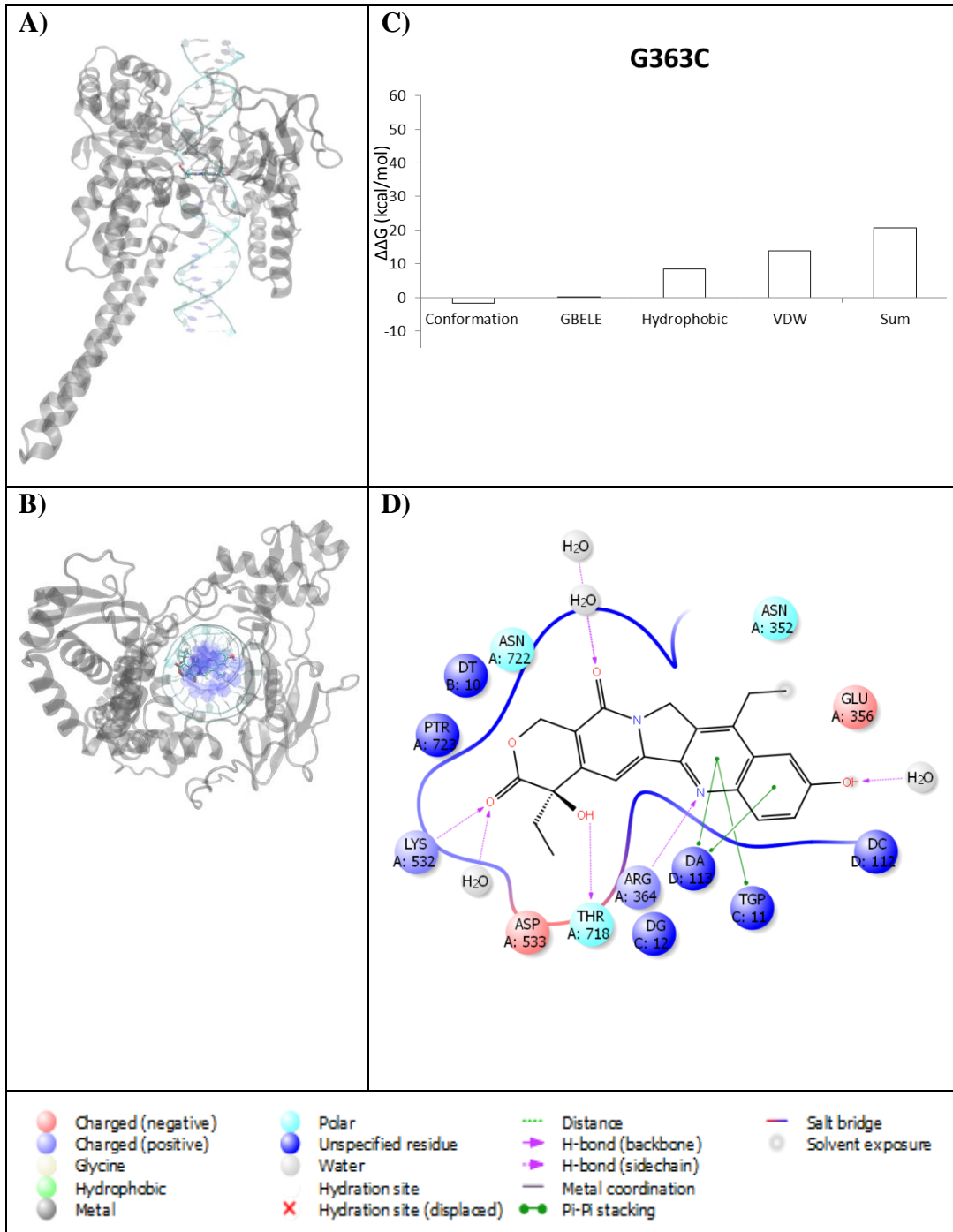




Figure S33. SN38 Bound to Complex T729A. **A)** 3D top view of complex **B)** 3D side view of complex **C)** Decomposition of  $\Delta\Delta G$  **D)** 2D Representation of the binding within the complex

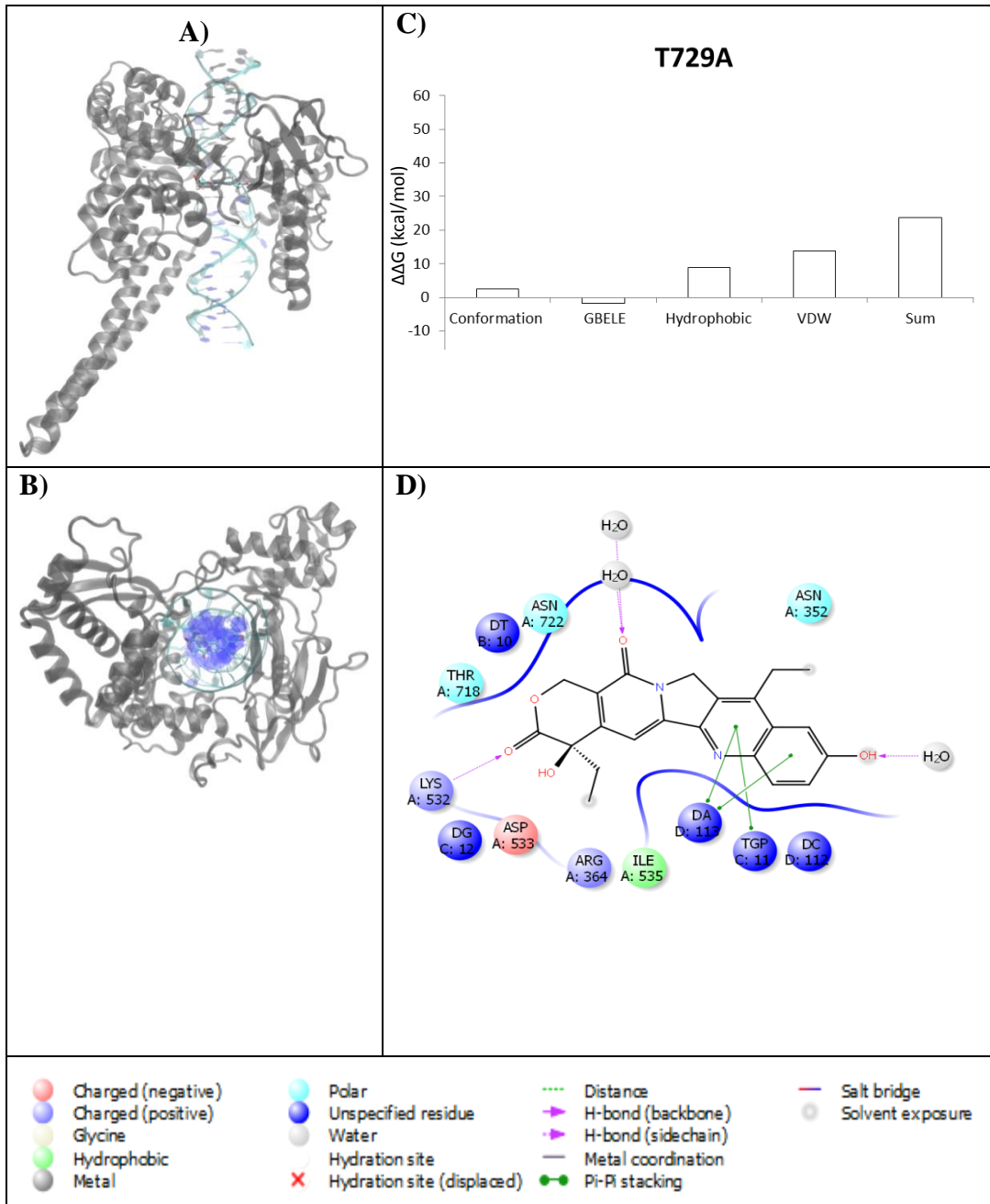




Figure S34. Lurtotecan Bound to Complex N722A. **A)** 3D top view of complex **B)** 3D side view of complex **C)** Decomposition of  $\Delta\Delta G$  **D)** 2D Representation of the binding within the complex

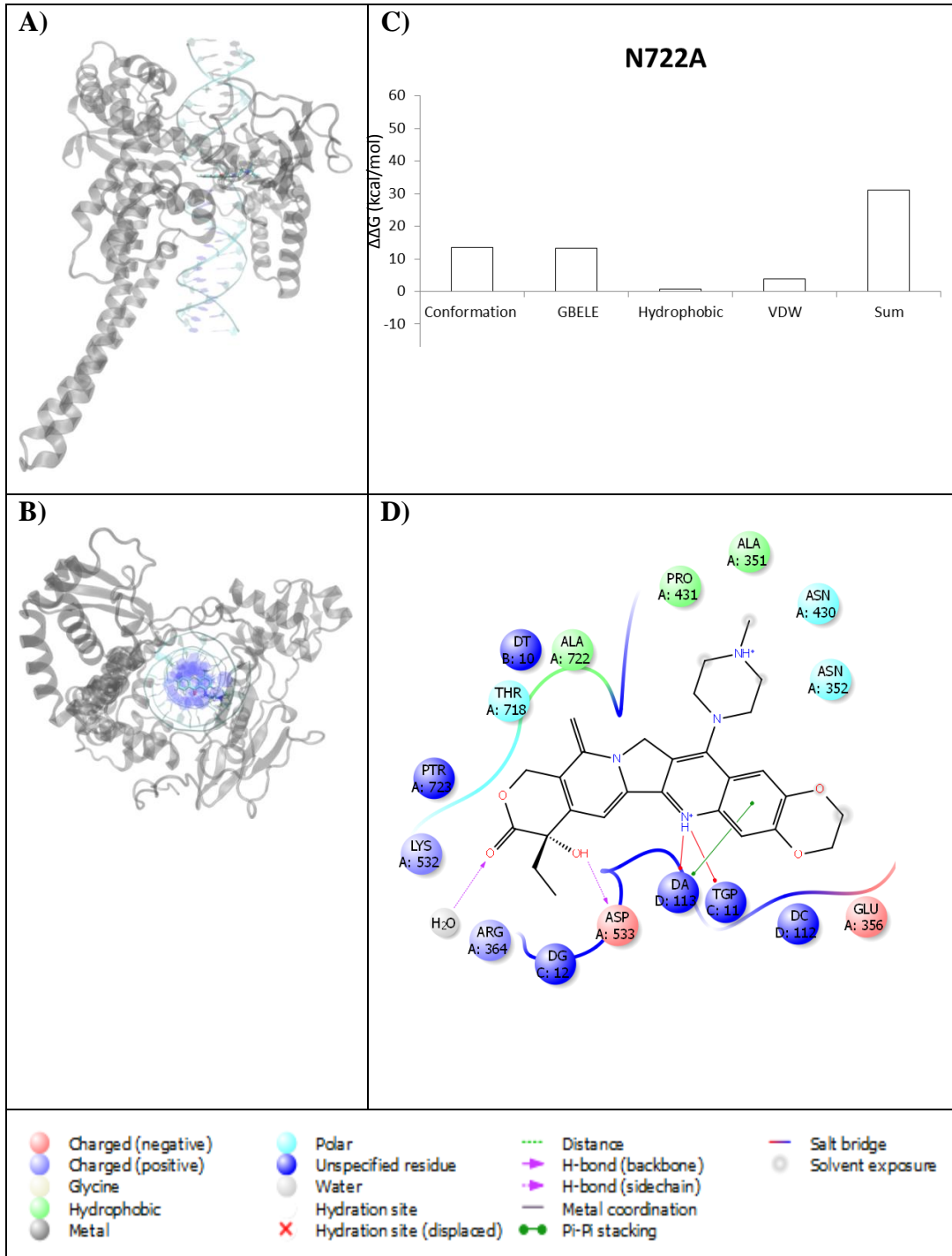


Figure S35. Lurtotecan Bound to Complex N722S. **A)** 3D top view of complex **B)** 3D side view of complex **C)** Decomposition of  $\Delta\Delta G$  **D)** 2D Representation of the binding within the complex

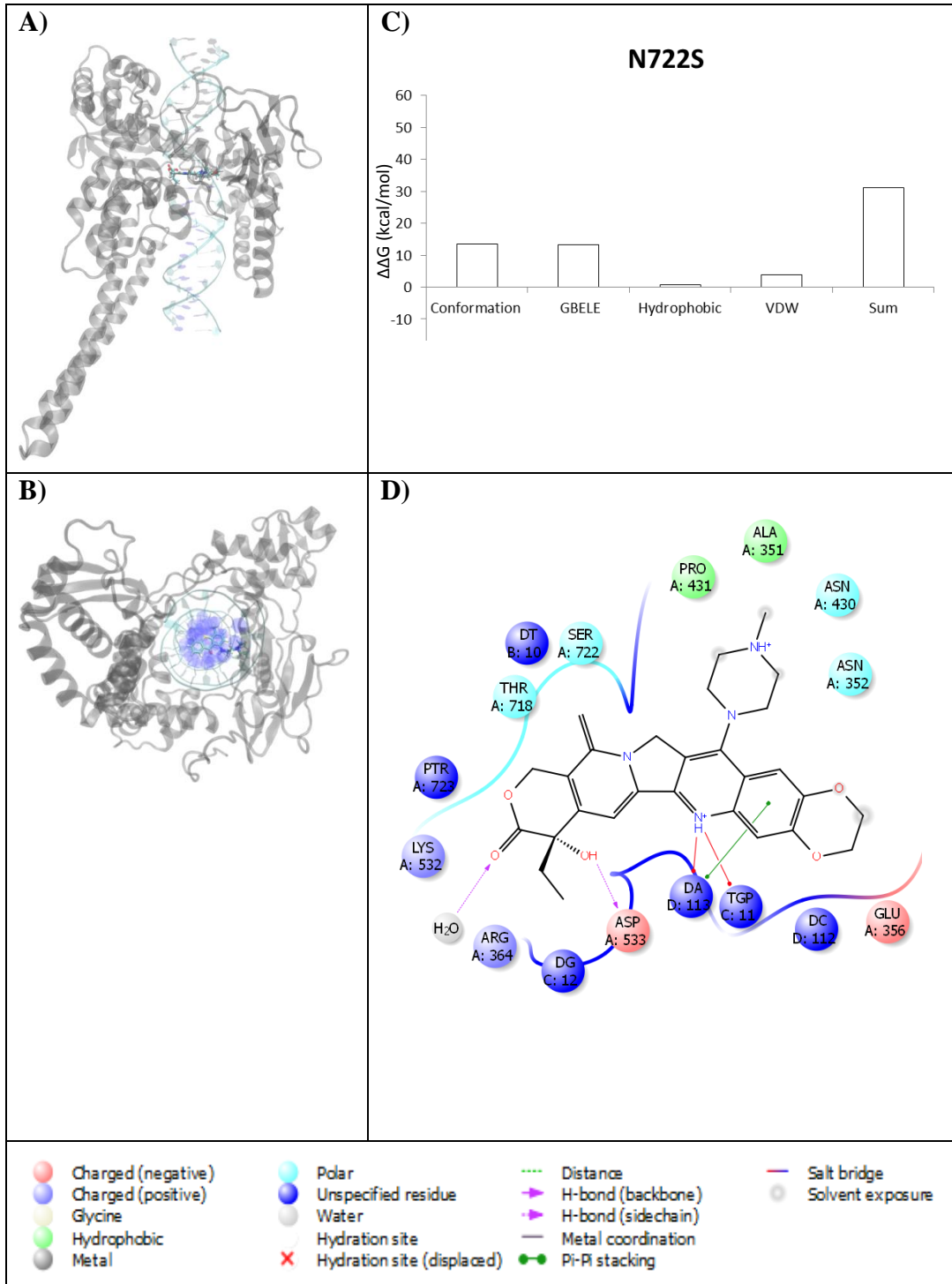


Figure S36. Lurtotecan Bound to Complex. **A)** 3D top view of complex **B)** 3D side view of complex **C)** Decomposition of  $\Delta\Delta G$  **D)** 2D Representation of the binding within the complex

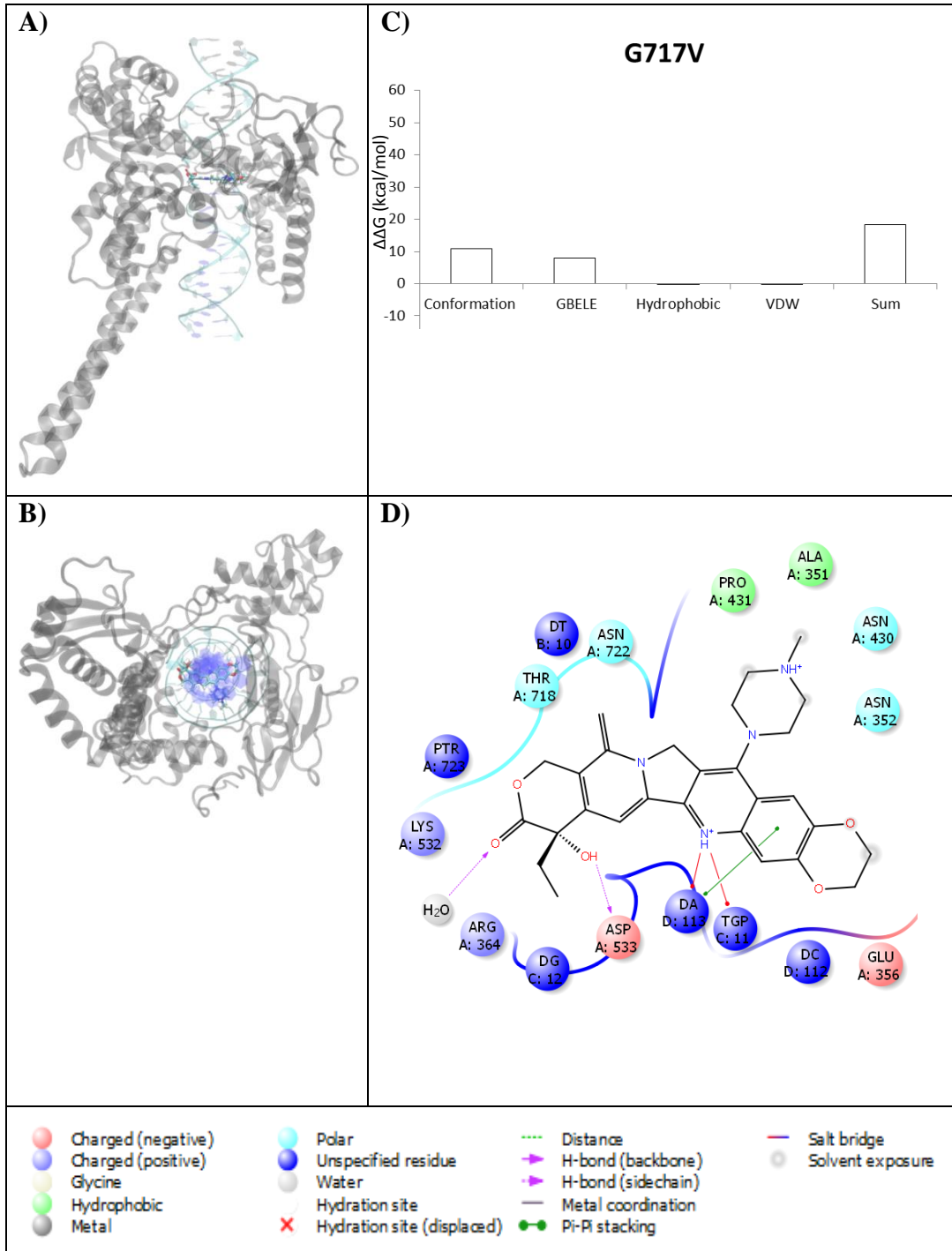


Figure S37. Lurtotecan Bound to Complex D533G. **A)** 3D top view of complex **B)** 3D side view of complex **C)** Decomposition of  $\Delta\Delta G$  **D)** 2D Representation of the binding within the complex

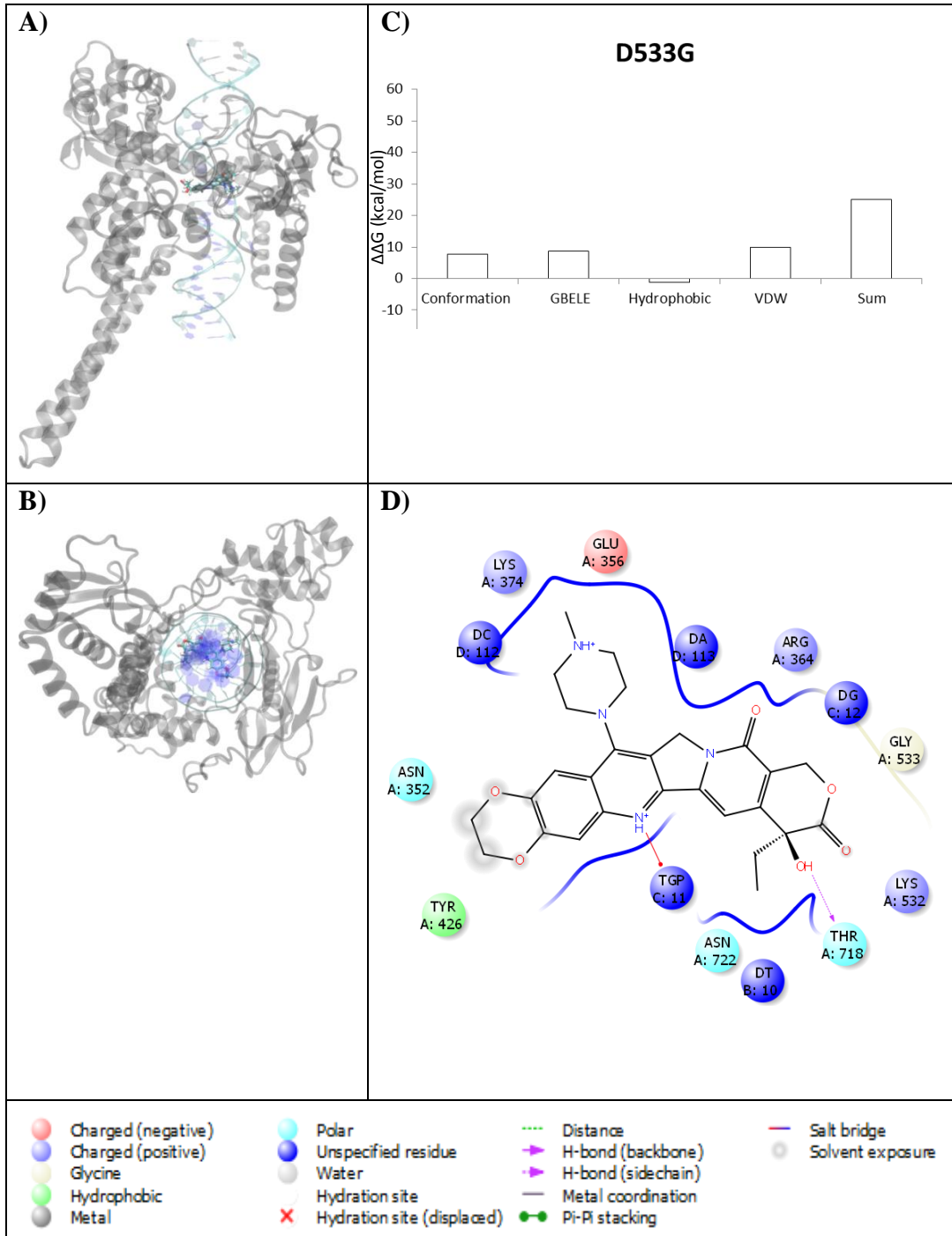


Figure S38. Lurtotecan Bound to Complex D533N. **A)** 3D top view of complex **B)** 3D side view of complex **C)** Decomposition of  $\Delta\Delta G$  **D)** 2D Representation of the binding within the complex

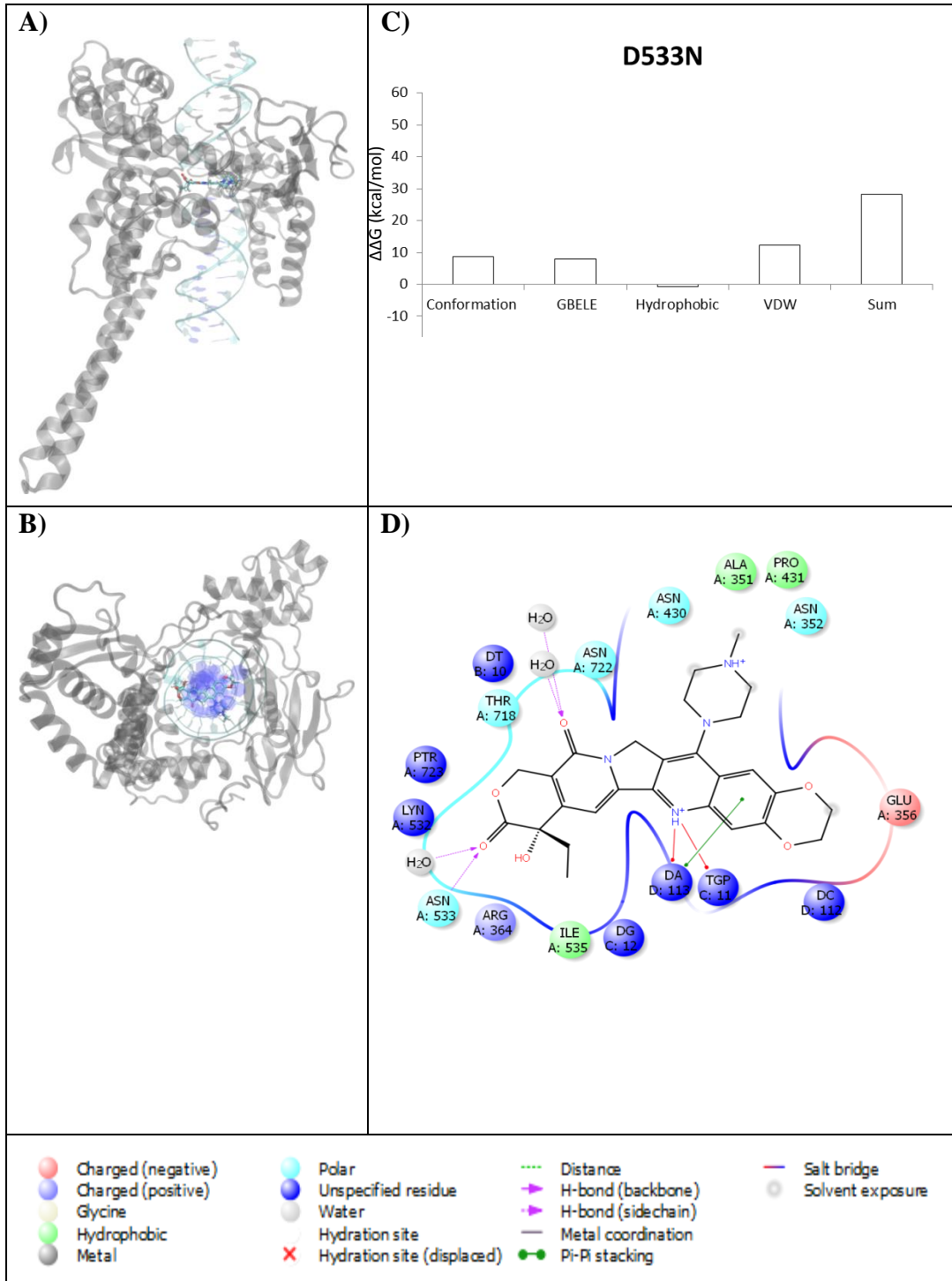


Figure S39. Lurtotecan Bound to Complex G503S. **A)** 3D top view of complex **B)** 3D side view of complex **C)** Decomposition of  $\Delta\Delta G$  **D)** 2D Representation of the binding within the complex

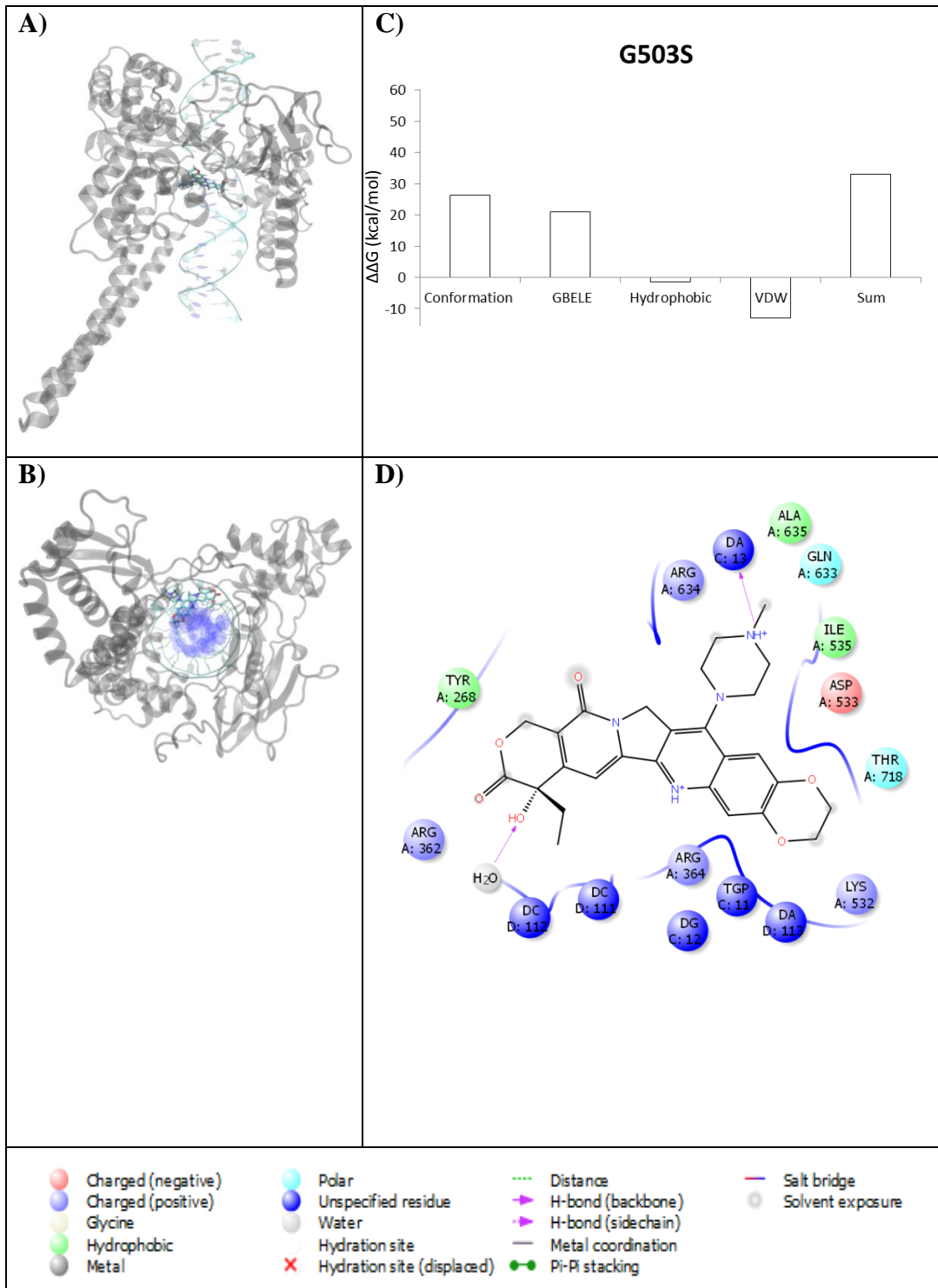


Figure S40. Lurtotecan Bound to Complex R364H. **A)** 3D top view of complex **B)** 3D side view of complex **C)** Decomposition of  $\Delta\Delta G$  **D)** 2D Representation of the binding within the complex

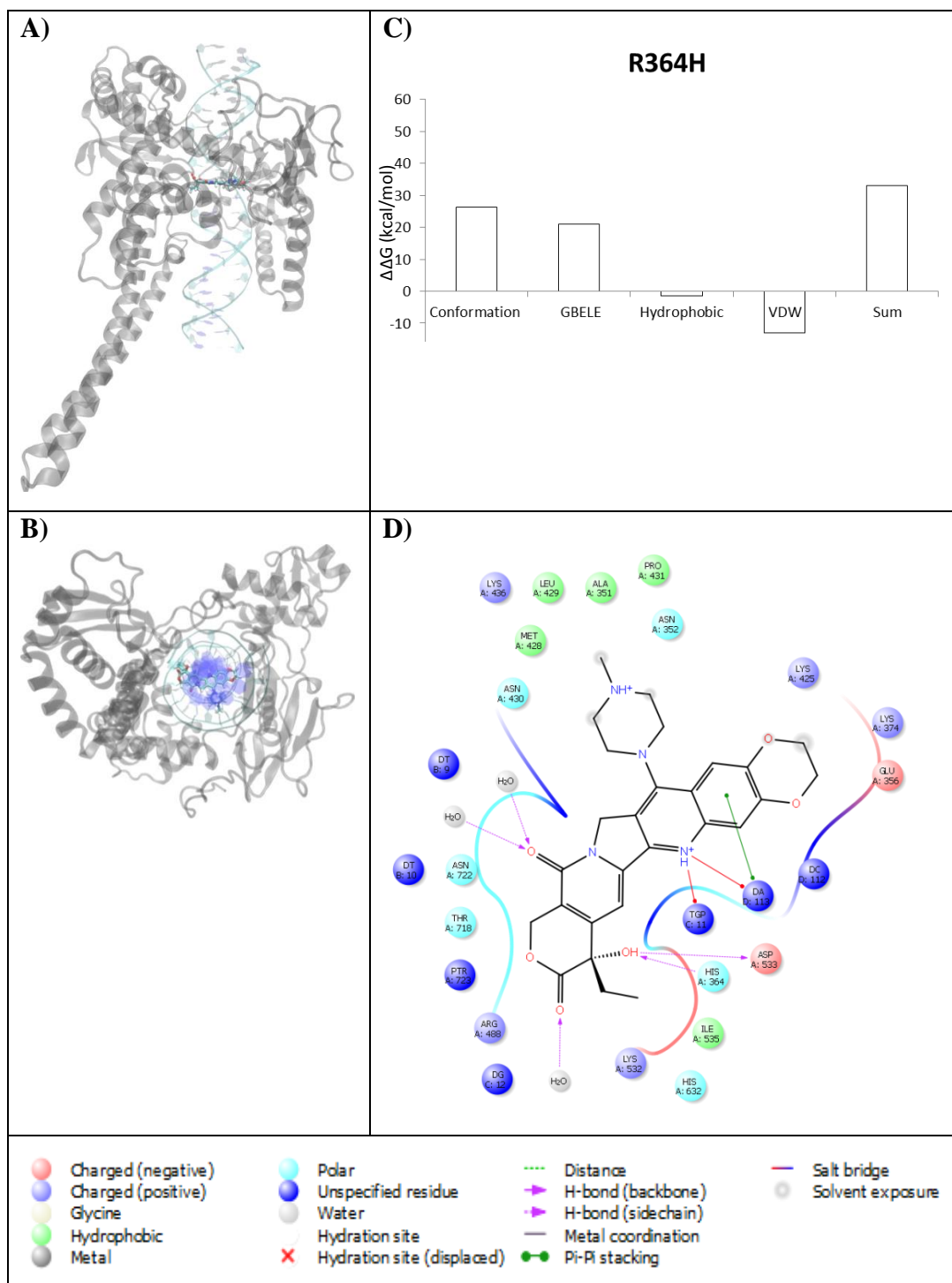




Figure S41. Lurtotecan Bound to Complex F361S. **A)** 3D top view of complex **B)** 3D side view of complex **C)** Decomposition of  $\Delta\Delta G$  **D)** 2D Representation of the binding within the complex

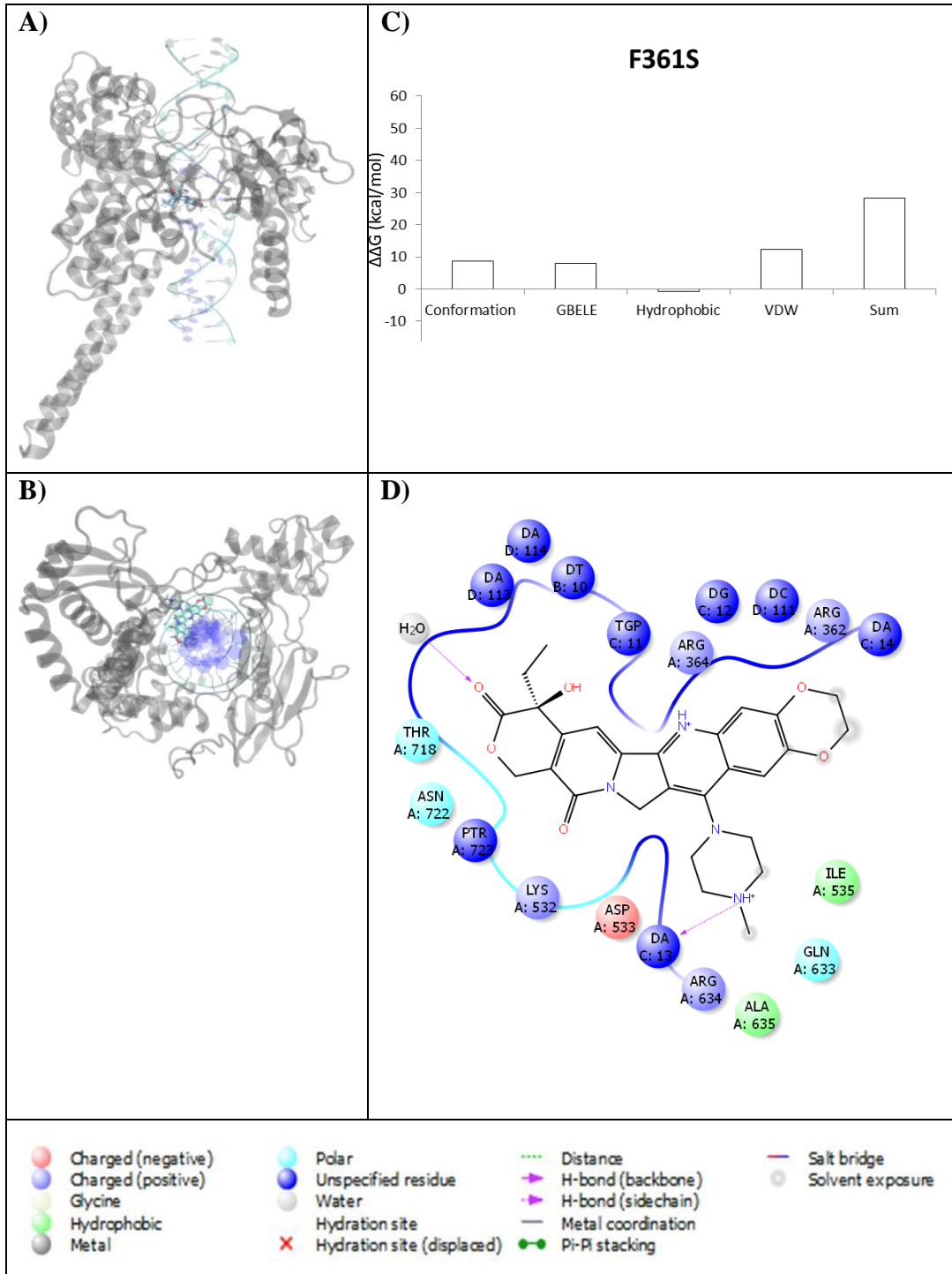




Figure S42. Lurtotecan Bound to Complex G363C. **A)** 3D top view of complex **B)** 3D side view of complex **C)** Decomposition of  $\Delta\Delta G$  **D)** 2D Representation of the binding within the complex

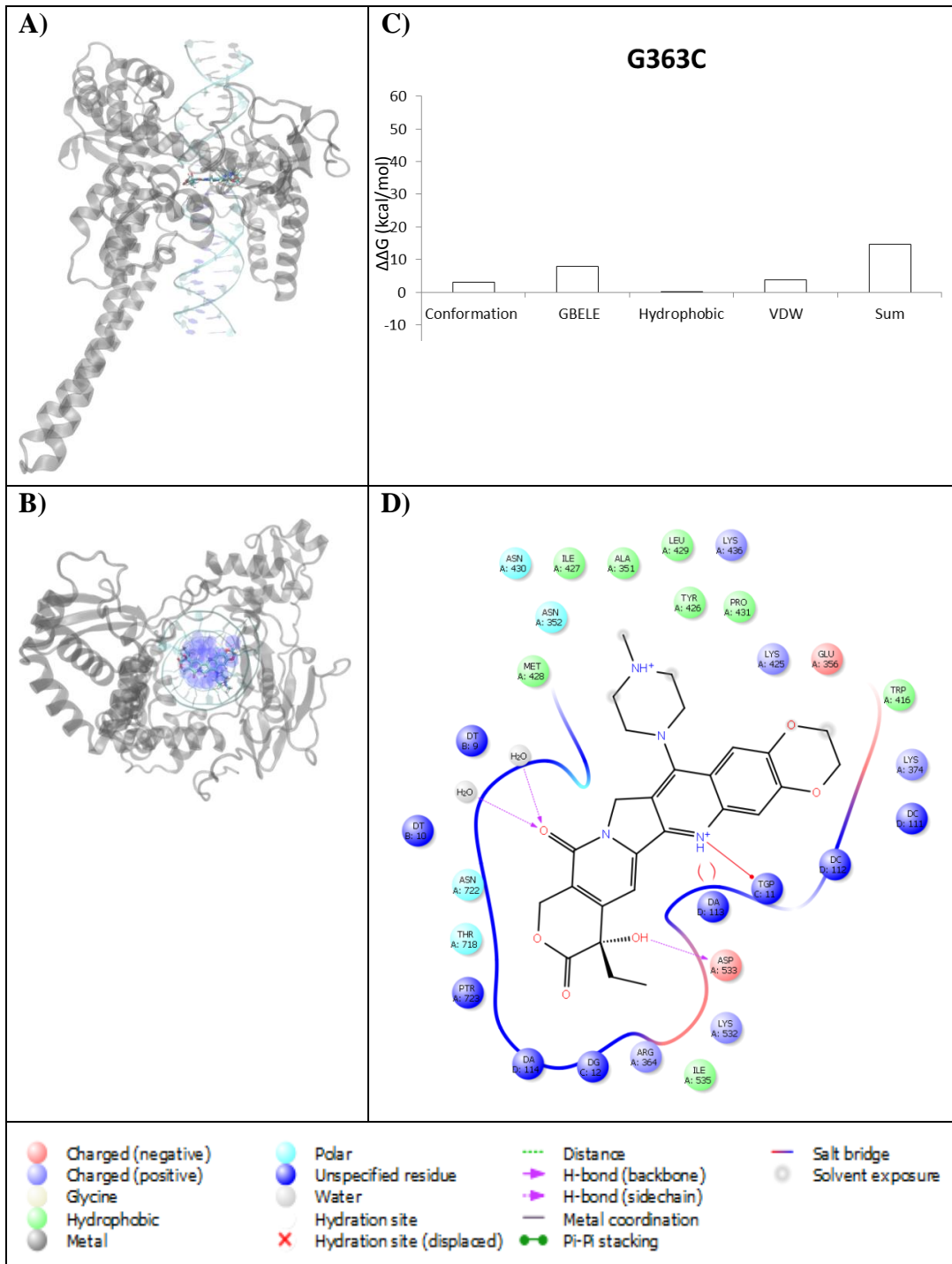


Figure S43. Lurtotecan Bound to Complex T729A. **A)** 3D top view of complex **B)** 3D side view of complex **C)** Decomposition of  $\Delta\Delta G$  **D)** 2D Representation of the binding within the complex

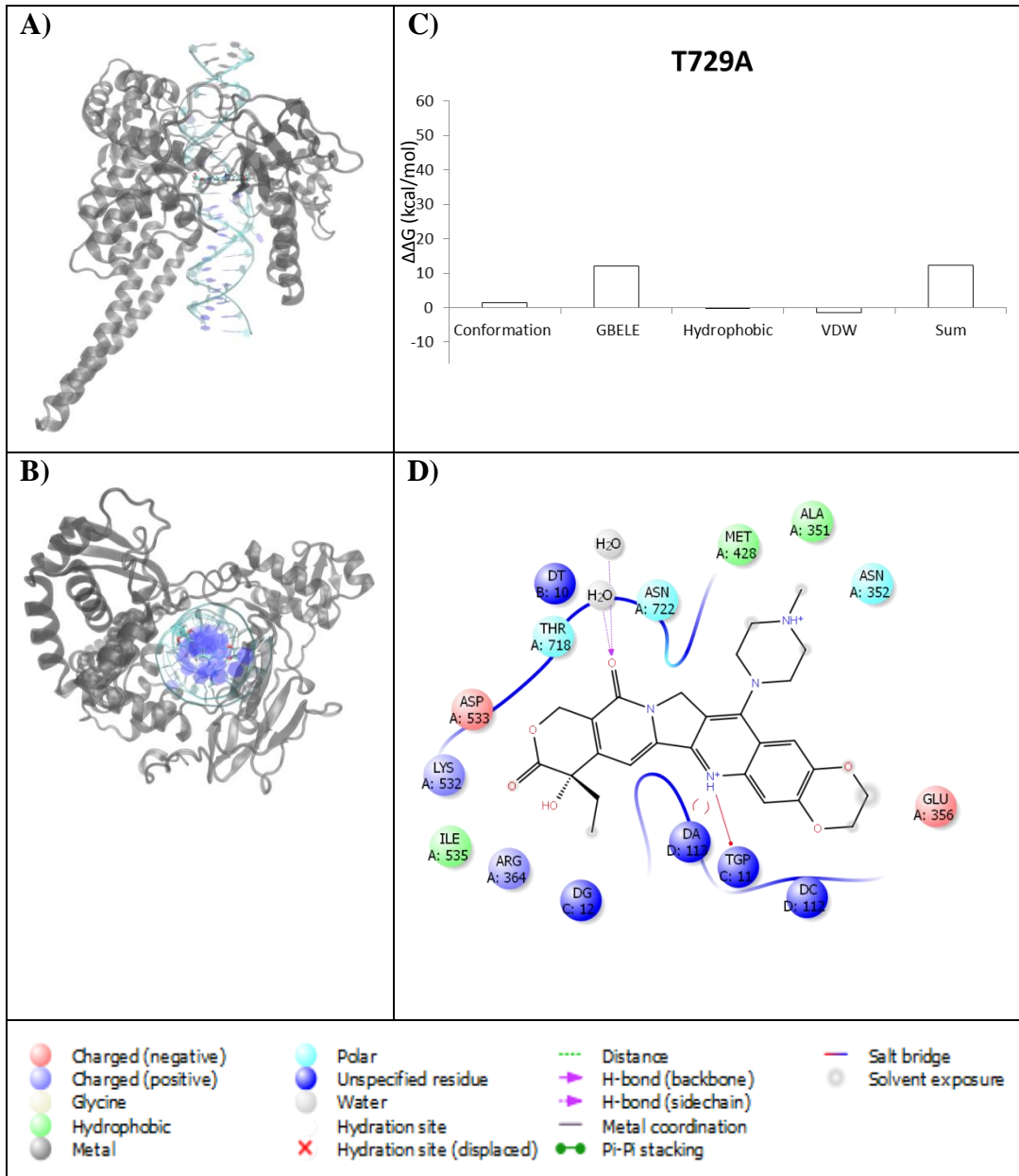


Figure S44. Exatecan Bound to Complex N722A. **A)** 3D top view of complex **B)** 3D side view of complex **C)** Decomposition of  $\Delta\Delta G$  **D)** 2D Representation of the binding within the complex

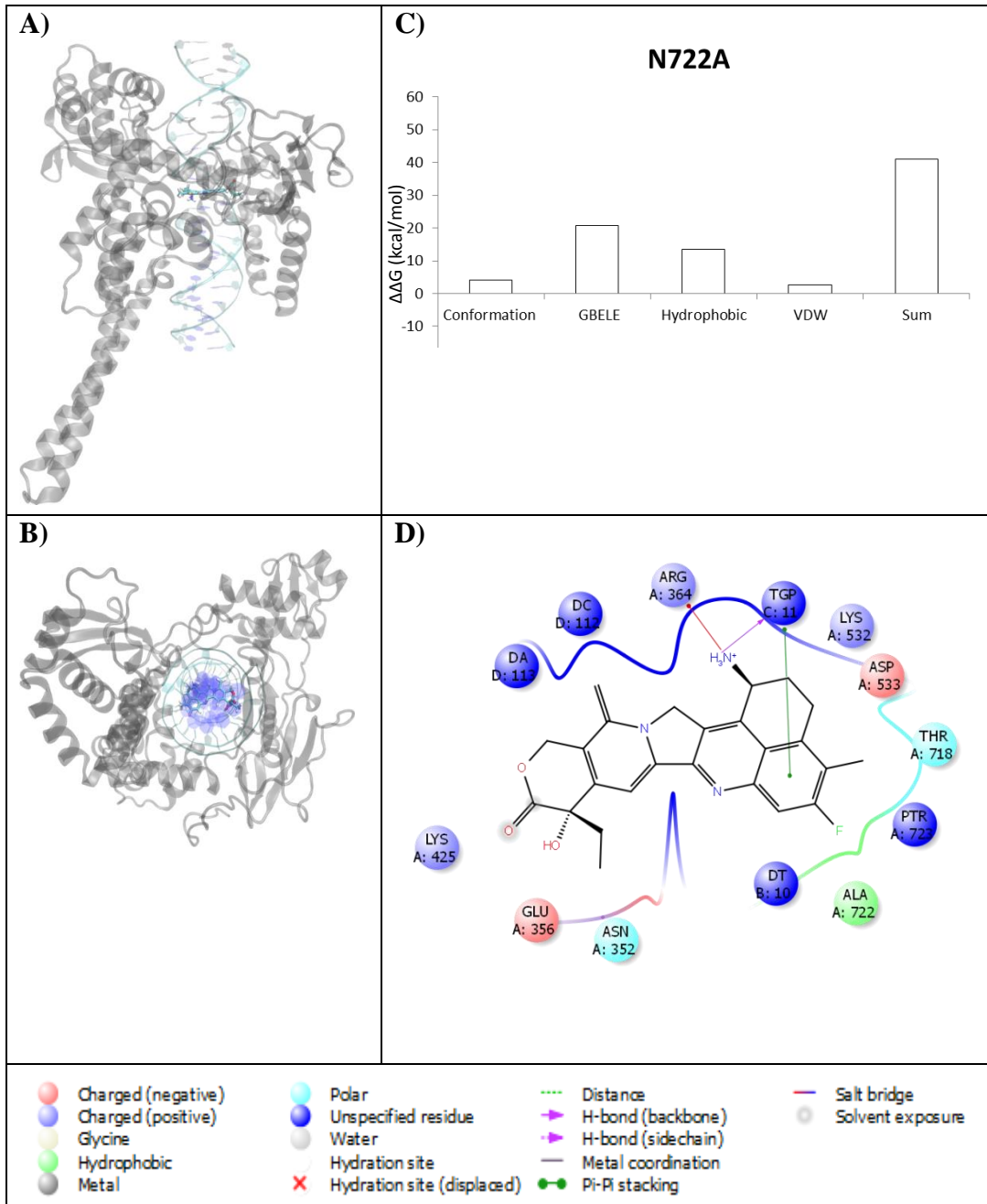


Figure S45. Exatecan Bound to Complex N722S. A) 3D top view of complex B) 3D side view of complex C) Decomposition of  $\Delta\Delta G$  D) 2D Representation of the binding within the complex

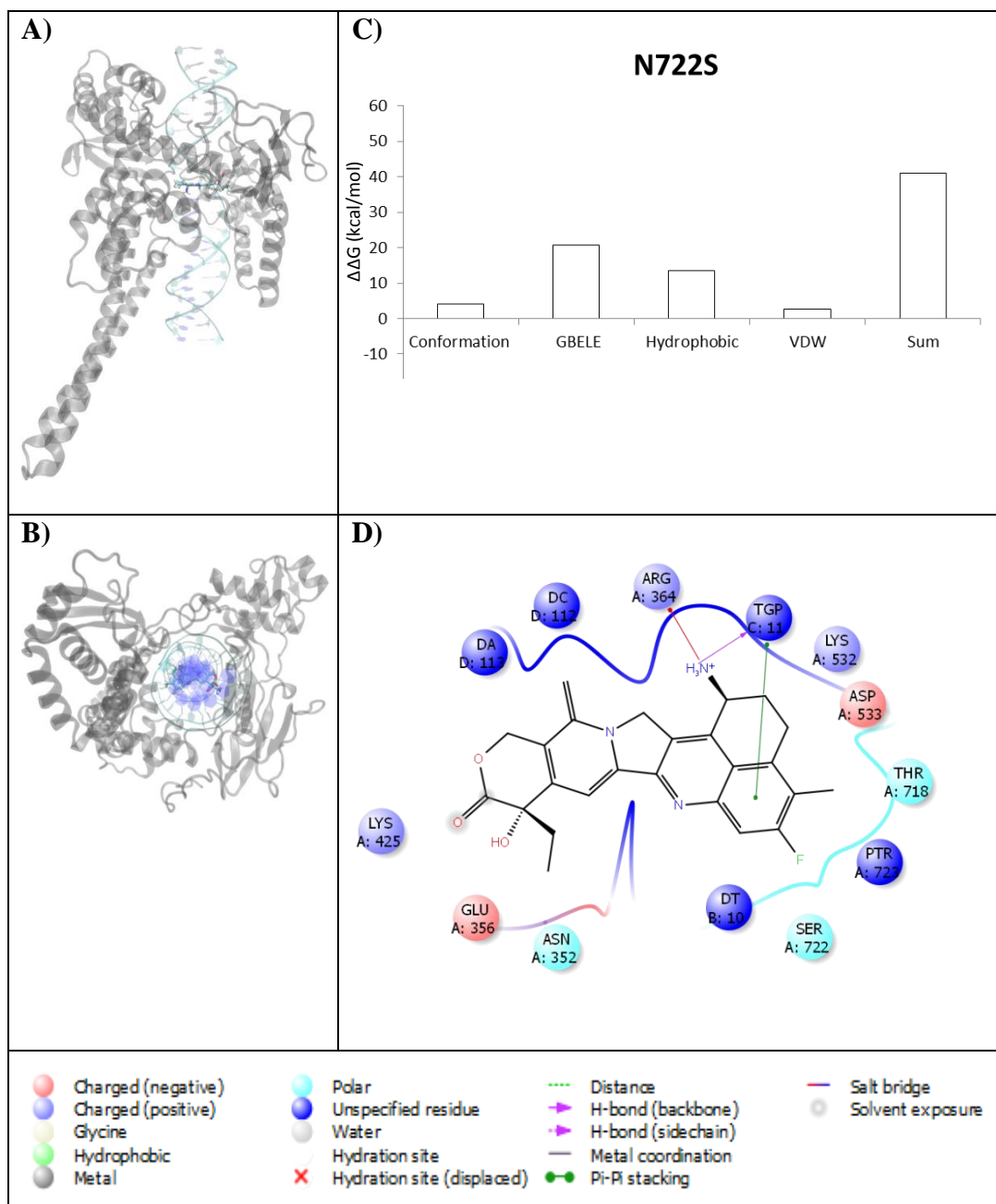


Figure S46. Exatecan Bound to Complex G717V. **A)** 3D top view of complex **B)** 3D side view of complex **C)** Decomposition of  $\Delta\Delta G$  **D)** 2D Representation of the binding within the complex

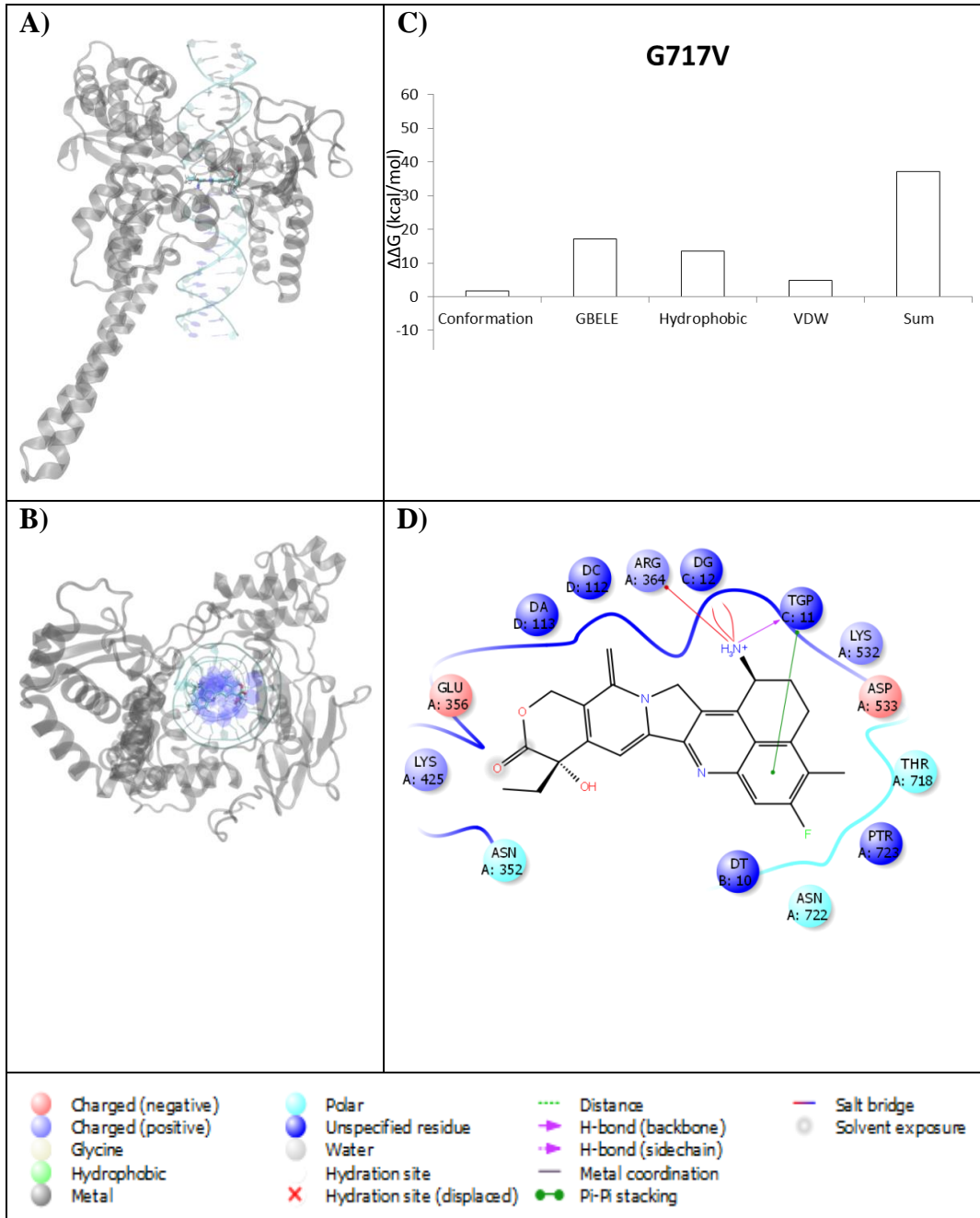


Figure S47. Exatecan Bound to Complex D533G. **A)** 3D top view of complex **B)** 3D side view of complex **C)** Decomposition of  $\Delta\Delta G$  **D)** 2D Representation of the binding within the complex

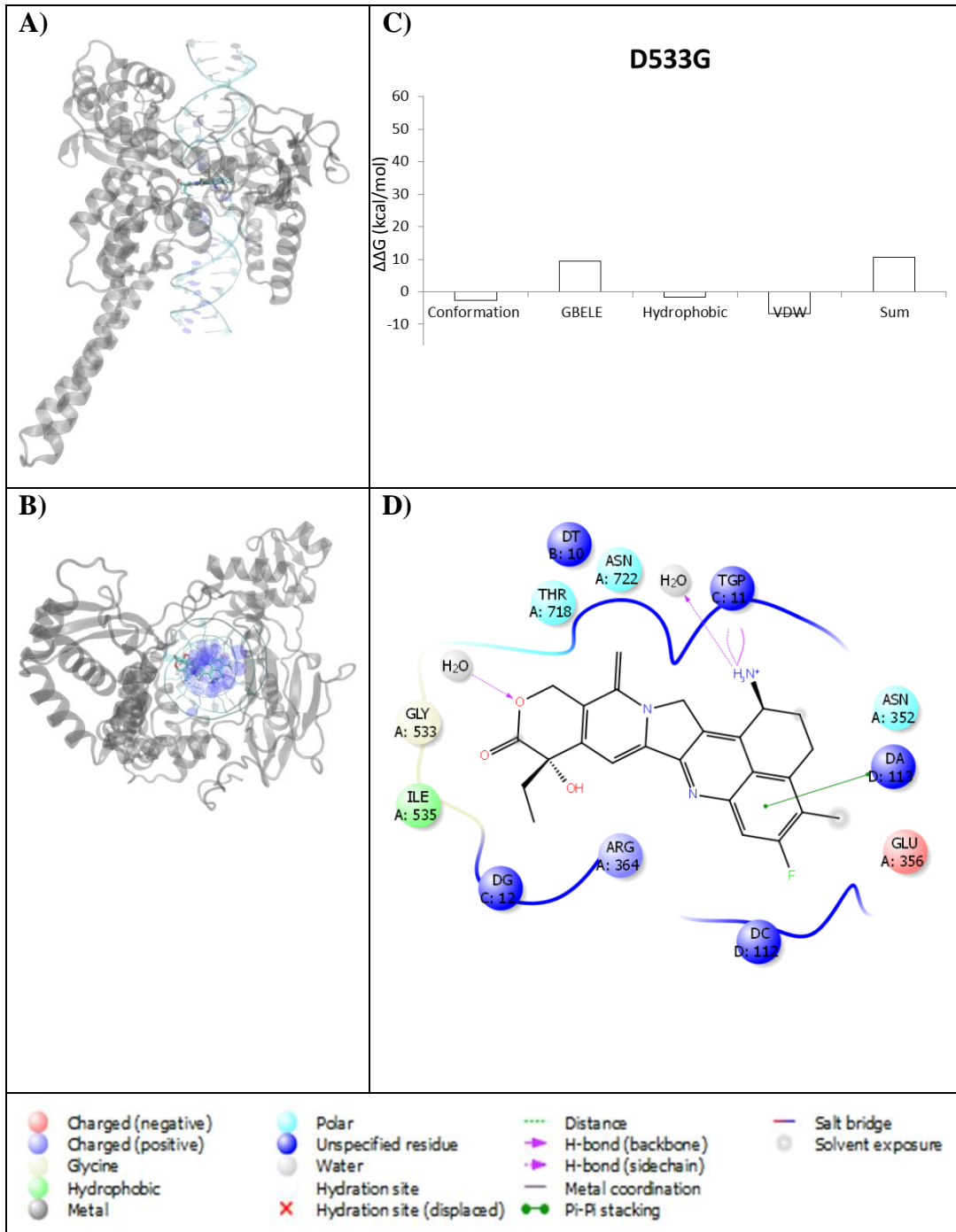


Figure S48. Exatecan Bound to Complex D533N. **A)** 3D top view of complex **B)** 3D side view of complex **C)** Decomposition of  $\Delta\Delta G$  **D)** 2D Representation of the binding within the complex

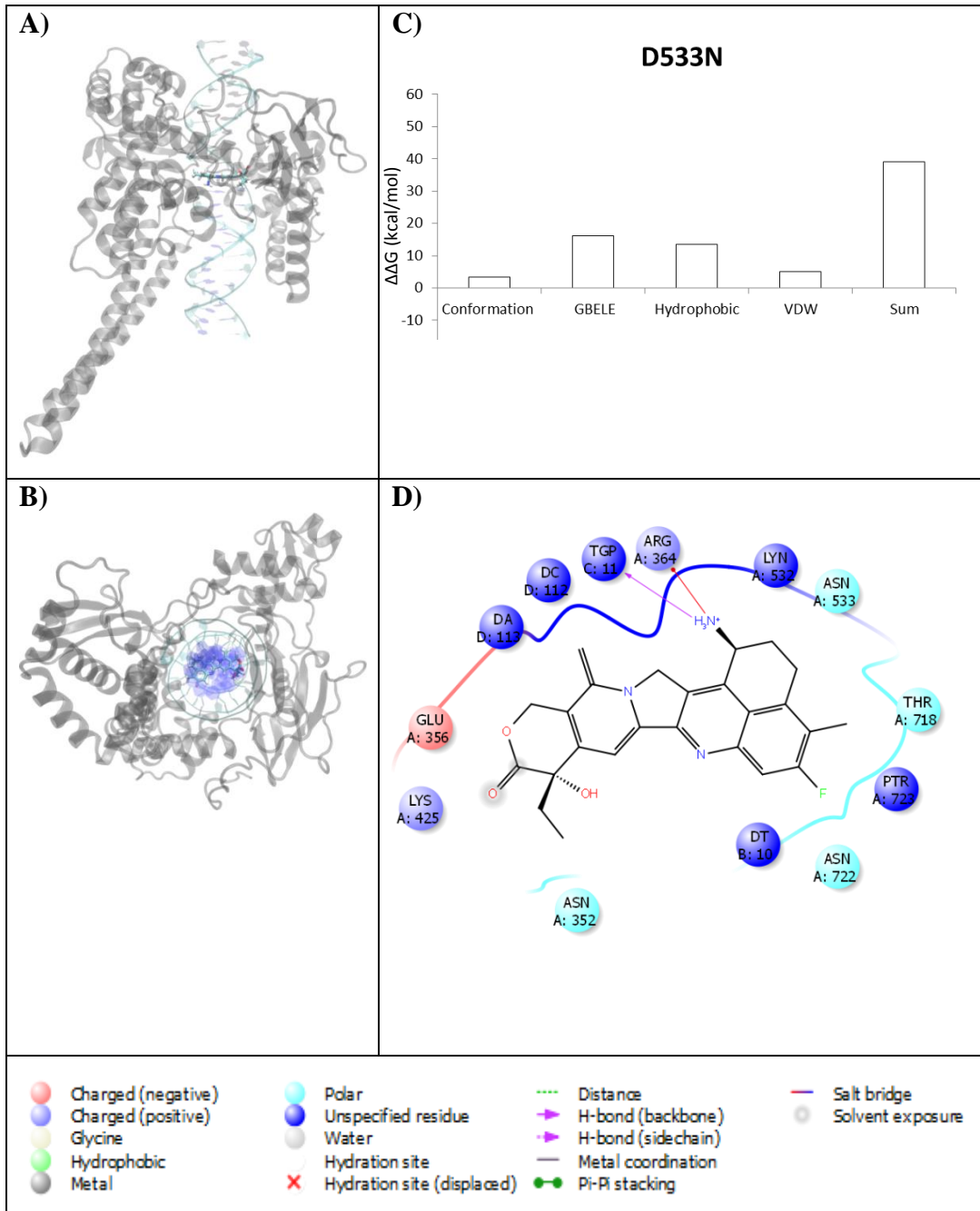




Figure S49. Exatecan Bound to Complex G503S. **A)** 3D top view of complex **B)** 3D side view of complex **C)** Decomposition of  $\Delta\Delta G$  **D)** 2D Representation of the binding within the complex

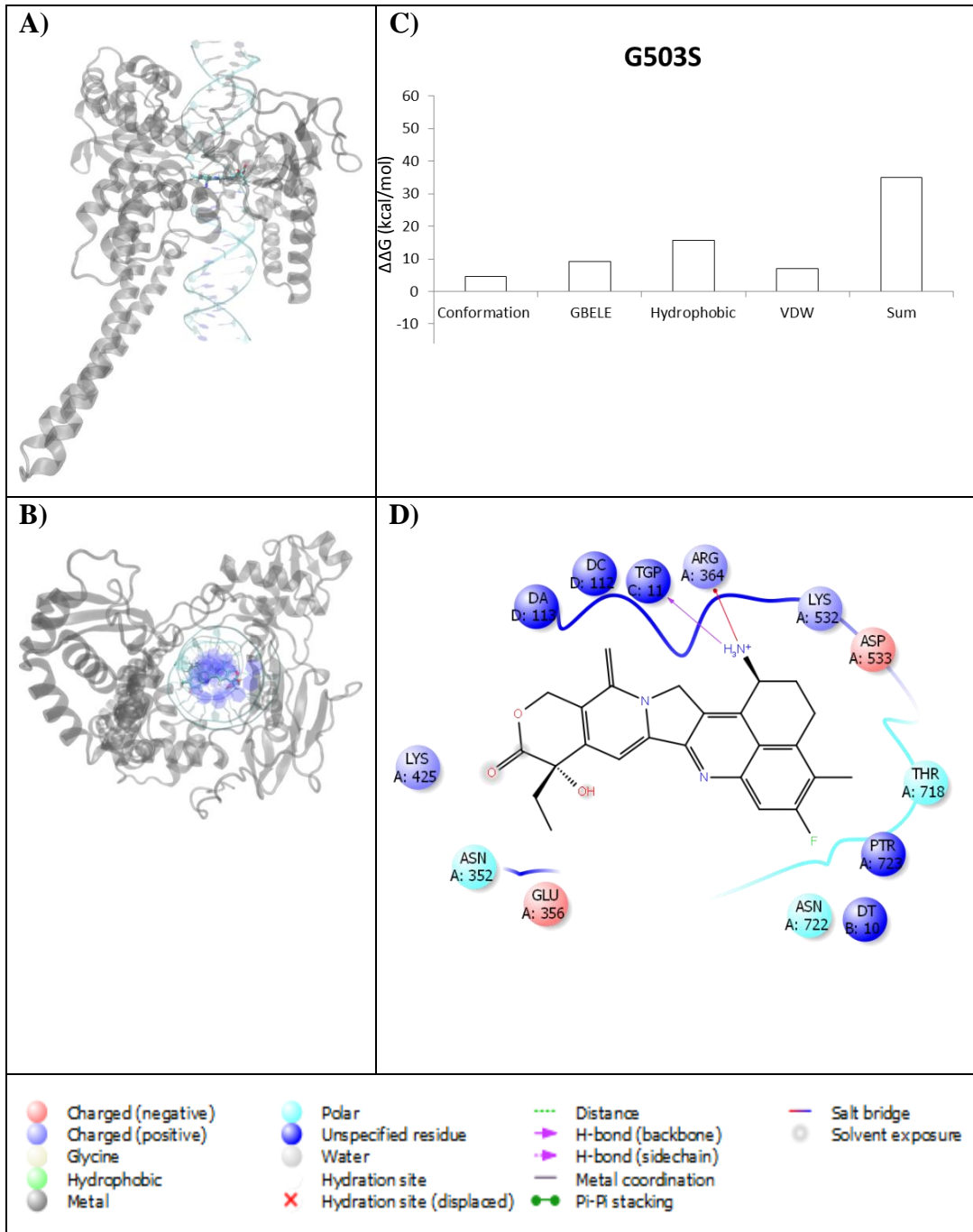




Figure S50. Exatecan Bound to Complex R364H. **A)** 3D top view of complex **B)** 3D side view of complex **C)** Decomposition of  $\Delta\Delta G$  **D)** 2D Representation of the binding within the complex

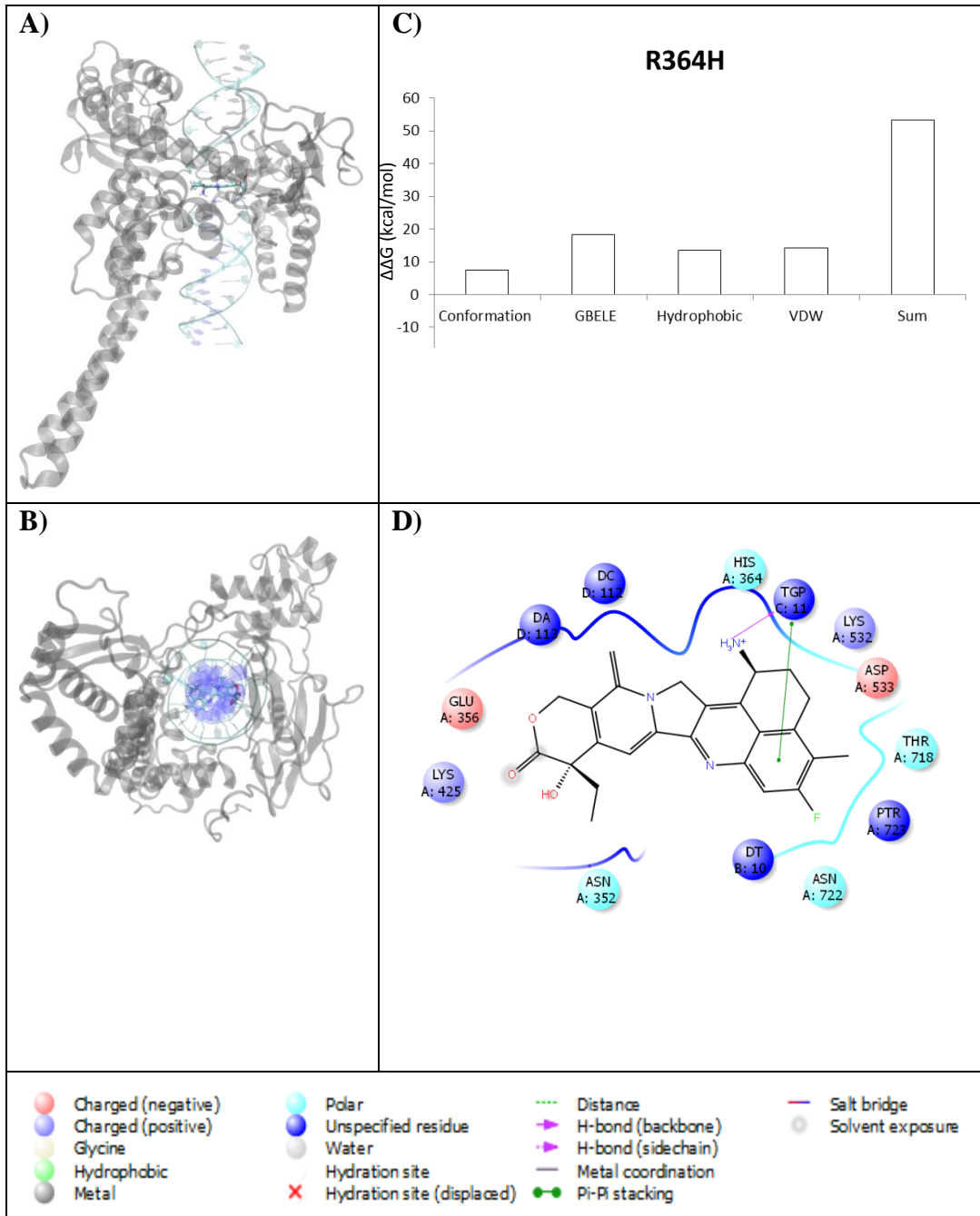


Figure S51. Exatecan Bound to Complex F361S. **A)** 3D top view of complex **B)** 3D side view of complex **C)** Decomposition of  $\Delta\Delta G$  **D)** 2D Representation of the binding within the complex

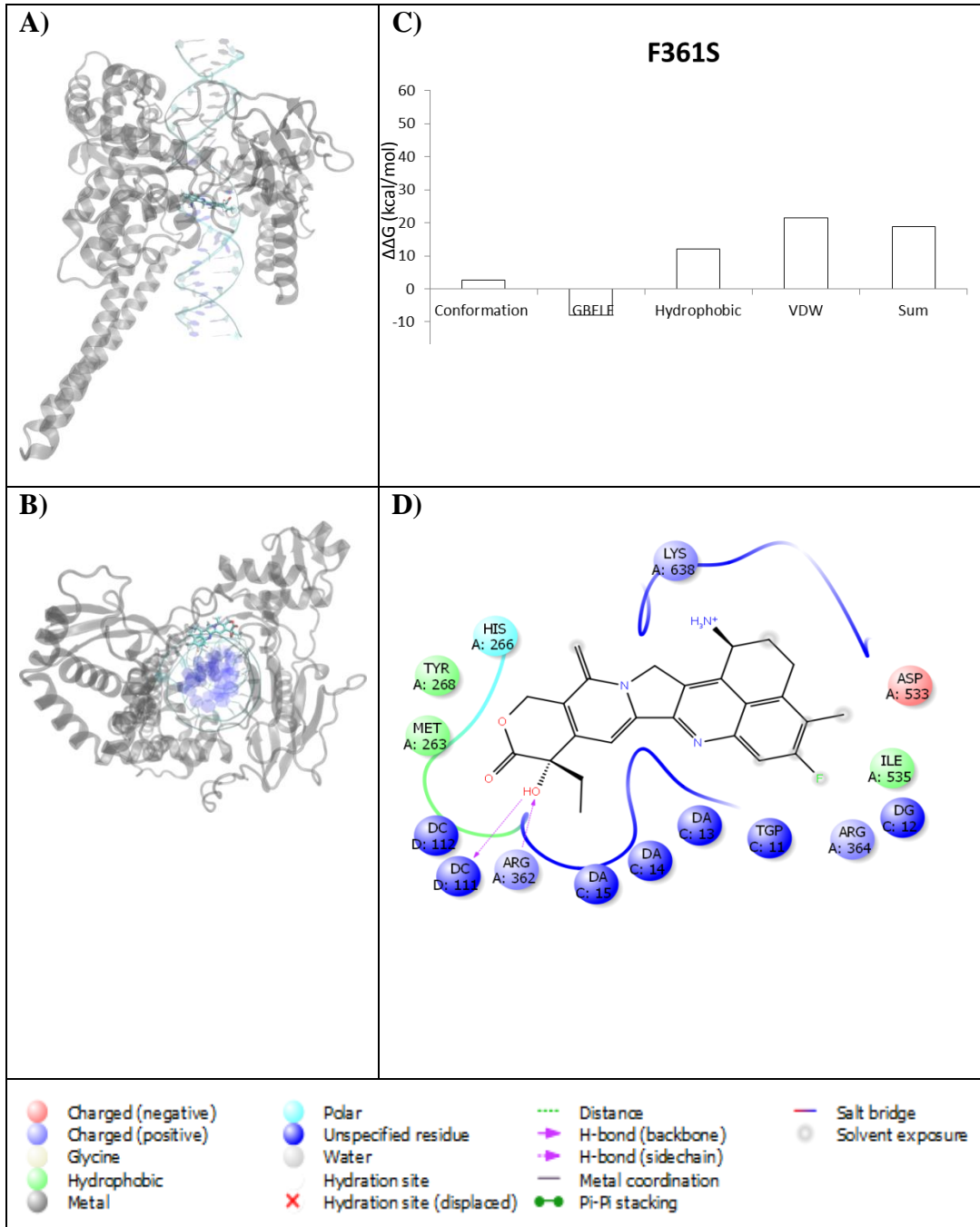


Figure S52. Exatecan Bound to Complex G363C. **A)** 3D top view of complex **B)** 3D side view of complex **C)** Decomposition of  $\Delta\Delta G$  **D)** 2D Representation of the binding within the complex

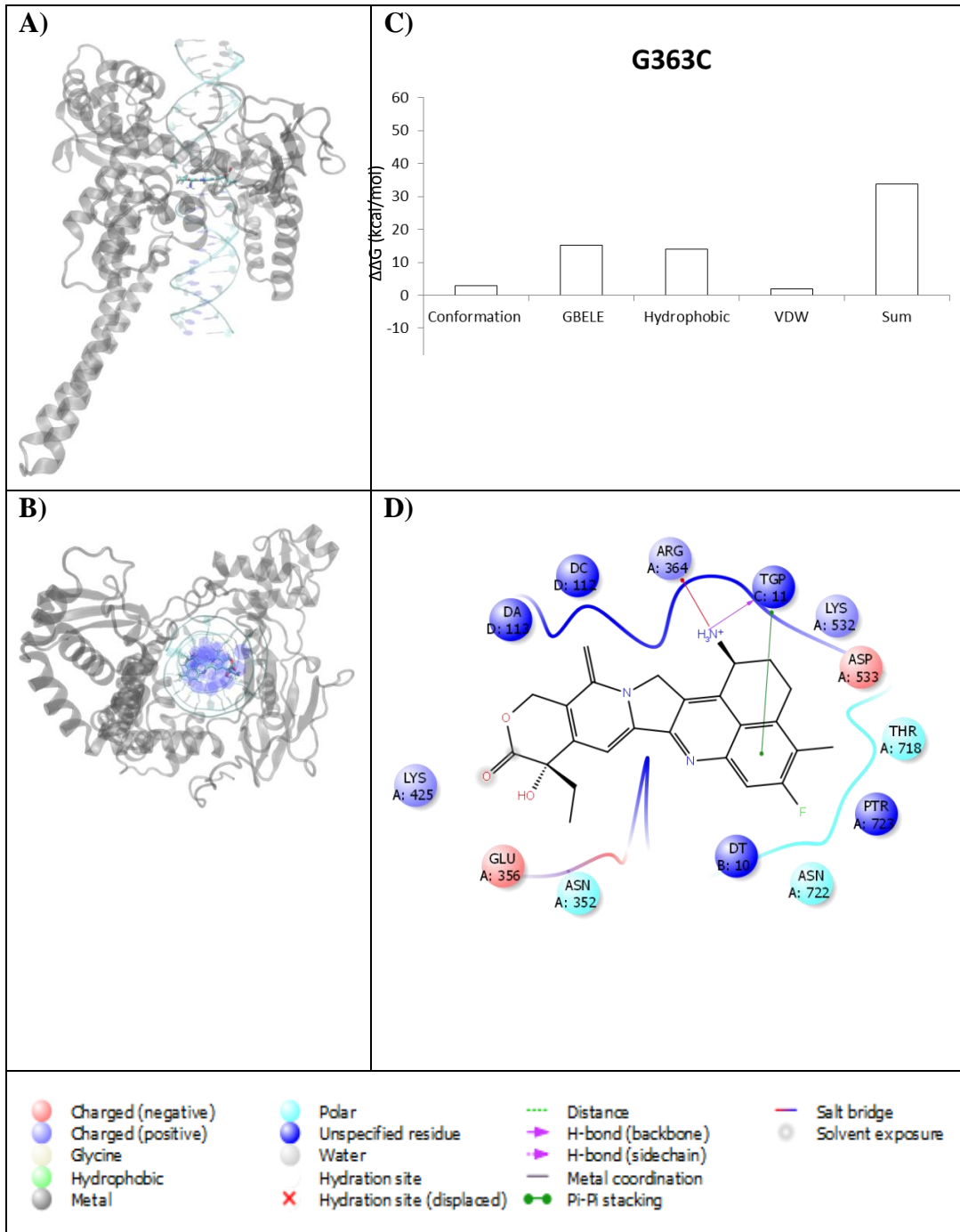


Figure S53. Exatecan Bound to Complex T279A. **A)** 3D top view of complex **B)** 3D side view of complex **C)** Decomposition of  $\Delta\Delta G$  **D)** 2D Representation of the binding within the complex

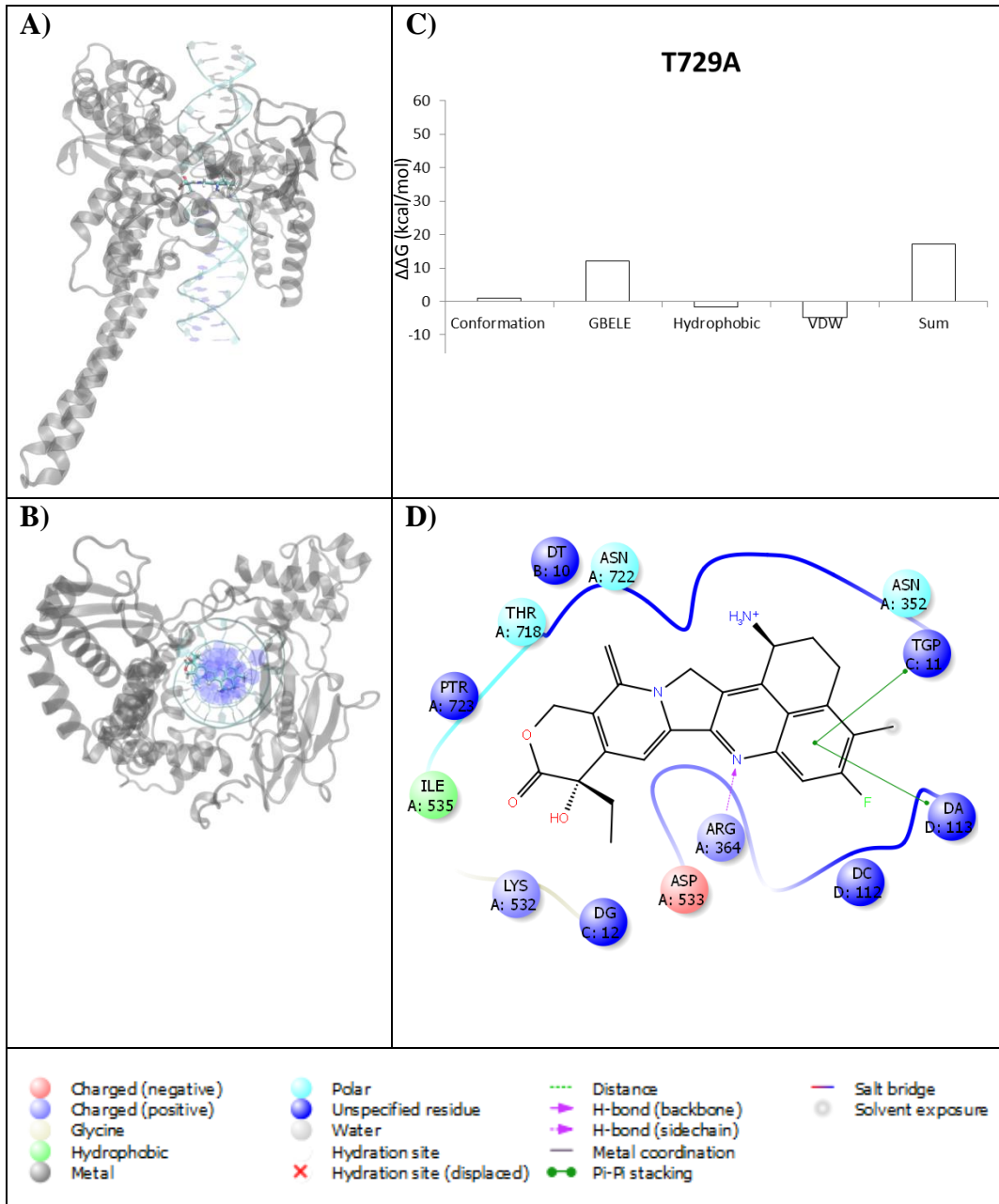


Figure S54. Gimatecan Bound to Complex N722A. **A)** 3D top view of complex **B)** 3D side view of complex **C)** Decomposition of  $\Delta\Delta G$  **D)** 2D Representation of the binding within the complex

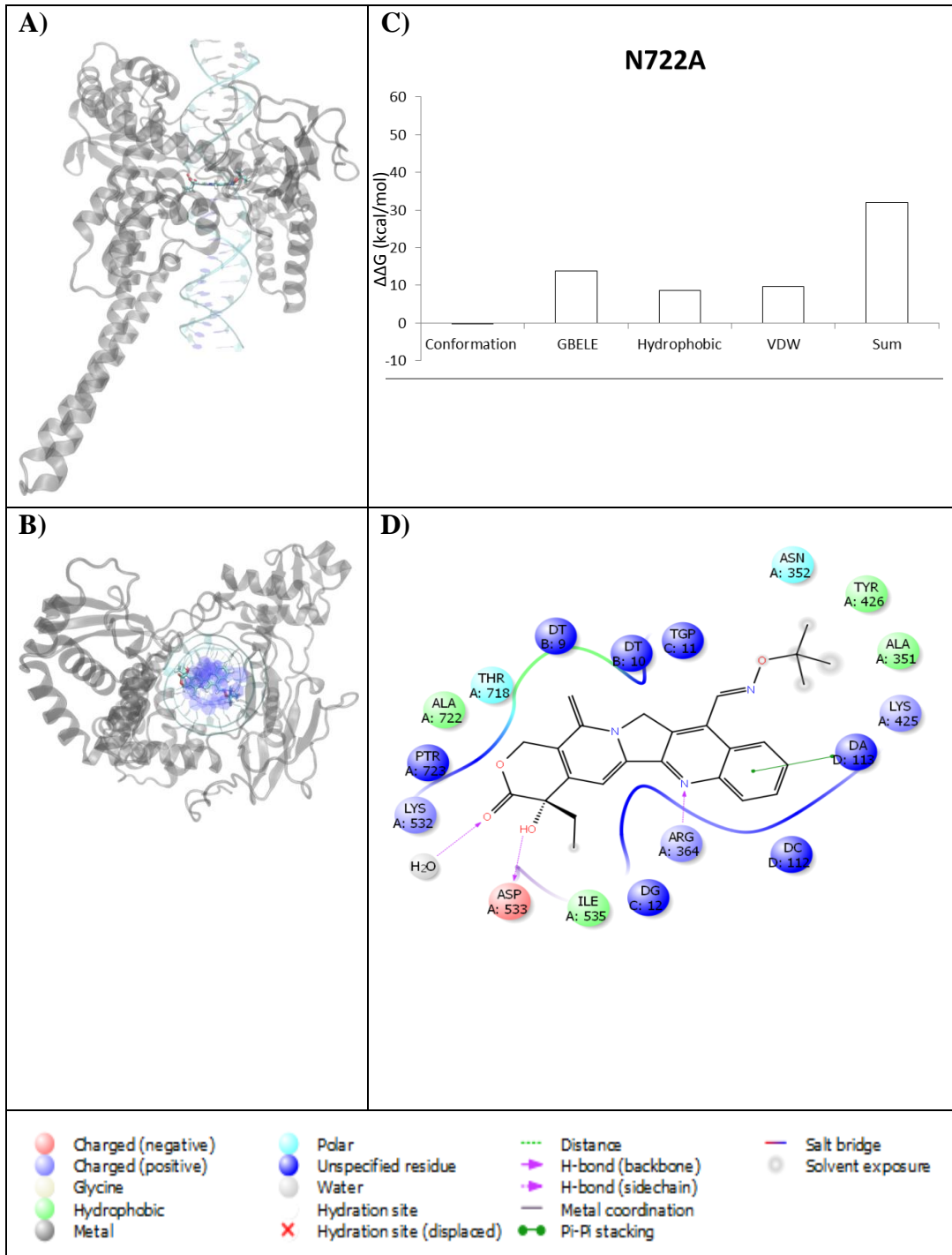


Figure S55. Gimatecan Bound to Complex N722S. **A)** 3D top view of complex **B)** 3D side view of complex **C)** Decomposition of  $\Delta\Delta G$  **D)** 2D Representation of the binding within the complex

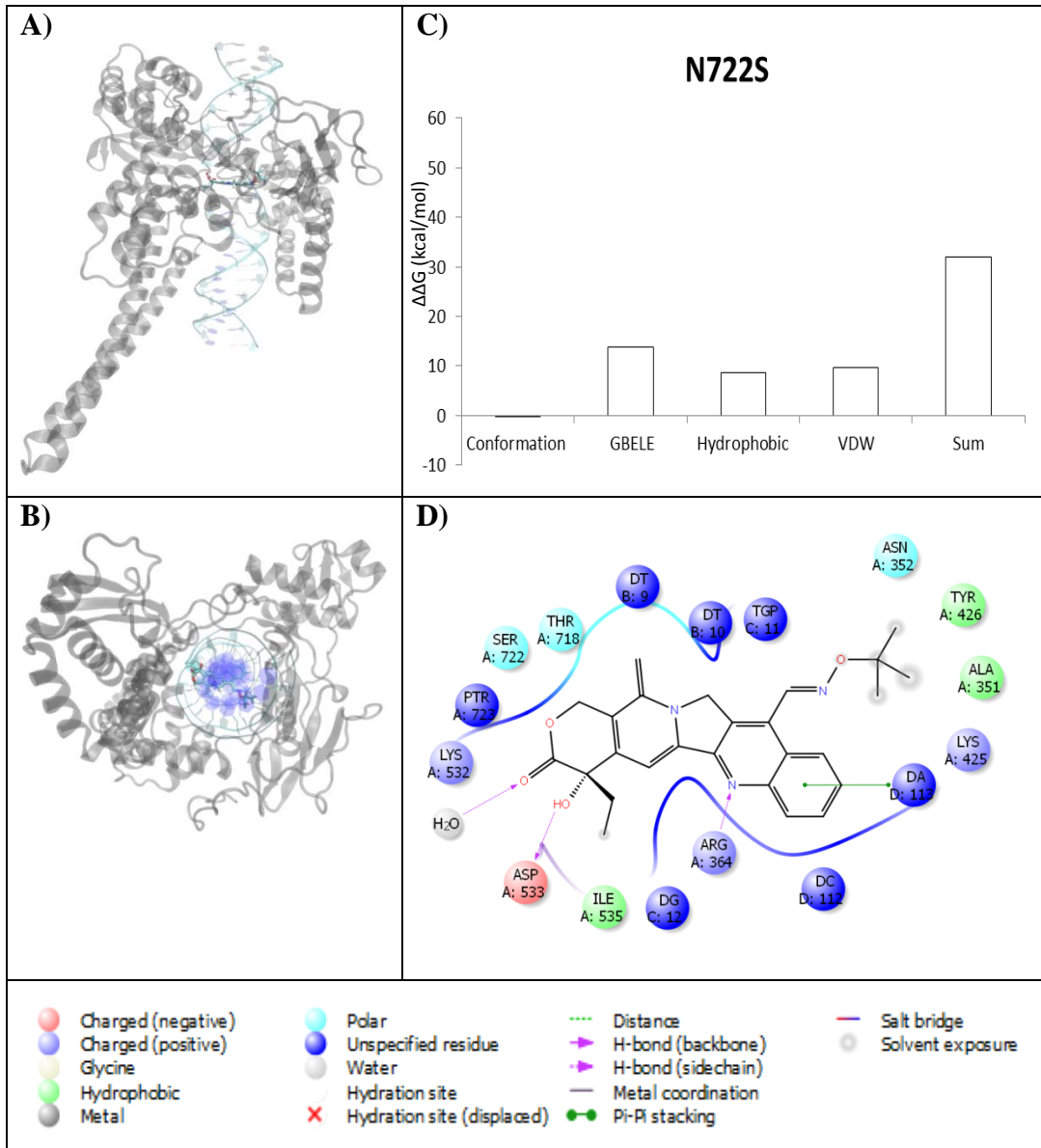


Figure S56. Gimatecan Bound to Complex G717V. **A)** 3D top view of complex **B)** 3D side view of complex **C)** Decomposition of  $\Delta\Delta G$  **D)** 2D Representation of the binding within the complex

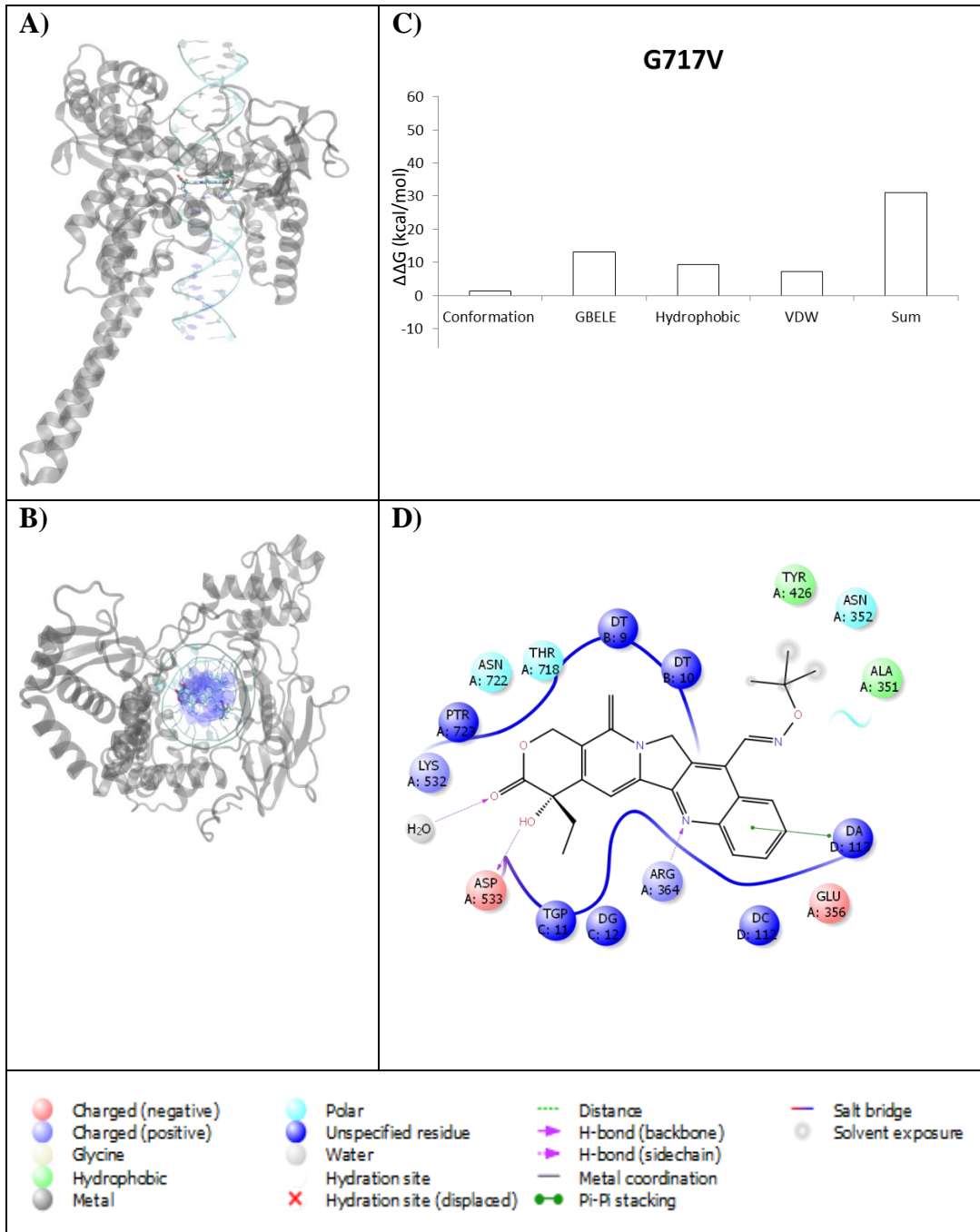




Figure S57. Gimatecan Bound to Complex D533G. **A)** 3D top view of complex **B)** 3D side view of complex **C)** Decomposition of  $\Delta\Delta G$  **D)** 2D Representation of the binding within the complex

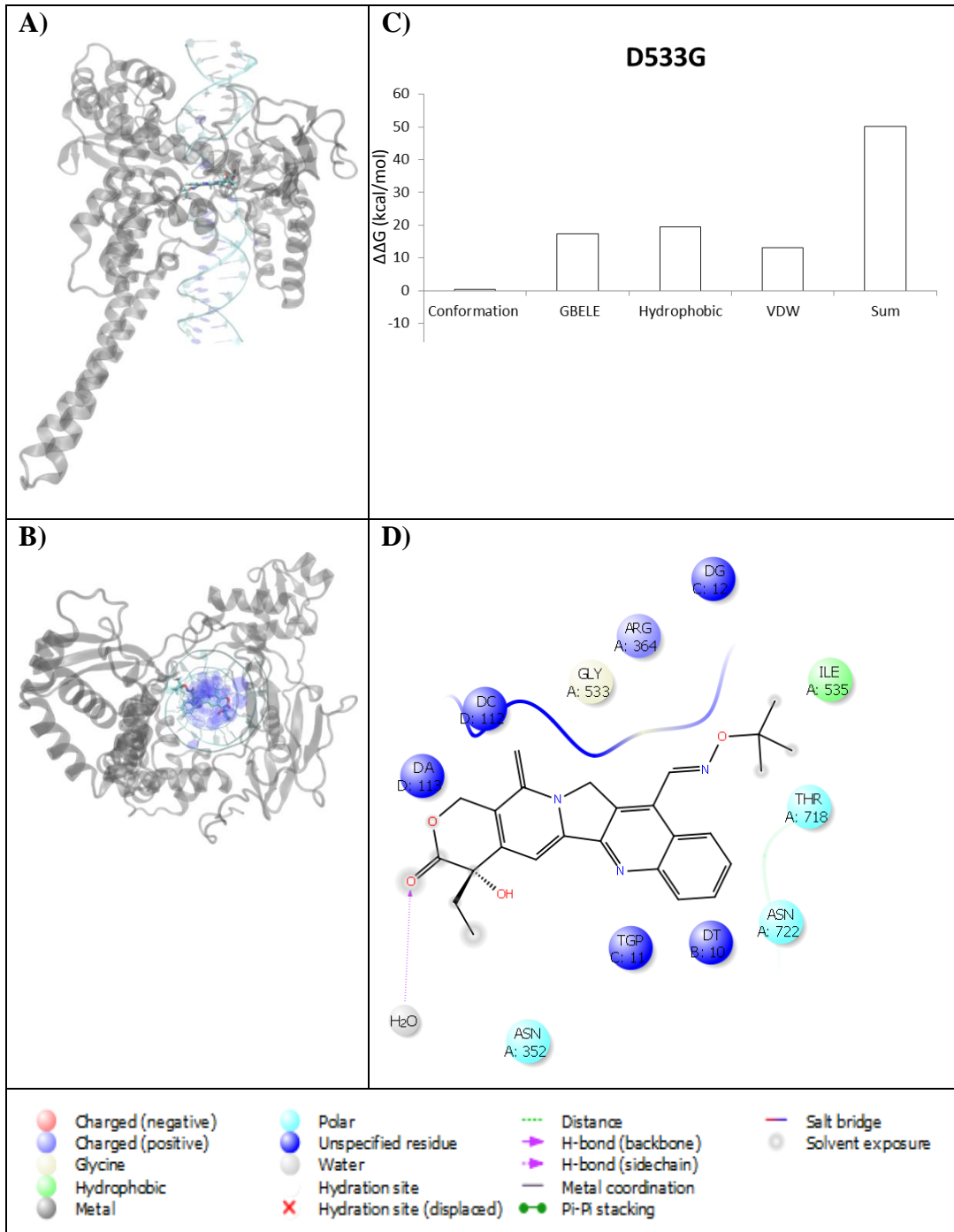




Figure S58. Gimatecan Bound to Complex D533N. **A)** 3D top view of complex **B)** 3D side view of complex **C)** Decomposition of  $\Delta\Delta G$  **D)** 2D Representation of the binding within the complex

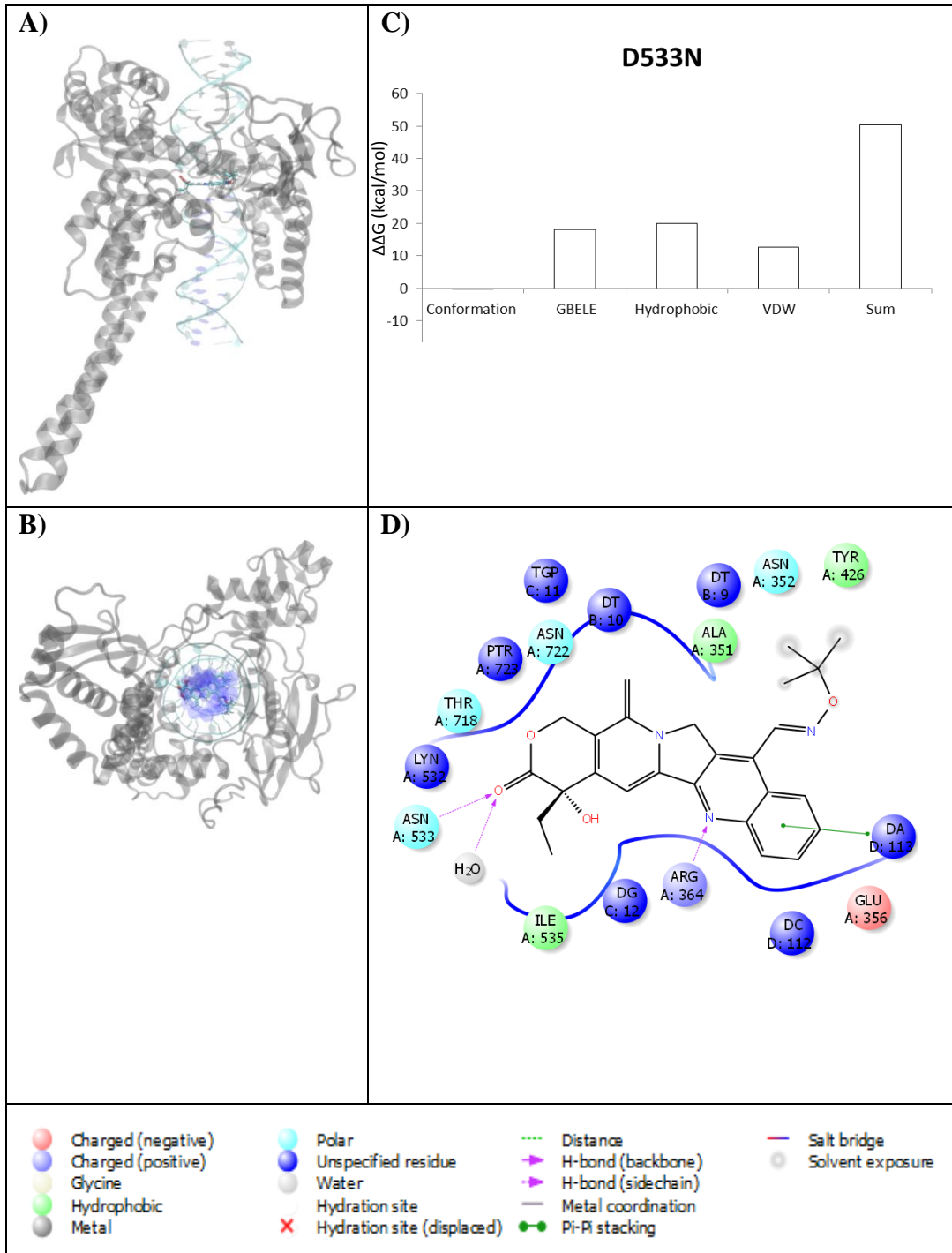


Figure S59. Gimatecan Bound to Complex G503S. **A)** 3D top view of complex **B)** 3D side view of complex **C)** Decomposition of  $\Delta\Delta G$  **D)** 2D Representation of the binding within the complex

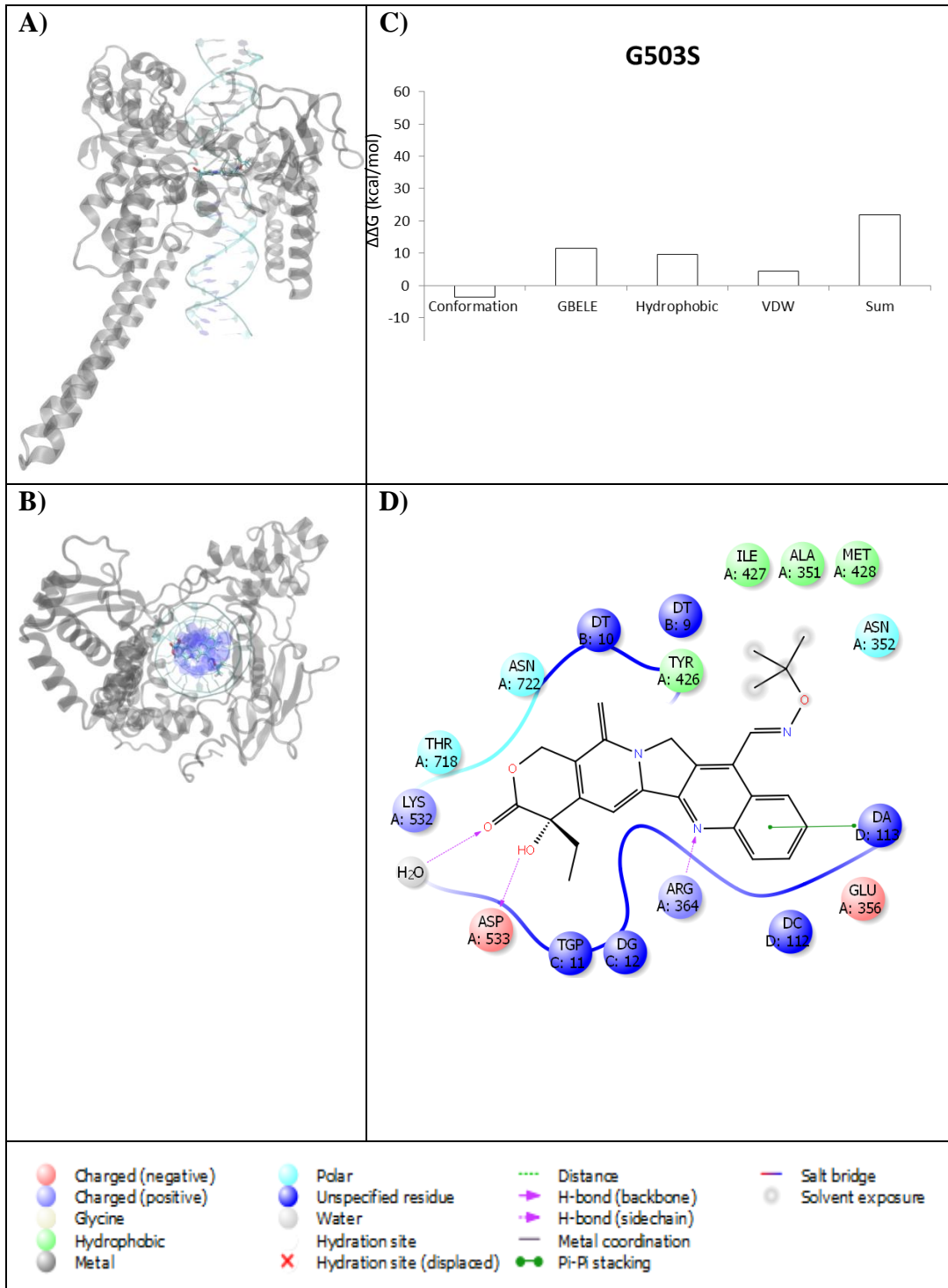


Figure S60. Gimatecan Bound to Complex R364H. **A)** 3D top view of complex **B)** 3D side view of complex **C)** Decomposition of  $\Delta\Delta G$  **D)** 2D Representation of the binding within the complex

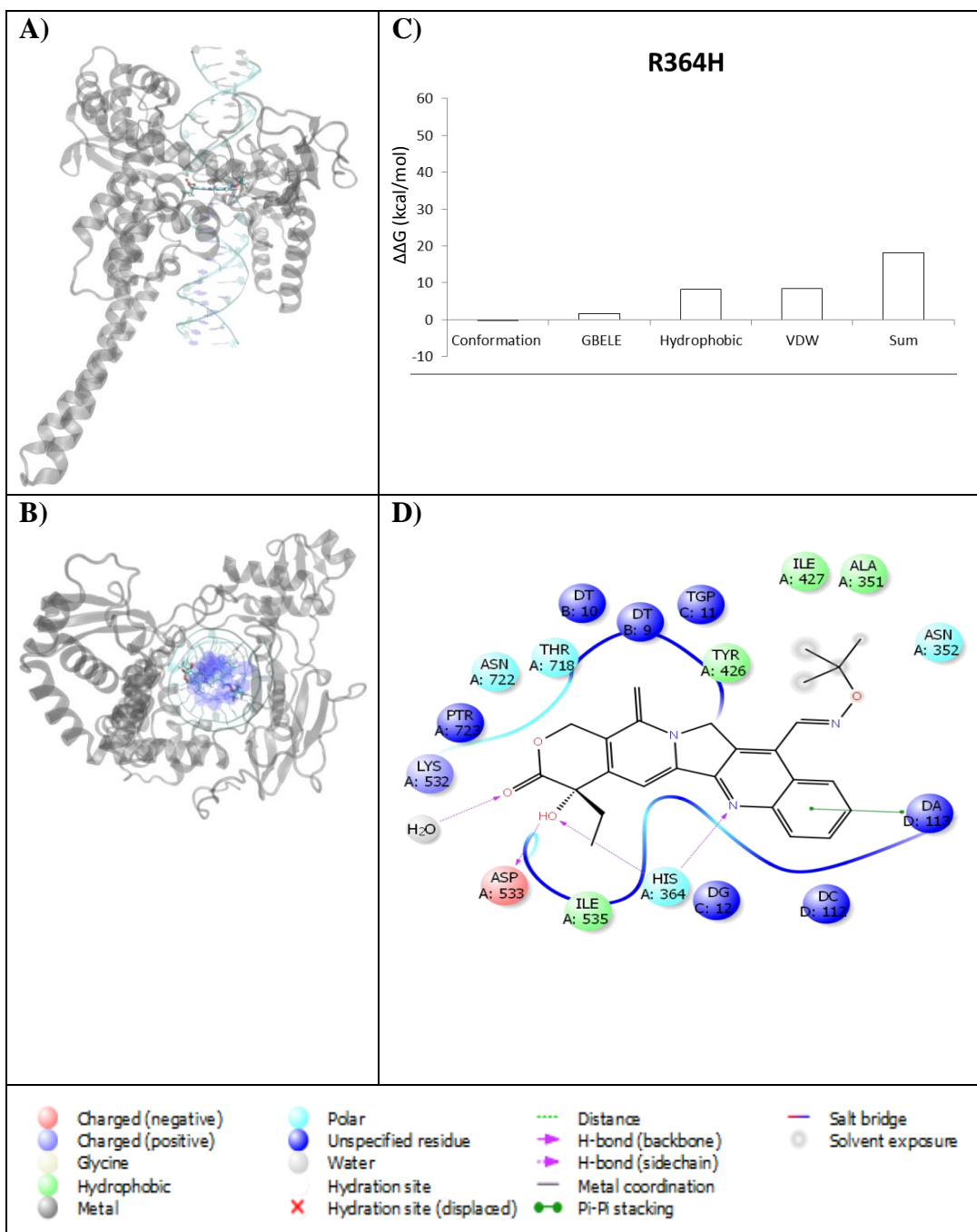


Figure S61. Gimatecan Bound to Complex F361S. **A)** 3D top view of complex **B)** 3D side view of complex **C)** Decomposition of  $\Delta\Delta G$  **D)** 2D Representation of the binding within the complex

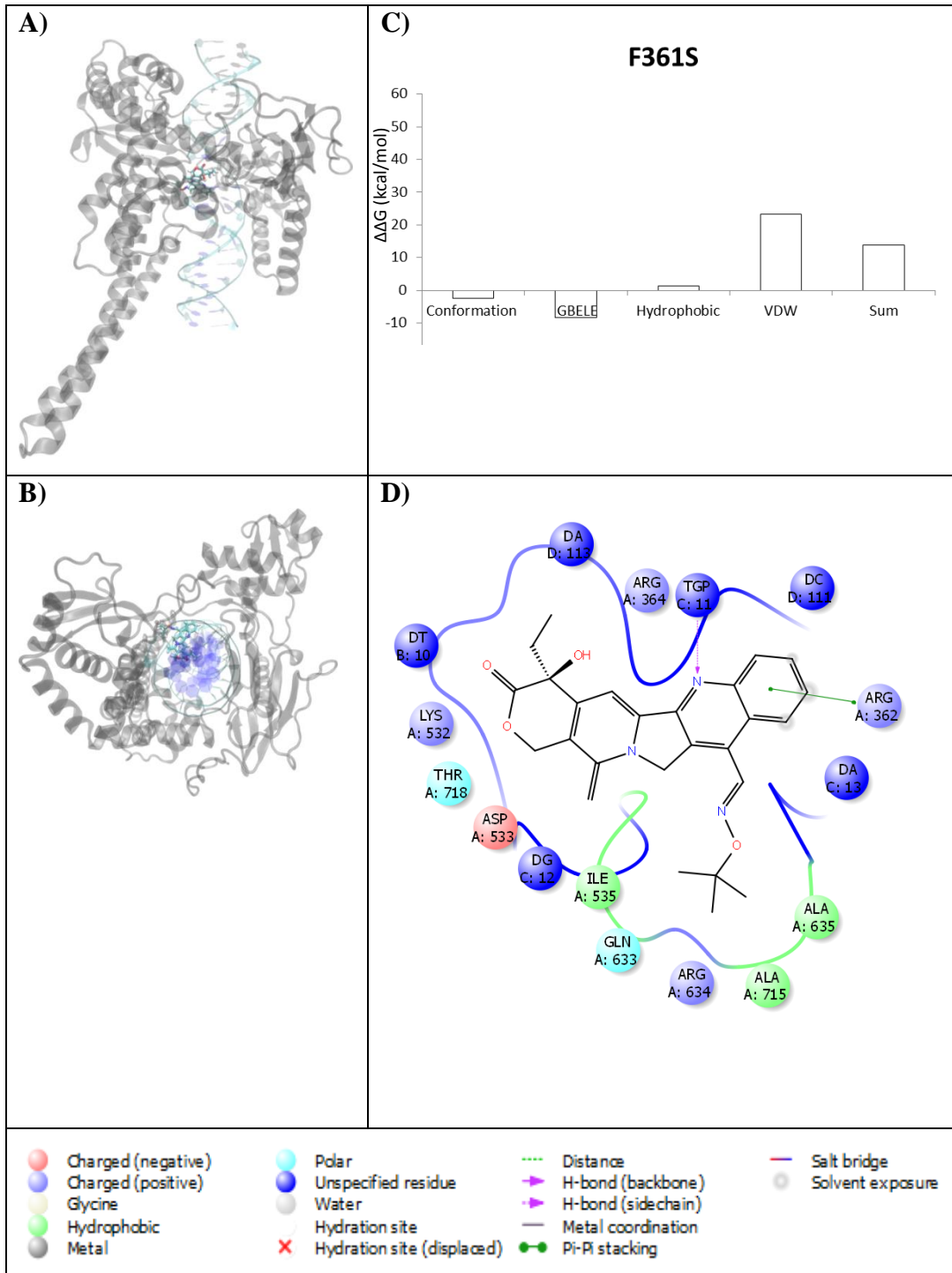


Figure S62. Gimatecan Bound to Complex G363C. **A)** 3D top view of complex **B)** 3D side view of complex **C)** Decomposition of  $\Delta\Delta G$  **D)** 2D Representation of the binding within the complex

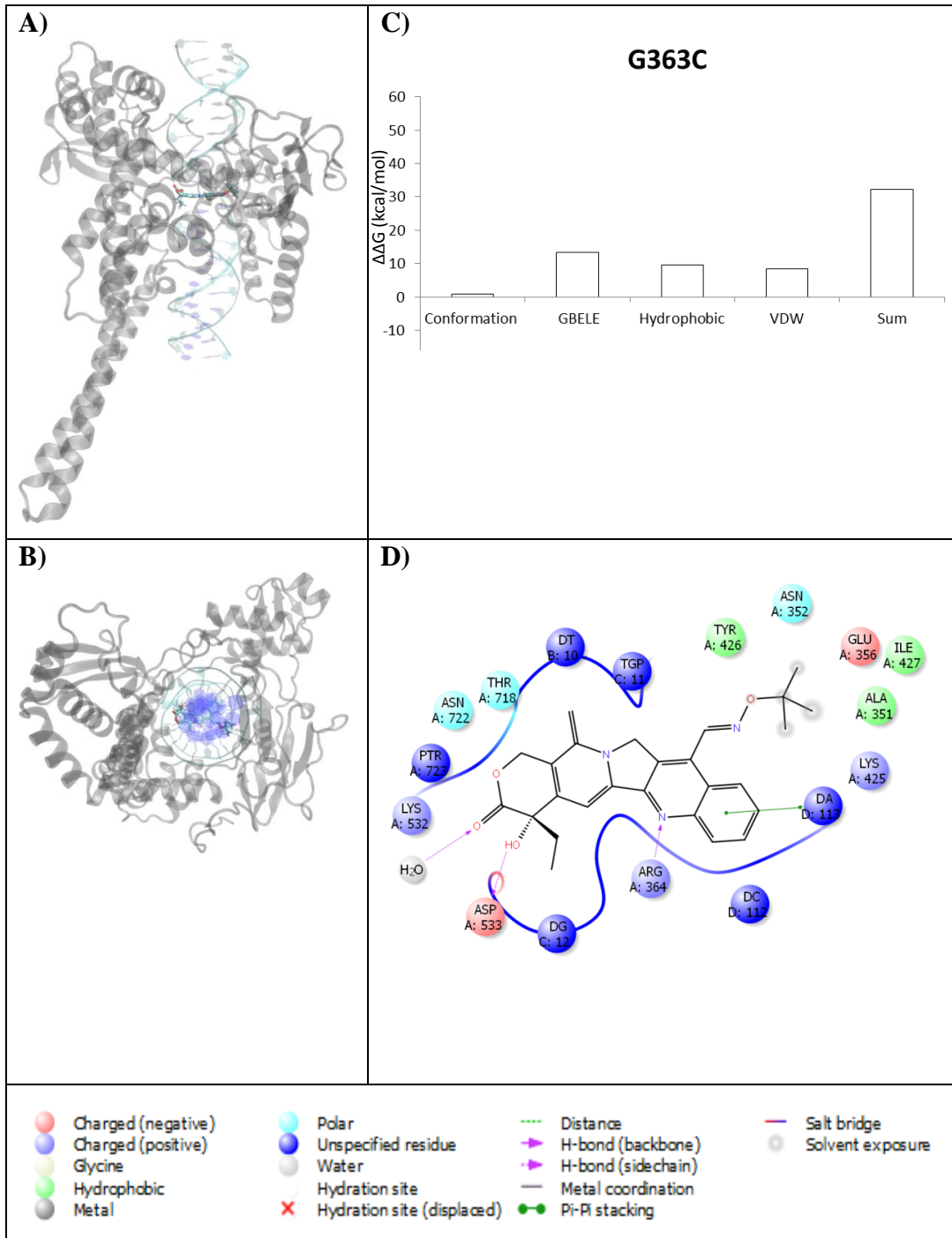


Figure S63. Gimatecan Bound to Complex T729A. **A)** 3D top view of complex **B)** 3D side view of complex **C)** Decomposition of  $\Delta\Delta G$  **D)** 2D Representation of the binding within the complex

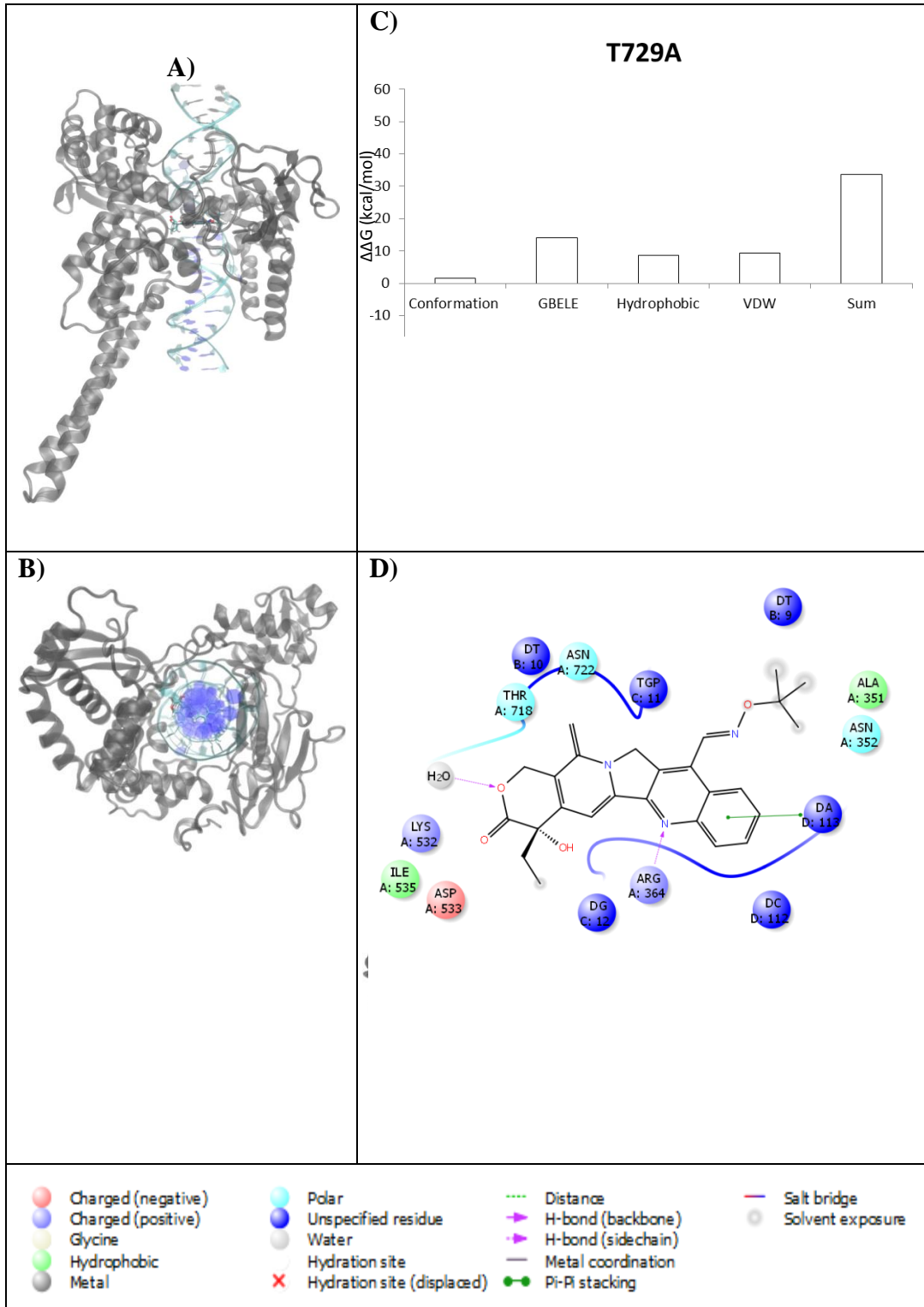


Figure S64. Belotecan Bound to Complex N722A. **A)** 3D top view of complex **B)** 3D side view of complex **C)** Decomposition of  $\Delta\Delta G$  **D)** 2D Representation of the binding within the complex

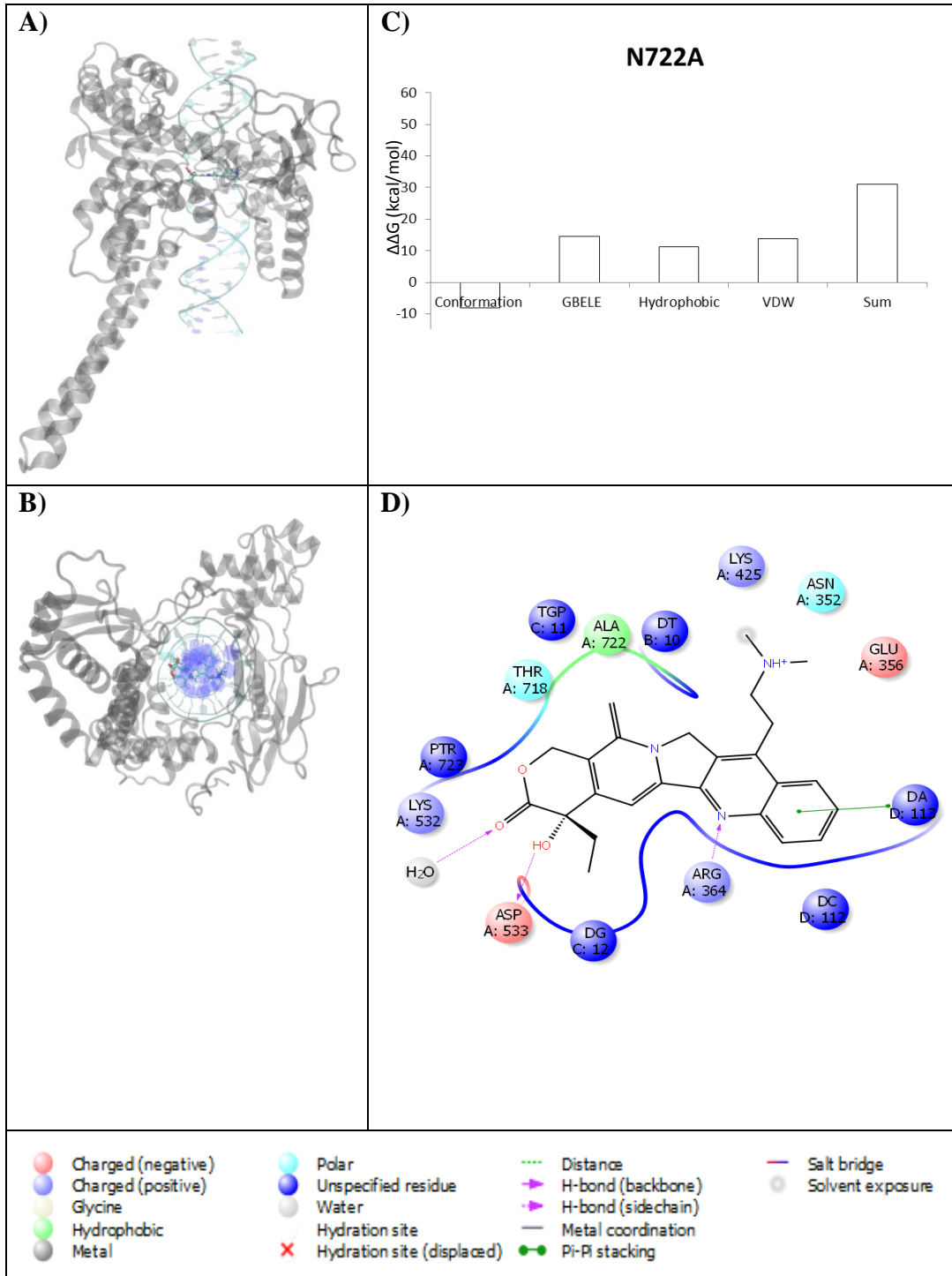




Figure S65. Belotecan Bound to Complex N722S. **A)** 3D top view of complex **B)** 3D side view of complex **C)** Decomposition of  $\Delta\Delta G$  **D)** 2D Representation of the binding within the complex

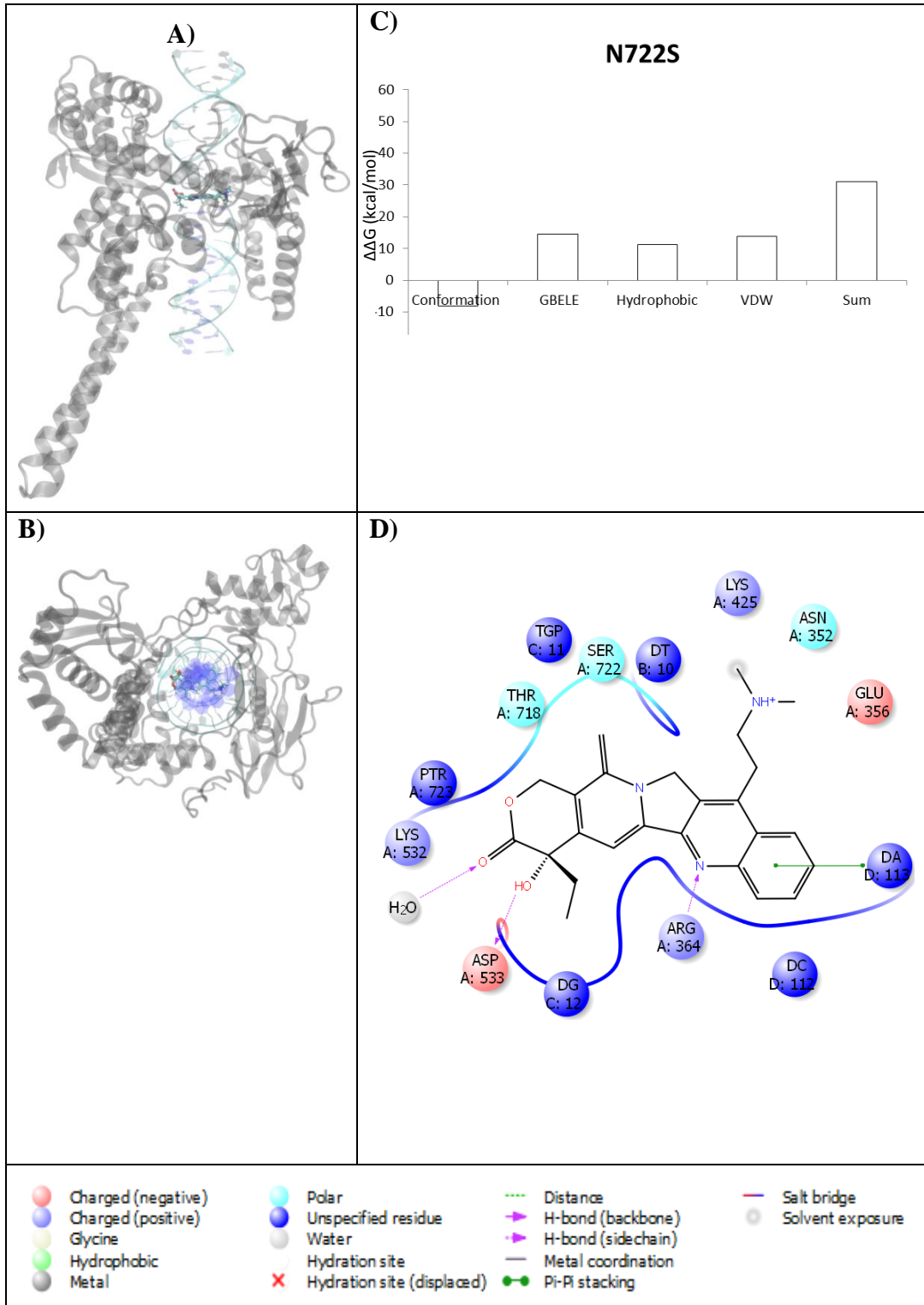




Figure S66. Belotecan Bound to Complex G717V. **A)** 3D top view of complex **B)** 3D side view of complex **C)** Decomposition of  $\Delta\Delta G$  **D)** 2D Representation of the binding within the complex

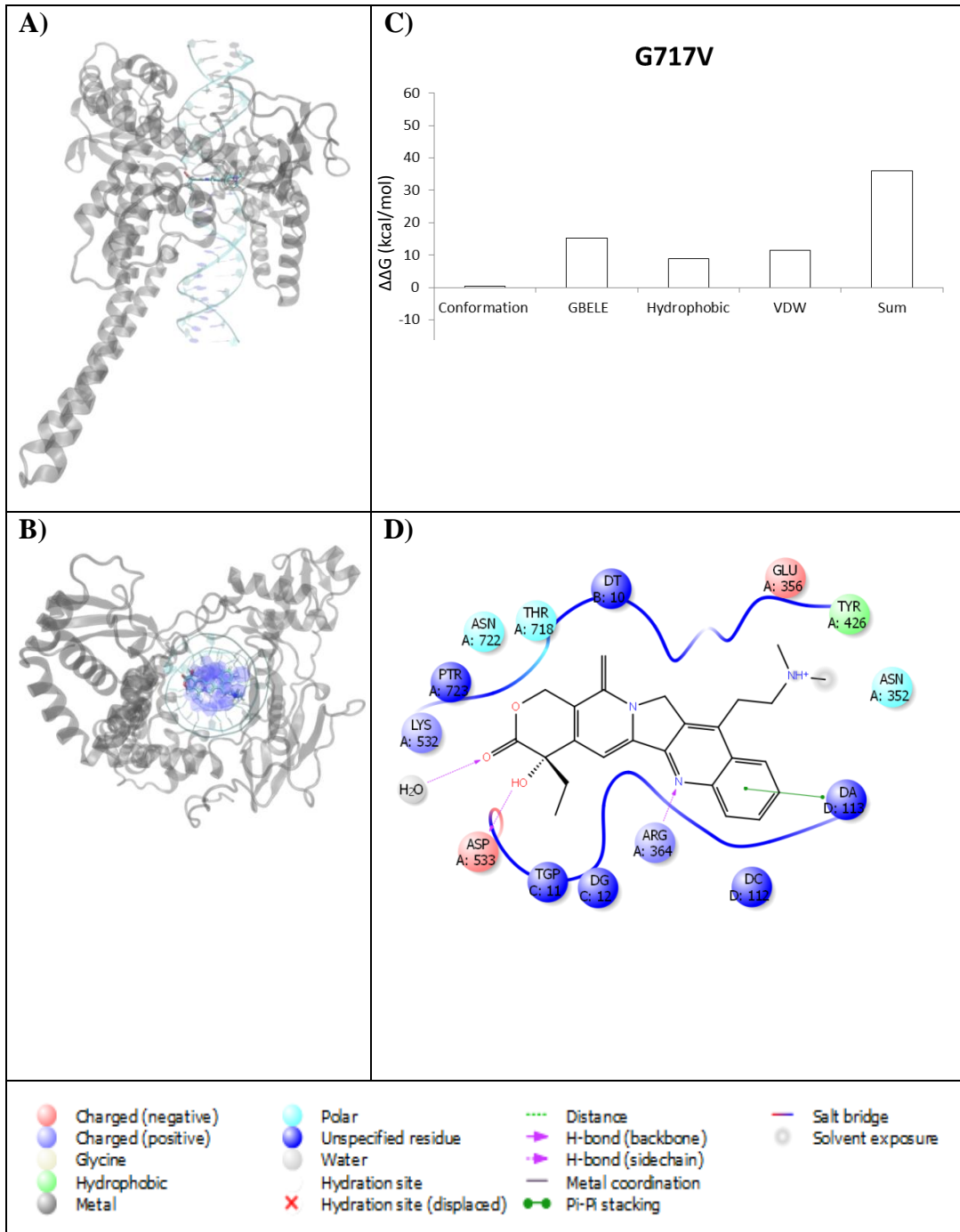


Figure S67. Belotecan Bound to Complex D533G. **A)** 3D top view of complex **B)** 3D side view of complex **C)** Decomposition of  $\Delta\Delta G$  **D)** 2D Representation of the binding within the complex

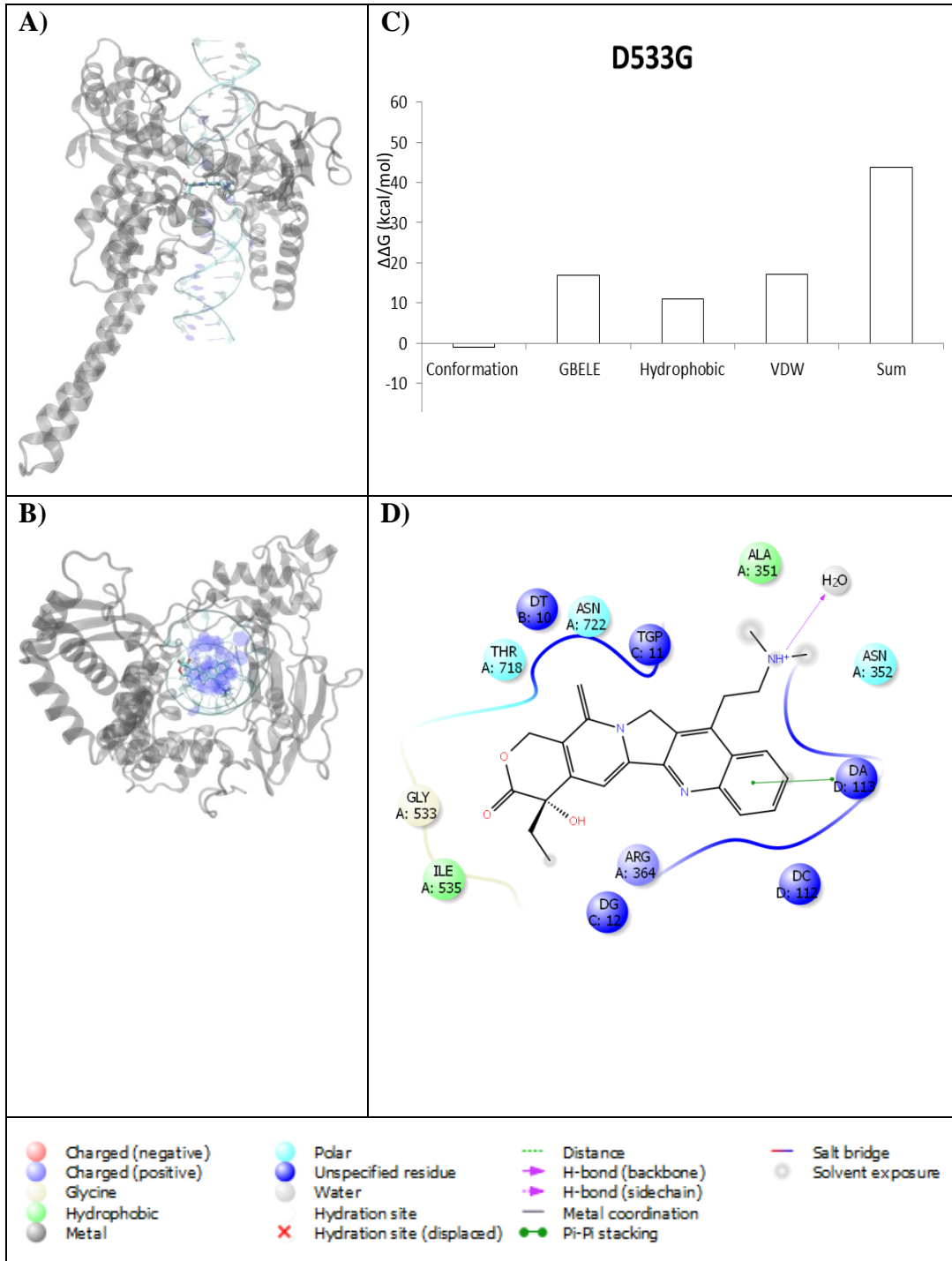


Figure S68. Belotecan Bound to Complex D533N. **A)** 3D top view of complex **B)** 3D side view of complex **C)** Decomposition of  $\Delta\Delta G$  **D)** 2D Representation of the binding within the complex

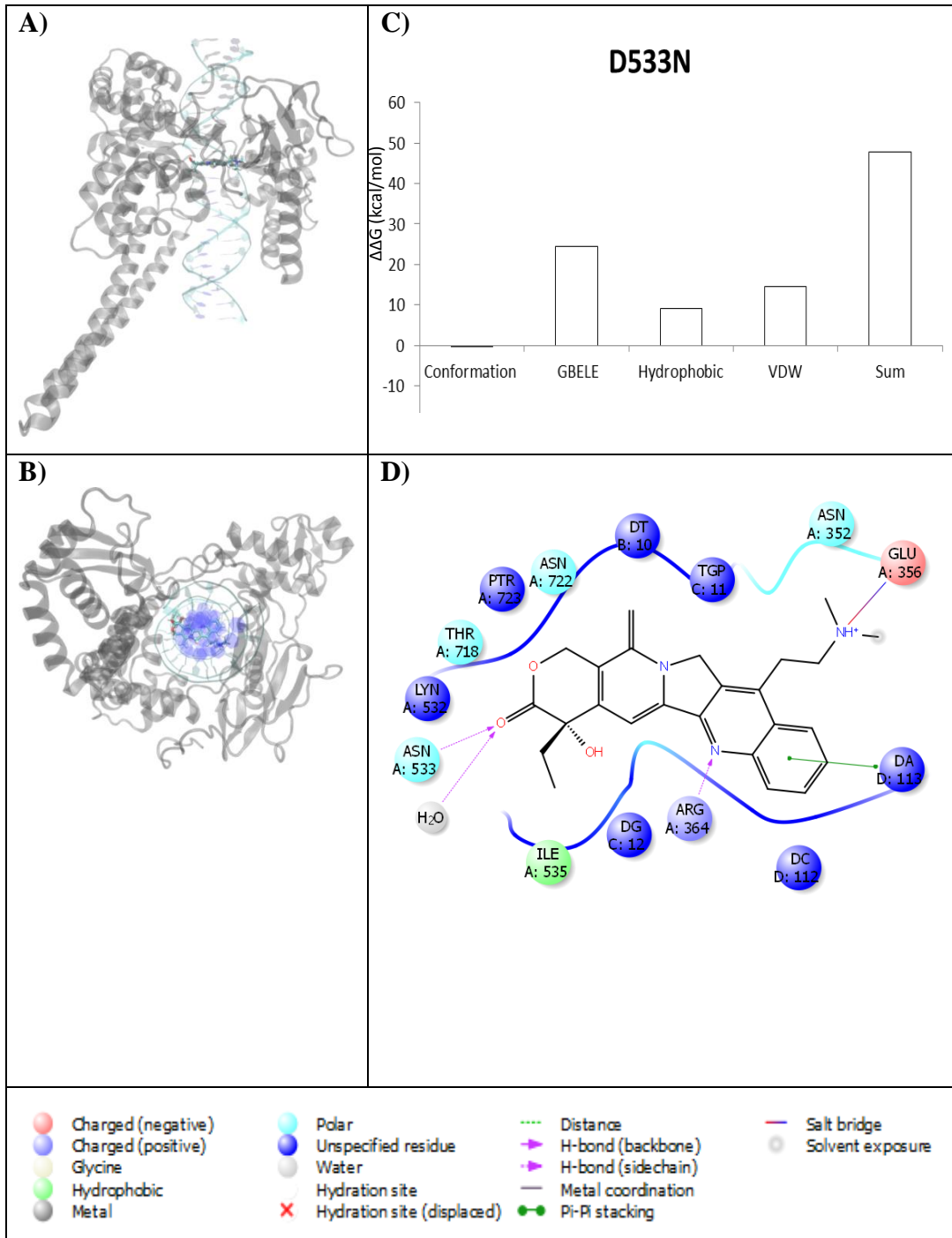


Figure S69. Belotecan Bound to Complex G503S. **A)** 3D top view of complex **B)** 3D side view of complex **C)** Decomposition of  $\Delta\Delta G$  **D)** 2D Representation of the binding within the complex

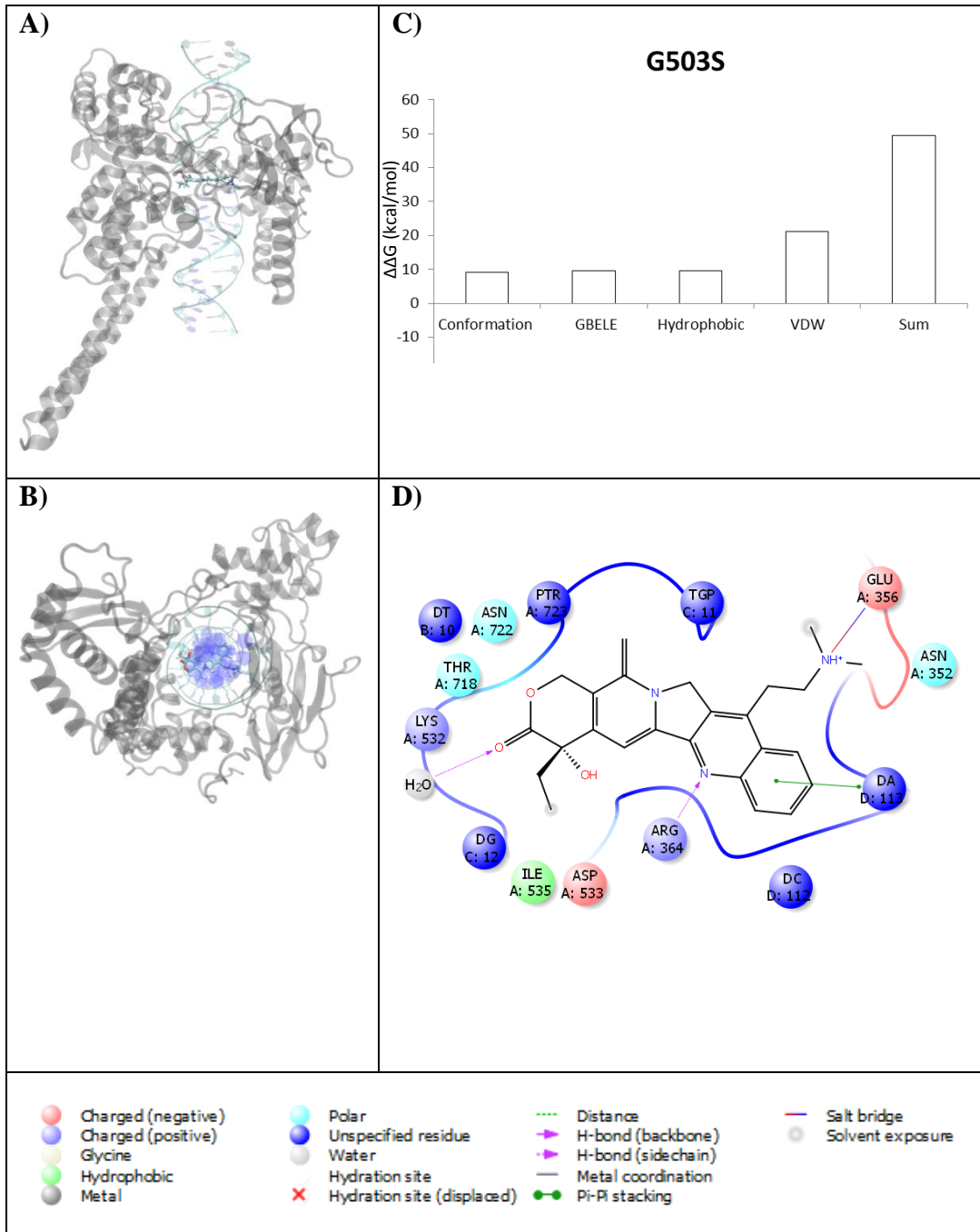


Figure S70. Belotecan Bound to Complex R364H. **A)** 3D top view of complex **B)** 3D side view of complex **C)** Decomposition of  $\Delta\Delta G$  **D)** 2D Representation of the binding within the complex

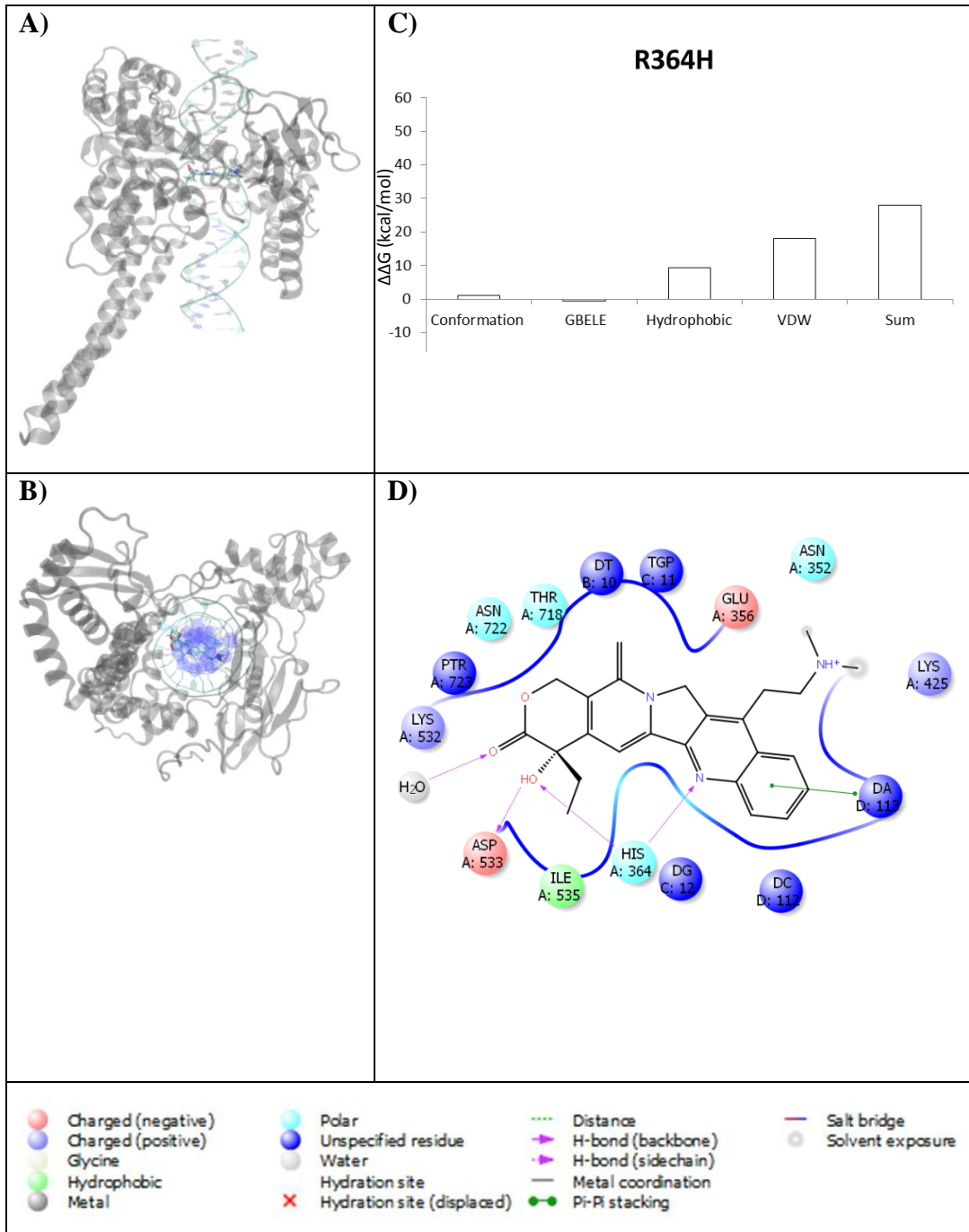


Figure S71. Belotecan Bound to Complex F361S. **A)** 3D top view of complex **B)** 3D side view of complex **C)** Decomposition of  $\Delta\Delta G$  **D)** 2D Representation of the binding within the complex

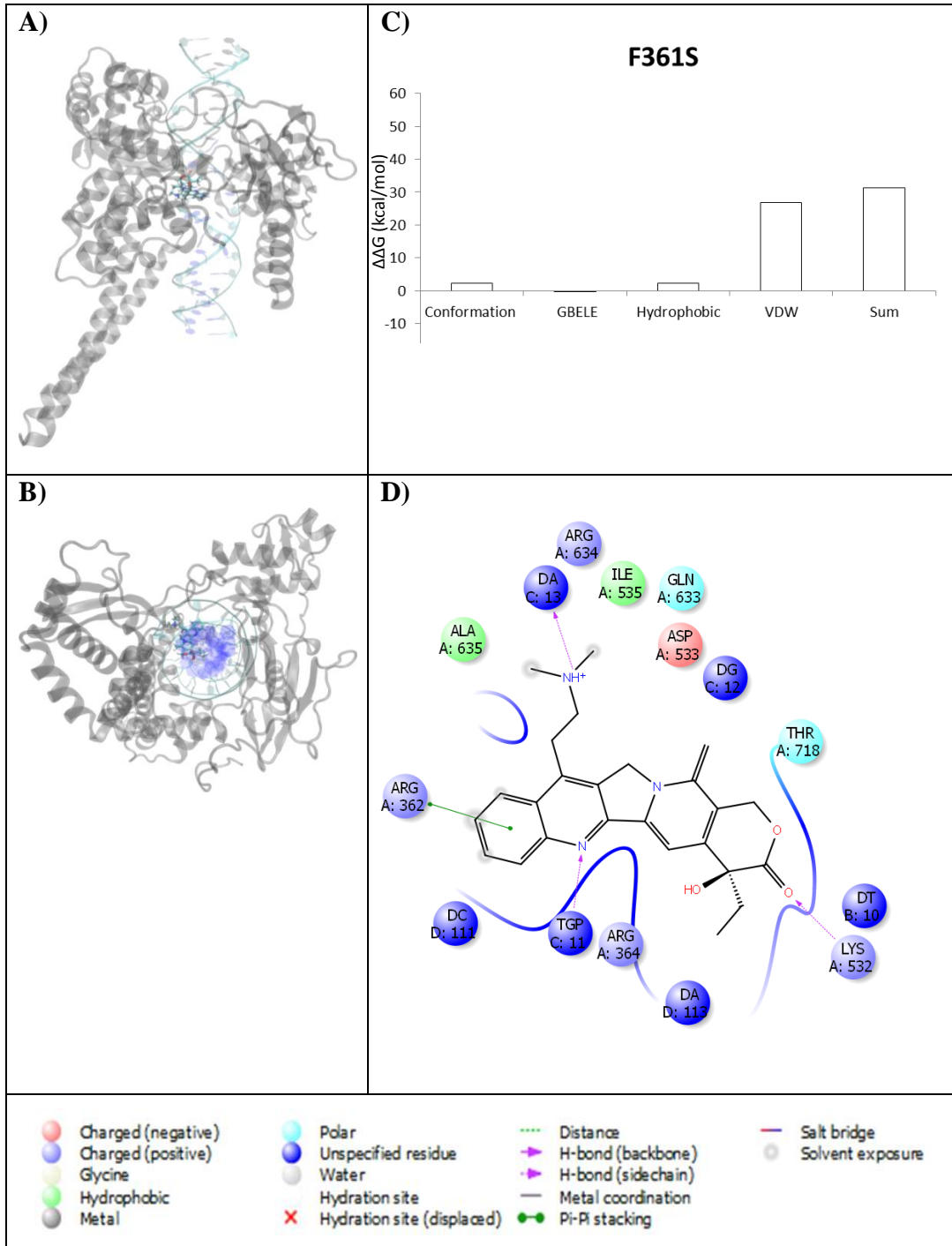


Figure S72. Belotecan Bound to Complex G363C. **A)** 3D top view of complex **B)** 3D side view of complex **C)** Decomposition of  $\Delta\Delta G$  **D)** 2D Representation of the binding within the complex

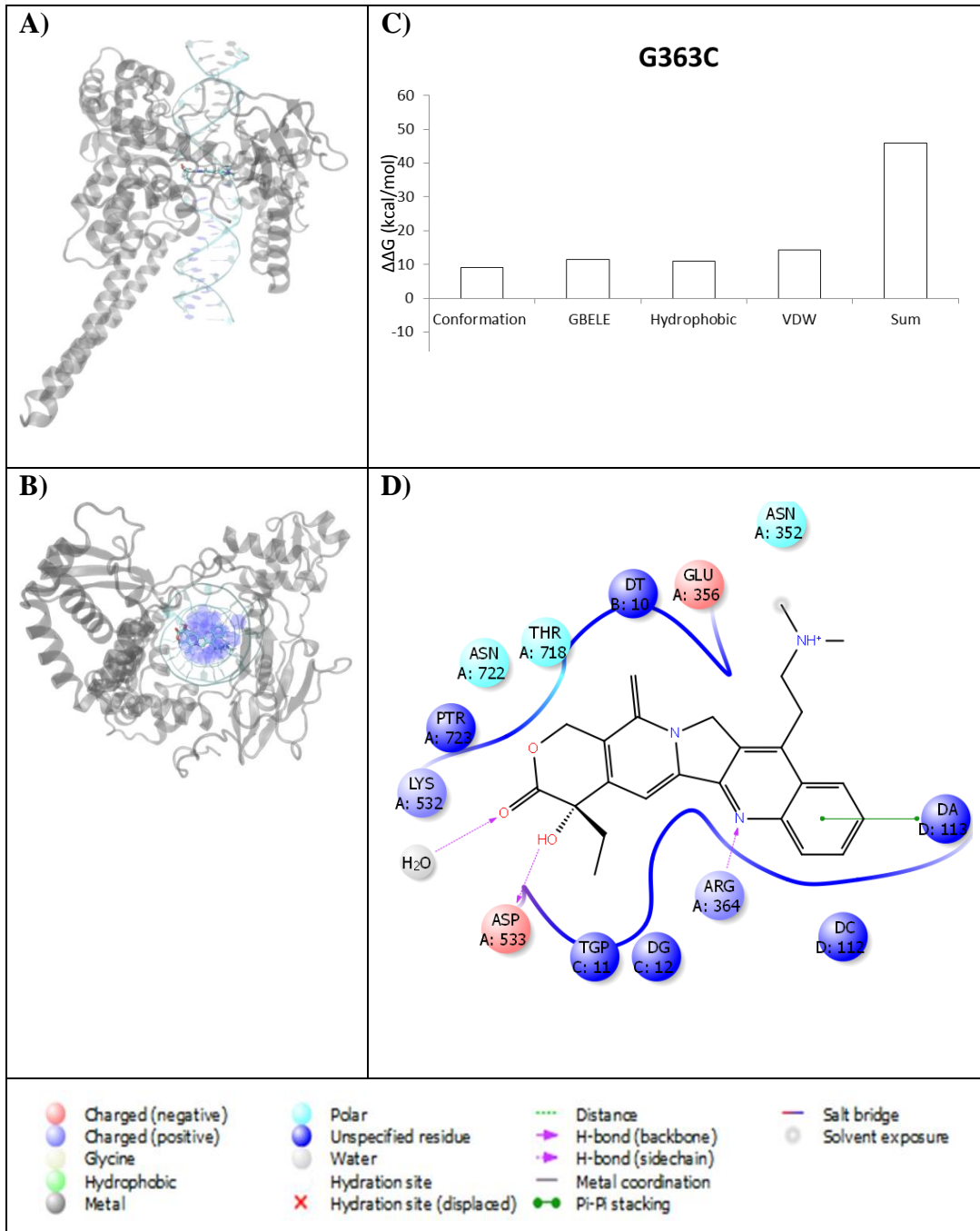




Figure S73. Belotecan Bound to Complex T729A. **A)** 3D top view of complex **B)** 3D side view of complex **C)** Decomposition of  $\Delta\Delta G$  **D)** 2D Representation of the binding within the complex

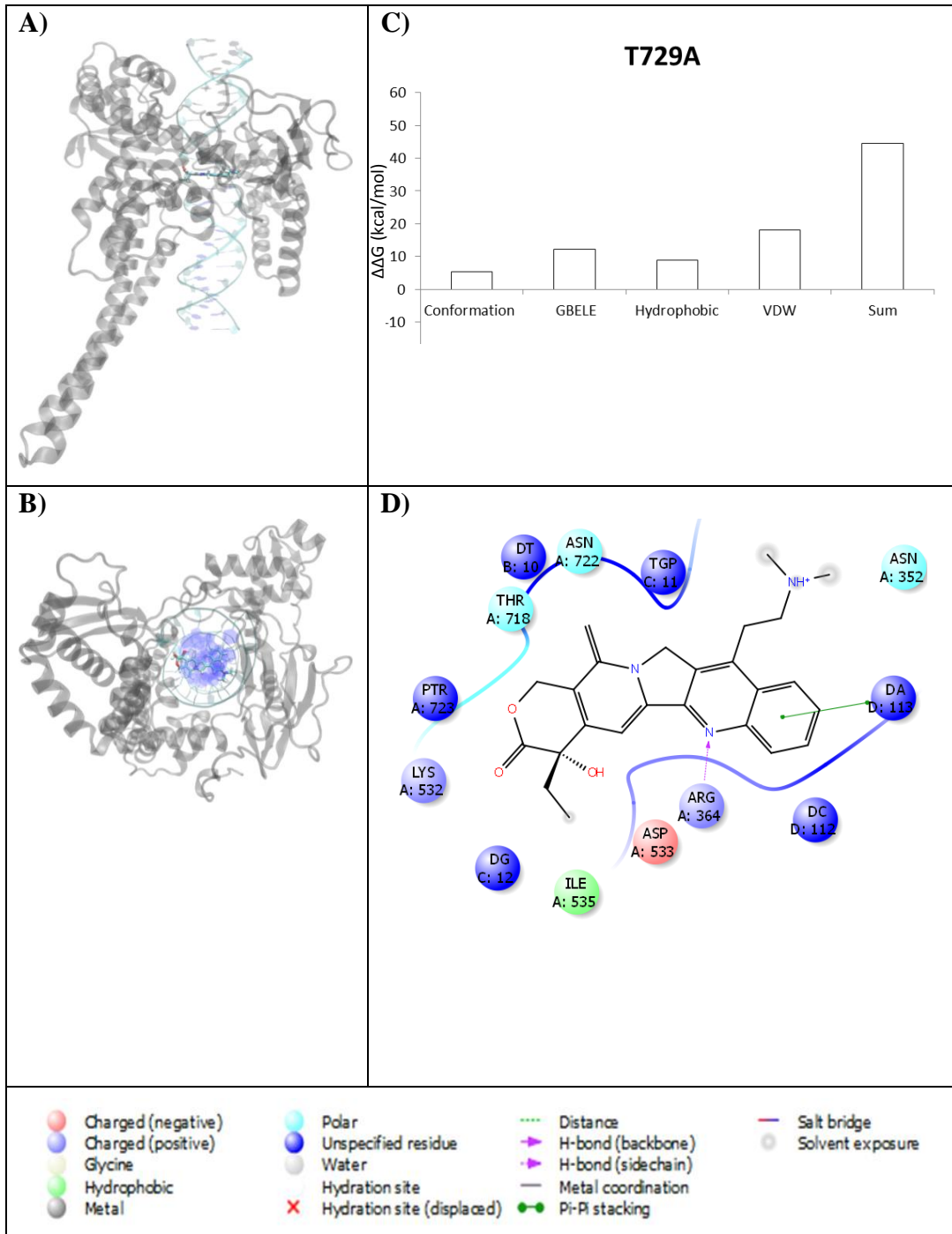




Figure S74. Lucahthone Bound to Complex N722A. **A)** 3D top view of complex **B)** 3D side view of complex **C)** Decomposition of  $\Delta\Delta G$  **D)** 2D Representation of the binding within the complex

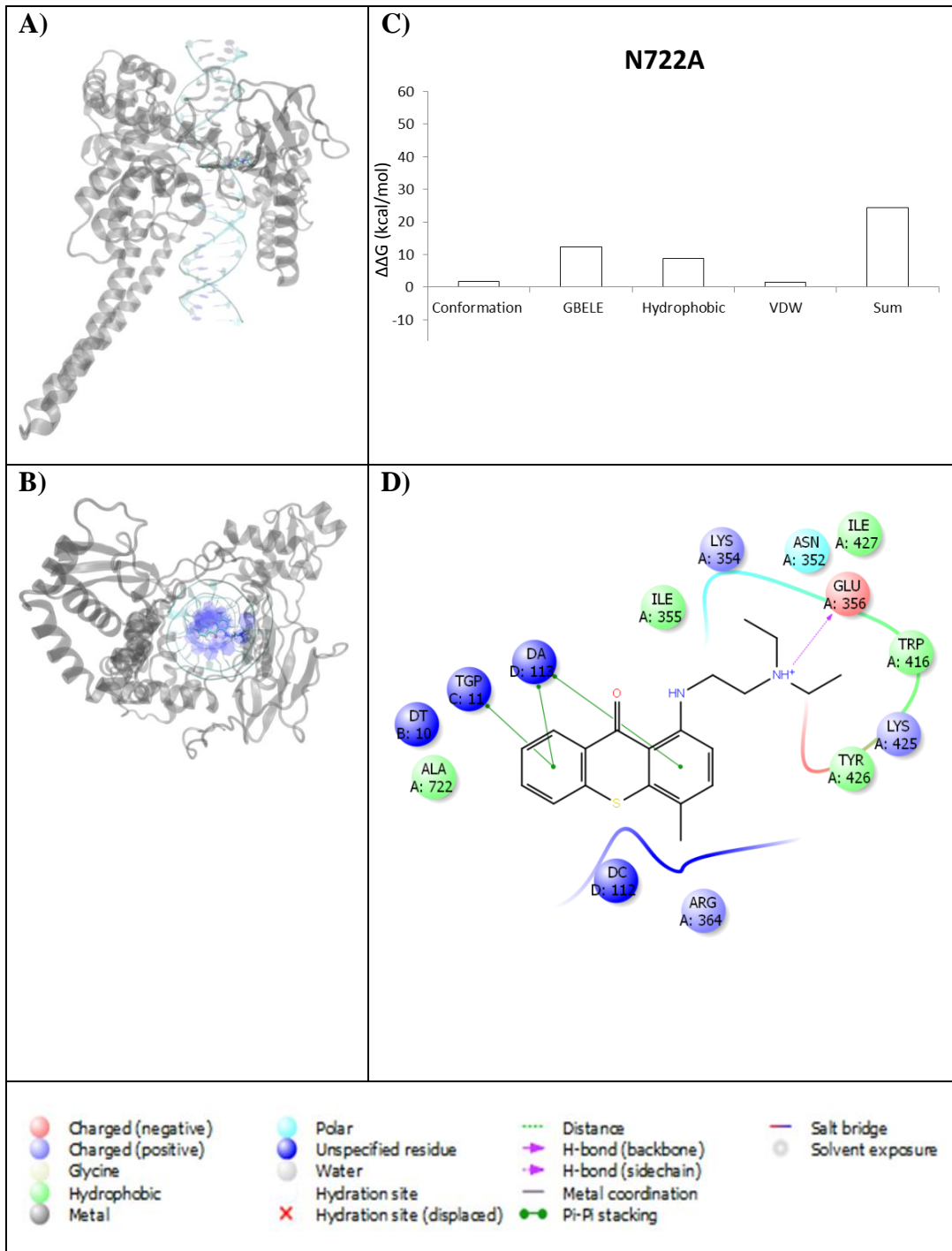


Figure S75. Lucanthonone Bound to Complex N722S. **A)** 3D top view of complex **B)** 3D side view of complex **C)** Decomposition of  $\Delta\Delta G$  **D)** 2D Representation of the binding within the complex

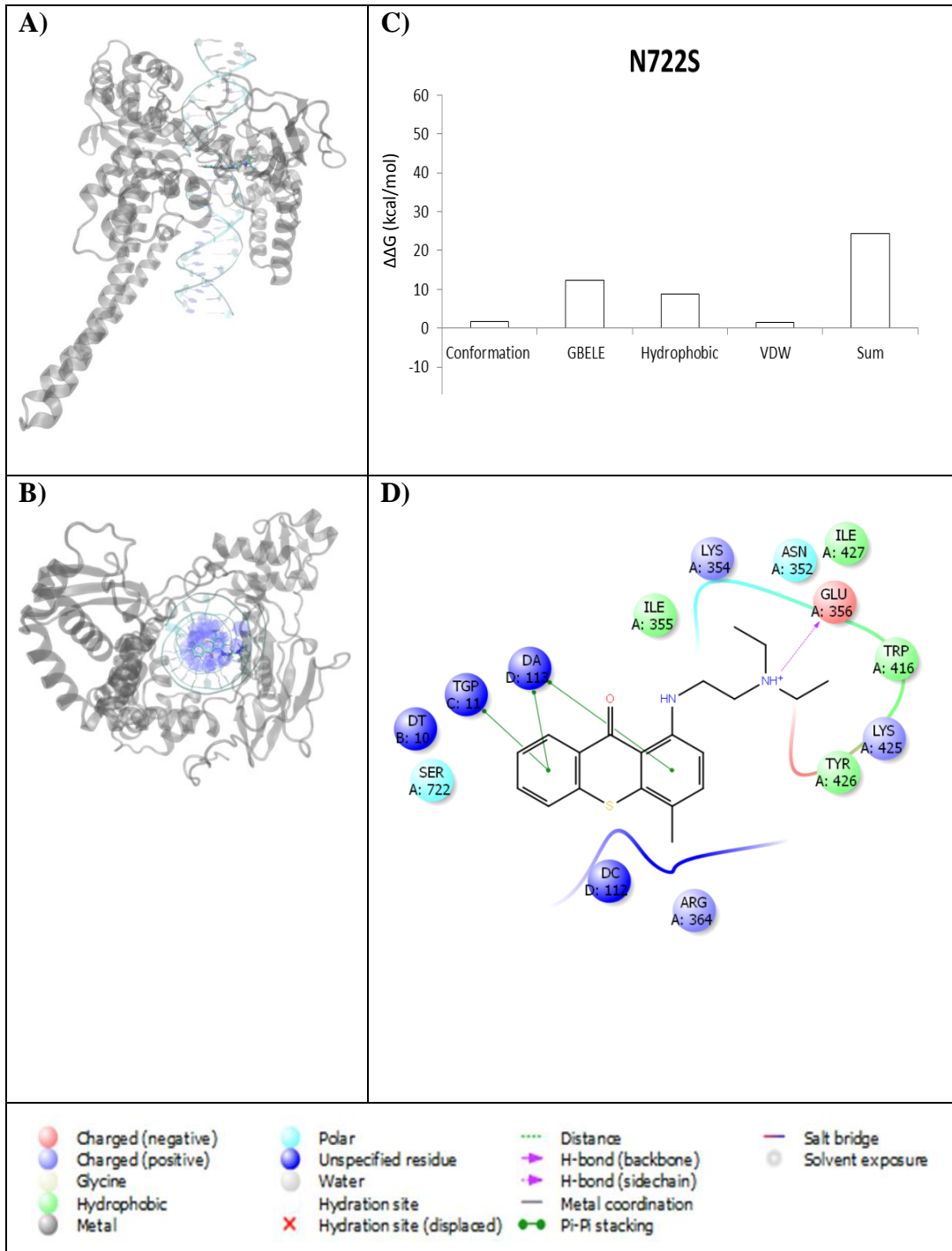


Figure S76. Lucanthonone Bound to Complex G717V. **A)** 3D top view of complex **B)** 3D side view of complex **C)** Decomposition of  $\Delta\Delta G$  **D)** 2D Representation of the binding within the complex

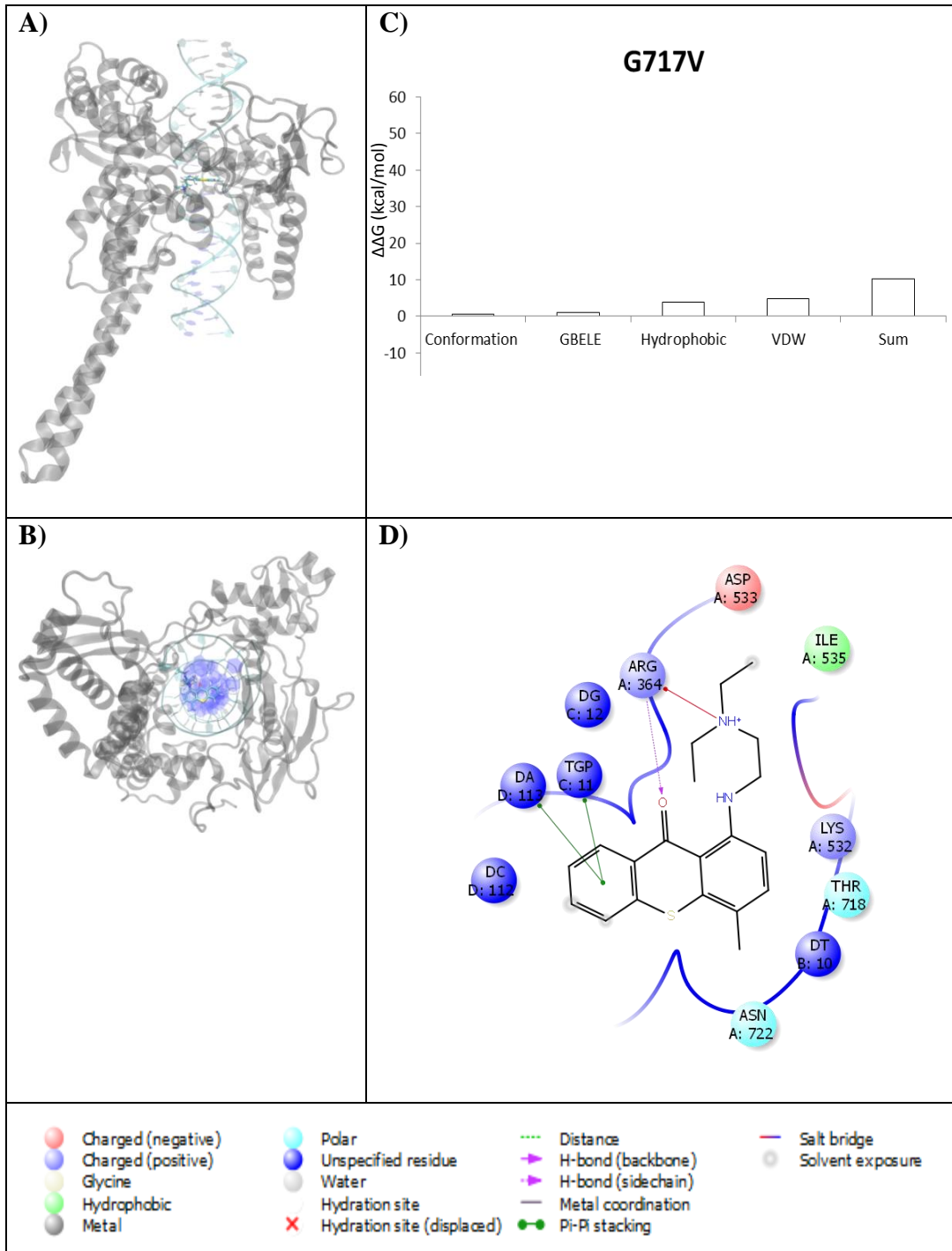


Figure S77. Lucanthonone Bound to Complex D533G. **A)** 3D top view of complex **B)** 3D side view of complex **C)** Decomposition of  $\Delta\Delta G$  **D)** 2D Representation of the binding within the complex

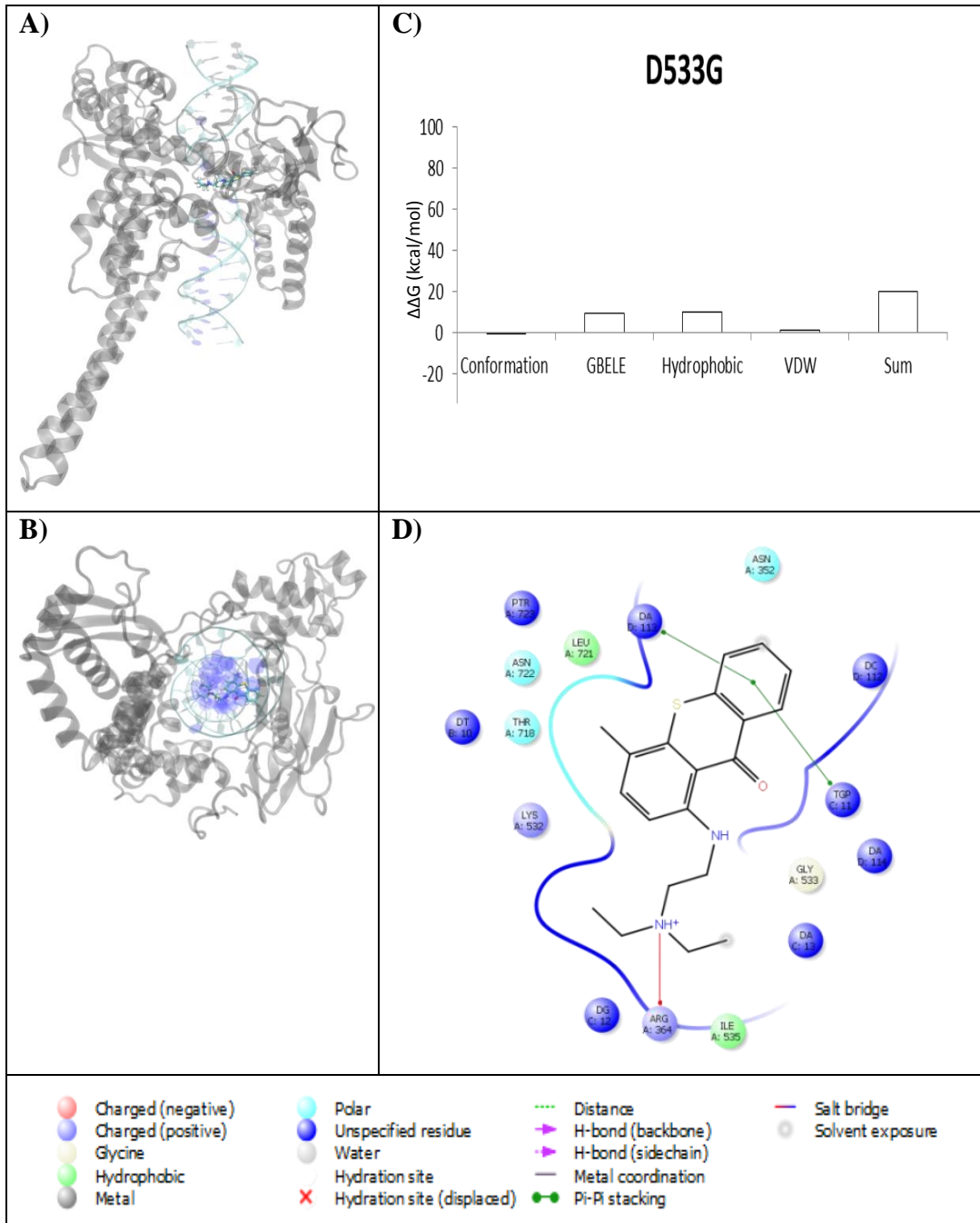


Figure S78. Lucanthonone Bound to Complex D533N. **A)** 3D top view of complex **B)** 3D side view of complex **C)** Decomposition of  $\Delta\Delta G$  **D)** 2D Representation of the binding within the complex

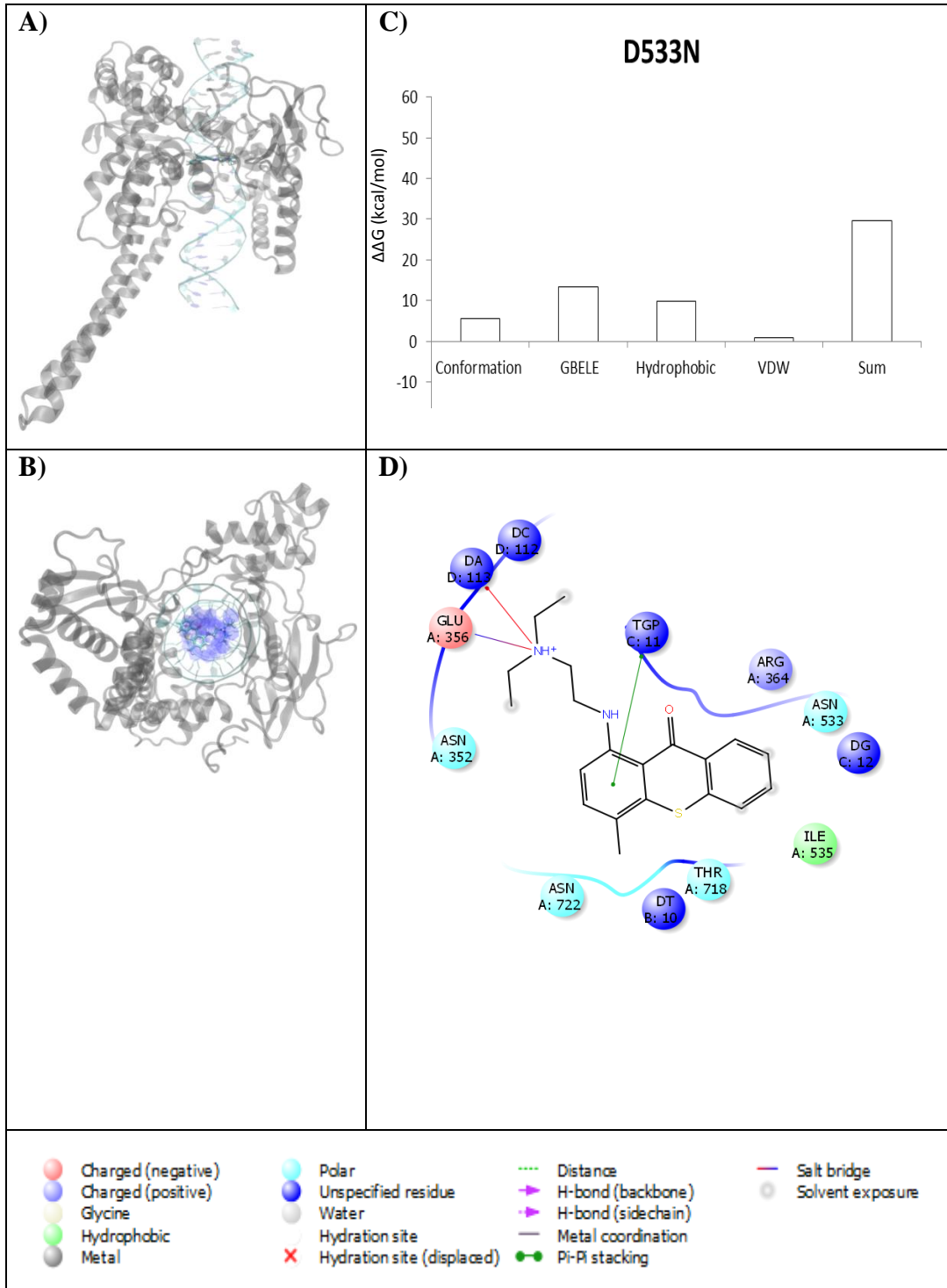


Figure S79. Lucanthone Bound to Complex G503S. **A)** 3D top view of complex **B)** 3D side view of complex **C)** Decomposition of  $\Delta\Delta G$  **D)** 2D Representation of the binding within the complex

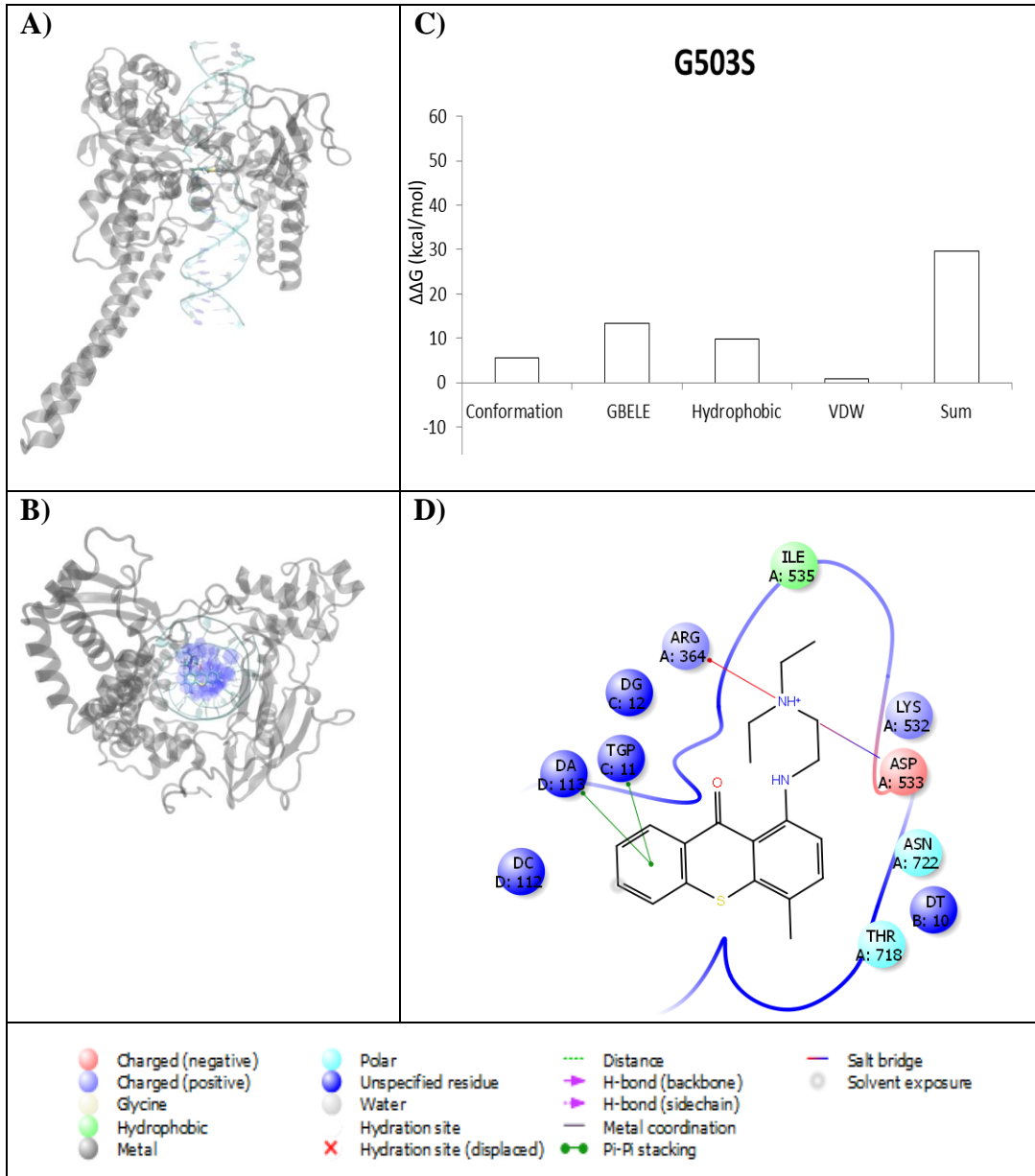


Figure S80. Lucanthonone Bound to Complex R364H. **A)** 3D top view of complex **B)** 3D side view of complex **C)** Decomposition of  $\Delta\Delta G$  **D)** 2D Representation of the binding within the complex

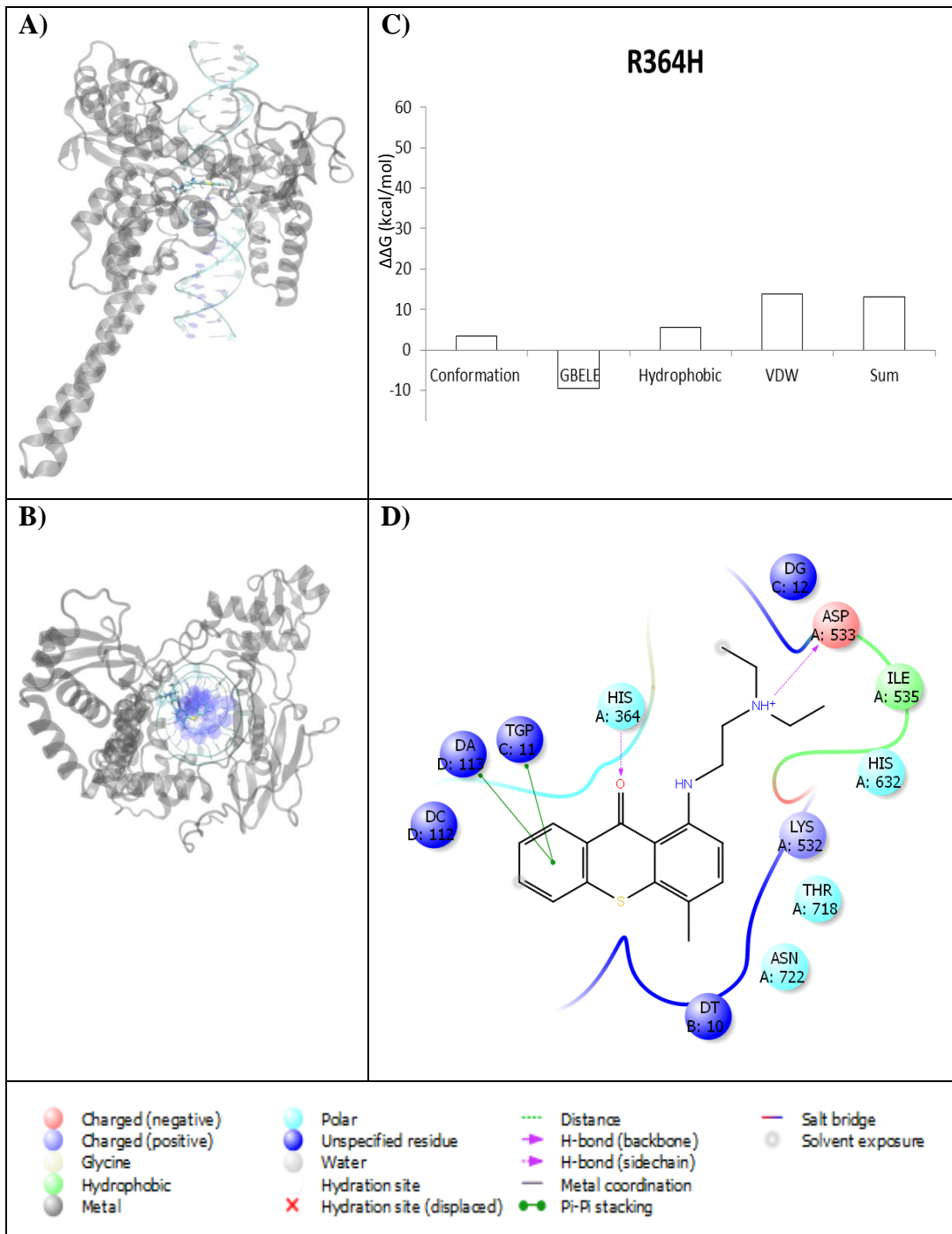




Figure S81. Lucanthonone Bound to Complex F361S. **A)** 3D top view of complex **B)** 3D side view of complex **C)** Decomposition of  $\Delta\Delta G$  **D)** 2D Representation of the binding within the complex

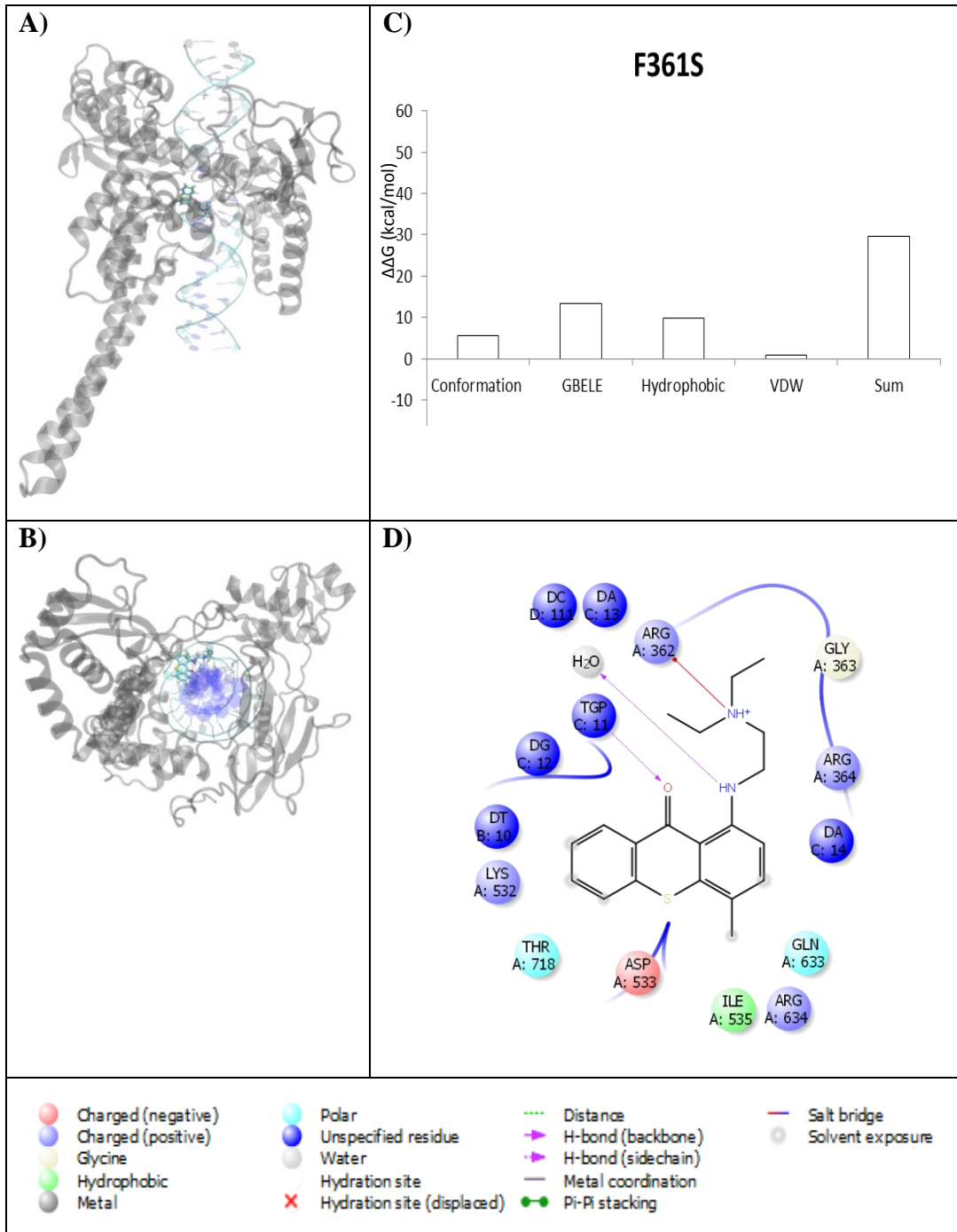




Figure S82. Lucanthonone Bound to Complex G363C. **A)** 3D top view of complex **B)** 3D side view of complex **C)** Decomposition of  $\Delta\Delta G$  **D)** 2D Representation of the binding within the complex

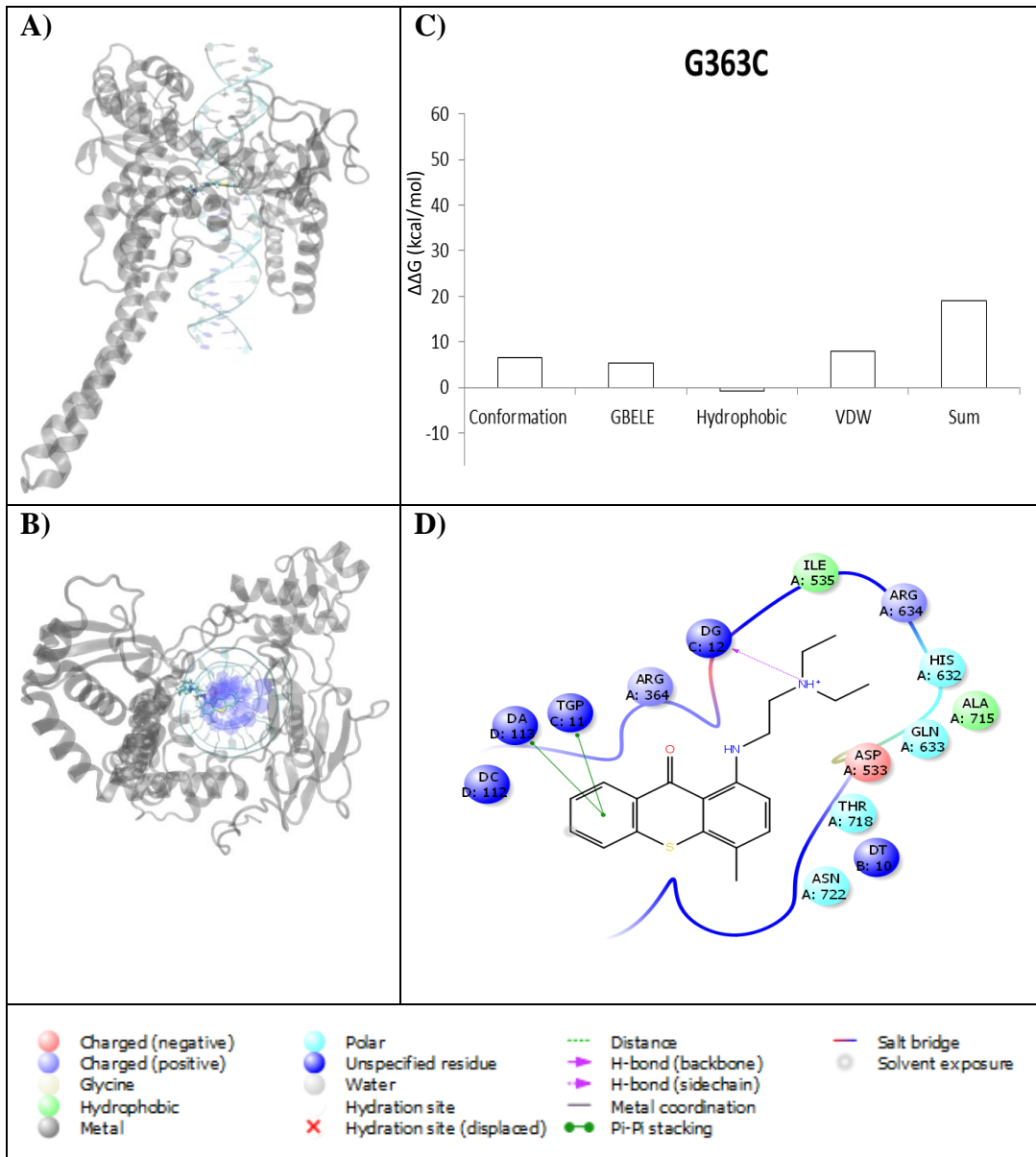
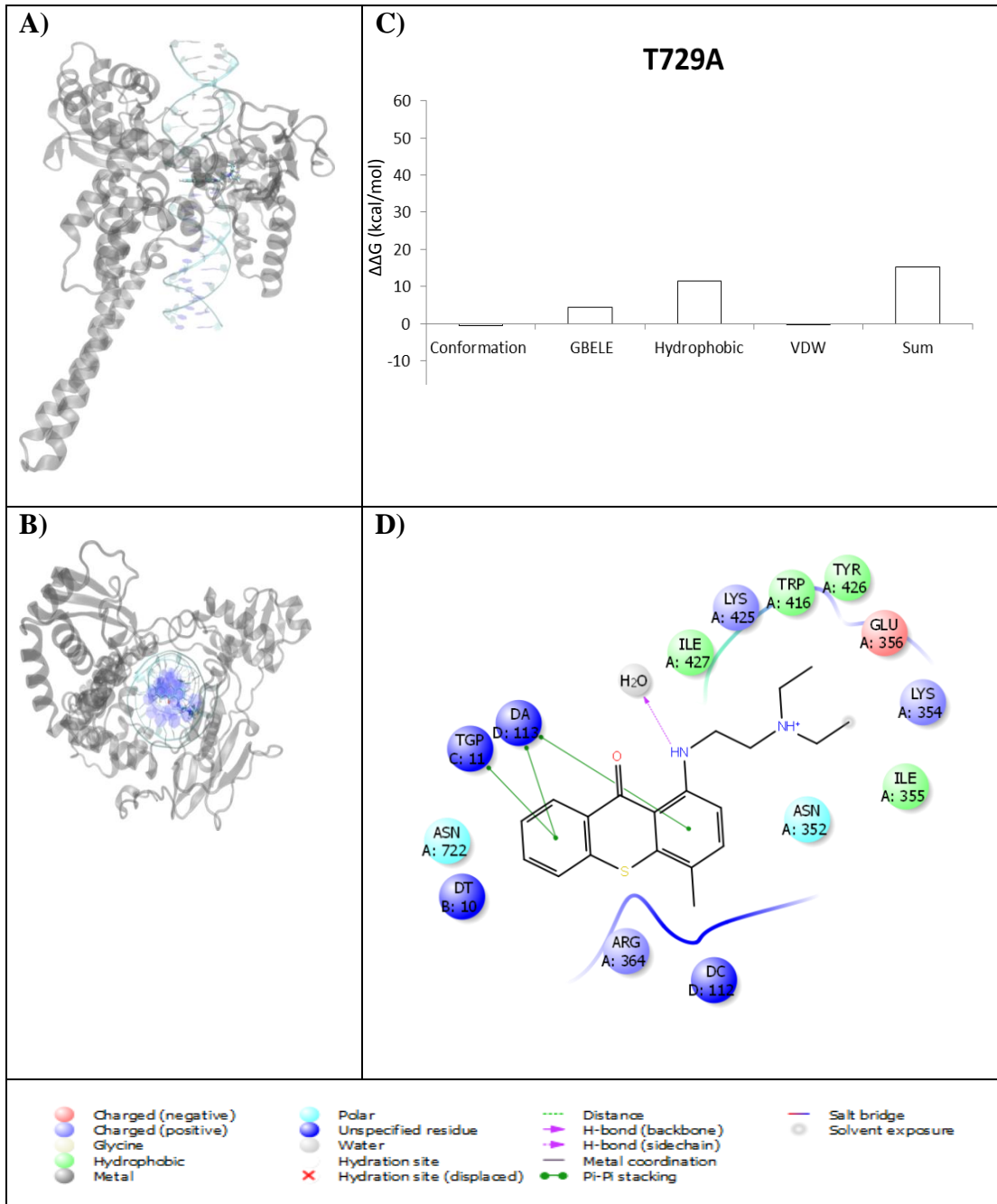


Figure S83. Lucahthone Bound to Complex T729A. **A)** 3D top view of complex **B)** 3D side view of complex **C)** Decomposition of  $\Delta\Delta G$  **D)** 2D Representation of the binding within the complex



## Appendix B

### Binding of Telomestatin to a Telomeric G-Quadruplex DNA Probed by All-Atom Molecular Dynamics Simulations

**Figure S84.** Initial structures of the first two simulation systems. 5' and 3' are indicated by a red and blue ball, respectively.

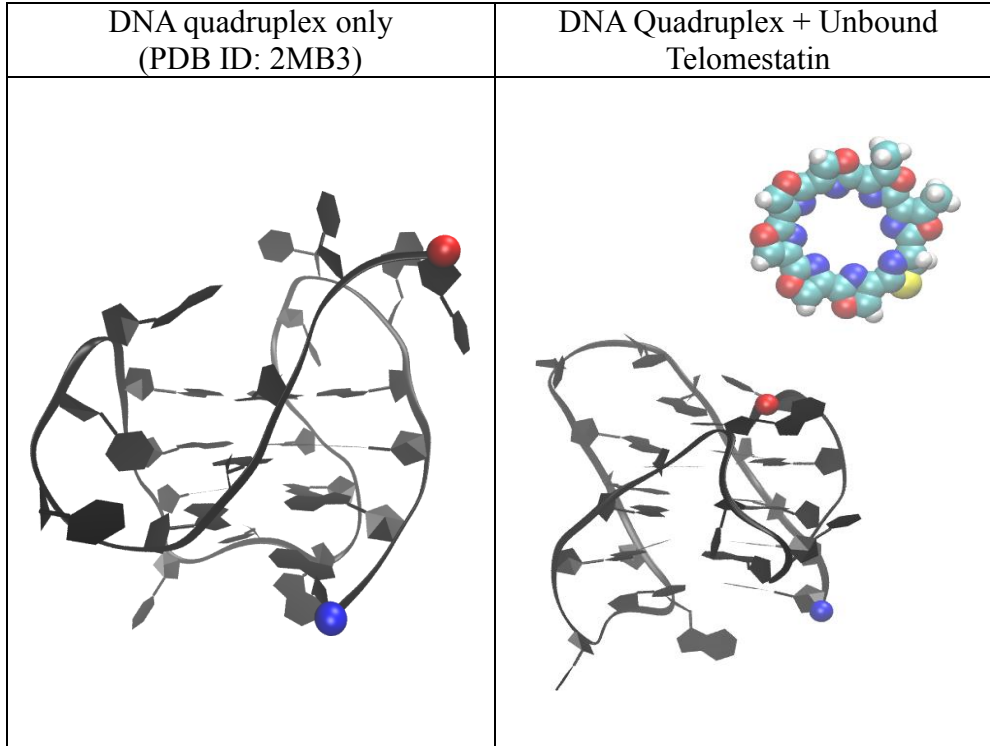
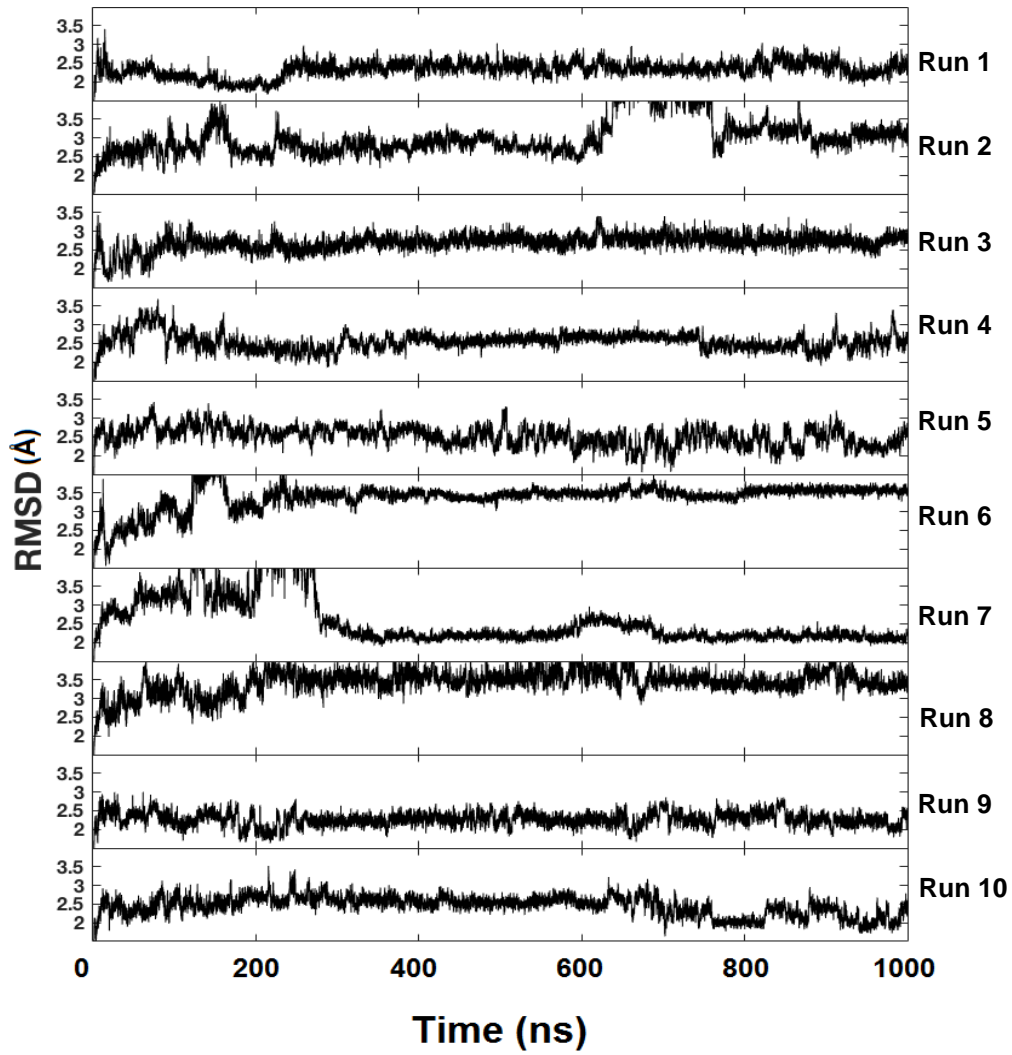
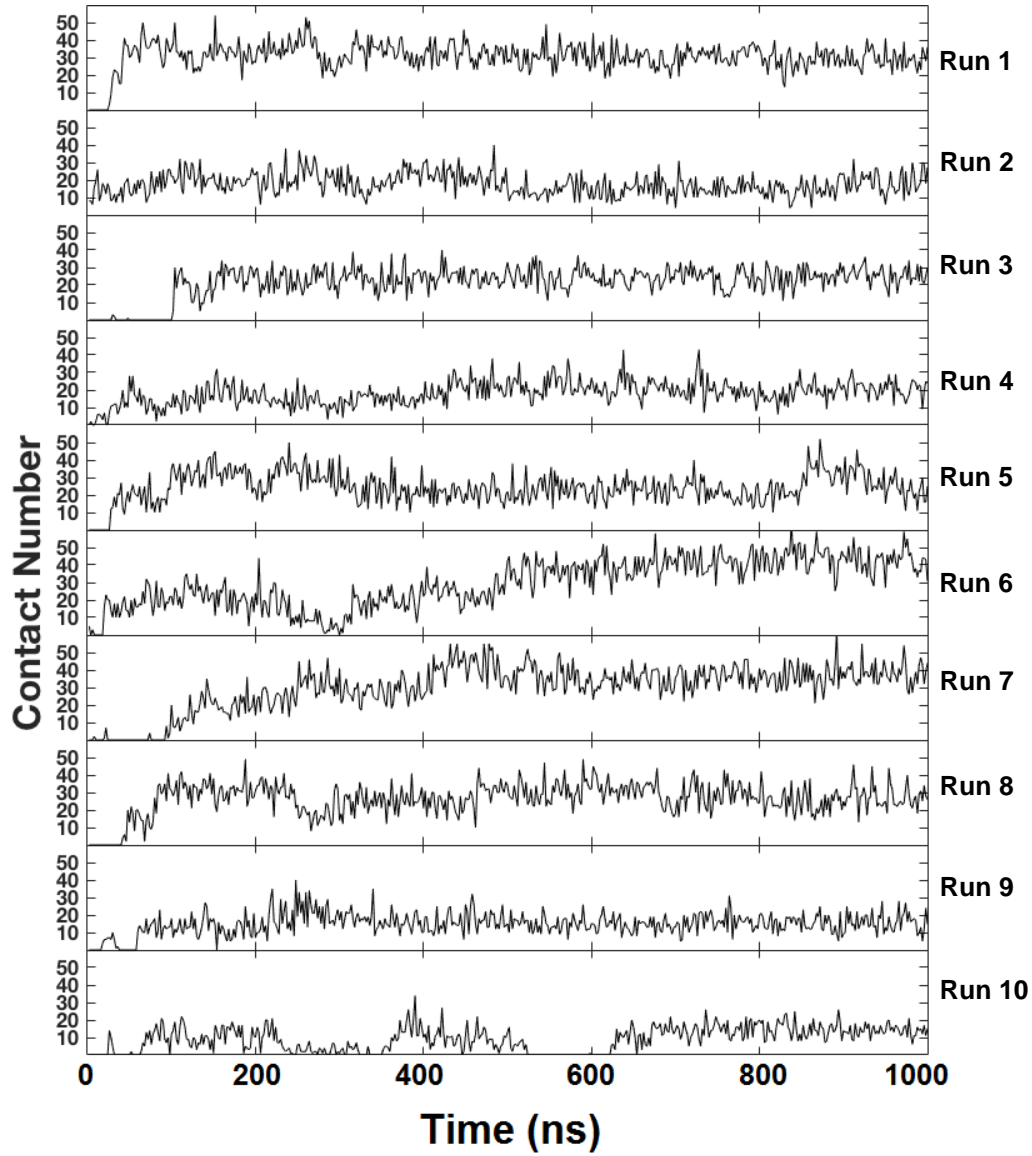


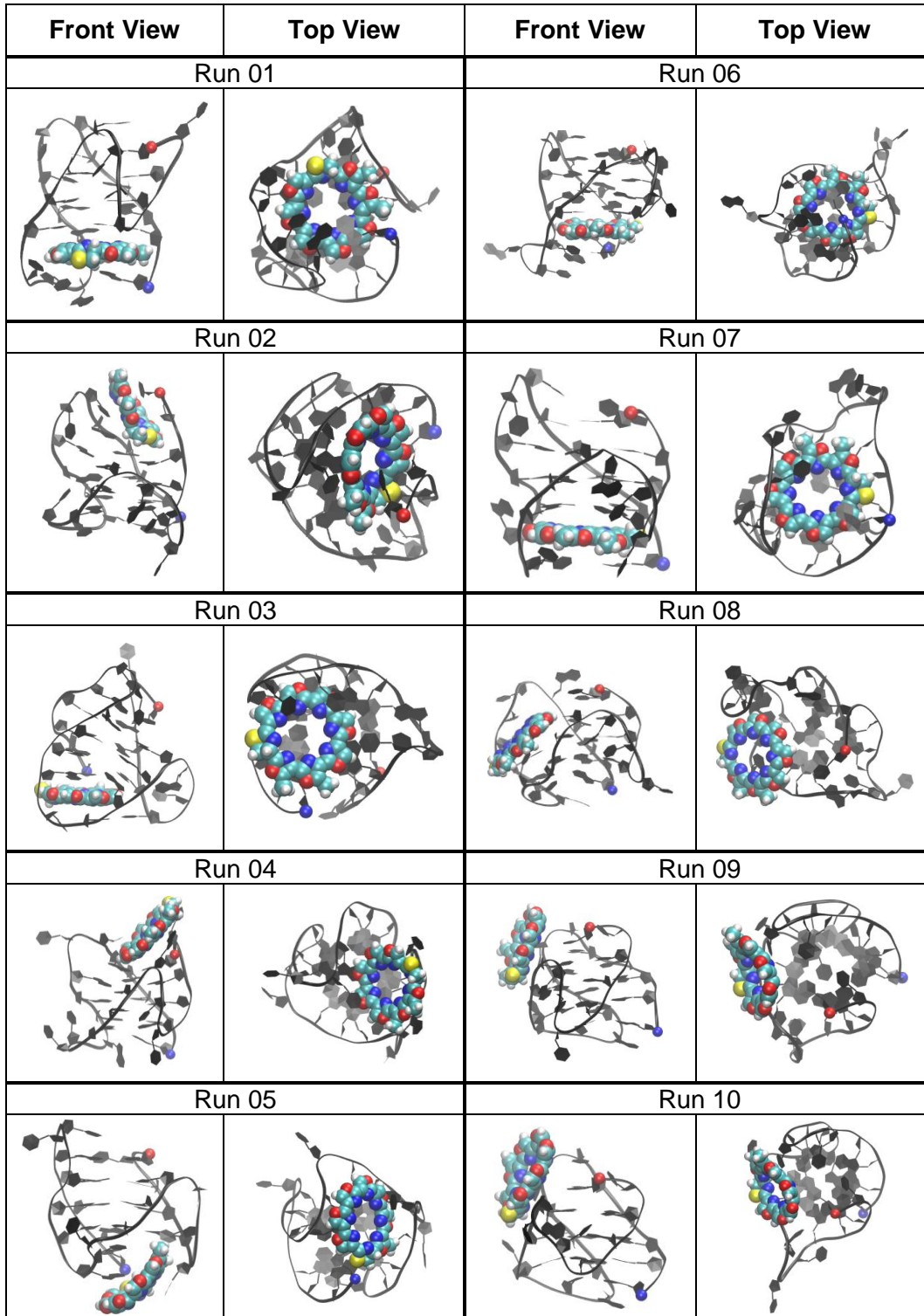
Figure S85. RMSD of system and ligand of each trajectory



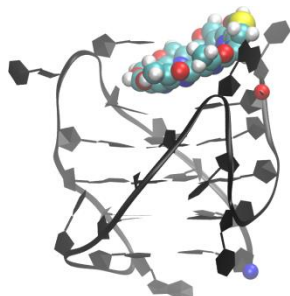
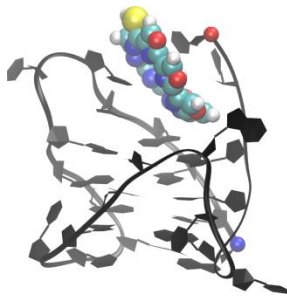
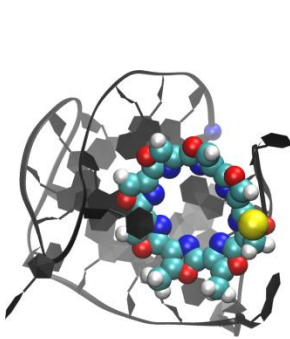
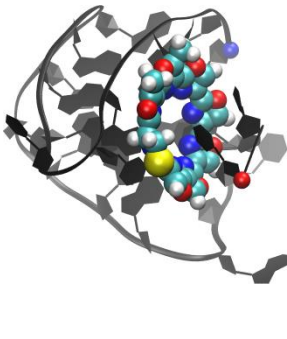
**Figure S86.** The contact number between telomeric G-quadruplex DNA and Telomestatin in ten runs.



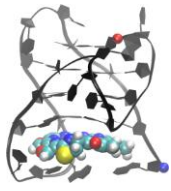
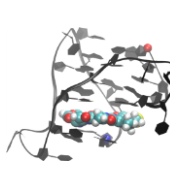
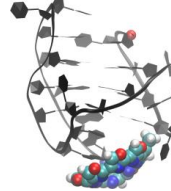
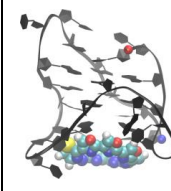
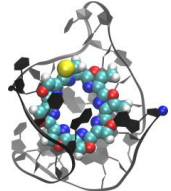

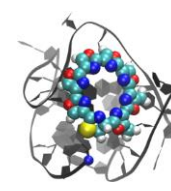
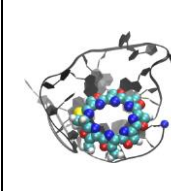
**Figure S87.** Last snapshots of quadruplex-telemestatin simulations (system 1, 1000 ns). 5' and 3' arced cd indicated by a red and blue ball, respectively.



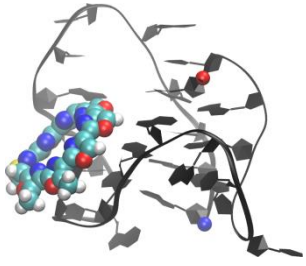
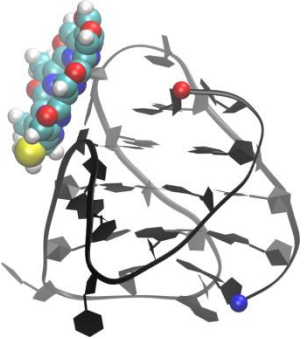
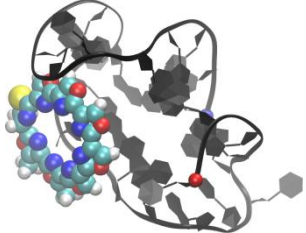
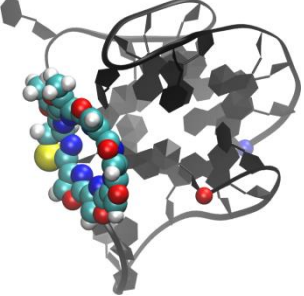
**Figure S88.** Representative structures of the most populated complex structure families (population  $\geq 1\%$ ) from the clustering analysis of the combined binding trajectories. 5' and 3' are indicated by a red and blue ball, respectively.

Binding model	End Stacking (Top)	
Cluster ID	A1	A2
Representative Structure (Front View)		
Representative Structure (Top View)		
Population (MMGBSA binding energy)	13% (-24.64 kcal/mol)	3% (-21.44 kcal/mol)

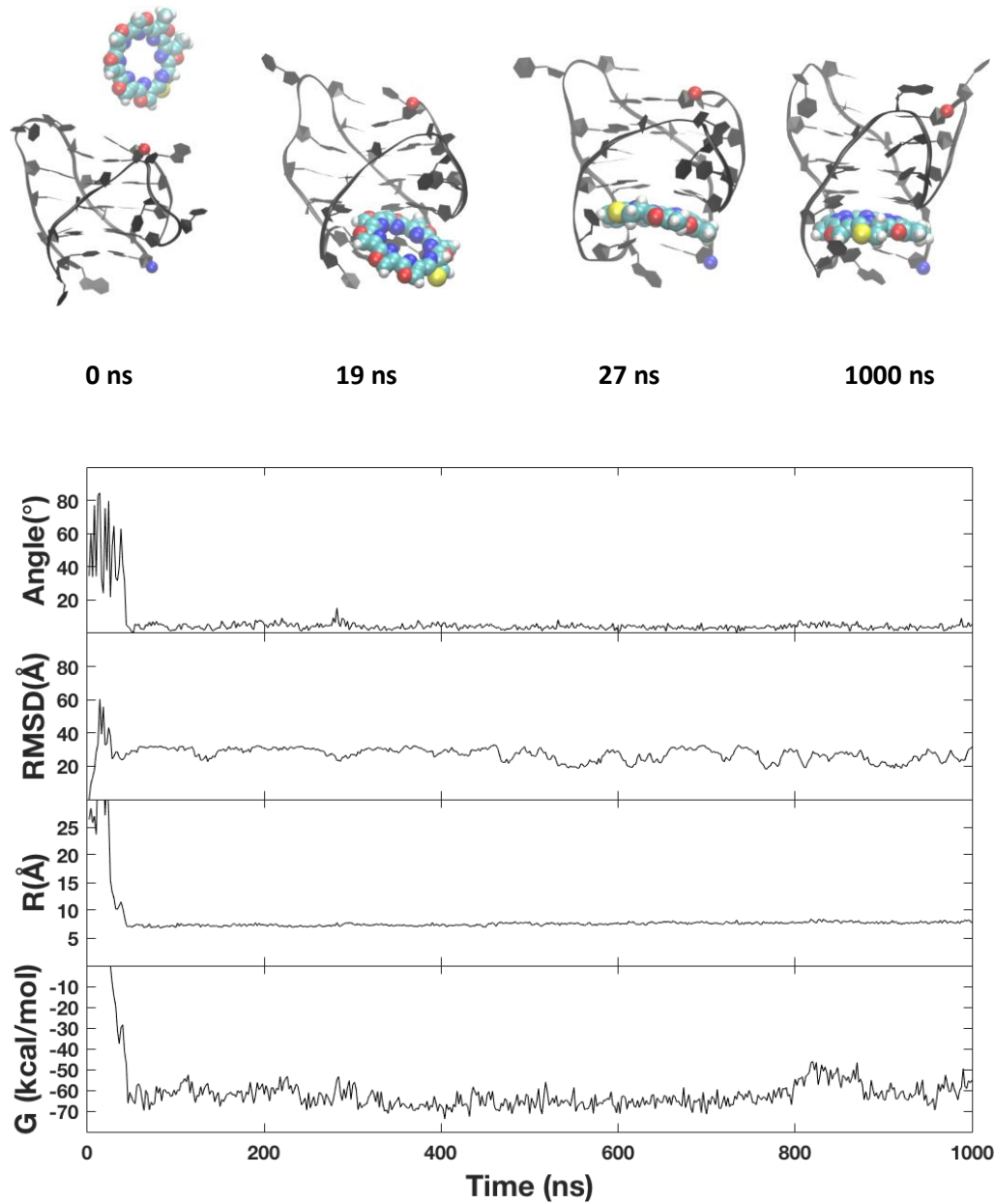


Binding model	End Stacking (Bottom)			
Cluster ID	B1	B2	B3	B4
Representative Structure (Front View)				
Representative Structure (Top View)				
Population (MMGBSA binding energy)	37% (-65.49 kcal/mol)	13% (-33.11 kcal/mol)	11% (-63.03 kcal/mol)	2 % (-28.79 kcal/mol)

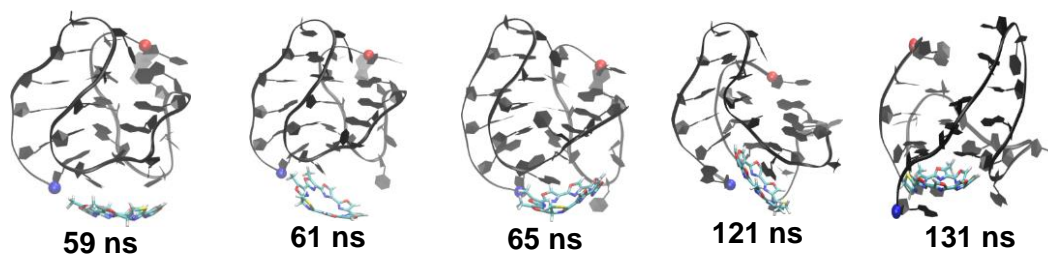


Binding model	Groove Binding	
Cluster ID	C1	C2
Representative Structure (Front View)		
Representative Structure (Top View)		
Population (MMGBSA binding energy)	13% (-32.57 kcal/mol)	3% (-16.65 kcal/mol)

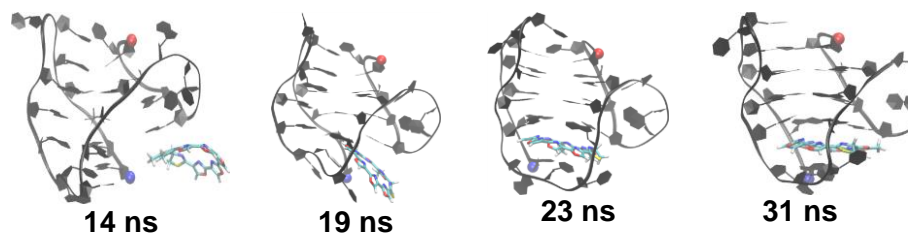
**Figure S89.** Additional trajectory of the bottom end stacking mode. **Top:** representative structures with time annotation. 5' and 3' are indicated by a red and blue ball, respectively. **Bottom:** Center-to-center distance (**R**), the drug-base dihedral angle, ligand RMSD and MM-GBSA binding energy (**G**).



**Figure S90.** The time evolution of flip-intercalation seen in the bottom end stacking mode of telomestatin-quaruplex.



**Figure S91.** A time evolution of intercalation of telomestatin into the short loop of the G-quadruplex. This can be seen in bottom end stacking mode.



**Figure S92.** AMBER GAFF force field of Telomestatin in Mol2 format.

@<TRIPOS>MOLECULE

ZINC03975327

56 64 0 0 0

SMALL

USER\_CHARGES

@<TRIPOS>ATOM

1 C1	-1.7520	8.7965	-4.4785	C.3	1 TEL	-0.0756
2 C2	-1.5640	7.4833	-3.7635	C.2	1 TEL	0.0245
3 C3	-2.5316	6.5930	-3.4550	C.2	1 TEL	0.0532
4 N1	-1.9403	5.5571	-2.7937	N.2	1 TEL	-0.3885
5 C4	-0.6532	5.7934	-2.7328	C.2	1 TEL	0.2795
6 O1	-0.3957	6.9761	-3.3116	O.3	1 TEL	-0.1850
7 C5	0.3202	4.8794	-2.0972	C.2	1 TEL	0.0492
8 C6	1.6720	4.9468	-2.1590	C.2	1 TEL	0.0243
9 O2	2.1492	3.9137	-1.4412	O.3	1 TEL	-0.1912
10 C7	1.1049	3.2471	-0.9205	C.2	1 TEL	0.2039
11 N2	0.0032	3.7961	-1.3365	N.2	1 TEL	-0.3876
12 C8	1.2113	2.0673	0.0016	C.3	1 TEL	0.1684
13 H1	1.3664	2.4475	1.0202	H	1 TEL	0.1428
14 C9	2.4448	1.2090	-0.3681	C.3	1 TEL	-0.0941
15 S1	1.7183	-0.4638	-0.1457	S.3	1 TEL	-0.1953
16 C10	0.0021	-0.0041	0.0020	C.2	1 TEL	0.3015

17 N3	-0.0156	1.2977	0.0092 N.2	1 TEL	-0.4672
18 C11	-1.1596	-0.9133	0.0903 C.2	1 TEL	0.0396
19 C12	-1.1468	-2.2127	0.4918 C.2	1 TEL	0.0015
20 O3	-2.4164	-2.6613	0.4246 O.3	1 TEL	-0.1780
21 C13	-3.1874	-1.6632	-0.0212 C.2	1 TEL	0.2685
22 N4	-2.4431	-0.5933	-0.2030 N.2	1 TEL	-0.3907
23 C14	-4.6403	-1.6861	-0.2954 C.2	1 TEL	0.0621
24 C15	-5.5406	-2.6706	-0.0733 C.2	1 TEL	-0.0065
25 O4	-6.7392	-2.2198	-0.5138 O.3	1 TEL	-0.1764
26 C16	-6.5629	-0.9903	-0.9999 C.2	1 TEL	0.2706
27 N5	-5.2996	-0.6443	-0.8538 N.2	1 TEL	-0.3902
28 C17	-7.5335	-0.0626	-1.6190 C.2	1 TEL	0.0599
29 C18	-8.8509	-0.2014	-1.8716 C.2	1 TEL	-0.0034
30 O5	-9.2668	0.9449	-2.4638 O.3	1 TEL	-0.1776
31 C19	-8.2157	1.7592	-2.5646 C.2	1 TEL	0.2715
32 N6	-7.1566	1.1662	-2.0550 N.2	1 TEL	-0.3889
33 C20	-8.1119	3.1224	-3.1301 C.2	1 TEL	0.0595
34 C21	-9.0435	3.9206	-3.6893 C.2	1 TEL	-0.0033
35 O6	-8.4207	5.0705	-4.0462 O.3	1 TEL	-0.1778
36 C22	-7.1354	4.9637	-3.7082 C.2	1 TEL	0.2718
37 N7	-6.9302	3.7901	-3.1482 N.2	1 TEL	-0.3888
38 C23	-6.0183	5.9182	-3.8748 C.2	1 TEL	0.0596
39 C24	-5.9870	7.1586	-4.4026 C.2	1 TEL	-0.0045
40 O7	-4.7062	7.5936	-4.3226 O.3	1 TEL	-0.1804
41 C25	-3.9786	6.6275	-3.7560 C.2	1 TEL	0.2790

42 N8	-4.7589	5.6096	-3.4699 N.2	1 TEL	-0.3916
43 C26	2.4859	5.9821	-2.8915 C.3	1 TEL	-0.0757
44 H2	-1.9424	9.5835	-3.7488 H	1 TEL	0.0981
45 H3	-0.8507	9.0350	-5.0432 H	1 TEL	0.0919
46 H4	-2.5988	8.7209	-5.1606 H	1 TEL	0.1002
47 H5	3.2700	1.3797	0.3233 H	1 TEL	0.1400
48 H6	2.7537	1.3748	-1.4002 H	1 TEL	0.1181
49 H7	-0.2821	-2.7791	0.8048 H	1 TEL	0.2370
50 H8	-5.3414	-3.6342	0.3719 H	1 TEL	0.2385
51 H9	-9.4602	-1.0637	-1.6444 H	1 TEL	0.2384
52 H10	-10.0891	3.6877	-3.8270 H	1 TEL	0.2384
53 H11	-6.8251	7.7029	-4.8121 H	1 TEL	0.2383
54 H12	2.6914	6.8204	-2.2259 H	1 TEL	0.0983
55 H13	3.4265	5.5395	-3.2194 H	1 TEL	0.0915
56 H14	1.9286	6.3352	-3.7592 H	1 TEL	0.0983

@<TRIPOS>BOND

- 1 1 2 1
- 2 1 44 1
- 3 1 45 1
- 4 1 46 1
- 5 2 6 1
- 6 2 3 2
- 7 3 41 1
- 8 3 4 1
- 9 4 5 2

10 5 6 1  
11 5 7 1  
12 7 11 1  
13 7 8 2  
14 8 9 1  
15 8 43 1  
16 9 10 1  
17 10 11 2  
18 10 12 1  
19 12 13 1  
20 12 17 1  
21 12 14 1  
22 14 15 1  
23 14 47 1  
24 14 48 1  
25 15 16 1  
26 16 17 2  
27 16 18 1  
28 18 22 1  
29 18 19 2  
30 19 20 1  
31 19 49 1  
32 20 21 1  
33 21 22 2  
34 21 23 1



35 23 27 1  
36 23 24 2  
37 24 25 1  
38 24 50 1  
39 25 26 1  
40 26 27 2  
41 26 28 1  
42 28 32 1  
43 28 29 2  
44 29 30 1  
45 29 51 1  
46 30 31 1  
47 31 32 2  
48 31 33 1  
49 33 37 1  
50 33 34 2  
51 34 35 1  
52 34 52 1  
53 35 36 1  
54 36 37 2  
55 36 38 1  
56 38 42 1  
57 38 39 2  
58 39 40 1  
59 39 53 1

60 40 41 1

61 41 42 2

62 43 54 1

63 43 55 1

64 43 56 1